



POLITECNICO DI BARI

D. R. R. S.

01

Doctor of Philosophy in Risk and Environmental,
Territorial and Building Development

2022

Coordinator: Prof. Michele Mossa

XXXIV CYCLE
ICAR/06 – Topography and Cartography

DICATECh

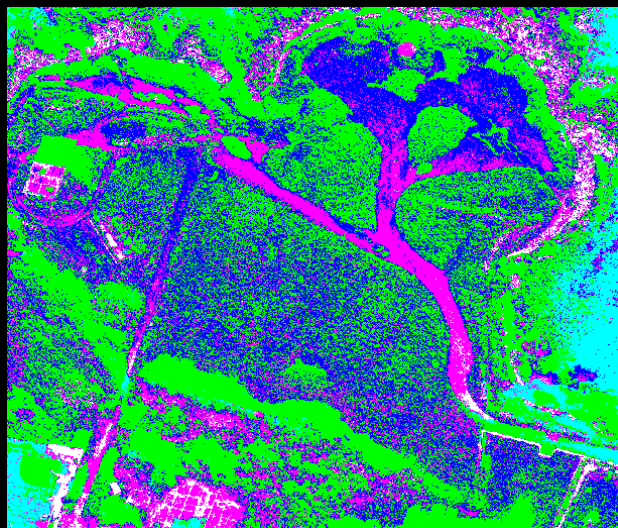
Department of Civil, Environmental, Land,
Building Engineering and Chemistry

Mirko Saponaro

**FROM LOW-COST TO HIGH-QUALITY:
A FOSS4G FRAMEWORK OF UAV PHOTOGRAMMETRIC
PROCESSING FOR GEOSPATIAL DATA EXTRACTION**

Prof. Eufemia Tarantino
DICATECh
Politecnico di Bari

Prof. Diofantos G. Hadjimitsis
Prof. Athos Agapiou
Cyprus University of Technology



La borsa di dottorato è stata cofinanziata con risorse del
Programma Operativo Nazionale Ricerca e Innovazione 2014-2020 (CCI 2014IT16M2OP005),
Fondo Sociale Europeo, Azione I.1 "Dottorati Innovativi con caratterizzazione Industriale"



UNIONE EUROPEA
Fondo Sociale Europeo



*Ministero dell'Università
e della Ricerca*



**Politecnico
di Bari**



Politecnico
di Bari

LIBERATORIA PER L'ARCHIVIAZIONE DELLA TESI DI DOTTORATO

Al Magnifico Rettore
del Politecnico di Bari

Il/la sottoscritto/a *SAPONARO MIRKO* nato/a *BARI* il *14/04/1989*

residente a *BARI (BA)* in via *STRADA STATALE 16 COMPLANARE OVEST 96/A E 96/B*
e-mail *mirko.saponaro@poliba.it / saponaromirko@gmail.com*

iscritto al 3° anno di Corso di Dottorato di Ricerca in *RISCHIO E SVILUPPO AMBIEN-
TALE, TERRITORIALE ED EDILIZIO* ciclo *XXXIV°*

ed essendo stato ammesso a sostenere l'esame finale con la prevista discussione
della tesi dal titolo:

***FROM LOW-COST TO HIGH-QUALITY: A FOSS4G FRAMEWORK OF UAV PHOTO-
GRAMMETRIC PROCESSING FOR GEOSPATIAL DATA EXTRACTION***

DICHIARA

- 1) di essere consapevole che, ai sensi del D.P.R. n. 445 del 28.12.2000, le dichiarazioni mendaci, la falsità negli atti e l'uso di atti falsi sono puniti ai sensi del codice penale e delle Leggi speciali in materia, e che nel caso ricorressero dette ipotesi, decade fin dall'inizio e senza necessità di nessuna formalità dai benefici conseguenti al provvedimento emanato sulla base di tali dichiarazioni;
- 2) di essere iscritto al Corso di Dottorato di ricerca *RISCHIO E SVILUPPO AM-
BIENTALE, TERRITORIALE ED EDILIZIO* ciclo *XXXIV°*, corso attivato ai sensi del

“Regolamento dei Corsi di Dottorato di ricerca del Politecnico di Bari”, emanato con D.R. n.286 del 01.07.2013;

- 3) di essere pienamente a conoscenza delle disposizioni contenute nel predetto Regolamento in merito alla procedura di deposito, pubblicazione e autoarchiviazione della tesi di dottorato nell'Archivio Istituzionale ad accesso aperto alla letteratura scientifica;
- 4) di essere consapevole che attraverso l'autoarchiviazione delle tesi nell'Archivio Istituzionale ad accesso aperto alla letteratura scientifica del Politecnico di Bari (IRIS-POLIBA), l'Ateneo archiverà e renderà consultabile in rete (nel rispetto della Policy di Ateneo di cui al D.R. 642 del 13.11.2015) il testo completo della tesi di dottorato, fatta salva la possibilità di sottoscrizione di apposite licenze per le relative condizioni di utilizzo (di cui al sito <http://www.creativecommons.it/Licenze>), e fatte salve, altresì, le eventuali esigenze di “embargo”, legate a strette considerazioni sulla tutelabilità e sfruttamento industriale/commerciale dei contenuti della tesi, da rappresentarsi mediante compilazione e sottoscrizione del modulo in calce (Richiesta di embargo);
- 5) che la tesi da depositare in IRIS-POLIBA, in formato digitale (PDF/A) sarà del tutto identica a quelle consegnate/inviolate/da inviarsi ai componenti della commissione per l'esame finale e a qualsiasi altra copia depositata presso gli Uffici del Politecnico di Bari in forma cartacea o digitale, ovvero a quella da discutere in sede di esame finale, a quella da depositare, a cura dell'Ateneo, presso le Biblioteche Nazionali Centrali di Roma e Firenze e presso tutti gli Uffici competenti per legge al momento del deposito stesso, e che di conseguenza va esclusa qualsiasi responsabilità del Politecnico di Bari per quanto riguarda eventuali errori, imprecisioni o omissioni nei contenuti della tesi;
- 6) che il contenuto e l'organizzazione della tesi è opera originale realizzata dal sottoscritto e non compromette in alcun modo i diritti di terzi, ivi compresi quelli relativi alla sicurezza dei dati personali; che pertanto il Politecnico di Bari ed i suoi funzionari sono in ogni caso esenti da responsabilità di qualsivoglia

natura: civile, amministrativa e penale e saranno dal sottoscritto tenuti indenni da qualsiasi richiesta o rivendicazione da parte di terzi;

- 7) che il contenuto della tesi non infrange in alcun modo il diritto d'Autore né gli obblighi connessi alla salvaguardia di diritti morali ed economici di altri autori o di altri aventi diritto, sia per testi, immagini, foto, tabelle, o altre parti di cui la tesi è composta.

Luogo e data
BARI, 07/12/2021

Firma

A handwritten signature in black ink, consisting of a stylized initial 'A' followed by a surname.

Il/La sottoscritto, con l'autoarchiviazione della propria tesi di dottorato nell'Archivio Istituzionale ad accesso aperto del Politecnico di Bari (POLIBA-IRIS), pur mantenendo su di essa tutti i diritti d'autore, morali ed economici, ai sensi della normativa vigente (Legge 633/1941 e ss.mm.ii.),

CONCEDE

- al Politecnico di Bari il permesso di trasferire l'opera su qualsiasi supporto e di convertirla in qualsiasi formato al fine di una corretta conservazione nel tempo. Il Politecnico di Bari garantisce che non verrà effettuata alcuna modifica al contenuto e alla struttura dell'opera.
- al Politecnico di Bari la possibilità di riprodurre l'opera in più di una copia per fini di sicurezza, back-up e conservazione.

Luogo e data
BARI, 07/12/2021

Firma

A handwritten signature in black ink, identical to the one above, consisting of a stylized initial 'A' followed by a surname.



POLITECNICO DI BARI

D.R.R.S

01

PhD Program in Environmental and Building Risk and Development

2022

Coordinator: Prof. Michele Mossa

XXXIV CYCLE
ICAR/06 – Topography and Cartography

DICATECh

Department of Civil, Environmental, Building Engineering and Chemistry

**FROM LOW-COST TO HIGH-QUALITY:
A FOSS4G FRAMEWORK OF UAV PHOTOGRAMMETRIC
PROCESSING FOR GEOSPATIAL DATA**

Prof. Eufemia Tarantino
DICATECh
Politecnico di Bari

Prof. Diofantos G. Hadjimitsis
Prof. Athos Agapiou
Cyprus University of Technology

Mirko Saponaro



POLITECNICO DI BARI

D.R.R.S

01

Dottorato di Ricerca in Rischio e Sviluppo
ambientale, territoriale ed edilizio

2022

Coordinatore: Prof. Michele Mossa

XXXIV Ciclo
ICAR/06 - Topografia e Cartografia

DICATECh

Dipartimento di Ingegneria Civile, Ambientale,
del Territorio, Edile e di Chimica

**Dal Basso Costo all'Alta Qualità:
Un Framework FOSS4G di Processamenti
fotogrammetrici basati su UAV per l'Estrazione di
Dati Geospaziali**

Prof. Eufemia Tarantino
DICATECh
Politecnico di Bari

Prof. Diofantos G. Hadjimitsis
Prof. Athos Agapiou
Cyprus University of Technology

Mirko Saponaro

EXTENDED ABSTRACT (eng)

One of the topics of Earth sciences most encouraged by the Big Data revolution is related to Earth Observation technologies and techniques. Recent developments in Remote Sensing and computing techniques have triggered an explosive growth of this data. New satellite, airborne, and terrestrial systems characterised by high spatial, temporal, and radiometric resolution are continuously evolving, and the large masses of data thus flow into Big Geospatial Data, geared to cross-sectorally help multiple industries and academia with a new approach. Whereas this data contains powerful information, it is at the same time heterogeneous, multi-source, multi-temporal, multi-scale, highly dimensional, highly complex, and unstructured, and difficulties emerged in data storage, processing, validation of results and even analysis. From the hardware perspective, the introduction of low-cost computers and sensors has expanded the potential for data acquisition. On the software side, the adoption of increasingly performant and specialised Free and Open-Source Software for Geospatial (FOSS4G) platforms is revolutionising the way of working, driving a shift towards open science, knowledge sharing, accessibility and reproducibility. It is evident that these renovations require the tailored implementation of high-level value chain frameworks. Given the numerous challenges in this field in which the scientific community appears to be rigorously engaged, an increasing share of interest is being placed in the progress of Unmanned Aerial Vehicles (UAVs). Aerial imagery captured by UAVs is playing an increasingly important role in various industries due to its efficiency, flexibility, transversality, and versatility of use. However, UAV technologies and techniques based on them are still under development and several problems need to be solved. Among the many already discussed by the scientific community, it was pointed out that manual interpretation and analysis of integrated data is no longer ade-

quate, which is why sophisticated automatic analysis methods are needed to make the process efficient and effective. This dissertation thus seeks to develop a FOSS4G framework for pre-processing and post-processing of photogrammetric products, useful for the automatic extraction of near real-time information applied to high-resolution, multiscale, multi-temporal, and multi-sensor data for environmental monitoring and technical inspection of buildings. Therefore, it goes through the structure focusing on the currently low-cost UAV platforms equipped with economic sensors, on the configuration and optimisation of the field acquisition and pre-processing activities in order to reduce both the ancillary costs and the effort of operations and, at the same time, testing different methodologies to extract information from data characterised by different spectral and spatial resolutions. The validation procedures of the products obtainable from the process chain are proposed to identify their placement among the different more usual alternatives of Earth Observation data. As a result, this thesis reconstructs a repeatable and reproducible procedure, tests and validates the products that can be rendered, and proposes innovative image-based and point-based analysis methods. The work therefore sought to address some of the limitations regarding the collection and pre-processing of information in a timely and cost-effective manner, and the lack of an accredited framework for processing photogrammetric data that could be considered reproducible, repeatable, and widely accessible in the context of the Data Science democratisation. The strategic placement of UAV-based products among those of more established technologies is thus theorised and validated. Finally, the work proposes a response to the complexity of dealing with high spectral and spatial resolution data, such as large amounts of data in real-time applications, to extract targeted information to solve specific issues. Hence, the process of structuring the current research work goes through four main stages: (1) conceptual maturation of the platforms and sensors and their integration, (2) structuring of a FOSS4G processing framework, (3) geometric and radiometric pre-processing of the acquired datasets, and (4) image-based and point-based analysis and information extraction. In view of all this, the main contributions of this thesis were to organize a comprehensive open-source framework ranging from acquisition

strategy and georeferencing step, geometric and radiometric pre-processing, output processing, and analysis. At the same time, to apply open methodologies for pixel-based and point-based analysis of producible photogrammetric results for multi-scale, multi-temporal, and multi-sensor surveys, and achieve these targets with high quality but using low-cost technologies and techniques to increase their accessibility. Important technical and technological implications, based on the automation of operations, result from the adoption of the proposed framework.

key words

Unmanned Aerial Vehicle, Big Spatial Data, FOSS4G, Photogrammetry, Geospatial Data Extraction, Low-Cost, High-Quality.

EXTENDED ABSTRACT (ita)

Uno degli argomenti delle scienze della Terra più incoraggiati dalla rivoluzione dei Big Data è legato alle tecnologie e alle tecniche di Osservazione della Terra. I recenti sviluppi nel Telerilevamento e nelle tecniche di calcolo hanno innescato una crescita esplosiva di questi dati. Nuovi sistemi satellitari, aerei e terrestri caratterizzati da un'alta risoluzione spaziale, temporale e radiometrica sono in continua evoluzione, e le grandi masse di dati confluiscono così nei Big Geospatial Data, orientati ad aiutare in modo intersettoriale molteplici industrie e il mondo accademico con un nuovo approccio. Mentre questi dati contengono importanti informazioni, sono allo stesso tempo eterogenei, multi-sorgente, multi-temporali, multi-scala, altamente dimensionali, altamente complessi e non strutturati, e sono emerse difficoltà nell'archiviazione dei dati, nell'elaborazione, nella convalida dei risultati e anche nella loro analisi. Dal punto di vista dell'hardware, l'introduzione di computer e sensori a basso costo ha ampliato il potenziale di acquisizione dei dati. Dal punto di vista software, l'adozione di piattaforme sempre più performanti e specializzate Free and Open Source Software for Geospatial (FOSS4G) sta rivoluzionando il modo di lavorare, guidando un orientamento verso la scienza aperta, la condivisione delle conoscenze, l'accessibilità e la riproducibilità. È evidente che questi rinnovamenti richiedono l'implementazione su misura di frame della catena del valore di alto livello. Date le numerose sfide in questo campo in cui la comunità scientifica sembra essere rigorosamente impegnata, una quota crescente di interesse viene posta nel progresso degli Unmanned Aerial Vehicles (UAV), Sistemi Aeromobili a Pilotaggio Remoto. Le immagini aeree catturate dagli UAV stanno giocando un ruolo sempre più importante in varie industrie grazie alla loro efficienza, flessibilità, trasversalità e versatilità d'uso. Tuttavia, le tecnologie UAV e le tecniche basate su di esse sono ancora in fase di sviluppo e diversi problemi de-

vono essere risolti. Tra i molti già discussi dalla comunità scientifica, è stato evidenziato che l'interpretazione e l'analisi manuale dei dati integrati non sono più adeguate, motivo per cui sono necessari sofisticati metodi di analisi automatica per rendere il processo efficiente ed efficace. Questa tesi cerca quindi di sviluppare un framework FOSS4G per il pre-processing e post-processing di prodotti fotogrammetrici, utile per l'estrazione automatica di informazioni quasi in tempo reale, applicati a dati ad alta risoluzione, multi-scala, multi-temporali e multi-sensore per il monitoraggio ambientale e l'ispezione tecnica degli edifici. Si percorre quindi la struttura concentrandosi sulle piattaforme UAV attualmente a basso costo dotate di sensori economici, sulla configurazione e ottimizzazione delle attività in campo di acquisizione e preelaborazione al fine di ridurre sia i costi accessori che il sovraccarico delle operazioni e, allo stesso tempo, testando diverse metodologie per estrarre informazioni da dati caratterizzati da diverse risoluzioni spettrali e spaziali. Vengono proposte le procedure di validazione dei prodotti ottenibili dalla catena di processo per individuare la loro collocazione tra le diverse alternative più consuete dei dati di Osservazione della Terra. Come risultato, questa tesi dà forma ad una procedura ripetibile e riproducibile, testa e convalida i prodotti che possono essere restituiti, e propone metodi innovativi di analisi basati sul trattamento di immagini e sui punti. Il lavoro ha quindi cercato di affrontare alcune delle limitazioni riguardanti la raccolta e la preelaborazione delle informazioni in modo tempestivo ed economico, e la mancanza di un quadro accreditato per l'elaborazione dei dati fotogrammetrici che possa essere considerato riproducibile, ripetibile e ampiamente accessibile nel contesto della democratizzazione della Data Science. Viene così teorizzata e validata la collocazione strategica dei prodotti basati su UAV tra quelli di tecnologie più consolidate. Infine, il lavoro propone una risposta alla complessità nel trattamento e gestione di dati ad alta risoluzione spettrale e spaziale, come le grandi quantità di dati nelle applicazioni in tempo reale, per estrarre informazioni mirate per risolvere problemi specifici. Quindi, il processo di strutturazione del presente lavoro di ricerca passa attraverso quattro fasi principali: (1) maturazione concettuale delle piattaforme e dei sensori e la loro integrazione, (2) strutturazione di un quadro di elaborazione FOSS4G, (3) preelaborazione geometrica e radiometrica dei dataset ac-

quisiti, e (4) analisi ed estrazione di informazioni basate su immagini e punti. In vista di tutto ciò, i principali contributi di questa tesi alla ricerca sono stati quelli di organizzare un quadro completo open-source che andasse dalla strategia di acquisizione e la fase di georeferenziazione, passando per la preelaborazione geometrica e radiometrica, sino all'elaborazione dell'output e l'analisi. Allo stesso tempo, anche quella di applicare metodologie aperte per l'analisi basata sui pixel e sui punti derivati da processamenti fotogrammetrici ottenibili da indagini multi-scala, multi-temporali e multi-sensore, e di raggiungere questi obiettivi con alta qualità ma utilizzando tecnologie e tecniche a basso costo per aumentarne l'accessibilità. Importanti implicazioni tecniche e tecnologiche, basate sull'automazione delle operazioni, risultano dall'adozione del quadro proposto.

key words

Sistemi Aeromobili a Pilotaggio Remoto, Big Spatial Data, FOSS4G, Fotogrammetria, Estrazione di Dati Geospaziali, Basso-Costo, Alta-Qualità.

INDUSTRIAL PHD THESIS

This PhD project belongs to the Italian “National Operative Program of Research and Innovation 2014-2020” which promotes innovation in research, believing in the synergic collaboration among European Universities and Italian industrial companies. It may achieve reciprocal advantages in information, production, commercial, and products that can have very significant results. This collaboration aims to increase the capacity to produce innovation by quality research to trigger smart, sustainable, and inclusive development.

The project called “Development of a framework for extracting geospatial information from multi-resolution data for spatial analyses” (DOT130UZWT) run at the Department of Civil, Environmental, Land, Construction and Chemistry (DICATECh) of the Polytechnic University of Bari (POLIBA), has been developed in synergy with the Cyprus University of Technology (CUT) in Limassol (Cyprus), and in collaboration with the Italian company SIPAL S.p.A. in Grottaglie (Apulia Region, Italy). In particular, the XXXIV Cycle doctoral student in the PhD program "Risk and Environmental, Territorial, and Building Development" has assisted the research teams of the ERATOSTHENES Centre of Excellence in the EXCELSIOR H2020 Teaming Phase 2 Project, and the SIPAL's research and development (R&D) team in the POR Puglia 2014/2020 project named "Unmanned Vehicles and Virtual Facilities".

The investigation activities were carried out in three different places: at the CUT in remote working for 6 months, at the R&D site of SIPAL S.p.A. for other 6 months, and at the POLIBA for 24 months. Depending on the state of research, the activities have been segmented in such a way as to acquire the knowledge necessary for the strategic development of the project.

INDEX

INTRODUCTION	15
RESEARCH MOTIVATIONS	19
RESEARCH OBJECTIVES	21
<i>Technical Configuration of Sensing Platforms and Available Sensors</i>	23
<i>Development and Validation of a FOSS4G Framework</i>	24
<i>Geometric and Radiometric Pre-Processing of Acquired Datasets</i>	26
<i>Structuring of Pixel- and Point-Based Analysis of Geospatial Data</i>	28
RESEARCH'S CONTRIBUTION	28
MANUSCRIPT STRUCTURE	29
1. MULTI- SENSOR MULTI- RESOLUTION GEOSPATIAL DATA	31
1.1. MULTI-SOURCE PLATFORMS	37
1.2. CONSUMER UAV BREAKTHROUGH	40
1.2.1. COTS Visible-Bands Sensors	43
1.2.2. Light-Weight Multispectral Sensors	45
1.2.3. Other Common Sensors	46
1.2.4. Fields of Application	49
2. LOW-COST UAV-PHOTOGRAMMETRY POTENTIALITIES	53
2.1. SFM-MVS TECHNIQUES	60
2.2. RELATED PHOTOGRAMMETRIC PRODUCTS	67
2.3. STRUCTURING A COMPREHENSIVE WORKFLOW	70
2.3.1. Acquisition Activities	72

2.3.2. <i>Data Pre-Processing</i>	75
2.3.3. <i>Workspace Settings</i>	76
2.3.4. <i>Alignment Step</i>	76
2.3.5. <i>Filtering and Block-Optimization</i>	77
2.3.6. <i>Georeferencing and Scaling Step</i>	78
2.3.7. <i>Iterative Bundle Block Adjustment</i>	78
2.3.8. <i>Dense Matching Processing</i>	79
2.3.9. <i>Post-Processing Node</i>	79
2.4. OVERVIEW OF PHOTOGRAMMETRIC SOFTWARE.....	80
2.4.1. <i>Agisoft Metashape</i>	82
2.4.2. <i>Pix4D Mapper</i>	88
2.5. SCRIPTING A FOSS4G PROCESSING PIPELINE.....	96
3. GEOREFERENCING STRATEGIES IMPACTS.....	108
3.1 GEOREFERENCING METHODOLOGIES	110
3.2. TERMS OF GEOMETRIC ACCURACY STANDARDS.....	115
3.3. COMPARING GNSS AND TS TECHNOLOGIES	118
3.4. IMPROVEMENT OF THE GCP/CP NETWORK	123
3.4.1. <i>Optimize the Number of GCPs</i>	124
3.4.2. <i>Optimize the Distribution of GCPs</i>	127
3.4.3. <i>Suitable Allocation of Check Points</i>	129
3.5. ACCURACY ASSESSMENT AMONG DIFFERENT SOFTWARE PLATFORMS ..	131
4. GEOMETRIC PRE-PROCESSING OF CAMERAS	139
4.1. CAMERA CALIBRATION METHODOLOGIES	141
4.2. CAMERA LENS MODELS	145
4.3. INFLUENCE OF UAV FLIGHT PLANNING ON CAMERA CALIBRATION	147
4.4. CAMERA CALIBRATION OVER-PARAMETRISATION ISSUE	151
4.4.1 <i>Preliminary Correlation Analysis</i>	153

4.4.2. <i>PCA and Synthetic Indexes Definition</i>	164
4.4.3. <i>Predictive Function Detection</i>	167
4.4.4. <i>Discussion</i>	171
5. <i>PIXEL-BASED ANALYSIS</i>	173
5.1. <i>RADIOMETRIC CALIBRATION OF IMAGES</i>	176
5.1.1. <i>Pilot Sites and Materials</i>	180
5.2. <i>EMPIRICAL LINE METHOD (ELM)</i>	182
5.2.1. <i>Extract Regression Lines</i>	184
5.2.2. <i>Radiometric Validation</i>	187
5.3. <i>VEGETATION HEALTH MONITORING</i>	189
5.4. <i>RGB-BASED VEGETATION INDICES</i>	192
5.4.1. <i>Separability Capabilities</i>	195
5.4.2. <i>Influences of Spatial Resolution and Masking</i>	196
5.4.3. <i>Analysis of Results</i>	201
5.5. <i>CLASSIFICATION ALGORITHMS IMPACTS</i>	204
5.5.1. <i>Supervised Random Forest Algorithm</i>	208
5.5.2. <i>Unsupervised K-Means Cluster Algorithm</i>	220
5.5.3. <i>Confusion Matrix Metrics</i>	225
5.5.4. <i>Discussion</i>	236
6. <i>POINT-BASED ANALYSIS</i>	239
6.1. <i>PCA FEATURE EXTRACTION</i>	243
6.1.1. <i>Eigenvalues and PCA results</i>	249
6.1.2. <i>Anisotropy and Omnivariance</i>	253
6.1.3. <i>Linearity and Planarity</i>	254
6.1.4. <i>Eigenentropy Values</i>	256
6.2. <i>M3C2 ALGORITHM ENHANCEMENTS</i>	258
6.2.1. <i>Algorithm Parametrisation Performance</i>	262

6.3. MULTI-EPOCH CLOUD-TO-CLOUD.....	265
6.3.1. <i>Co-Registration Methods</i>	265
6.3.2. <i>Co-Alignment Approach</i>	267
6.3.3. <i>Improvements of Co-Registration Step</i>	269
6.4. MULTI-SENSOR DATA FUSION	277
6.4.1. <i>Comparison between UAV- and TLS-clouds</i>	279
6.4.2. <i>Merging Techniques Peculiarities</i>	285
6.5. ONE STEP TOWARDS BIM	287
6.5.1. <i>From Dense Point Clouds to BIM</i>	290
CONCLUSIONS	293
LIST OF ABBREVIATIONS	299
LIST OF TABLES	303
LIST OF FIGURES	305
ACKNOWLEDGEMENTS	310
REFERENCES	311
CURRICULUM VITAE	340

Canterò le mie canzoni per la strada
ed affronterò la vita a muso duro
un guerriero senza patria e senza spada
con un piede nel passato
e lo sguardo dritto e aperto nel futuro.
E non so se avrò gli amici a farmi il coro
o se avrò soltanto volti sconosciuti
canterò le mie canzoni a tutti loro
e alla fine della strada
potrò dire che i miei giorni li ho vissuti.

(A muso duro – Pierangelo Bertoli)

*To you still in the womb,
in calmness and safety,
with the hope of returning you
a better world.*

INTRODUCTION

The era of Big Data is now concrete: it is revolutionising the understanding of our planet (Huang and Wang, 2020) and is the key to promoting sustainable and focused socio-economic development in every country (Guo et al., 2017). Indeed, these immense masses of data occupy the tactical level of knowledge-driven economies and prove to be an innovative strategic resource for all government agencies (Guo, 2017). The technological evolution in the management of this data has become a national representation of scientific and technological capability, economic strength, and national security (Guo, 2017). The International Data Corporation in the Worldwide Big Data and Analytics Spending Guide expresses a clear definition of Big Data by characterising them as “a new generation of technologies and architectures, designed to economically extract value from very large volumes of a wide variety of data, enabling high-speed acquisition, discovery and/or analysis” (Vesset and George). These massive streams of data, available from different sensors and devices, offering different perspectives on complex phenomena, allow us to identify deep articulated patterns of reality. Effectively, Big Data analysis is no longer based on understanding causality from empirical tests, but thus on demonstrating deep statistical relationships between a multitude of monitorable variables (Boulton, 2018).

In this context, datasets can serve as inputs to modernise and validate current theories that are already scientifically accredited, but more importantly, they are able to provide unlimited sources of new forms of learning without the need to broadly model the phenomena under study. In particular, one of the areas most affected by this revolution is the earth sciences. This has undergone a transformation from a traditional, theory-driven science based on the collection of empirical data from which to generate a computational simulation, to a research methodology designed to explore the

correlation between huge multidisciplinary or interdisciplinary datasets (Guo et al., 2017).

Using analytical induction applied to a large amount of data, the analyst searches, compares, groups, and statistically classifies possible relationships and builds a very complex network capable of holistically describing the phenomenon under study. In concrete terms, by exploiting the great potential of these data, the scientific reductionism oriented towards the interpretation of complex natural phenomena as sums of more elementary phenomena or parts is overcome, opting for holism which, on the contrary, maintains that the system as a whole contributes to determining the behaviour of the parts (Guo et al., 2020).

Indeed, correlation analysis can reveal a certain relationship between the values of two or more variables. It can also aim to uncover hidden correlated networks within datasets. New patterns can be identified, new knowledge can be discovered, and new rules, hidden behind the data, can be established in order to help understand and interpret the real world and guide people towards correct decisions and efficient performance (Guo et al., 2017).

A paradigm shift from a science-driven by mathematical models, preferably simplified, to data-driven science, i.e. a scientific approach defined as data-intensive, is therefore evident (Guo, 2017). In their work, (Yu et al., 2018b) define Big Data as the fourth technological paradigm that allows researchers and practitioners to conduct efficient analysis of large amounts of data, moreover, made available through simple, cheap, and widespread acquisitions.

Whole R&D and industrial sectors are taking this sudden turn, intent on reaping the benefits as soon as possible. Difficult or previously impenetrable problems become solvable through real-time dynamic monitoring and analysis of various related data. In some cases, the data itself can become the object and tool of research: contrary to the past, data become the basis for conceiving, designing, and implementing research (Guo, 2017). Operating with big data for the extraction of useful information to reinforce decision-making is one of the competitive advantages for organisations to-

day. Enterprises are balancing analytical power in order to formulate detailed strategies in every aspect and operation to minimize business risk (Huang et al., 2018).

The unprecedented proliferation of data has posed significant challenges in the management, processing, and interpretation of this Big Data. Big Data does not simply refer to the volume and velocity of data exceeding storage and computing capacity, but also to its variety and complexity (Ma et al., 2015). Commonly Big Data is characterised by the five Vs, including Volume, Velocity, and Variety. To these are added Veracity, meaning the need to document quality and uncertainty, and Visualization, meaning the need to present the complex structure of the data and the richness of the information effectively. In some works in the literature, the term Value is also added, indicating the need to filter data for valuable information (Nativi et al., 2015).

In other words, heterogeneous Big Data contains rich information ready to be extracted and used in more sophisticated and innovative technological frameworks, e.g., Artificial Intelligence (AI), Internet of Things (IoT), and Digital Twins (Guo et al., 2020). Data processing and management frameworks are structured to transform the multitude of acquired information into knowledge. Such knowledge is not obtained directly but is rather immersed in the ocean of data (Li et al., 2018). In order to obtain it, extensive data mining is conducted. However, due to the volume, speed, variety, and veracity of data, it is difficult to effectively extract useful information from big data. For example, it is particularly difficult to conduct data mining on a dataset containing spatio-temporal information, resulting in a situation of massive data, missing information, and unavailable knowledge. Therefore, an unprecedented challenge arises: the development of comprehensive theories and algorithms for spatiotemporal data mining, including data heterogeneity and retrieval, data selection, semantic description, semantic interpretation, uncertainty, and knowledge representation (Li et al., 2018).

From this it follows how data mining applied to Big Data is still in its infancy, and at the same time there is an urgent need for the development of methodologies and techniques to transfer, store, manage, process, compute, and share them (Guo et al., 2017).

One of the areas of Earth sciences most encouraged by the Big Data revolution is related to Earth Observation (EO) technologies and techniques. EO data are growing in size and variety at an exceptionally fast pace (Huang and Wang, 2020). Indeed, recent advances in remote sensing (RS) and computing techniques have triggered an explosive growth of this data. New satellite, airborne, and terrestrial RS systems characterised by high spatial, temporal, and radiometric resolution are continuously evolving. The data stream offered to users worldwide every day would be about 20 TB, which also means more than 630 million data files (Ma et al., 2015). The increase in RS data also leads to the rapid growth of metadata. In this regard, large RS applications, overwhelmed by massive RS data, can easily be considered typical data-intensive issues (Ma et al., 2015). While increasing computing power enables global-scale simulations with unprecedented accuracy, on the other hand, new types of sensors and applications transform even tablets, smartphones, and car navigators into crowdsourced observing systems that provide an incredible amount of information (Huang and Wang, 2020).

The large masses of data thus flow into Big Earth Data, often also identified as Big Geospatial Data, geared to cross-sectorally help multiple industries and academia in understanding the earth with a new approach (Guo et al., 2017). In the last decade, the RS data industry has boomed, and the processing chain from raw data to a wide variety of products is gently emerging and becoming more detailed. Therefore, the developing market of RS data requires the industry to define and establish the supply chain management and processing of this data (Yu et al., 2018b). While this data contains rich information, it is at the same time heterogeneous, multi-source, multi-temporal, multi-scale, highly dimensional, highly complex, and unstructured (Guo et al., 2017). The difficulties lie in data storage, processing, validation of results, and even analysis.

The scientific community is called upon to respond to these issues. Big Geospatial Data are made up of several pieces and it is essential to have full control and awareness of each one of them. On the other hand, in order to exploit their full potential, it

will be necessary to learn the relationships between them and to structure management frameworks that are both open and shared, to increase their accessibility. If these challenges could not be adequately overcome, big data RS would become a treasure trove that we would not be able to explore (Ma et al., 2015).

RESEARCH MOTIVATIONS

With the increasing focus on Big Geospatial Data, it is becoming evident that this thriving multitude of geospatial information plays an important role in optimizing the ability to monitor and understand anthropogenic and natural environments, and to prevent or react to urban and spatial problems even as spatial and temporal dimensions change (Guo et al., 2017). As stated by (Guo et al., 2020), the science of Big Earth Data involves methodological and technological activities to examine these Big Data as an analytical ecosystem, i.e., an organization that supports the systemic discovery of information from data concerning Earth. Consequently, this ecosystem must be able to integrate different types of input within a geographical context, to be accessible to different communities, thus guaranteeing the democratisation of data and information, breaking down technological barriers (hardware and software). All this will have to be traced in a multi-scale and multi-temporal framework, from local to global and vice versa, in a variety of aspects.

From the hardware perspective, the introduction of low-cost computers and sensors has expanded the potential for data acquisition and new data sources are consequently emerging (Guo et al., 2020). On the software side, the adoption of increasingly performant and specialised Free and Open Source Software for Geospatial (FOSS4G) platforms is revolutionising the way of working, driving a shift towards open science, knowledge sharing, and reproducibility (Brovelli et al., 2017). This conception is complemented by the need to further strengthen data resource management and accelerate the construction of an EO data-sharing platform on global change for the realization of effective data resource sharing (Guo et al., 2015).

These transformations require the tailored implementation of high-level value chain frameworks. This consists of three wide-ranging tasks: (a) collecting, aggregating, and purifying Big Geospatial Data, (b) extracting valuable inferences from them, optimising their processing and building targeted analytics, and (c) interpreting these findings in the context of real-world problems to prepare intelligence to support societal needs (Guo et al., 2020). To date, it is still an open question to find optimised methodologies to manipulate big data and convert it into targeted, effective, and accurate data for specific tasks or to aggregate it with other data at a higher level. It turns out to be basic for users to determine how to effectively extract useful and valuable information from this big data to improve analysis, answer questions and solve problems (Chen and Wang, 2018).

Despite the massive and urgent challenges mentioned above, the potential value of these Big Geospatial Data from RS is extraordinary (Chi et al., 2016). There are countless fruitful applications where RS techniques have brought added value: such as agricultural applications, ocean applications, urban planning, urban and environmental monitoring, water quality monitoring, global warming, global forest resource assessment, the discovery of ancient sites, and so on.

A new phase of geomatics development has been titled "Connected Geomatics" by (Li et al., 2018): a multidisciplinary science and technology that uses systematic approaches and integrates methods of spatiotemporal data acquisition, information extraction, network management, knowledge discovery, spatial detection, and recognition, as well as intelligent location-based services related to any physical object and human activity on earth (Li et al., 2018). In this perspective, returnable thematic maps visualise unstructured data and support spatial analysis even in real-time. Obviously, the increasing demand for real-time or near real-time processing capabilities by many time-critical RS applications has certainly worsened the problem of data intensity (Kamilaris et al., 2017).

Using multiple data sources together improves performance in terms of coverage, spatio-temporal resolution, and interpretation capabilities through techniques such as image fusion (Huang and Wang, 2020). However, each remotely sensed image has

intrinsic peculiarities, heavily conditioning the choice of processing methods, affecting the (geometric and thematic) correspondence of the final products.

Compared to conventional data sources, these new forms of data have better coverage at a lower cost, but on the other hand, are often of lower quality. A further challenge is therefore to make these data valid and comparable to more traditional resources so that they can be considered as alternatives or at least complementary.

Given the numerous challenges in the field of EO in which the scientific community appears to be rigorously engaged, an increasing share of interest is being placed in the advancement of remotely piloted aerial vehicles (RPAS), better known as Unmanned Aerial Vehicles (UAVs) (Yu et al., 2018b). Aerial imagery captured by UAVs is playing an increasingly important role in various industries due to its efficiency, flexibility, transversality, and versatility of use. Aerial imagery can be captured with very high spatial resolution and processed much faster than satellite imagery. However, UAV technologies and techniques based on them are still under development and several problems need to be solved. Among the many already discussed, manual interpretation and analysis of integrated data are no longer adequate, which is why sophisticated automatic analysis methods are needed to make the process efficient and effective (Yu et al., 2018b).

RESEARCH OBJECTIVES

This dissertation seeks to develop a FOSS4G framework for pre-processing and post-processing of photogrammetric products, useful for the automatic extraction of near real-time information applied to high-resolution, multiscale, multi-temporal, and multi-sensor data for environmental monitoring and technical inspection of buildings. Many industries would benefit from a standardisation of photogrammetric processes and results. The adoption of low-cost technologies and the preference for open-source management and processing software makes the whole structure highly innovative, as it is accessible, sharable, and implementable at any time and in any place. Conscious of the holistic vision of the fourth scientific paradigm, the procedure

to reach the definition of an effective framework, between technologies and techniques, implies the deepening and the combination of many domains such as RS in a broad sense, classical topography, and Computer Vision (CV). Therefore, the process of extracting the various information goes through four main stages: (1) conceptual maturation of the platforms and sensors and their integration, (2) structuring of a FOSS4G processing framework, (3) geometric and radiometric pre-processing of the acquired datasets, and (4) image-based and point-based analysis and information extraction.

Therefore, the present research goes through the structure focusing on the currently low-cost UAV platforms equipped with common non-metric sensors, on the configuration and optimisation of the field acquisition and pre-processing activities and, at the same time, testing different methodologies to extract information from data characterised by different spectral and spatial resolutions. The validation procedures of the products obtainable from the process chain are proposed to identify their placement among the different more usual alternatives of EO data.

Numerous researchers have examined the potential offered by UAVs in surveying large portions of territory, infrastructures, and buildings of particular interest. Many experiments and models have been developed in order to identify the relationships existing between parameterizations, field choices and final products, and several authors have analysed comparisons between the products that can be returned by these innovative technologies and more traditional ones (satellites, terrestrial laser scanners (TLS), etc.). However, looking at the scientific literature, these works provide a specific view of the problem addressed, without a global framework useful for generating shared knowledge. This thesis, therefore, reconstructs a repeatable and reproducible procedure, tests and validates the products that can be returned, and proposes innovative image-based and point-based analysis methods. During the paragraphs, an attempt will be made to respond to the limitations identified in the different monitoring applications, i.e., concerning:

- the collection and pre-processing of information in a time and cost-effective manner;

- the lack of an accredited photogrammetric data processing framework that is reproducible, repeatable, and widely accessible;
- the lack in UAV-based products of a place among those from more established technologies;
- the complexity of dealing with high spectral and spatial resolution data and large amounts of data in real-time application to extract specific information for solving certain problems.

In the following paragraphs, the specific purposes that will be discussed and examined in the course of the thesis are thus deepened.

Technical Configuration of Sensing Platforms and Available Sensors

EO data are characterised by significant heterogeneity due to historical and technological reasons, including different acquisition sensors, different methodologies to describe real-world phenomena and different encoding formats. The volume of EO data continues to multiply exponentially due to the launch of new flying or ground-based platforms, which host increasingly powerful, efficient, and accurate sensors (Nativi et al., 2015). In RS, many different types of data have therefore been observed, starting from optical data (RGB, multispectral, hyperspectral, and thermal cameras), passing over radar and laser devices equipped indifferently on satellites, aircraft, and ground sensors, often referred to as proximal sensors (Chi et al., 2016). For more than a decade now, advances in control engineering and computer science have made possible the development of UAVs that allow to easily obtain an “overhead view” of the environment (Athanasios et al., 2019). Aerial imagery captured via UAVs is playing an increasingly important role in responding to multidisciplinary problems, due to their efficiency and versatility of use. UAVs can carry various types of sensors, including cameras, infrared and ultraviolet sensors, radiation sensors, deep L-sensors, spectrum analysers, and LiDAR reflectors. Simple images and/or videos from UAVs can provide real-time, decision-relevant situational information (Yu et al., 2018b), while simultaneously being useful for photogrammetric processing to return three-dimensional (3D) reconstructions, thematic maps, and ultra-high resolution or-

thomosaics. The introduction of UAV spectral RS techniques leads to excellent advantages in monitoring and inspection applications, as they allow multiple targets to be analysed in large areas with also high temporal resolution. Therefore, concerning the platform, the study focuses on these UAV platforms because, although satellite or airborne platform techniques are more established, it is evident that UAV-based products can provide greater accessibility but at the same time a necessary regulation emerges. However, the selection of the most suitable sensor proves to be complex and often linked to instrumentation costs. Most commercial UAV platforms are usually equipped with simple RGB cameras but in the field of spectral sensors other choices can be adopted such as multispectral, hyperspectral, thermal, etc. In the same classification, metric and low-cost technologies can be distinguished: the latter are of particular interest as they are more widespread and used for professional purposes. The first point addressed in this research concerns the optimal configuration of the low-cost platform-sensor system, therefore functional for a wide range of users, useful in all photogrammetric applications. It is well known that the use of a non-metric sensor and an inexpensive platform brings with it weaknesses for the export of specialised products. Although widely discussed by the scientific community and used in industrial sectors, several aspects have not yet been resolved, linked, for example, to the technical limits in relation to the commissioned requirements, the significance of the information that can be extracted, and a scientifically shared approach from the acquisition phase through to restitution. Devoted techniques and software to solve these problems are still under development.

Development and Validation of a FOSS4G Framework

In addition to the hardware for data acquisition, object detection, and characterisation, the development of a processing chain is necessary, which is independent of the technology used and the scale defined. Generally, the processing of remotely sensed data consists of a well-defined chain of processes, each of which is dedicated to certain processing of the raw data. The organizing and sharing of the entire processing flow are affected by the structuring and validation of each processing seg-

ment. Theoretically, the different processing segments can be grouped into three classes that identify their processing stage: pre-processing, processing, post-processing. In the pre-processing step, different techniques and procedures are used: radiometric correction, geometric correction, image enhancement to remove noise and correct inconsistencies. In the processing step, data georeferencing procedures, orientation, and fine adjustment, orthorectification, mosaicking, and so on are applied (Ma et al., 2015). Not all segments can be considered indispensable: whether or not to start one of them is clearly dependent on the commissioned task. Finally, in post-processing, result analysis methodologies oriented towards information extraction and thus the findings of various information products are implemented.

From the perspective of Big Geospatial Data, the structuring of these processing chains should be designed to systematically address the problems of information processing, extraction, and interpretation in the different RS domains. While data processing and analysis represent a multi-step pipeline that is already complex to organise, the adoption of data-driven methods, which are significantly different from the point of view of specific applications and domains, may complicate matters even more. Due to this heterogeneity and high dimensionality of big data in RS, important computational and statistical challenges related to processing scalability, noise accumulation, spurious correlation, accidental endogeneity, and measurement errors certainly need to be addressed (Chi et al., 2016). To address these challenges, the scientific community is making efforts to develop computing platforms, algorithms, and software systems that can overcome these impasses. These technologies include high-performance platforms, mass storage technology, full automation, efficient computation, data sharing, and service systems to make Big Earth Data manageable and valuable (Guo et al., 2017).

Often, however, the most widely used platforms show up as real "black boxes", i.e., users are able to obtain results but are not fully aware of the parameterizations at each stage and the mechanisms they operated. The commercial orientation proposes rapid "on-demand" and even real-time solutions, in which the optimal parameterisation of the process chain is sacrificed in order to provide quick and easy service. De-

spite considerable developments in the field such that reliable products can still be returned, the choice to undertake default parameterisation and lack of knowledge of the operations "behind the curtain" often generates artefacts and gross errors. On the other hand, it follows that not being aware of the structure of the processing chain, products deriving from several platforms cannot be considered effectively comparable. Hence the need to establish scientifically shared workflows, in which the relationships between the variables involved and the parameterisation of the operations are highlighted and the products obtainable can be considered independent of the platform adopted. The aim of this thesis is therefore to build shared knowledge of the processing of multi-resolution and multi-technique photogrammetric data in open-source platforms. Tests have therefore been produced to identify the relationships between the choices that can be adopted just from the acquisition phases and the photogrammetric products that can be returned. The validation of these methodologies makes this structure repeatable and reproducible.

Geometric and Radiometric Pre-Processing of Acquired Datasets

In general, Big Data, particularly even the latest generation of EO data, are characterised by low veracity and high uncertainty. Often due to the limitations of measurement instruments and data processing technologies, these acquisitions suffer from uncertainty, errors, noise, and large-scale deficiencies (Chen and Wang, 2018). In many applications, these are underestimated, or at worst even omitted. The question of how good these data are is difficult to answer, but certainly identifying their limitations would make them more functional. It is a challenging task to adequately characterise the uncertainty and track those associated with large volumes of data. Moreover, some traditional data analysis and learning algorithms are no longer appropriate to process this type of data. How to deal with the different uncertainties and errors of the acquisitions is particularly important before using them. Hence, the different methods and approaches developed to deal with this uncertainty problem were investigated in order to consider the different acquisitions as true, comparable, and in some cases interchangeable.

At the same time, the validation of methods and approaches needs to be standardised and made publicly available. In the vision of integrating multiple data sources, this can contribute to the improvement of data quality and completeness, but the validation of individual data remains crucial before any integration. Acquisitions from different sensors need to be improved with anomaly detection to identify erroneous data due to, for example, system failure or incorrect data collection methods. Research and activities related to the use of the synthesized information and predictive analysis results derived from these approaches should improve our ability to answer the assumed demand and plan subsequent processing adaptively (Yu et al., 2018b).

The scientific literature suggests that the raw images acquired directly from the various remote sensors, from the most powerful ones on board satellites to the cheap, non-metric ones on board, should not be used. The data must be corrected for deformations due to interactions between components, atmospheric conditions but also according to the profiles of the scenarios under investigation. The corrections typically include radiometric and geometric corrections (Huang et al., 2018). A full radiometric correction is related to the sensitivity of the remote sensor, the topography, and the angle of incidence of the sun, dispersion, and atmospheric absorption. Atmospheric correction is complex, in general, because it requires the data and information of atmospheric conditions during image acquisition but can be neglected in UAV-based acquisitions. It should be noted that data and information typically vary with time and location.

On the other hand, geometric correction aims to correct for the crushing, twisting, stretching, and displacement of RS image pixels relative to their actual position on the ground, which are caused by the tilt of the RS platform, altitude and speed, the sensitivity of the remote sensor, the topography of the earth's surface and the angle of the sun.

In this thesis work, approaches for the recognition and adoption of geometric corrections of sensors used in the photogrammetric field were analysed. Starting from the geometric corrections, a predictive analysis of the geometric accuracy achievable with the photogrammetric processing itself was developed. Subsequently, the radio-

metric calibration methodologies of UAV-based photogrammetric products were analysed, in particular orthomosaics. The performance of the Empirical Line Method (ELM) (Smith and Milton, 1999), which is able to perform empirical radiometric corrections without using spectroscopic data acquired in the field, was analysed and validated.

Structuring of Pixel- and Point-Based Analysis of Geospatial Data

It is known that the use of the UAV platform also has the advantage of allowing multi-view, multi-sensor, and multi-scale data collection. The analysis of such multi-modal datasets and the multitude of products that are rendered can be useful in monitoring applications because they simplify the process of interpreting and extracting targeted information. At the same time, however, manual interpretation and analysis of these combined and integrated data are no longer convenient and sufficient, which is why sophisticated automatic analysis methods are needed to make the process efficient and effective (Yu et al., 2018b). However, the use of these data types in combination with automatic information extraction techniques requires further investigation.

For this thesis work, two approaches to analysing and extracting information from photogrammetric products based on UAV acquisitions were explored and tested. In particular, two critical ways of examining these were identified: one oriented towards the extraction of geometric characteristics from the 3D reconstructions of the scenes under investigation, and the other aimed at the recognition of spectral characteristics of the objects present in the scene under investigation. Point-based and Pixel-based analyses were employed, respectively, using open-source software tools.

RESEARCH'S CONTRIBUTION

Because of the open problems discussed and the motivations that have arisen for carrying out the research work described in the previous sections, the main contributions of this thesis are to:

- investigate multi-sensor and multi-resolution EO platforms and in-depth study UAV technologies used for photogrammetric operations;
- structure a comprehensive open-source framework ranging from acquisition strategy and georeferencing step, geometric and radiometric pre-processing, output processing, and analysis;
- apply open methodologies for pixel-based and point-based analysis of producible photogrammetric results for multi-scale, multi-temporal, and multi-sensor surveys;
- achieve these with high quality but using low-cost technologies and techniques to increase their accessibility.

The research work presented in this PhD thesis has been published in some articles in peer-reviewed journals and the proceedings of several national and international conferences.

MANUSCRIPT STRUCTURE

The general structure of the study is essentially divided into eight chapters, including this chapter of Introduction. In detail, chapter 1 proposes an overview of EO platforms, deepening the UAV technology and the most equipped sensors. Chapter 2 gives a detailed overview of digital photogrammetric techniques and, in particular, of Structure from Motion (SfM) and Multi-View Stereo (MVS) algorithms. After an extensive discussion of the processing steps, an open-source SfM-MVS processing framework for UAV data is proposed. Chapter 3 deals with a study on the impacts due to the georeferencing strategy adopted, first in the field operations and then in the processing chain already analysed. Chapter 4 provides a background and literature review on the calibration methodologies of cameras and lens models. The influence of acquisition planning choices on the effectiveness of camera calibrations is analysed. In the same chapter, an innovative method to predict the accuracy of the paper from the camera calibration is presented. Chapter 5 and Chapter 6 propose pixel-based and point-based analysis methodologies, respectively. Chapter 5 presents the methodolo-

gies of radiometric calibration of images in the visible bands from UAVs, applies the ELM and evaluates the results by analysing the impacts on vegetation indices and classification algorithms. Chapter 6, on the other hand, explores the techniques for extracting the characteristic geometries of the point clouds from the Principal Component Analysis of the clouds themselves. Given the enhancements of cloud-to-cloud comparisons, the possibility of using co-alignment as a co-registration methodology between photogrammetric products is analysed, especially useful in multi-temporal analyses.

Finally, the Conclusions chapter presents the observations and findings deduced from this thesis work, proposing future scenarios in which the scientific community will be called upon.

1. MULTI- SENSOR MULTI- RESOLUTION GEOSPATIAL DATA

Big EO Data are characterised by being massive, multi-source, heterogeneous, multi-temporal, multi-scale, highly dimensional, highly complex, non-stationary, and unstructured. Indeed, this is the case since they formally consist of multi-degree subsystems used for EO. Each subsystem has its own spatio-temporal scale, spectral, radiometric, and geometric properties, and resolutions. In addition, the EO data of each subsystem are characterised by a significant heterogeneity due to both historical and technological reasons: different acquisition mechanics, different methodologies to describe real-world phenomena, different encoding formats. There is no doubt that the volume of these data continues to multiply exponentially due to the launch of new platforms, both flying and not, that host increasingly powerful sensors, with important spectral characteristics and geometrically very accurate. (Nativi et al., 2015) propose a tabulation of the challenges and solutions that emerge for the five Vs that characterise Big EO Data. In the field of RS, many different types of data are involved, from optical data to radar or laser data, all derived from sensors that may be mounted on aircraft, satellites, or ground-based devices. Numerous types of data sources can be integrated into RS problems, such as those generated by active learning and crowdsourcing techniques, which also entail low or no costs (Chi et al., 2016). These acquired EO data have different rules and characteristics at different scales. Just integrating all these different types of data with a single system or platform is, in itself, a highly complicated task, even without considering subsequent processing and analysis.

Indeed, traditional geospatial information service models, which are usually built for a given type of sensor or data for a specific professional application, cannot integrate multiple types of sources, including multiple sensor sources, processing sources,

and distributed information/knowledge sources in different locations (Li et al., 2018). There is an urgent need to develop innovative theories and approaches for the scientific and professional exploitation of this large EO data. The efficient extraction of the knowledge contained in them is still at an early stage. Moreover, all these data face the challenge of constructing and quantitatively analysing complex geoscientific processes and spatio-temporal systems that also express and impact socio-economic processes.

Thus, Multi-Sensor Multi-Resolution (MMT) techniques for the management of heterogeneous and disaggregated data are stated, oriented towards the structuring and implementation of EO data fusion methods.

The effective use of multi-platform observation data with multi-sensors can avoid the problems related to information extraction and precariousness that arise with the use of a single sensor (Guo et al., 2015). For each of the sensors, the information captured about the observed objects is typically partial or inconsistent in terms of quality, coverage, accuracy, and timeliness, thus being missing or incomplete for a certain analysis purpose. In contrast, multi-source observations provide stable and long-term spatial data for scientific research, compensating for inconsistent spatiotemporal observations and playing a key supporting role in global change research (Guo et al., 2015). For example, given the rapid evolution of the health of natural environments, it is indeed difficult to archive relevant, homogeneous, and long-term data, and it, therefore, becomes necessary to establish a monitoring plan capable of exploiting increasingly interchangeable but, above all, integrable data acquisition technologies. The use of multi-sources allows for greater accuracy than existing techniques (Villareal and Tongco, 2019).

For a specific observation task, the sensor resources need to be scientifically configured according to the location, shape, size, timeliness, spatial resolution and imaging mode of the observation task, and the sequence of observation operations of each sensor needs to be scientifically organised. However, due to the different imaging capabilities and imaging constraints of various sensors, it is necessary to study the op-

timization method of the collaborative observation task of the cross-platform sensor to meet the user's needs at the maximum capacity (Li et al., 2018).

RS based on satellite and manned airborne systems includes expensive platforms, which are significantly restrictive due to availability limitations and/or complex logistics. In addition, satellite, airborne imaging, and LiDAR have significant disadvantages in terms of spatial and temporal resolution and data acquisition flexibility. In the last decade, substantial technological advances have been made in the production of unmanned aerial platforms, in lightweight and inexpensive active/passive sensing devices, and in the integration of microelectronics (Adamopoulos and Rinaudo, 2020). With the widespread advent of these UAVs, mainly equipped with consumer off-the-shelf (COTS) sensors (Berra and Peppia, 2020), photogrammetric products, for example, are now characterised by higher spatial resolutions than satellite data but for small to medium areas, less so in spectral resolution even in cases where more sophisticated sensors are mounted onboard (Fawcett et al., 2020). Moreover, the accessibility of the technology in terms of cost and their versatility makes them easily usable in any scenario, in a wide range of disciplines, with an unlimited time to revisit (Berra and Peppia, 2020). A highly detailed topographic survey at minimal cost and effort has always been one of the developing areas of scientific interest (Deliry and Avdan, 2021).

UAVs cannot compete with traditional platforms in terms of spatial extent, however, with appropriate processing and analysis frameworks, data from UAVs offer substantial opportunities to augment and improve the data collected by more traditional platforms (Dash et al., 2018, Zou et al., 2018). Given their potential, they require validation practices to scientifically deem them comparable, complementary, or in some cases even alternative to the products that can be generated by more established technologies.

These practices are very disparate even for the same or similar application, mainly due to the fact that the data acquisition and sensors to be used are characterised to be more flexible than traditional ways (Yao et al., 2019). Furthermore, these practices are often developed through a process of learning by doing.

There is generally a lack of systematic analysis on how the acquisition, pre-processing, processing, and post-processing operations alter solutions for typical RS tasks. Thus, this raises challenges in identifying common and scientifically shared practices for UAVs to be used for both specific and more default tasks. While performing RS analysis using UAVs consists of joint efforts in generating knowledge about both data acquisition and processing, there is still a lack of studies analysing the uncertainties associated with these processes, as well as work standardising the achievable interpretation results (e.g., classification and change detection) in a controlled manner (Yao et al., 2019).

At the same time, given the validation of UAV-based procedures and the aforementioned MMT conception, it becomes encouraging to address scientific researches regarding the combination of the peculiarities of satellites, UAVs, field surveys, and downhole data to achieve enormous benefits from integrated and synergistic monitoring of various technologies and techniques (Ren et al., 2019).

The synergy between UAVs and various EO data is essential for understanding the different dynamics of phenomena and/or sectoral applications. Each EO system has specific acquisition characteristics that result from a trade-off among resolutions (spatial, spectral, and temporal), swath and signal-to-noise ratio (Figure 1.1). While waiting for new technology with all the required characteristics, it is necessary to combine data from different sources to improve observations.

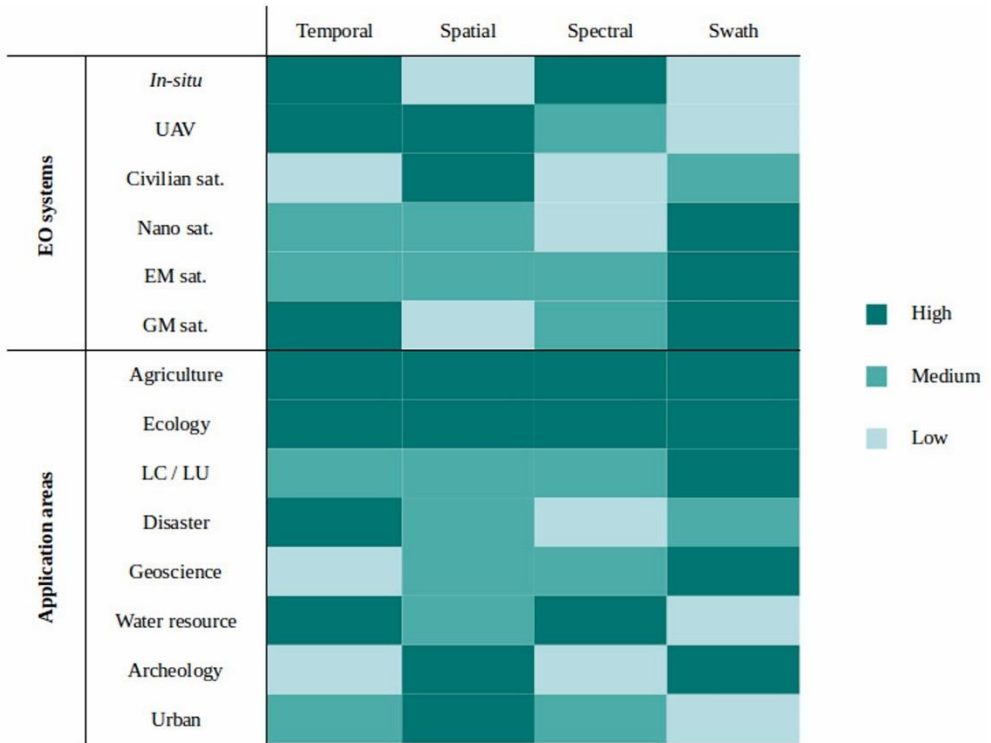


Figure 1.1. Resolution demands (temporal, spatial, spectral and swath) in the main fields of application of RS and supply of data sources. Figure based on (Emilien et al., 2021). EO: Earth Observation; EM: Environmental Monitoring; GM: Global Monitoring; sat.: satellite; LC: Land Cover; LU: Land Use.

Actually, it is considered necessary to use this synergy to bridge the gap between the capabilities of current EO systems and the data needs of different application domains. Synergy can be considered strong if combining data yields more information than using each data source separately (" $1 + 1 = 3$ ") (Figure 1.2) (Pohl and Van Genderen, 1998). On the contrary, synergy is defined as weak when it only compares advantages and disadvantages to determine which data source is the most suitable. For satellite data, their quality and interoperability are guaranteed by the Committee on Earth Observation Satellites (CEOS), whose original function was to standardise data formats and ensure validation, inter-calibration, and inter-comparison of satellite products. For UAV data, however, there is no guarantee of data quality, as data acquisition skills are transferred to users. In fact, acquisition and pre-processing protocols may vary between users and sensors, which does not guarantee consistent data,

making multi-source interoperability difficult (Emilien et al., 2021). Ensuring this interoperability is a major challenge because models based on the synergy between UAV data and various EO data are sensitive to the quality of the input data (Belgiu and Stein, 2019). Data inter-calibration (geometric and radiometric) and uncertainty estimation in multisource models are therefore essential steps to ensure the quality of the results of this synergy (Figure 1.3) (Emilien et al., 2021). At the same time, identifying and validating acquisition, pre-processing, and result analysis protocols based on UAV data becomes a crucial step to seize the opportunities presented to us by this new technology.

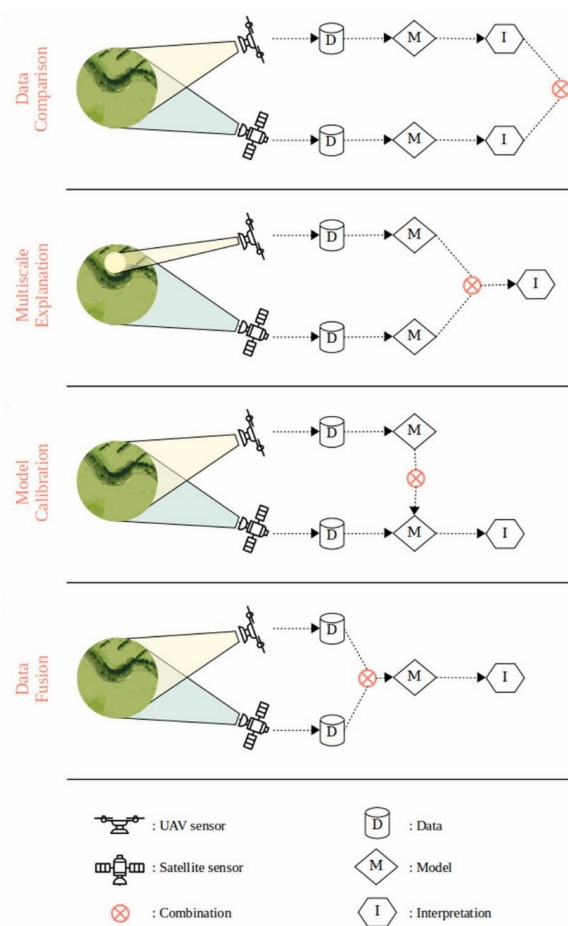


Figure 1.2. Diagram of UAV/Satellite synergies. Figure based on (Emilien et al., 2021)

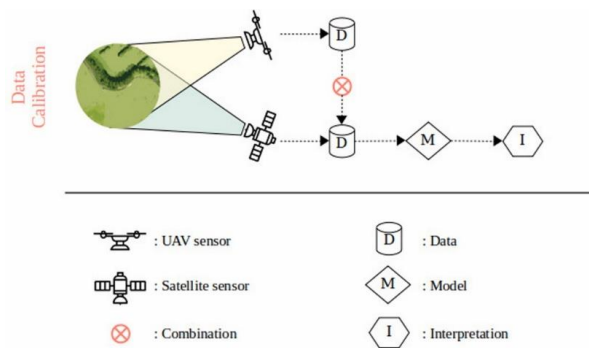


Figure 1.3. Data inter-calibration strategy. Figure based on (Emilien et al., 2021).

1.1. MULTI-SOURCE PLATFORMS

In an MMT vision, the wide range of sensors that can be adopted in the various fields of application will necessarily have to be positioned on stable platforms, i.e., a system of mechanical and/or electronic components to support data collection and recording. In general, it is possible to distinguish between remote and proximal sensing platforms according to the distance of the sensor from the object or area under investigation. In some cases, platforms can be considered hybrids and lie in the middle between the two classes of distinction (e.g., UAVs are both remote and proximal platforms due to their short distance to the target). Technological evolution and continuous technical progress lead to a recurring reform of classifications, which may be convenient at a given point in time but become obsolete soon after.

For this thesis work, it is, therefore, preferable to adopt the most general distinction, i.e., distinguishing three classes according to distance from the ground: terrestrial, aerial, and space platforms. The placement in one class less than another is linked to many criteria according to:

- observation space and ground coverage in terms of areal extent, from which derives the spatial resolution, evaluated in terms of Ground Sample Distance (GSD), i.e., the smallest portion of territory or object that is represented in the digital image;
- Geometric, radiometric, and spectral accuracy;

– frequency of data acquisition and revisit time.

Spatial platforms are synthetically satellite platforms. Conventional RS from these platforms has a significant limitation regarding spatial resolution, which is unfortunately coarse for many applications (Mohd Noor et al., 2018). There are few examples of commercial satellites (e.g., GeoEye-1 and Pleiades) that provide images with a sub-metric spatial resolution (spatial resolution < 1 m for panchromatic and > 1 m for multispectral). Conversely, high spectral and radiometric resolutions characterise the sensors onboard these platforms. The revisiting times are quite long and, above all, the services for obtaining these data are characterised by quite high prices. In addition, commercial satellites usually take seven days to provide processed images and therefore cannot be considered for real-time operations. Satellite imagery may be the right solution for large areas, although weather conditions may be a limitation.

Aerial RS was the primary source of geospatial data until the introduction of commercial satellite systems about a decade ago. High cost and limitations in the planning of surveys, however, were the main drawback that led to a gradual replacement by space-based systems. In recent decades, however, UAVs of various shapes, sizes, and capabilities have been developed. The adoption of these technologies in civil applications is exponential and, in both research and professional contexts, a real revolution is taking place. In fact, compared to conventional satellite and airborne platforms, several features make these vehicles very functional for RS: first of all, they can now be considered a low-cost technology (Said et al., 2021); they can perform missions and acquire data autonomously with minimal human interaction (Mancini et al., 2017); manoeuvrability and flexibility of use, which is ideal for operations in complex environments (Ren et al., 2019); the ability to operate in adverse weather conditions and hazardous environments (Urban et al., 2019); inter- and intra-disciplinary transversality, linked both to the possibility of equipping them with a variety of sensors and the versatility of the vehicle for a wide range of operations (Yao et al., 2019). Consequently, images taken from low-altitude RS platforms such as UAVs effectively provide an alternative (Cummings et al., 2017).

Instead, ground sensing is performed using platforms placed on the earth's surface. In this case, sensors are either mounted on common vehicles, such as cars, or vehicles specifically designed for field monitoring, such as ground rovers, or traditionally placed on fixed mounts (Caprioli et al., 2007, Lague, 2020).

As is evident, each class realises some criteria less than others. The choice of a class will often depend on the commissioned application. However, the multi-platform approach transforms this choice by making it less conditional (Cooper et al., 2021). The adoption of one platform does not exclude the involvement of another, so as to maximise the information that can be extracted (Abate and Sturdy-Colls, 2018, Emilien et al., 2021).

A multi-platform approach and the integration of different technologies and methodologies for acquiring and processing geospatial data result in top-down multi-resolution documentation methods capable of exploiting all the inherent potential of current techniques (Abate and Sturdy-Colls, 2018).

While the advantages of such an approach appear evident, major challenges emerge in managing multi-resolution semantic complexity and application perspectives. For example, (Yu et al., 2018a) propose a multi-scale hierarchical representation to integrate high-resolution images from UAVs and satellite images to detect large-scale objects and small-scale objects simultaneously. On the other hand, several works in the literature address the search for the benefits and optimisation of segmentation and classification processes concerning multi-resolution datasets for the extraction of global knowledge and/or point information (Jayanthi and Vennila, 2020, Koley and Jeganathan, 2020, Safonova et al., 2021). (Cong et al., 2020) states that multi-resolution images have insufficient cognition and, at same time, super-resolution features but multi-resolution performance cannot be interpreted with existing methods. Meanwhile, scale factor and resolution play an important role in Geographic Information System (GIS) applications. (Doumit and Pogorelov, 2017) discuss methods for optimal detection and their effects on final products. What is most evident from most of the present literature is the need to enrich understanding and practice in this new orientation.

It follows, however, that in order to take advantage of these synergies, each platform must be harmonised with the others (Tmušić et al., 2020).

1.2. CONSUMER UAV BREAKTHROUGH

Initially introduced for military purposes as early as the 18th century, the breakthrough to civil use has only fully taken place in the last few decades. Currently, the integration of UAVs into civil RS is significantly changing the field. Experienced scholars, enthusiasts, and novices alike are gravitating towards UAVs to enhance their ability to explore the world (Cummings et al., 2017).

So far, the acronym UAV has been widely used, but the term 'drone' is widely the term commonly and vulgarly used to refer to unmanned aircraft. Looking at the literature, however, there is no shortage of alternative names and acronyms for these same aircraft without humans on board: Remotely Piloted Aircraft (RPA) or Vehicle (RPV), Remotely Operated Aircraft (ROA), and Uninhabited Aerial Vehicles (UAV(*)). In technical terms, there are differences between these statements (Colomina and Molina, 2014) but there also appears to be a case of semantic confusion. For example, the latter UAV(*) generally refers to devices used in military applications, unlike the already used acronym UAV employed in civil applications such as RS. In the European Regulation on remotely piloted aircraft, the European Commission preferred to define the term Unmanned Aerial System (UAS) at EU level (Bassi, 2020, Kandra et al., 2020), suggesting that an aircraft is a system of systems: a set of complementary technologies brought together to perform a specific task and as such there are a variety of different systems (Colomina and Molina, 2014).

Numerous researchers have developed their classification systems, resulting in a lack of uniformity worldwide, and have emphasised their main characteristics (e.g., weight, flight altitude, payload, endurance, and range) (PS and Jeyan, 2020, Said et al., 2021). However, two main types of drones can be identified: fixed-wing or rotary-wing. The reader is referred to the work of (Shahmoradi et al., 2020), where the specific characteristics are described at length. Fixed-wing drones resemble a passenger

aircraft with great strength and flight speed. The job of the wings is to create a lifting motion that is created by the air flowing over them at high speed and inclination, in response to the speed of forwarding acceleration. They are faster, require some take-off space before they can fly and are preferable for covering a large area, while rotary-wing drones may be preferable for obtaining high spatial resolution measurements and carrying more than one sensor. The multi-rotor lift mode works like that of a helicopter, relying on numerous rotating blades to generate the lifting and propelling motion. The categories under multi-rotor are numerous such as tri-copter, quadcopter, hexacopter and so on. They are preferred for their ability to take off and land vertically, vary the speed, and hover in the air at various angles, giving flexibility in capturing photos. Although they are highly flexible systems, the limitations of multirotor platforms are their endurance (<30 minutes) and speed, which limits them to a relatively small area (<5 km²). In general, the latter is the technology with the largest consumer market, due to its versatility and affordability. The most common solutions involve small systems, defined by a maximum total weight of 25 kg that can operate locally under minimal legal restrictions.

The characteristics of these aircraft play a significant role in the efficiency of EO. The more uniform the observation space, the greater the observability. There are several approaches to improve the observation potential from a platform. Besides cooperative sensing promoted by using multiple platforms (Skorobogatov et al., 2020), as mentioned above, the current trend is also to use multiple sensors in different orientations on the same platform.

Concretely, the body of these media only provides a stable flight platform for the various embedded sensors to measure and provide results (Cummings et al., 2017). These sensors are broadly classified into two: active and passive sensors. Active sensors send electromagnetic rays to the targeted point on the ground and collect the reflected rays; passive sensors work by collecting waves of electromagnetic energy that are reflected from the sun or the targeted object on the ground. A more detailed overview of these equipable sensors and their applications in the field is proposed in the following sub-sections.

For drones to perform various functions, additional lightweight and intelligent devices are incorporated into the drones to allow them to function properly. During the flight, rotation and tilt are crucial to ensure that the drone is steered to the desired position, and this is achieved by using inertial measurement units (IMUs) installed on board (Shahmoradi et al., 2020). These include the magnetometer to indicate the orientation of the magnetic field to ascertain the direction, the accelerometer to calculate linear movement in all directions and the gyroscope to determine tilt and rotation rate (Figure 1.4). One of the key devices to control the misdirection and tilt of the equipped sensors is the gimbal, a pivoted mount that allows the rotation of the sensor itself around a maximum of three axes. In this way, the sensor remains independent of the rotation of the aircraft.

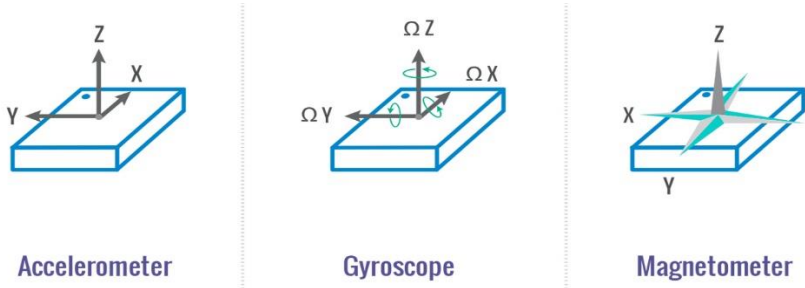


Figure 1.4. Components of an IMU. Image posted by Stephanie Stocker in Optimize your IMU (CEVA's Experts Blog).

For the precision and accuracy of drone manoeuvrability, Global Navigation Satellite System (GNSS) receivers are used to know the position of drones above the ground (Kraft et al., 2016). These receivers typically print the coordinates of the drone's position in the acquisition metadata, allowing users to learn their spatial information. The performance of these devices tends to be sufficient to perform these simple tasks (Rehak and Skaloud, 2017); in other cases, the drones can be equipped with more sophisticated sensors, which, however, summarily impacts their accessibility in terms of cost (Padró et al., 2019).

The following section presents the main types of sensors.

1.2.1. COTS Visible-Bands Sensors

Rapid technological advances in passive and active sensors have enhanced the capability of drones in various types of missions. Sensors on drones facilitate the acquisition of images at centimetre level and unlimited temporal resolution. Clearly, the sensors that can be equipped on a UAV depend on the size of the drone and the mission to be accomplished (Shahmoradi et al., 2020). However, depending on the objective of the aerial survey and the lighting conditions, various types of sensors could be useful. One of the aims of this research work is to investigate the potential of COTS sensors, i.e., those that are easily accessible and widely used in the technical field. Many existing (and expensive) RS instruments for aerial and satellite platforms are now embracing their miniature, low-cost versions for these UAV platforms, such as multispectral, hyperspectral, thermal, and light detection and ranging (LiDAR) cameras. The study of the peculiarities and limitations of these sensors will generate shared knowledge between professionals and simple users in performing specific RS tasks (Yao et al., 2019).

Each camera has an image chip inside: the CCD (charge-coupled device) chip or the CMOS (complementary metal-oxide-semiconductor) chip, which are the main actors in the conversion of radiant energy into Digital Numbers (DNs) values in the three aforementioned bands. The DN values are stored in elementary image units, defined as pixels. Nowadays, digital cameras offer an increasing number of pixels at an economical price, ensuring a good ratio of noise level to pixel size (Said et al., 2021). The characteristics of the image data depend on the resolutions of the sensor: spatial, radiometric, and spectral. The spatial resolution depends on the ground pixel size and is expressed in meters. It affects the resolution of the scene details and is related to the altitude of the platform and the instantaneous field of view (IFOV). The IFOV is the minimum solid angle through which the radiant energy reaches a single detector element. The radiometric resolution, also called radiometric sensitivity, describes the sensitivity of the sensor to discriminate very slightly different energy intensities. It relates to the number of divisions of the bit depth (e.g., 255 by 8 bits) in the data collected by a sensor.

The spectral resolution is the ability of the sensor to define fine ranges of wavelengths for each spatial sample. Thus, the higher the spectral resolution, the better the sensor's ability to exploit differences in spectral signature. The spectral resolution indicates the number of bands the sensor can acquire and the bandwidth. Thus, spectral resolution limits the number of bands the sensor can acquire. Depending on the spectral resolution, the classification of optical sensors includes:

- panchromatic (PAN) imaging sensor: single-channel detector in a wide wavelength range;
- RGB imaging sensor: three-band detector in the visible domain;
- multispectral imaging sensor (MSI): can acquire a few bands (from 2-9 bands) within a narrow wavelength band. The most operational sensors capture images in the visible to near-infrared (NIR) domain;
- hyperspectral imaging sensor (HSI): can collect more than 10 continuous narrow spectral bands (10-20 nm) in the spectral range from 0.4 to 2.5 μm . However, it is worth noting that some authors report further discrimination between superspectral and hyperspectral sensors, where superspectral sensors can collect a continuous narrow spectral band of 10-16, while HSI can collect more than 16;
- thermal imaging sensor: single-band detector that can operate in the wavelength spectrum from 5 μm to 14 μm ;
- Short-wave infrared (SWIR) imaging sensors: can acquire bands in the 1.5 μm to 3 μm wavelength spectrum.

As expressed by (Adamopoulos and Rinaudo, 2020), the UAV datasets used in research are mostly recorded with RGB sensors. Several works propose a comparison of the wide range of sensor options when considering professional applications.

Sensors in the visible bands take information in three bands: red, green and blue (RGB). These cameras are designed to capture data from the visible portion of the electromagnetic spectrum (Figure 1.5). Each channel can be considered as the strength of the signal within the selected wavelengths: red (650-750 nm), green

(495-570 nm), blue (450-495 nm). The standard parameters for choosing an RGB camera are lens, resolution, chip quality, and shutter type.

They are usually highly integrated into platforms; they are miniaturised and have affordable costs. Such a system, being highly engineered in terms of sensor integration (at low cost) has become very accessible (Yao et al., 2019).

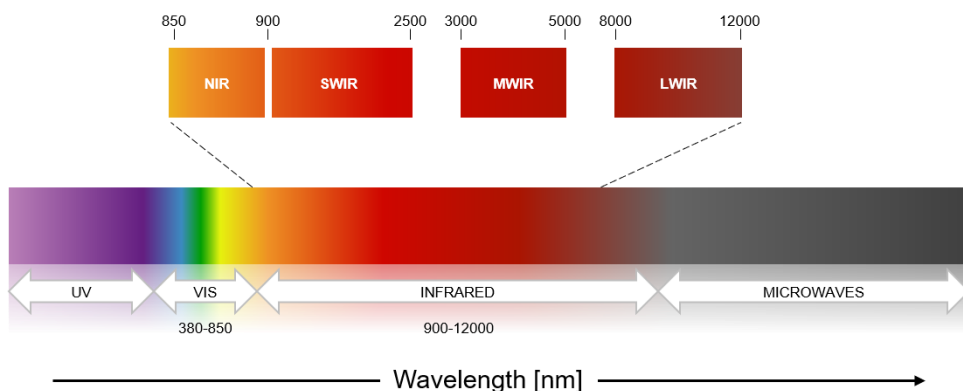


Figure 1.5. Electromagnetic reference spectrum for equipable sensors.

1.2.2. Light-Weight Multispectral Sensors

MSI are one of the most used sensors besides RGB cameras in the UAV sensor family, due to their advantages of obtaining spectral information in the red and near-infrared bands for vegetation applications in extremely high resolution (compared to products available from other platforms) (Al-Ali et al., 2020). Briefly, these MSI are designed to contain up to a few tenths more bands than those already seen. In general, they are characterised by the ability to record in the NIR band. Each channel is sensitive to radiation within a narrow wavelength band. The most commonly used spectral cameras have separate lenses and sensors containing filters for the different wavelengths (Said et al., 2021). The result is a multilayer image that contains both spectral information and the brightness of the observed lenses. The MSI can be divided into two categories based on bandwidth: narrowband and wideband. Narrowband refers to a camera with a small spectral range. A small spectral range generally corresponds to a more accurate spectral measurement (Effiom et al., 2019). Broad-

band means cameras with wide spectral ranges, which are usually like those on satellites. The use of these types of cameras simplifies the application of the algorithms used for satellite sensors. The results derived from narrowband and wideband cameras are quite similar.

As with the RGB camera, the response functions of the sensor are important for image interpretation. A critical factor for the MSI is radiometric calibration to determine spectral accuracy and reflectance-based derivatives. Before using multispectral images, radiometric calibration is a prerequisite and an essential step, where the DN value recorded by the camera can be converted to spectral reflectance. Some MSI allows pre-flight calibration, while others require a vicarious procedure.

Similarly, such multispectral cameras are still metric cameras by design and therefore can be easily processed with photogrammetric methods to produce standard orthophotos and DSMs (Labbé et al., 2012).

A major advantage for UAV-based MSI is the rendering of data with a much higher resolution that is normally not attainable in conventional multispectral RS (Yao et al., 2019).

Regardless of these features, and compared to RGB cameras, MSI are more expensive due to the extra hardware to handle the additional bands. Further barriers for these cameras are the compatibility of the data format with capable software packages. As the market is still relatively small and various manufacturers produce MSI with images in different formats, seamless processing software packages, especially data pre-processing management, are relatively limited to certain multispectral camera models (Yao et al., 2019).

1.2.3. Other Common Sensors

Given the distinction between active and passive remote sensors, this section examines those most used in both the research and professional fields, highlighting the advantages and limitations of each.

As drone technology continues to grow, infrared camera designs are becoming increasingly miniaturised and lightweight. This sensor captures temperature in images

to enable thermal analysis using, for example, heat flux profiles and thermal modelling (Said et al., 2021). They are widely used in various measurements of surface temperatures and thermal emission even over large areas.

Given these potentials, the classical problem of determining kinetic temperature and emissivity through the intensity and its distribution in the wavelength region of sensors onboard UAVs may be slightly different from thermal sensors onboard aircraft or those in space. For UAV sensors, atmospheric effects can be considered ignorable, calibration at the laboratory level is more accessible, and temperature measurements are theoretically more accurate. However, in view of the limited payload, light infrared thermal sensors are generally not equipped with cooled detectors, which causes a lower capture rate, lower spatial resolution, and lower sensitivity to achieve a reduced signal-to-noise ratio. As a result, they require sensors, such as RGB sensors, to support spatially integrated analysis despite their high instrumental costs (Yao et al., 2019).

Recently, lightweight hyperspectral imaging (HSI) sensors have been developed for use on drones. Hyperspectral sensors evaluate the reflected radiation as a series of narrow, contiguous wavelength bands (Gevaert et al., 2014). Typically, the bands are measured at intervals of 10-20 nm by hyperspectral sensors. Certainly, these sensors can provide information that is not accessible by traditional methods (Shahmoradi et al., 2020).

On the other hand, they are less accessible due to their high cost and stringent constraints on sensor compatibility with drones. In order to capture images with hundreds of narrow bands, most of the current lightweight hyperspectral sensors are linear-array cameras, which although the model has been mathematically well interpreted, it is practically complicated to process due to the limited meta-information that sensor manufacturers offer (Gevaert et al., 2014). Another limitation is that high spectral resolution is at the expense of spatial resolution. What is more, these light hyperspectral cameras normally have half the spectral ranges (400-1100 nm or 1100-2500 nm) compared to airborne hyperspectral cameras due to the payload limitation, which means that for wider spectral ranges, two or more light hyperspectral cameras may

be needed, either simultaneously or sequentially with different flights (Yao et al., 2019).

In addition to all the passive sensors seen, active sensors provide their energy source for illumination such as LiDAR. Two general categories can be distinguished depending on the platform on which they are fixed. Ground-based LiDAR is known as terrestrial laser scanning (TLS), while airborne LiDAR is known as airborne laser scanning (ALS). Its mode of operation is through laser transmission to the targeted object in the study area and records it again after its reflection on the sensor (Qi et al., 2018).

The time difference between the emission of the laser beam and the recording after it has been reflected from the object allows the calculation of the distance from the drone to the object under study. This sensor offers a highly accurate and faster method of acquiring data in real-time (Said et al., 2021). Their advantages over photogrammetry are their high reliability and ability to penetrate vegetation through multiple returns. However, being a sensor that strongly depends on the accuracy of the direct positioning of the host platform, LiDAR carried by UAVs is rather rudimentary compared to UAV photogrammetry (Klápště et al., 2020). GNSS/IMU devices in a consumer UAV platform are very commonly inaccurate concerning sensor resolution, and the platform is also more unstable during flight. Thus, even with well-calibrated and lightweight LiDAR sensors, the accuracy of the resulting point clouds is relatively low. Highly accurate LiDAR systems onboard UAVs are normally those that come with differential GNSS systems (Gerke and Przybilla, 2016), where high-precision positional measurements can be obtained in addition to very accurate IMU measurements. But while one advantage of UAV-based mapping is their relatively low cost, LiDAR sensors, even those with a relatively low cost, are still an order of magnitude higher than RGB cameras and require higher payloads (up to a few kilos) (Räsänen and Virtanen, 2019). Thus, in terms of cost and sensors required for integration, the UAV LiDAR system is still not as affordable as UAV-based photogrammetric mapping systems (Yao et al., 2019).

Among the active sensors that can be equipped are those capable of measuring microwaves (Radio Detection And Ranging - RADAR), or Sound Navigation and Ranging

(SONAR), which, as in the LiDAR case, require very high expertise and cost. This sensor offers a highly accurate and faster method of acquiring data in real-time (Said et al., 2021). Their advantages over photogrammetry are their high reliability and ability to penetrate vegetation through multiple returns.

1.2.4. Fields of Application

Beyond conventional RS, UAVs are ready for tangible impacts in marketing, service delivery, and healthcare, including drug delivery and outpatient care. UAVs are transforming cinematography and photography, search, and rescue operations. In essence, UAVs are changing our perceptions of how tasks that had traditionally been confined to satellites and aeroplanes can be accomplished (Cummings et al., 2017). On the other hand, UAVs of various sizes and functionalities are now available to ordinary consumers like any other electronics product. Periodically, new products are brought onto the market and are increasingly high-performance and equipped with very high-resolution sensors but still at low cost. New forms of use are emerging on the agenda.

Drone technology covers a wide variety of civil and military uses, both indoors and outdoors. Depending on the camera or sensors installed in drones, they can be used for various missions that are classified in terms of purpose, environment, and the nature of the flight area (outdoor or indoor).

Aerial imagery captured by UAVs is playing an increasingly important role in disaster response due to its efficiency in situational awareness (Yu et al., 2018b). Although these images are captured with very high spatial resolution, they are processed much faster than satellite imagery. In addition, it is possible to capture oblique and close-up images that can detect cracks, degradation and more (Kerle et al., 2020). With the use of UAVs, first responders can better understand which structures have been affected by a given event and can determine the extent of the damage caused to these structures.

Images and video provide real-time situational information relevant to the decisions of transport planners examining damaged roads, evacuation routes, and supporting

transport logistics (Kubota et al., 2019). Clearly, with the combined use of UAV imagery, satellite, and aerial data, it becomes possible to identify damage to building facades and roofs by integrating geometric transformation and environmental information (Athanasios et al., 2019).

Drones have been widely used in monitoring national parks to track wildlife, assess the impact of climate change, and study the biodiversity of various environments (Tmušić et al., 2020). Drones also have the ability to recognise and investigate environmental hazards such as burning forests and melting snow resulting in avalanches in mountainous regions (Theule et al., 2015). They have been used to monitor the state of mangroves, which are difficult to monitor from the ground (Warfield and Leon, 2019). Drones used to monitor ocean shores offer cheaper surveillance, real-time monitoring, and coverage of large areas in a short time. (Zhang et al., 2019b) used drones to study the potential of this technology for long-term forest canopy monitoring. This study reported that drones can monitor forests over a long period by providing high-resolution data at an economical cost.

Numerous researchers have studied the application of drones in engineering, architecture, and construction over the past decade (Adami et al., 2019). Many papers have dealt with the use of photogrammetric acquisitions from drones for the generation of a digitised 3D model (Caroti et al., 2019). Models from drone imagery have been shown to be as accurate and reliable as those derived from more usual technologies. (Nettis et al., 2020) studied the possibility of using drones to inspect the structures of viaducts and bridges. (Bappy et al., 2015) studied the efficiency of using multispectral drone imagery using RGB and thermal cameras to locate fault signals in bridges. The study proposed the use of drone technology for effective fault detection. (Eschmann et al., 2012) established the effectiveness of using cameras in drones to monitor and detect cracks with millimetre accuracy.

The use of drones has been widely used in the monitoring and protection of historical structures such as temples, castles, and churches due to their accuracy and efficiency (Themistocleous et al., 2019).

Further research elaborated that drone images are reliable enough for automatic fault identification and accurate 3D restoration (Jafari et al., 2017).

These reports have indicated that drones have outperformed conventional surveying techniques in the creation of infrastructure models, although their efficiency is affected by time.

Numerous studies have indicated that drones embedded with various sensors can be used at different stages of mining to monitor and collect information in real-time, thus aiding the mine safety, planning, scheduling, and security process.

(Devoto et al., 2020) used drones equipped with a camera to capture landslide movements. Due to the high-resolution orthomosaic and digital terrain model, the study recommends the use of drones for these operations. In their research work, (Carvajal et al., 2011) studied landslide movements using geodetic GNSS receiver coupled with drones and concretised that drone results are more accurate and effective for monitoring, as they have a variance of less than 0.12 m. On the other hand, the study by (Shi and Liu, 2015) highlights the use of drones to locate and determine slope instabilities through rapid landslide mapping and debris flow modelling. This was achieved by generating higher-resolution 3D models in which volumes, contours, and crosslines were obtained.

Numerous studies have investigated the application of drones in calculating the volume of earth material moved by heavy machinery and compared it with the conventional method of tachometry (Hämmerle et al., 2016). These studies have proposed the use of drones for calculating the volume of earth material which have been integrated with software for calculating the volume. Several studies suggest the use of drones because of their greater work efficiency, safety, and convenience.

However, UAVs are still under development and several problems need to be solved; such as short battery life, leading to a limited area of coverage; unpredictable behaviour in different weather conditions; limited scope of pilot training for users; and legislation that severely restricts the use of UAVs in most countries. Due to the high resolution of the sensors onboard the UAVs, privacy issues also arise. Finally, manual interpretation and analysis of embedded data is no longer adequate, which is why so-

phisticated automatic analysis methods are needed to make processes efficient and effective.

2. LOW-COST UAV-PHOTOGRAMMETRY POTENTIALITIES

Concisely, 3D reconstruction is the process of capturing the geometry and appearance of an object or an entire scene and proposing a digitised version of it. Over the years, a variety of techniques and algorithms for 3D modelling have been developed to meet different needs in various fields of application ranging, as seen in Chapter 1, from active methods that require the use of advanced and expensive equipment to capture geometric information (e.g., laser scanners, structured lights, microwaves, ultrasound, etc.) to passive methods that rely only on optical imaging techniques. The latter techniques do not require special devices or equipment and are therefore easily applicable in different contexts. One of the major goals of researchers has always been to look for a low-cost alternative to overcome the operational limitations imposed by the former methods. (Rieke-Zapp et al., 2001) have shown that, among passive methods, photogrammetry is a convincing tool for generating 3D models with accuracy and resolution comparable to those from laser scanners (Figure 2.1).

In the field of photogrammetry, on the other hand, the rise of UAVs in the last decade has strengthened its potential and indeed represented the most significant innovation for it. Photogrammetric surveying has thus developed its traditional method of acquisition and processing with the assistance of advanced UAV technology (Erenoglu et al., 2017). In fact, photogrammetry is a relatively old technique (Eltner and Sofia, 2020). In this field, pioneer reconstruction efforts date back to the 1840s, where they tested a pair of ground cameras separated by a fixed baseline to estimate the shape of the terrain (Maybank, 2012).

With the introduction of aeroplanes and then space acquisitions, the development of photogrammetry had its exploit: 2D photographs were used to rectify images into ap-

appropriate coordinates, multiple frames were mosaicked to estimate structures or terrain elevation. In parallel, the scientific community developed on the one hand the first CV algorithms for reconstructing 3D scenes from stereo images (Marr and Poggio, 1976), and on the other hand the first techniques on motion-based reconstruction (Ullman, 1979).

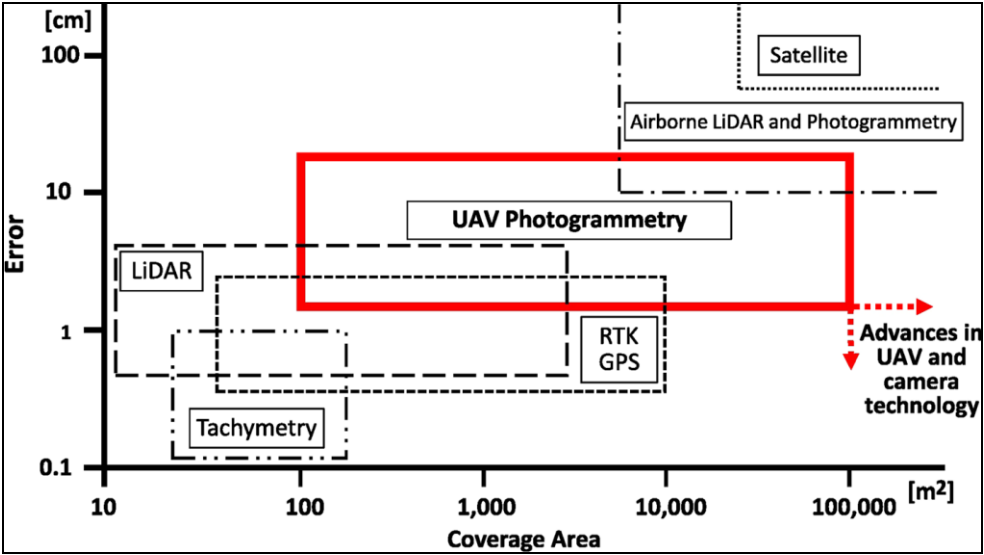


Figure 2.1. Accuracy potentialities employing UAV photogrammetry in surveying. Image based on (Deliry and Avdan, 2021)

The formalisations and validations of these two developments have structured the fundamental theory about Structure from Motion (SfM) techniques. However, subsequent advances in SfM were then stimulated primarily by the wide range of modern applications. This wide range of applications of SfM results in research with different objectives, thus emphasising multiple ways of addressing SfM problems in space and time (Eltner and Sofia, 2020). This innovative technique has proven to have the potential to democratise 3D topographic surveying, offering rapid acquisition of 3D point clouds at the minimal expense (Smith et al., 2016).

When it comes to the costs of a SfM-photogrammetric application, they can vary depending on the sensors, the complexity of the survey, and the georeferencing targets distributed in the area, if any.

In most of the works, the sensors used are based on consumer-type cameras. These sensors can vary substantially in price and complexity, but the trade-offs between these and the resulting data quality are not well constrained (Cook, 2017). In general, however, the availability of these sensors, and the opportunity to apply SfM-photogrammetry to satellite imagery (Sofia et al., 2016), historical photographs, or opportunistic sensors have dramatically reduced survey costs compared to more established technologies.

At the same time, the availability of free or low-cost fully automated photogrammetric software and the recent rise of drones also in the private and public sector allows virtually anyone to generate 3D models for several objectives (Remondino et al., 2017). A wide range of multi-sector practitioners has been quick to adopt SfM techniques, as seen in the recent and growing proliferation of studies using and testing its benefits (Anderson et al., 2019). For example, the high flexibility of SfM-photogrammetry allows repeated data acquisition and thus multi-temporal observations of the Earth's surface with varying frequencies. Furthermore, the method can be applied to existing image information allowing the reconstruction of past shapes.

As shown by (Iglhaut et al., 2019), there has been a gradual increase in our ability to collect topographic data in recent decades. In an order-of-magnitude overview, starting from 10^1 - 10^2 measurements per day with a traditional optical layer, moving to 10^3 - 10^4 in GNSS survey campaigns, more than 10^6 measurements per day are achieved with laser scanning technology and modern photogrammetry techniques (Figure 2.2).

Improvements in precision and accuracy have been considerable, but more modest. From the Figure 2.2, each new development has required new technology, typically more expensive (often >10,000 Euros). A step change has been seen in SfM-MVS techniques, which are able to offer similar data quality to high-resolution surveying techniques but with minimal expense.

Total Station (TS) or Electronic Distance Measurement (EDM) surveys provide high precision at mm level of 3D accuracy of the land surface (Fernández-Hernandez et al., 2015, Saponaro et al., 2020b). TS points are selectively sampled by the operators

and can be strategically placed to describe the morphology of terrain for relatively small areas. The main disadvantage of TS surveys is the density of points obtainable in a survey campaign, which is conditioned by the measurement time and the accessibility of the scenario. A further limitation is due to subjectivity in the generation of the measured point network, which can introduce a bias towards accessible locations and variability among operators (Bangen et al., 2014a). This bias can therefore be significant because the interpolation required to produce a topographic model inherits any biases from the specific geometry of the survey points. Data provided by GNSS surveys can have similar accuracy to TS surveys (Bangen et al., 2014b), depending on the duration of occupation of a point and the survey mode. RTK surveys are common in professional practice where a direct radio or mobile network link between a rover and a base station can provide the detector with information on the final accuracy of the solution relative to the base station coordinates (Wheaton et al., 2010). As such, GNSS surveys are subject to many of the same advantages (accuracy, precision, selectivity) and disadvantages (low point density) as TS surveys. The accuracy of RTK-GNSS surveys is on the centimetre scale, although higher accuracies can be achieved with the static continuous recording mode. Accuracy, at the same time, depends on the number and geometry of satellites used to calculate a point, so a clear view of the sky and removal of environmental disturbances is also necessary.

The Airborne Laser Scanner (ALS), also known as airborne LiDAR, has become a well-established survey tool over the last two decades. Remote platforms and the resulting large survey range, generally taken to altitudes between 300 and 4000 m Above Ground Level (AGL), make ALS naturally suited to landscape-scale surveys, resulting in point resolution and accuracy at the decimetre scale. The TLS looks like essentially the same technology mounted statically on a conventional survey tripod (Medjkane et al., 2018, Saponaro et al., 2020b, Seier et al., 2017) but also on mobile systems (Sonnessa et al., 2020). The shorter range and static setting of TLS results in millimetre-scale precision and accuracy. The main advantage of LiDAR systems is the acquisition speed, which can reach hundreds of thousands of points per second. Both ALS and TLS are expensive surveying solutions (>30,000 € for a TLS) that pro-

duce large amounts of data that must then be decimated to produce useful information. These instruments also typically weigh 5-10 kg and require a lot of ancillary equipment, limiting their portability.

Conventional photogrammetry is the closest existing technique to SfM-MVS and has contributed greatly to the development of the SfM-MVS workflow (Eltner and Sofia, 2020). Conventional photogrammetry uses precise knowledge of the 3D position and poses of the cameras, or the 3D position of a set of control points located in the scene of interest, to reconstruct the geometry of the scene. The achievable spatial resolution is a function of pixel size, but digital photogrammetry has been applied over a range of scales from plots of 10^1 m² (Carbonneau et al., 2003) to scenes of $>10^6$ m² (Westaway et al., 2000). For photogrammetry, once the equipment has been set up, data collection takes only a few minutes. Fine resolution and accurate millimetre-scale topography can be achieved at distances of several metres, although the accuracy achievable decreases as the distance between the camera and the object of interest increases. However, the main weaknesses of conventional photogrammetry are the grade of expertise required, the effort and cost of finding the large amount of a priori information required, the relative rigour of the image geometry, such as the degree of overlap, which can make it not appropriate for some applications, and finally the limited capacity for multi-temporal revisiting.

Acquisitions from ALS, TLS, and products from conventional photogrammetry and modern SfM-MVS are defined as non-selective methods, i.e., methods in which each data point is not selected for inclusion in the survey individually by the surveyor. With SfM-MVS techniques, point densities similar to (or greater than) laser scanner techniques can be achieved, and while point precision and accuracy are mostly determined by the survey range, even sub-cm scale errors are achievable (Smith and Vericat, 2015). Perhaps the biggest disadvantage of SfM-MVS is the fact that the quality of the resulting surface model depends on many different factors related to the single survey. SfM-MVS data are generally not as accurate as those from TLS, however, the technique is flexible enough to be applicable on survey areas from 10^{-2} - 10^6

m² (Smith and Vericat, 2015). On the other hand, however, accurate scaling and georeferencing require the use of TS and/or GNSS measurements.

Each of the techniques described above has different strengths and weaknesses and is better suited to different tasks. Certainly, SfM-MVS is not a complete replacement for these other methods, however, under different circumstances, SfM-MVS is an efficient and cost-effective survey method.

EO research today is a data-rich environment, where the latest advancement is not only the resolution of the data but the variety and speed with which geo-referenced data can be acquired (Miller and Goodchild, 2015). From a citizen science perspective, this can enhance research but suffers from the need for specialised training and simplified methodologies that can reduce research outputs (Eltner and Sofia, 2020). The ease of use of SfM-photogrammetry with a range of low-cost sensors may allow the opportunity for crowdsourced participatory and opportunistic sensing. It is important to note, however, that this has a hidden cost: most users are often unaware of the strengths and weaknesses of the methodology and software used, employing it as a black box where photographs can be entered on one side and a completed 3D model retrieved on the other. It is crucial, therefore, to provide geospatial tools integrated with properly designed processing methodologies.

Although algorithmic advances and software tools make the application of SfM-photogrammetry straightforward in its use for topographic reconstruction, basic knowledge of photogrammetric principles is still required for robust accuracy evaluation (Carbonneau and Dietrich, 2017), to prevent potential bias in the 3D model leading to misinterpretation of outcomes. The increased awareness in this regard is evidenced by the increased interest in correct parameter settings and their effect on the final model.

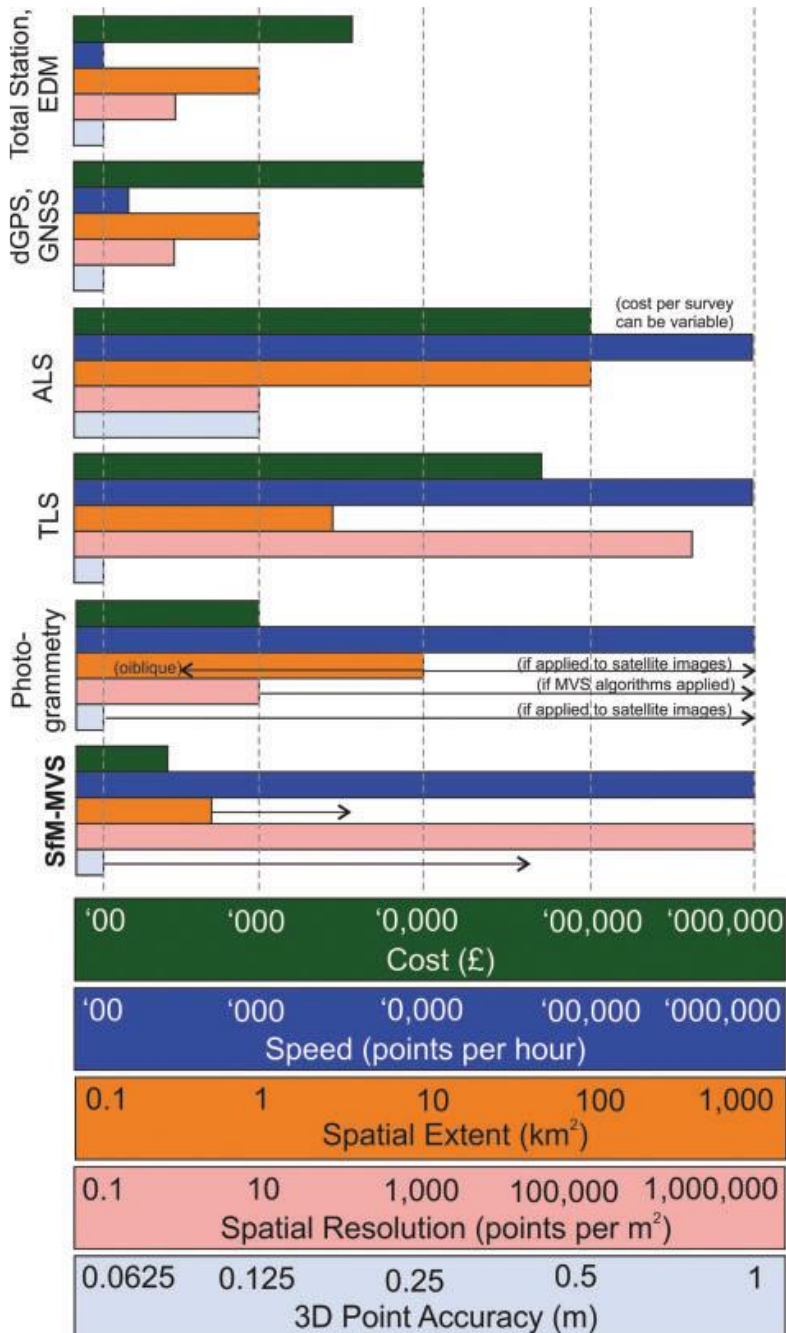


Figure 2.2. Comparison of geomatic techniques and technologies for the acquisition of objects and territories. Image based on (Smith et al., 2016)

2.1. SFM-MVS TECHNIQUES

In the field of AI, CV has two main scopes, which are recognition and reconstruction. Leaving aside the details concerning recognition, there are various techniques of reconstruction based on different principles and each with precise merits, defects, and preferred areas of application. Typical techniques are:

- Shape from stereo
- Shape from silhouette
- Shape from texture
- Shape from focus
- Shape from still image
- Shape from shading (photometric stereo)
- Structure from Motion.

SfM procedures has been refined in recent years to the point where they have become an interesting data manipulation tool in response to the increasingly vital demands for reliable documentation in various fields of work. These methods of analysis, which exploit simple photograms, become part of the spatial narrative, generating cognitive tools that help define environmental qualities, integrating quantitative information related to the place.

The SfM pipeline allows the reconstruction of 3D structures from a series of images acquired from different observation points. As asserted by (Carrivick et al., 2016), SfM is not so much a single technique but rather a workflow that employs multiple algorithms developed from CV, traditional photogrammetry, and more conventional surveying techniques. These algorithms enable computers to understand and interpret the visual information present in images, i.e., they undertake a numerical analysis of the images to discover what is present in the images and where it is located. In other words, evaluative tools that, starting precisely from the photographic data, translate and encode the physical and dynamic space of the place anew in a completely virtual model, also making its meanings explicit.

At this point, it is useful to define what is meant by SfM. Strictly, the technique only refers to one element of the flow of the entire photogrammetric work. In several

works, the SfM-derived point cloud is interpreted as the final product (Dandois and Ellis, 2010; Fonstad et al., 2013), but in most studies Multi-View Stereo (MVS) photogrammetry algorithms are then implemented to increase the point density by several orders of magnitude. Consequently, it is more correct to refer to the entire photogrammetric flow as SfM-MVS (Figure 2.3).

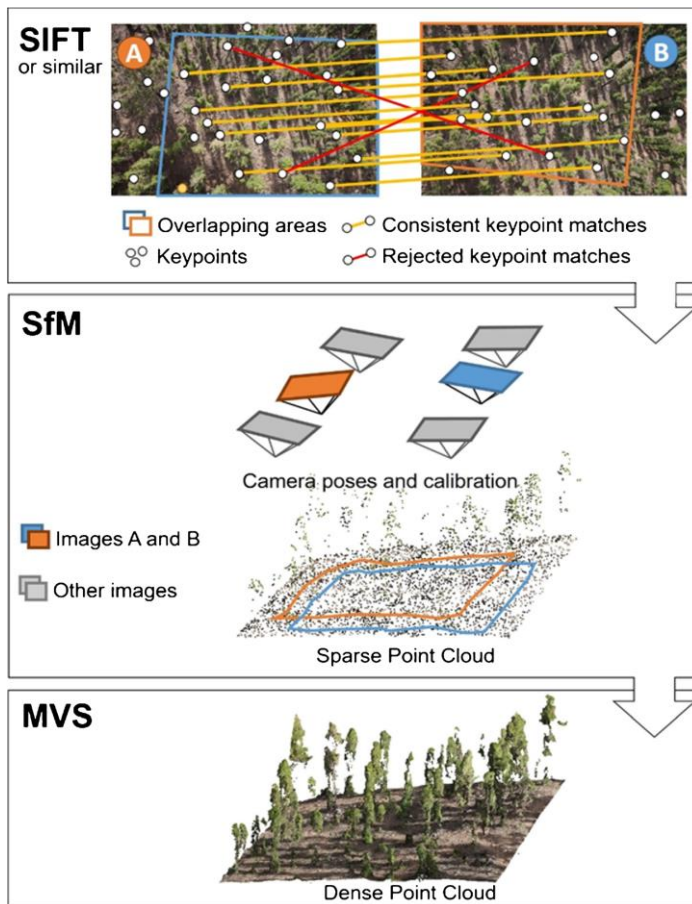


Figure 2.3. The three key phases in a SfM-MVS workflow: (1) key point identification and matching (e.g., SIFT), (2) SfM with camera parameters and a sparse point cloud as output, and (3) the densified point cloud following MVS. Image based on (Iglhaut et al., 2019)

Traditional photogrammetry methods are based on an analogy of binocular human vision. If the relative position of two points is known, from these latter, depth can be perceived. However, depth, volumes, or 3D features can also be perceived from a

single observation point if the observer or object is moving. SfM is a technique that is based on both principles. Motion-based or structure-by-motion reconstruction was introduced by (Ullman, 1979) in the late 1970s but only became popular in the 2000s due to the further efforts of several authors, including (Lowe, 2004b), (Snavely et al., 2006), (Furukawa and Ponce, 2009), in developing specific CV algorithms. It differs from traditional photogrammetry mainly in three respects:

- i. features can be automatically identified and matched in images at different scales, viewing angles and orientations, which is of particular advantage when considering small unstable platforms such as UAVs;
- ii. the equations used in the algorithm can be solved without information on camera positions or Ground Control Points (GCPs), although both can be added and used;
- iii. camera calibration can be automatically resolved or refined in the process.

This technique can therefore automatically provide photogrammetric models without requiring strict homogeneity in image overlays, camera poses, and calibrations.

With a set of images of a scene taken from multiple viewpoints, the first step is to identify features, called key points, in each image and assign a unique identifier to these regardless of the perspective and scale of the image (Figure 2.4). To be most successful for the SfM-MVS procedure, this identification of key points should be valid for images taken at relatively wide baselines, i.e., the perspectives can be different. This is done by particular algorithms that synthesise operators of interest, such as the one implemented by (Lowe, 2004b) called Scale Invariant Feature Transform (SIFT), often identified as the parent of all subsequent evolutions. The identification of sets of pixels that are invariant to changes in scale and orientation and suitable for matching wide baselines has been a long-standing issue in CV. Currently, popular feature detection algorithms improve on traditional correlation-based approaches in that they geometrically normalise the feature-containing region and correct for photometric distortions (e.g., illumination) to ensure rotational and photometric invariance. Several alternative methods for identifying features have been published, including SURF, ASIFT, BRIEF, and LDAHash (Leng et al., 2018). The fundamental criterion for evalu-

ating the real efficiency of an operator of interest is represented by its ability to identify the same detail (i.e., to provide homologous points) even on frames that differ in scale, a different viewpoint, lighting conditions, etc. In other words, the more efficient an operator of interest is, the greater its degree of invariance with respect to more general geometric and radiometric transformations (Leng et al., 2018).

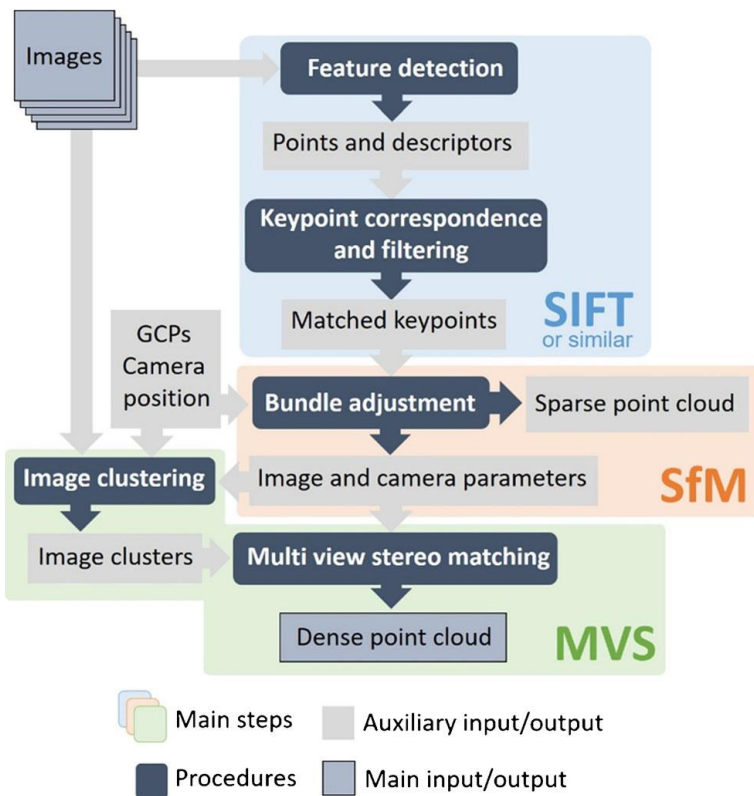


Figure 2.4. Schematic workflow of the SfM-MVS process resulting in a dense point cloud from image sets. The point cloud is georeferenced by providing positional information for images and/or GCPs.

The next step requires the identification of correspondences between key points in several images. SIFT (or similar) generates numerical descriptors for each point in each image. There is no guarantee that every key point is represented in every image, so a threshold is applied to identify matches. The consistency of the key point matches is checked using a coarse reconstruction of the image geometry and the relative position of the key points on it. The ratio of the Euclidean distance of the nearest

neighbour to that of the second nearest neighbour is considered, called the “distance ratio”, specifying a minimum value, typically 0.6-0.8. Clearly, in this high-density space, a brutal Euclidean nearest-neighbour search is computationally demanding, and thus k-dimensional trees (also called k-d trees) modified for approximate matching are applied as an efficient approximate solution. For example, the Approximate Nearest Neighbour (ANN) solution allows for relative error in identifying the nearest neighbour and searching only the top candidates can result in substantial time savings.

A further filter of key point matches is then applied to try to identify and remove any remaining mismatches. Taking any pair of images with multiple common key points, a fundamental matrix (F-matrix) is calculated. This F-matrix specifies the relationship between the two images and reconstructs the scene up to a projective transformation in which collinearity between points is preserved. Candidate F-matrices are examined using the RANdom SAmple Consensus (RANSAC) method (Fischler and Bolles, 1981) in which key points, contained in various subsets and used in the construction of the F-matrix, are randomly sampled and a difference between the returned F-matrix and that returned by other sampled key points is computed. Beyond a certain threshold, the key point is judged to be an “outlier” and is not considered part of the model. Iteratively, sampling is repeated until there is a 95% probability that the subset contains only 'inliers' for which the F-matrix is returned. After further refinement, all outlier matches are removed. At this stage, other tests can be implemented, such as the maximum likelihood estimation of the sample consensus or the Hough transformation. The reader is referred to more specific texts for a better understanding.

Once the geometrically correct feature matches are obtained, the SfM initiates the BA algorithms to simultaneously estimate the 3D geometry of the investigated scene, the different camera poses, defined as extrinsic orientation, named Exterior Orientation (ExO), and the intrinsic camera parameters, i.e., the Interior Orientation (IO) of the model (Ullman, 1979). The presence of a camera calibration would help the adjustment of the beam. Where such a camera calibration is not available, SfM employs both the Exchangeable Image File Format (EXIF) tags in the images and the redundan-

cy offered by a large dataset of images and key point matches to estimate the parameters that outline the camera calibration matrix (further details will be provided in Sections 4.1 and 4.2). The BA results in a minimization of a cost function, which jointly returns a 3D structure and the optimal camera parameters (Eltner and Sofia, 2020). The step is generally identified as Bundle Block Adjustment (BBA), or simply Bundle Adjustment (BA). The algorithm used for BA is generally the Levenberg-Marquardt, also known as Damped Least-Squares. It allows the resolution of the least-squares method for the non-linear case. There are various other implementations and subsequent evolutions in the literature. This step has a high computational cost and must be performed for each image that is added to the reconstruction (Bianco et al., 2018). Precisely, the term "bundle" refers to the beams of light that connect the camera centres to the 3D points, and "adjustment" refers to the minimisation of the non-linear cost function that reflects the measurement error (Szeliski, 2011). This error term can incorporate many sources of information, including errors in the projection of individual image features into object space, so-called reprojection errors (RE). Parameter values must be assigned initial values before calculating a non-linear optimisation of the beam setting parameters. Sequential methods take an initial pair of images, which typically show many common key points and a large baseline. The traces between the key points are then triangulated to give initial estimates of the feature positions. Errors between the projections of each trace and the corresponding key points are minimised as part of a two-frame BA. The camera containing the largest number of traces whose 3D position is already known is then selected and added to the optimisation. Using these known 3D positions, the 2D coordinates of the new image are mapped into the 3D object space and the intrinsic camera parameters are estimated. In many SfM implementations, an additional BA is performed with only the new parameters allowed to change. In each step, key points with high REs are removed. With each image added in sequence, a global BA is then performed to refine the entire model. The output of the SfM stage is a scattered, unscaled 3D point cloud in arbitrary units along with the models and camera poses.

A minimum of three GCPs is required to scale and georeference the SfM-products: using a seven-parameter linear similarity transformation, three global translation parameters, three rotation parameters, and one scaling parameter are mined (Szeliski, 2011). In these cases, one speaks of indirect georeferencing (IG) (Padró et al., 2019). Unlike conventional photogrammetry, each photograph does not need to contain visible GCPs but takes advantage of the photogrammetric block belonging to eventually inherit metric and spatial information. Alternatively, direct georeferencing (DG) and scaling are applied from known camera positions derived from GNSS measurements and IMUs (Padró et al., 2019). A hybrid mode sees the implementation of the two georeferencing approaches uses DG to provide approximate camera positions to initialise the BA and then uses external GCPs to better constrain the solution (Padró et al., 2019). Identifying GCPs and entering their coordinates in the previous step provides additional information on the 3D geometry that can be used to further refine the estimates of the intrinsic camera parameters and the geometry of the reconstructed scene. The known coordinates and error estimates of these points provide an additional source of error in minimising the non-linear cost function during the BA step. With this external information included in the model, the BA can be re-run to optimise the image alignment in light of this new information, minimising the sum of the RE and the georeferencing error.

The final step of the workflow is the application of the MVS algorithms to the previously scaled and georeferenced sparse points cloud and camera calibration parameters. Before MVS densification, and for computational efficiency or even feasibility, images are clustered according to their position (Furukawa and Ponce, 2009). In this way, the dense point cloud of each cluster is calculated separately.

MVS usually increases the density of the point cloud by at least two orders of magnitude.

In general, during processing, pixels are back-projected onto all images and triangulated by the spatial intersection to form a 3D surface without abrupt irregularities using energy-minimisation and gradient-based algorithms.

A dense point cloud, with colour/spectral information obtained from the input imagery, is the core output of the SfM-MVS workflow.

2.2. RELATED PHOTOGRAMMETRIC PRODUCTS

Subsequent processing steps, especially for aerial surveys, typically involve the derivation of a Digital Elevation Model (DEM) and an orthomosaic (Eltner and Sofia, 2020).

Initially, spatial interpolation algorithms are applied to sparse, or rather dense, points clouds. These make it possible to determine the characteristics of the reconstructed model in continuous form, even in non-discretized points. The result of this technique is the generation of a surface, called as statistical surface. The interpolation techniques usually used are:

- IDW or Inverse Distance Weighted;
- RBF or Radial Basis Function;
- Influence polygon method, based on TIN representation and Delaunay triangulations;
- Geostatic Kriging method;
- other methods such as visual techniques, Fourier series, contour search, trend, spline, nearest point tessellation, moving average

whose discussion is referred to the specific literature.

These statistical surfaces, defined as DEMs, spatially represent the distribution of the heights of territory in a raster format, associating to each pixel the attribute relative to the absolute height with respect to a chosen geodetic reference system. In truth, the DEM cannot be considered a two-dimensional (2D) product, but neither can it be considered 3D: the scientific community, therefore, defines it as a 2.5D product.

The study of DEMs provides extremely interesting quantitative and qualitative information, especially for environmental and territorial analysis applications.

Generally, DEMs are misrepresented with Digital Surface Models (DSM) and/or Digital Terrain Models (DTM) characterised by the 3D representation mode. DTMs, unlike

DSMs, filter the scene taken by buildings, objects, trees, etc., to give a mere representation of the bare terrain.

Once the distribution of the elevations of the examined surface has been analysed, it is possible to orthographically project the images being processed onto the respective portion of the surface taken. Orthophotos are generated by means of orthorectification techniques of the original images. The orthorectification algorithms analyse the estimated pose orientations, for each implemented image, and evaluate the projection considering the distribution of the elevations of the points, in the relative areas of the model and the pose of the cameras calculated in the SfM-MVS passes. Through this process, the image is restored to a central perspective of the object, with constant scale. At the end of the image orthorectification process, further stitching algorithms combine the various newly generated orthophotos in an orthomosaic process. The final orthomosaic will therefore be 2D processing of the surveyed images characterised by a correct and proportionate representation of the objects captured (Ludwig et al., 2020). This photogrammetric product is essential for measurement and photo-interpretation activities.

Starting from a dense cloud of points and the normal vectors associated with each of the points, it is possible to compute a polygon model, commonly referred to as a polygon mesh (Lague et al., 2013a). In 3D computer graphics and solid modelling, a polygon mesh is a collection of vertices, edges and faces that define the shape of a polyhedral object. Vertices are points in space, derived from the dense points cloud, which therefore have 3D coordinates and form the basis for defining edges, i.e., the segments that join two vertices in space. In turn, edges define faces through their connection and closure. The faces are usually made up of triangles (triangle mesh), quadrilaterals (quads), or other simple convex polygons (n-gons), as this simplifies rendering, but they may also be more generally composed of concave polygons or even polygons with holes. In areas where the datum is absent, the algorithm generates the same as polygons, the result of directional interpolation of the other areas where the datum is present. There are numerous algorithms for constructing a polygonal model: the one most frequently used by the software evaluated in this field of

study is based on Poisson reconstruction. The Poisson algorithm is a classic method for solving the problem of reconstructing a Lambertian surface by exploiting the matrix formulation of Lambert's Law. Generally, in almost all software that enables mesh reconstructions, the possibility of transferring the RGB information of the point cloud to the mesh vertices is offered. This operation gives a type of colouring called vertex colour where the faces are coloured by interpolating the values between the vertices that compose them. Alternatively, it is possible to texturize the polygonal model by directly associating portions of frames to the generated faces.

In addition, image metrics such as radiance/reflectivity values and texture can be extracted. Finally, rasterization can offer the opportunity to explore the detected information in greater depth when statistics are calculated for each cell. In addition to computational analysis, the models generated by high-resolution SfM-MVS appear visually realistic, providing experts with a near-real representation of the scene. Intuitive to understand, SfM models, therefore, have an important advantage over coarser RS methods, allowing for rapid visual assessment and/or validation.

As with all RS data, these will always only approximate the earth's surface and some limitations will always remain. In analytical terms, although a projectively equivalent geometry to the real one can be provided analytically, the orientation parameters are different from the real ones, as is the geometry of the object itself but equivalent in terms of residuals in the collinearity equations (Saponaro et al., 2018). As SfM-photogrammetry is a new technology, the boundaries and quantification of these limitations are not yet fully tested. Some of the main challenges of SfM-photogrammetry that the scientific community is facing concern reproducibility. Variations in illumination, weather, and seasonal conditions are inevitable between different photogrammetric acquisitions of the same scenario. As a passive sensing technique, these variations are directly reflected in the data and therefore in the replicability of the analysis. To ensure the use of SfM data on-demand, allowing acquisitions at different times of the year, it is, therefore, crucial to develop pre-processing protocols for various conditional scenarios and models that take into account variations in the data.

A crucial challenge concerns the lack of acquisition and processing protocols. The success of an SfM-based photogrammetric acquisition relies heavily on the sensor used, the photographic path and viewing angles along with the chosen image overlay, as well as the composition of a scene. Adjustments to the acquisition approach to ensure quality data are currently undertaken based on the experience of the detector. Indeed, protocols need to be established to enable certainty of SfM results while minimising acquisition efforts. At the same time, processing protocols designed to provide data appropriate to the research question and to optimise processing speed are required (Iglhaut et al., 2019).

2.3. STRUCTURING A COMPREHENSIVE WORKFLOW

The SfM-MVS pipeline has become a standard workflow for UAV image processing as it can handle mixed geometries of non-vertical, unordered, and unmarked image blocks.

Nevertheless, several recent studies have revealed the presence of systematic errors in the automated SfM-MVS pipeline (Carbonneau and Dietrich, 2017, Eltner et al., 2016, James et al., 2017a). Such systematic errors usually originate from image sensor characteristics, camera distortion models included within the SfM-MVS software, workspace settings, imaging network configurations, GCP characteristics, the structure of the studied scenario, as well as over-parameterization.

Effectively, each step seen in Sections 2.1 and 2.2 can exploit different algorithms to solve the problem at hand and therefore many different SfM-MVS pipelines (and subsequent processing) can be built. There are many SfM pipelines available in the literature and the scientific community has always tried to prototype a unique workflow that is both flexible and exhaustive. (Bianco et al., 2018) ask: how to choose the best among them? To date, there is no comprehensive synthesis of the practical options available to mappers when planning a modern photogrammetric survey, the errors that can be expected from each choice, and most importantly the underlying processes that take place as part of the SfM-MVS workflow. The clear similarities between

conventional photogrammetry and SfM-MVS may lead to the assumption that the latter is simply an incremental development of photogrammetry. However, several facets of SfM-MVS have a totally different source, originating instead from advances in 3D CV algorithms. Instead, photogrammetric principles and techniques are part of this SfM-MVS workflow (Micheletti et al., 2015).

The typical workflow implemented by many SfM-MVS software packages is presented and summarised in Figure 2.5. The specifics of this workflow vary from one software package to another, but there is a clear commonality. The specific values of the parameter settings for each step will vary between the different SfM-MVS packages but the user may not be able to adjust these values (Casella et al., 2019, Kingsland, 2020, Serifoglu Yilmaz et al., 2018). In fact, users might not be aware of or might simply be adjusting a global accuracy quality setting implemented within particular SfM software packages, or using default values, as is often the case. Going beyond this 'black box' approach, an understanding of the entire SfM-MVS workflow implemented is useful for mappers to identify and minimise potential sources of error in the resulting topographic data but more importantly generate reproducible, repeatable, and comparable photogrammetric products. The aim of this study is therefore to generate a workflow that is independent of the software platform used, the scenario investigated, and the expertise of the operator.

The idea of protocolling a univocal line of processing can be a winning strategy in the standardisation of results and their derivable interpretations.

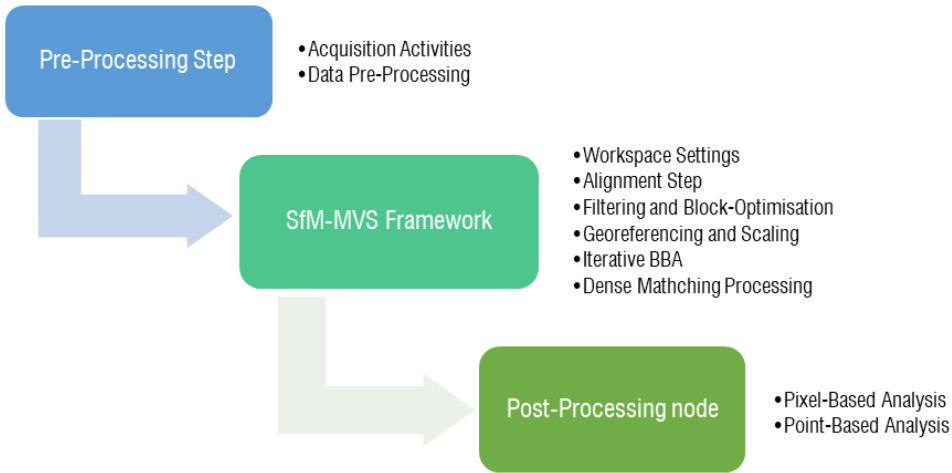


Figure 2.5. General framework for the SfM-MVS pre-treatment, processing, and post-processing manipulation of UAV-based datasets.

Given the processing configuration presented in this paragraph, in the following chapters (3, 4, 5, and 6) the various steps in Figure 2.5 will be further investigated and refined, introducing innovative methods of pre-processing and post-processing of SfM-MVS data and products.

2.3.1. Acquisition Activities

More than a few influences were found on the quality of the 3D model related to the whole photogrammetric process discussed (James et al., 2019). Careful evaluations are required during both data acquisition and processing. On the upside, several works in the literature have addressed the study of possible solutions and trade-offs to achieve more consistent and conforming photogrammetric reconstructions (Eltner et al., 2016, Smith et al., 2016).

Although algorithmic processing makes up almost the entire procedure, field acquisition activities represent a delicate phase to which the mapper must pay close attention.

In contrast to classical photogrammetry (Mancini et al., 2013, Smith et al., 2016, Wolf et al., 2014), the SfM approach is very effective for processing images acquired from platforms with an irregular acquisition schedule. However, although this is not mandatory in the SfM-MVS procedure, a well-defined and prepared image acquisition plan leads to more accurate results (Kingsland, 2020).

Being a passive technique, photogrammetry results are highly influenced by the input image data. SfM-photogrammetry, which employs an automated process to identify and match features through CV, is fundamentally dependent on image quality. Sensors, settings, and acquisition designs have to be considered very carefully.

Surface properties, e.g., texture, and lighting conditions significantly influence feature detection and matching. Overcast conditions are preferred to strong shadows, in any case, acquisitions with an inclination of the sun to the horizon greater than 35° are preferable. With regard to surface properties, on the one hand, the surface texture should be sufficient but on the other hand, it should not be too complex, e.g., vegetation, whose appearance changes distinctly within short distances and minimal changes in perspective. In cases where complexity is high, distributing artificial targets in those areas can facilitate the operation of SfM-MVS algorithms.

Thus, to obtain reliable 3D models, it is important to start by choosing the right camera and configuration for optimised image acquisition (Mosbrucker et al., 2017). It is important to note that each parameter setting can improve image quality, and the optimal choice is a compromise between camera settings that consider the application at hand (Mosbrucker et al., 2017, O'Connor et al., 2017). The main points for optimal image quality (Mosbrucker et al., 2017, O'Connor et al., 2017) are:

- Images should be captured in RAW format rather than JPEG, due to the significantly higher bit depth, e.g., 12-16-bit vs. 8-bit of image information, respectively.
- Cameras with larger sensors should be favoured because they allow a higher signal-to-noise ratio, as the pixels are generally larger, and therefore more light can be captured.

- The dynamic range of the camera is the ability of the camera to resolve the brightest (saturation level) and darkest (minimum detection level) signals, which depends on the resolution of the analogue-to-digital signal converter. This range should be set as high as possible to capture the full luminance range of an observed scene.
- As far as lenses are concerned, a good compromise between overlap and distortion effects has to be chosen. For example, lenses with wider angles allow for more image overlap, but in most cases also represent more radial distortion.
- For close-up applications, the depth of field has to be considered, and therefore the aperture should be chosen accordingly.
- In addition, exposure settings are important, which can be evaluated using the exposure triangle with ISO, aperture, and shutter speed at each corner. The ISO should be chosen as low as possible because less noise and a higher dynamic range are the consequences. The shutter speed should also be as low as possible to avoid blurring due to movement, but still get enough light on the sensor. These settings change with different lenses, object distances and moving objects.
- Lastly, it should be noted that high-quality images can be obtained even with compact cameras when considering fixed lenses and large sensors, which is important considering the payload aspects in UAV applications.

A detailed description of the data and their processing allows a complete evaluation of the 3D model recovery. Therefore, for a better evaluation and comparability of image quality, data including metadata on settings during image acquisition should be made available in an open access repository (O'Connor et al., 2017). This could supplement the spreadsheet of documents introduced by (Eltner et al., 2016) that aims to record data acquisition configurations during field campaigns and parameter settings during subsequent data processing.

The distance between the camera and the interest area affects the accuracy and resolution of the reconstructed surface model, disclosing an inverse relationship between

distance and model accuracy (Eltner et al., 2016, Smith and Vericat, 2015). However, instead of referring only to this distance value, (Mosbrucker et al., 2017) suggest also consider the ground sampling distance (GSD), which describes the ratio between the distance in image space and the distance in object space. Different cameras with different focal lengths and different sensors (and thus pixel pitch) lead to different GSDs, even when objects are captured from the same distance.

The orientation and position from which the imagery is taken is a crucial factor for reliable 3D reconstruction. Images should have a high overlap from different view perspectives. The distance between the images (called as baseline) should be large enough to avoid intersections of light rays due to very small parallax angles. At the same time, the images should not be taken too far apart to avoid changes in the appearance of the image content so large that homologous points are not detected. Each point for which 3D geometry is to be retrieved should be seen in at least three images. The more images, the better, because it increases redundancy in image measurements. In addition, the geometry of the image network should include converging images, if possible, to avoid systematic errors such as domes (James and Robson, 2014).

2.3.2. Data Pre-Processing

At this stage, the pre-processing operations of the acquired data are undertaken. Data pre-processing refers to operations that affect geometric, radiometric, and spatial information. Deferring the discussion of these to Chapters 3 and 4, operations are characterised that can be used by any user regardless of the purpose of the work. Among them, image quality assessment is considered of major significance because SfM photogrammetry is based on the efficient detection and matching of image features, which is one of the key tasks of photogrammetry (Gruen, 2012). Since image quality significantly affects these early stages, making sharp, well-exposed images is the fundament for accurate subsequent data processing (O'Connor et al., 2017). Many software platforms provide the possibility to analyse the quality of the images loaded into the workspace, while others require a manual inspection in order to pos-

sibly remove images characterised by excessive problems (noise, blurring, chromatic aberrations, etc.). For example, lighting differences are caused by incorrect exposure camera settings or lighting variations during a UAV flight. Overexposing bright areas or underexposing dark areas can change the distinctive properties of surface features, thus adversely affecting the detection of the matching point.

2.3.3. Workspace Settings

It tends to be underrated as a step and often preferred over a predefined parameterisation, but it is fundamental and necessary for reliable, repeatable, and reproducible products (Mayr et al., 2020). In any software, a reasonable workspace setting affects the plausibility of its operations, clearly then aiming to specify the workflow for particular case studies. In a general view, the choice of a shared reference system, both in view of the data acquired in the field and the factors involved in solving the equations underlying the photogrammetric algorithms, establishes consistency in the orientation and scale of the final models.

Most commercial software is not fully adjustable, turning into real black boxes. On the other hand, other software presents laborious parameterizations that induce the user to errors by hyper-parametrization. At this stage, it is, therefore, necessary to identify the most significant variables and determine their correct weight in the algorithms implemented in the process chain.

Finally, the arrangement of the calibration parameters of the camera and its lever arm optimises the estimates of the IOs, a source of propagation of a multitude of distortions in the final accuracy values. This setting can be derived from rigorous operations in the laboratory or obtained through self-calibration from the acquired data, which is often preferred and returns totally reliable values compared to the former.

2.3.4. Alignment Step

The objective of this step is to automatically search and collect key points, define matches, resolve the orientation of the camera poses (defined as image alignment), and then generate the sparse point cloud. Being the core of the whole SfM

procedure, it is good to call all available hardware resources to process the available datasets in the highest quality mode. It is preferable not to set any automatic threshold limitation in the search for key and tie points precisely to avoid uncontrolled filtering of the measured points. In case there is positional information of the images in EXIF and additional markers found in the scenes, these can increase the accuracy of the estimates and reduce the computation time.

2.3.5. Filtering and Block-Optimization

Once the sparse point clouds have been generated, systematic errors mainly caused by non-linear lens distortions are estimated. These measured points can be manually filtered to optimise the estimates and minimise the distortions of the image blocks. The literature shows that three criteria can be considered effective in centring the target (Mayr et al., 2020): a) photogrammetric restitution uncertainty; b) projection accuracy; c) reprojection error.

(a) aims to remove points with low base-to-height ratios, i.e., all those points located at the edges of the images, generally characterised by a higher degree of restitution uncertainty, which mainly depends on too small an overlap between images. It does not appreciably affect the final accuracy but purifies the point clouds by eliminating most of the outliers. On the contrary, (b) aims at detecting and cleaning the less reliable matching points, i.e., characterised by a low projection accuracy on the images on which they are back projected; (c) aims at removing all the points with a large residual value in the RE to drastically decrease the restitution errors, improving the estimates of the orientation parameters. It is worth mentioning that residuals also have a direct impact on the representativeness of the Root Mean Square Error (RMSE) of GCPs and CPs, making it a matching parameter to define the actual final accuracy of the measurements.

The three criteria mentioned above make it possible to remove most of the inaccurate points from the clouds, thus improving the consistency between model and reality. Several research works, given the adopted software platforms, define appropriate ranges for each criterion, which are quite generalisable for any investigated scenario

(Mayr et al., 2020). As a fundamental condition, however, filtering must never reduce the cloud to less than 20% of the starting cloud: once this threshold is exceeded, the block optimisation is declared to be inadequately pivoted.

2.3.6. Georeferencing and Scaling Step

The accuracy and distribution of the reference and control data, i.e., GCPs and Check Points (CPs, which are GCPs not implemented during BA), respectively, are important to ensure and control the quality of the final scalar model. The accuracy weights of the image measurements of GCPs and CPs have to be chosen accordingly, to avoid model errors due to overfitting at GCPs. In addition, REs at CPs should not be much higher than those at GCPs (James et al., 2017a). In general, GCPs should surround the area of interest and they should be well distributed. Recent advances in DG, where models are referenced directly considering the orientation and location from which the cameras were triggered, indicate that GCPs may become less important in future applications in geomorphology.

Moreover, (Remondino et al., 2014) suggested that when GCPs provide the “ground truth” for the SfM-MVS workflow, they should be detected in an independent manner, providing an expected accuracy at least three times better than the predicted results. Since different parameters are involved at different stages of the SfM-MVS pipeline, errors propagate through the process (Eltner et al., 2016). In the geometric accuracy assessment, incorporated in this step, typical quality indicators of a photogrammetric process are provided by the calculated covariance and correlation matrices in the BA.

2.3.7. Iterative Bundle Block Adjustment

A large number of observations from hundreds of images and many parameters estimated in the self-calibration may hinder matrix inversion, which is essential for covariance estimation. Thus, another possible source of systematic errors is hyper-parameterization, which cannot be easily controlled with SfM-MVS software packages. Thus, an ordered and linear parameterization of the parameters most influencing the final results is preferred, as better explained in section 5.3. The workflow

therefore involves iterative BA procedures, incorporating corrections from point cloud filtering, georeferencing and scaling into the various steps.

2.3.8. Dense Matching Processing

As seen in section 2.1, sparse point clouds often cannot be defined as exhaustive in representing the scenario under study. Starting the Dense Matching algorithms pushes the software to search for further correspondences between the pixels of the images. This generates densification of the starting sparse point cloud by about an order of magnitude. The dense point cloud represents the final stage of the whole SfM-MVS procedure from which different processing paths can be branched according to the commissioned or useful work requests.

2.3.9. Post-Processing Node

Once this node has been reached, it is possible to undertake different processing paths according to the commissioned requests or the research objectives. As described in paragraph 2.1, the products most in-demand in the geospatial field are DEMs and orthomosaics of the areas under examination, but often, taking advantage of the radiometric characteristics acquired, it is possible to carry out classifications of images. In other cases, it is possible to extract geometric information from point clouds to characterise morphology. Detailed discussions of these topics are proposed in Chapters 5 and 6.

Different algorithms are used for each step of the SfM-MVS method. Although the photogrammetric principles are embedded in the SfM-MVS workflow, as seen in section 2.1., many aspects of this latter have completely different roots resulting from the various developments of CV algorithms. This complexity is often compounded by the issue that the specific procedures applied are often not detailed by many commercial SfM-MVS software packages (Deliry and Avdan, 2021). Consequently, isolating or correcting the exact source of errors becomes so challenging when using these black-box software packages, as they hardly provide well-explained BA reports.

Hence, the need to structure a pipeline in the FOSS4G domain, characterised by the use of license-free software and tools accessible to any user. It is, therefore, necessary to define a parameterization in accordance with the criteria commonly accepted by the scientific community, to structure a basis of comparison with licensed software platforms in such a way as to be defined as interchangeable, and finally to offer a validation against accepted accuracy standards.

Given the current software landscape in the industry, the steps will be analysed, and comparisons established between the most widely used software in the professional field. A FOSS4G pipeline will then be constructed to better explain the algorithms used, the parameterizations chosen and the errors that can be made: this guarantees the user full control and verification of the operations.

2.4. OVERVIEW OF PHOTOGRAMMETRIC SOFTWARE

The progression of phases seen in the workflow brings to light the need for software capable of implementing the algorithms, encoding the acquired frames, and translating them into a dense points cloud and all other commissioned photogrammetric products. The development in recent times of SfM-MVS techniques has also attracted great interest from leading software-houses. The result is a multitude of software-packages, each reasonably performing for certain working conditions such as close-range photogrammetry, UAV photogrammetry, satellite photogrammetry and aerial photogrammetry.

They can mainly be classified into two categories: stand-alone software and software based on cloud-computing networks, i.e., the software producer develops, operates, and manages a web application (Software as a Service (SaaS)) and makes it available to its customers. The former identifies a category of software that is capable of processing independently of other software and hardware, with which it may interact. Processing can be carried out employing the central processing unit (CPU) of the individual computer, which will require quite considerable computing power in terms of microprocessors, usable Random-Access Memory (RAM) units and Solid-State

Memory (SSD) units, and through the Graphics Processing Unit (GPU) of the same computer. Some software also provides for the use of both modes during the same processing. Most of the software used in the scientific literature, whether open-source, freeware or licensed, falls into this category. Among the most widely used are: Metashape by Agisoft, Pix4DMapper by Pix4D SA, RealityCapture by Capturing Reality, IMAGINE Photogrammetry by Hexagon Geospatial, and 3DF Zephyr by 3DFLOW as far as licensed commercial software is concerned, while MicMac by IGN, OpenDroneMap (ODM) (also in the WebODM version), COLMAP (Schonberger and Frahm, 2016) and Python Photogrammetry Toolbox by Arc-Team are among the most widely used open-source software. Various authors in the literature have often made comparisons in order to identify similarities, peculiarities, and disadvantages (Jiang et al., 2020, Kingsland, 2020).

Cloud computing, on the other hand, exploits a distributed architecture in a local (LAN) or geographical (WLAN) network, each capable of providing its processing, storage, and retrieval capabilities. It follows that by exploiting cloud-computing technology, users connected to a cloud provider can carry out all these tasks, even via a simple internet browser, i.e., with online interfaces, or via special user interfaces designed exclusively for uploading data and downloading subsequent processing. This reduces the time needed to obtain the data but has the disadvantage of not having full control over the operations. All manufacturers of standalone software also tend to offer SaaS Pay per Use Photogrammetry Processing solutions.

Given the theoretical assumptions discussed in paragraphs 2.1 and 2.2 and the general structure of the photogrammetric processing chain in paragraph 2.3, the processing chains in the two most widely used licensed software in the research and professional field were studied: Agisoft Metashape and Pix4D Mapper. Once the workflows have been constructed, any differences will be analysed, highlighting the particularities useful for the subsequent development of an open-source framework in a MicMac environment. In the last few years, Agisoft has acquired a growing popularity in the scientific community, as pointed out by (Berra and Peppia, 2020), mostly due to its user-friendly, almost "black-box" workflow (Eltner et al., 2016). The number

of published studies has gradually increased compared to Pix4D, while there is a steady linear trend for the use of MicMac.

2.4.1. Agisoft Metashape

Agisoft Metashape is a stand-alone software product that performs photogrammetric processing of digital images and generates 3D spatial data for use in GIS applications, documentation of cultural heritage and land use, creation of visual effects, as well as for indirect measurements of objects at various scales.

The software allows UAV-based acquisitions to be loaded into different Chunks. A preliminary examination of the dataset of images is fundamental to be able to remove any that are affected by obvious distortions or lack of sharpness. The software has a simple 'Estimate Image Quality' tool that independently examines each image and estimates a quality index, thus avoiding manual analysis. Images with a quality index of more than 0.7 can be considered suitable for the intended processing chain.

The software autonomously recognises the information in the metadata of each uploaded image, reporting it on the screen, even the geo-tag coordinates of each image recorded at the time of the photoshoot. Otherwise, if the UAV is equipped with a high-precision GNSS receiver, the coordinates of the antenna's phase centre (APC) acquired in Real-Time Kinematic (RTK) at the time of the shot can be uploaded with the .txt file in the 'Reference' folder.

Subsequently, the calibration mode of the camera must be configured. In any photogrammetric processing, the IO of the camera is a key step in the subsequent resolution of the collinearity equations underlying the ExO. The IO is obtained by calibrating the camera used for frame capture. In Agisoft Metashape a self-calibration is generally adopted by means of the same SfM algorithms used for photogrammetric processing. Vice versa, it is possible to load a camera calibration coming from external software. Generally, the first method, giving a fairly reliable and robust estimate without manual procedures, is more widely used but with the necessary precautions.

In the "Camera calibration" panel, the camera self-calibration is configured by unchecking the "Fixed calibration" option, i.e., at the end of the camera alignment pro-

cess, the software will extrapolate the adjusted values of the camera parameters. Agisoft Metashape uses Brown's Model (Duane, 1971) as a template to represent the camera. A detailed description will be presented in sections 4.1 and 4.2.

In GPS/INS Offset the Lever-Arm vector is set, i.e., the distances along the three axes between the APC and the main point of the image, a fundamental value for the correct estimation of the IO of the camera. This value must be taken into account only in cases where it is not applied autonomously to the geo-tags by the control system onboard the drone.

The work area of the software platform needs a suitable parameterisation in order to guarantee the success of the consecutive operations. A fine-tuning of the algorithms that will have to operate during processing is carried out. In Reference Settings, a general Coordinate System is defined, or different Coordinate Systems are chosen for the cameras and markers (if these were acquired in a different system). Obviously, care is taken with the choice so as not to generate inconsistent products.

The two configuration areas parameterise the field measurement accuracies of the cameras in both metric and angular terms, i.e., the accuracy of the receiver onboard the UAV, the IMU sensor if integrated, and the accuracy of the GCPs in metres when (and if) they have been detected. It is therefore necessary to retrieve the various pieces of information from the manufacturer's datasheet and the field measurement sheet to transfer the correct parameterizations to the algorithms.

Below "Image Coordinates Accuracy" parameters are set for the accuracy in pixels of the Markers, i.e. how carefully the Markers can be positioned in the software workspace, and it is useful to set a fairly realistic value of 0.5 pixels, while "Tie Point Accuracy" identifies the accuracy in pixels with which the matching algorithm will search for homologous points between two images, and tends to set a value greater than 1 pixel, i.e. approximately 3 pixels.

In the first phase identified as "Align Photos", the software enables the algorithms to search for image-by-image "features". As it is a commercial platform it is not possible to know which algorithm is active with precision.

Once the characteristic points have been identified, the software starts the matching algorithms, i.e., the images are compared by searching for homologous points among those already recorded. Once the connections between the images have been defined utilizing the "tie points", considering the IO estimates of the cameras assisted by the positional information of the images, the geometric relations between the various images are constructed and then a sparse cloud of points is calculated (Figure 2.6).

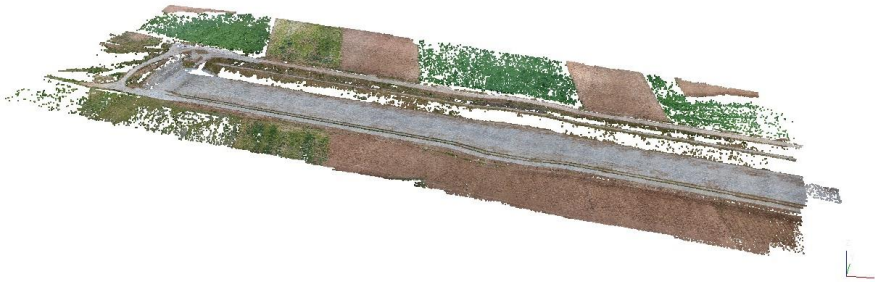


Figure 2.6. Sparse point cloud in Agisoft Metashape

The parameterisation for obtaining the sparse point cloud will depend on the case under study:

- Accuracy - High: chosen to make the software work at the original image resolution, i.e., the pixel will contain the information as recorded during acquisition. A reduction in the accuracy level halves the image resolution, speeding up the process but for reducing the quality of the product. The 'Ultra High' level doubles the original resolution but is a better choice for objects that require reconstruction detail (such as in archaeology).
- Generic preselection - Yes: no grid or analysis path is imposed on the algorithms.
- Reference preselection - Yes: a useful parameter if there is positional information in the images, to support subsequent estimates of relative geometry between shots.
- In Advanced: Key Point Limit and Tie Point Limit are set to 0. These two parameters make it possible to impose limits on the search for key points (features) and tie points, acting as a filter for ambiguous points. However, since

there is no possibility of inserting a correct filtering threshold that is valid in all scenarios, it is considered more reliable to impose a 0 value on the two parameters so as not to filter the searches at all and then to be able to filter the clouds manually.

- Adaptive Camera Model Fitting - Yes: it is chosen to correct and then calculate an adaptive camera model, i.e., the self-calibration of the camera.

In the Reference panel, under Error (pix) the average values of the REs for each image are analysed, identifying the maximum and minimum average values. The RE in pixels identify the difference between the estimated values of the points in an image and those projected in the sparse point cloud. Values of more than 1-pixel pose problems in achieving high model accuracy. Thus, an attempt is made to filter the clouds from points with large REs and thus obtain a model that is fairly consistent with reality.

The “Gradual Selection” option contains tools for filtering sparse point clouds. The tools used in this case are described below, taking care not to reduce the number of points in the cloud below 20% of the original number of points:

- *Reconstruction Uncertainty*: 10 - allows the removal of points that projected have low values of the ratio between the minimum and maximum RE of each point. That is, junction points located at the edges of the examined area generally have a higher degree of reconstruction uncertainty than those in the centre of the model, due to the low lateral overlap of the images. Removing these points does not affect the accuracy but beneficially lightens the model.
- *Projection Accuracy*: 3 - allows the identification of less reliable tie points. Poor quality matches are indicated by a parameter value of 3 which means that those points have 3 times the uncertainty of the minimum uncertainty points.
- *Reprojection Error*: 0.40 - is applied to remove erroneous points with large residuals. In fact, this parameter has the largest direct influence on the RMSE of GCPs and CPs and improves the orientation parameters considerably.

At the end of the filtering phase of the sparse point cloud, the BA process is started with “Optimize Cameras”. In the process window, it is possible to choose whether to

improve the estimates of the IO of the camera and which parameters to correct. It is considered optimal to deselect the parameters regarding distortions of an order higher than the second and therefore irrelevant on the final results. The software learns the corrections and improved information about the relative orientations of the images and fine-tunes the estimates made in the first alignment phase.

GCPs are imported into the workspace and need to be collimated image by image. In Reference, the Metashape software gives the possibility to observe the accuracy with which the points are being collimated through the RE value in the "Markers" sub-window. As a consequence of what has already been said above, the values should be kept as far below the 1-pixel value as possible to consider the collimation optimal and therefore not propagate the relative errors in the subsequent phases. The collimation phase is thus the most complex and time-consuming step.

The BA algorithms are restarted. It should be noted that, except for cases of DG, it is considered essential to uncheck ("Uncheck cameras") the images in the Reference panel so that, taking advantage of the estimates obtained also from their positional information, in the BA only the most accurate information deriving from the GCPs is used for the correction of the estimates.

The sparse cloud is made up of resulting points that are unambiguous and have very distinguishable features in the various images. However, in order to obtain model-containers of much more information, it is necessary to ask the software to re-examine the same images and, on the basis of the derived and corrected sparse points, generate other neighbouring ones that can be considered as reliable as the first ones. Dense Matching algorithms can then be started, the specifications of which cannot be known due to commercial confidentiality. In "Build Dense Cloud" the configuration window of the process parameters appears. The software gives the possibility to choose at which quality level to start the process, as already seen for the alignment phase (Figure 2.7). The dense matching algorithm computes a depth map for each image and offers the possibility to use a 'Depth Filtering' tool to filter the dense clouds in three modes: 'Aggressive' making the result much smoother, 'Mild'

giving the possibility to keep maybe some important details, 'Moderate' a middle ground between the first two choices.



Figure 2.7. Dense Points Cloud in Agisoft Metashape

In “Build DEM” it is possible to parameterize the restitution of the DEM (Figure 2.8). The software gives the possibility of estimating the values of the product, in the areas in which no information is present, by interpolation or by extrapolation, or it is possible to disable the function completely.

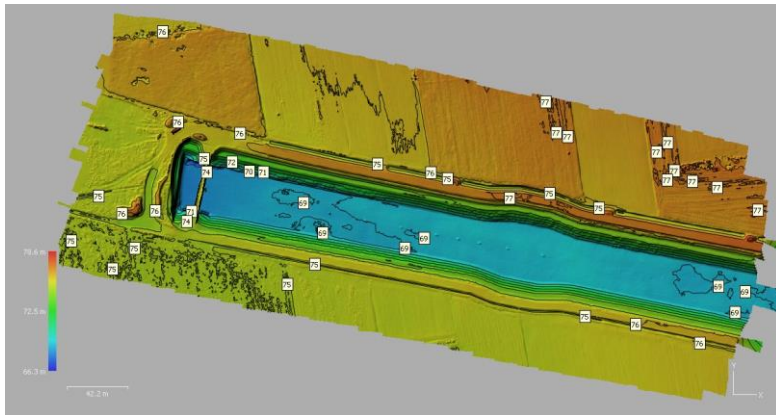


Figure 2.8. DEM of the examined area integrated of contour lines with altitude above sea level.

The last step in the entire photogrammetric workflow may be the generation of the orthomosaic of the surveyed area. As is well known, the orthorectification of the images is strictly dependent on the accuracy of the DEM obtained in order to ensure fairness of scale and zero distortion.

In "Build Orthomosaic", the process is parameterised as usual. There is a choice of different blending modes: 'Mosaic' by default mosaics the various available images,

'Average' blends the various images, or you can disable any type of blending (Figure 2.9).

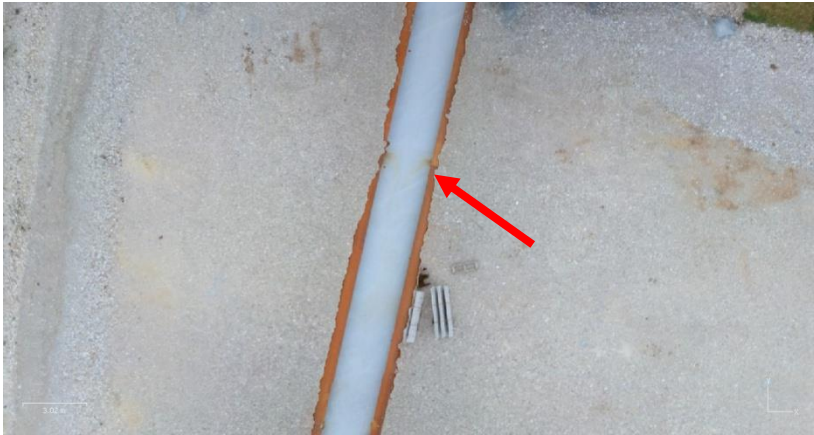


Figure 2.9. Distortions related to the blending mode in Agisoft Metashape

2.4.2. Pix4D Mapper

The commercial software Pix4D Mapper is a multi-purpose software for mapping professionals. It is widely used in the professional field as it features a chain of almost automated processes that do not require meticulous parameterisation but at the same time deliver products with a high degree of accuracy.

As the software is started, a “New Project” is created. The software asks to load the images to be processed and then to set up the workspace: in the “Image Properties” window, it is possible to set the Coordinate System characteristic of the geo-tags of the images, select the source from which to extract the positional information of the images, select the relative geolocation accuracy and finally choose the camera model used.

The camera model is then configured. Pix4D has an internal database that stores the calibration data of several commercial cameras. The software recognises the camera model from the EXIF and automatically searches for it in its database: if present, it loads the calibration values. The calibration parameters of a low-cost camera cannot be considered consistent as they are susceptible to variations due principally to optical-mechanical deterioration and temperature. These parameters, therefore, will be

subject to corrections calculated from the image processing in order to optimise the IO of the cameras.

Pix4D adopts a proprietary format model as the theoretical model for representing the camera. It is possible to transform these values into the most common formats (e.g., Brown's model adopted in Agisoft Metashape) using the transformation equations given in the online manual.

In the "Select the Output Coordinate System" window it is necessary to define the Coordinate System in which the outputs of the processes and GCP useful for georeferencing will be resumed.

The Pix4Dmapper software, unlike Agisoft Metashape, does not have a tool capable of independently examining image by image and estimating a quality index. The examination will therefore have to be carried out employing a manual analysis or, if necessary, once the basic information has been loaded into the software, by launching rapid low-resolution processing and finding any problems. Additional tools for equalising image brightness and reducing rolling shutter effects are not implemented in the platform, thus reducing its data processing potential.

In general, Pix4D Mapper gives the possibility of adjusting the algorithms in the same way as Agisoft Metashape, except for a single factor of absolute importance: the accuracy in pixels with which the matching algorithm searches for homologous points between two images.

Completely, Pix4D does not allow the Lever-Arm vector to be set to integrate it in the calculation, which could, on the contrary, distort the obtainable results.

Once the Output Coordinate System has been selected, the software offers a wide range of processing methods organised in predefined templates. These templates are briefly standardised processing options that make it easier for the user to achieve results immediately, without having to follow the processing step by step.

Pix4D Mapper distinguishes three phases of photogrammetric processing:

- 1) Initial processing
- 2) Points Cloud and Mesh
- 3) DSM, Orthophoto and Index

In the “Advanced” option, the software enables new sub-folders, useful for advanced parameterisation of the processing.

The specifications regarding the parameterisation chosen to obtain the sparse point cloud are shown below:

– General:

- *Image scale for generating key points*: Image scale for generating key points: This allows defining the image size at which the key points are extracted in relation to the initial image size. With the Integer option, the software is chosen to work at the original image resolution, i.e., the pixel will contain the information as recorded during acquisition. A reduction in the level of precision (options: Quick or Custom) reduces the image resolution, speeding up the process but reducing the quality of the product.
- *Quality Report*: enable the option to generate a preview of the orthomosaic and DSM in the Quality Report.

– Matching:

- *Image pair matching*: This allows the user to select a matching strategy between matching images. Two strategies have been tested: Air Grid or Corridor, which optimises pair matching for flight paths structured in grids or corridors, and Custom, where specific pair matching parameters can be adjusted to best suit your processing needs. The results are fully comparable.
- *Matching strategy*: enable the 'Use geometrically verified matching' option. Slower but more robust, it allows geometrically inconsistent matches to be filtered out and discarded.

– Calibration:

- *A number of marked key points*: This allows to set the number of key points to be extracted. As it is not possible to enter a maximum limit and especially as it is not possible to filter the points later, the Automatic option is preferred;
- *Calibration*: This allows to select how the camera's internal and external parameters are optimised.

- Calibration Method: the Alternative option is optimised for aerial images acquired at nadir with accurate geolocation, low texture content, and relatively flat terrain. If orientation IMU values are matched to each image, the most satisfactory option in terms of final calibration accuracy is Accurate Geolocation and Orientation.
- Camera Optimisation: Defines which camera parameters will be optimised.
- Internal Parameter Optimisation: All internal camera parameters are optimised.
- Optimisation of external parameters: All of which optimise the values for the rotation and position of the camera in space. These corrections will then affect the final position of the cloud in space.
 - *Rematch*: This allows to add more matches after the initial processing, and usually tends to improve the quality of the reconstruction. The default option Automatic enables rematching only for projects with less than 500 images and is considered a reasonable option, in case the initial processing did not give good results, for obtaining models consistent with reality.
 - *Export*: allows to select the outputs.

In the first step identified as "Initial Processing", a sparse point cloud is computed (Figure 2.10).



Figure 2.10. Sparse Points Cloud in Pix4D Mapper

In the “GCP/MTP management” option, Pix4D provides a workspace for managing GCPs. The GCPs imported in this way into the workspace need to be collimated image by image. Pix4D provides two collimation modes in the GCP/MTP Editor: “Ray-Cloud Editor”, which uses the RayCloud interface to mark GCPs on the images after

the first processing, and “Basic Editor”, which is available even if no processing phase has been completed.

BA processing can be started after the georeferencing step, using the “Reoptimize” option. Attention is drawn to the absence in Pix4Dmapper of a tool capable of managing and filtering sparse point clouds.

Dense Matching algorithms are employed, the specifications of which cannot be known due to commercial confidentiality.

The second step consists of three sub-folders through which it is possible to structure the processing:

- Point Cloud:
 - Point Cloud Densification: This allows the user to define the parameters for densifying the point cloud. It contains the following options:
 - Scale: the image scale defines the scale of the images from which further 3D points are calculated. From the drop-down list, it is possible to select $\frac{1}{2}$ (half image size), i.e., the size of the images from which the new points in the cloud will be extrapolated is halved. This choice guarantees fast processing times and a reasonable point density.
 - Point density: this parameter defines the density of the point cloud. The Optimal option allows to calculate one 3D point for every $4/[\text{Pixel image scale}]$.
 - The minimum number of matches: represents the minimum number of valid reprojections of this 3D point in the images. It is preferable to set a value of 3, i.e., a point is only evaluated if it is reprojected in at least 3 images.
 - Point Cloud Classification: This allows the user to classify the point cloud.
 - Export: This allows the user to select the desired output formats for the densified point cloud.
- 3D Textured Mesh
- Advanced: This allows the user to edit the advanced processing options for the point cloud. It contains 4 sections, of which the two of interest are shown:

- *Densification of the point cloud*: This allows to define the parameters for densifying the point cloud but in this case about the size of the correspondences window, i.e., the size of the grid used to match the densified points in the original images (Figure 2.11). For aerial images from nadir, the 7x7 window is preferable, instead of the 9x9 more suitable for oblique and/or terrestrial images.
- *Point Cloud Filters*: allows you to select the filters that are taken into account for the generation of point clouds:
 - Use Processing Area: if a processing area has been drawn, it is used to filter the point cloud.
 - Use Annotations: If image annotations have been created, i.e., masked areas in the images by clicking on each image in the RayCloud, these can be used to filter the point cloud.
 - Automatically limit camera depth: Prevents the reconstruction of background objects.



Figure 2.11. Dense Points Cloud in Pix4D Mapper

“DSM, Orthophotos and Index” step consists of three sub-folders through which it is always possible to structure the processing (Figure 2.12):

- DSM and Orthomosaic: This allows the user to modify the processing options and the desired outputs for the generation of DSM and Orthomosaics. It is in turn divided into the following sections:
 - *Resolution*: This allows the user to define the spatial resolution used to generate DSM and Orthomosaic. With the setting Automatic, the resolution can be chosen in multiples of the DSM.

- *DSM Filters*: the following options are enabled:
 - Use Noise Filter: point cloud generation can lead to noisy and erroneous points. The noise filter corrects the altitude of these points with the average altitude of neighbouring points.
 - Use Surface smoothing: Once the noise filter is applied, a surface is generated using the points. This surface may contain areas with small erroneous bumps. Smoothing the surface corrects these areas by flattening them. In addition, the option allows to choose the smoothing mode, of which the one labelled 'Sharpness' was found to be useful. 'Sharpness' attempts to preserve the orientation of the surface and maintain sharp features such as corners and building edges; only almost flat areas are smoothed.
- *Raster DSM*: allows the user to select the output file format and options for raster DSM. The raster generation mode is selected as Triangulation, based on Delaunay triangulation, and the 'Merge Panes' option is enabled.
- *Orthomosaic*: This allows the user to select the format of the output file for the orthomosaic and its different options (Figure 2.13).
- Additional outputs: a useful option for the generation of the Level Curves extrapolated from the DSM.
- Index Calculator: in cases where the objective of the work is to obtain thematic maps.

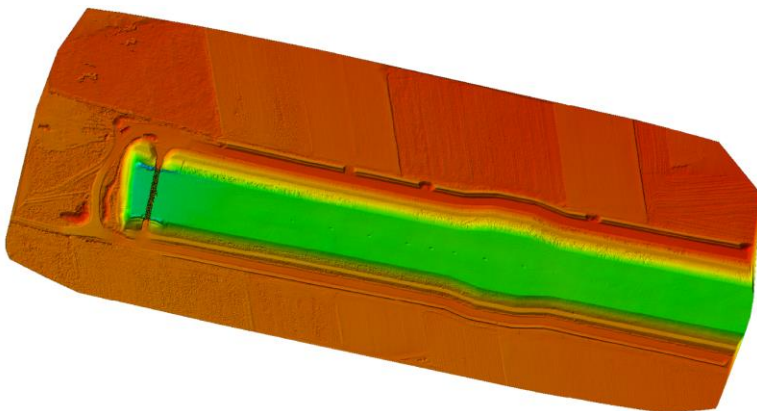


Figure 2.12. DSM of the surveyed area.

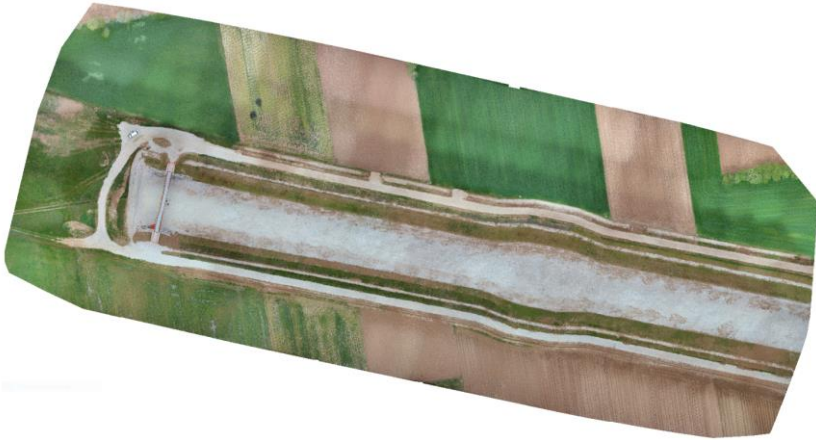


Figure 2.13. Orthomosaic of the surveyed area.



Figure 2.14. Distortions related to the blending mode in PIX4D Mapper software.

Not enough information can be deduced about how the DEM is generated, and the Orthomosaic afterwards, i.e., how the algorithms intervene in the empty spaces starting from the Delaunay triangulation: whether by interpolation, extrapolation, or none at all. Moreover, in the generation of the orthomosaic, the blending mode is not known, i.e., how the composition of the orthomosaic is done (Figure 2.14).

2.5. SCRIPTING A FOSS4G PROCESSING PIPELINE

Conscious of the methodological approach learned from the previous software, the structuring of a pipeline of processes in an open-source environment was performed using the photogrammetric suite MicMac (Multi-Images Correspondances, Méthodes Automatiques de Corrélation) of the French National Geographic Institute (IGN) and French National School for Geographic Sciences (ENSG) (Rupnik et al., 2017, Deseilligny and Cléry, 2011). The software presents itself as a meticulous tool suitable for research purposes but also employed in a professional context. On the other hand, however, it is not very intuitive and is quite difficult to use for processing. The present pipeline was structured and executed by installing the software on a Windows OS.

As there is not fully developed graphical user interface, the software is started directly by calling processing commands from the prompt in the directory where the image files are located. In general, the command line should be typed:

```
/path_images mm3d Command_Name Non_nominal_arguments
```

It is not possible to generate a configuration of the workspace for the processing, but it will be necessary to take care of the parameterization of every command to obtain a photogrammetric workflow that is robust and above all coherent with those covered in the software analysed in the previous paragraphs.

In the MicMac photogrammetric suite, like Pix4D Mapper, there isn't an instrument capable of autonomously examining image by image and estimating a quality index. Therefore, it is necessary to carefully acquire the data during the operational phases in order to avoid any possible pre-treatment of the images.

The first step in any pipeline is to search for and estimate the tie points. As it is open-source, the implemented search algorithms are known. In particular, the software gives the possibility of activating the basic SIFT++ algorithms, an evolution of D. Lowe's original SIFT (Lowe, 2004a, Lowe, 2004b), or in the latest versions also DI-

GEO algorithms, a further evolution of the SIFT algorithms that are much faster and more efficient.

The command used to perform these operations is called `Tapioca`. `Tapioca` is a simple interface that can be called up from the command line and can be executed in several modes.

If the `.txt` file in which the camera positions are indicated at the time of the acquisitions is available, it is useful to construct an `.xml` file that helps the search algorithm in `Tapioca` with File mode by defining the most suitable matches between images according to their position. To do this, the `OriConvert` command is called beforehand, which transforms the `.txt` file into a `.xml` file containing the most suitable matches between the images in the entire dataset. If the positional information of the images is recorded only in their metadata, it will be necessary to extrapolate it through the `XifGps2Txt` command to automatically generate the `.txt` file to be called up in `OriConvert`.

Once the `Tapioca File` command has been launched and the feature points have been identified, the software starts the matching algorithms, i.e., the images are compared by searching for homologous points among those already recorded (Figure 2.15).

```
mm3d OriConvert "#F= N X Y Z" Trincea_PC_rettilinee.txt rett MTD1=1 Name-  
Cple=FileImagesNeighbour.xml  
  
mm3d Tapioca File "FileImagesNeighbour.xml" -1 ByP=12 Detect=Digeo
```

Figure 2.15. Example of application of the `OriConvert` and `Tapioca` commands. Refer to the MicMac manual for more precise details of the arguments defined for each command.

When performing the first function, `OriConvert` requests that a conventional format be specified to read the data in the `.txt` (or even `.csv`) file: the default argument `OriTxtInFile` can be specified, or the format can be specified in the command line. `OriTxtInFile` identifies that the format is indicated in the first line of the file;

if it is not, it will be necessary to add a line specifying this format #F= N Y X Z K W P.

The third argument, for example named `rett`, represents the orientation database that will contain at the end of the process the positions of the camera centres at the time of shooting.

The optional `NameCp1e` argument indicates the name of the file in which the image pairs will be stored: at this stage the name chosen is `FileImagesNeighbour.xml`.

`MTD1=1`, set to 0 by default, instead indicates to the `OriConvert` command that the information present in the metadata (e.g., focal length, image resolution, etc.) can also be extracted only from the EXIF of the first image, remaining the same for all the others.

Finally, based on the analysis of the camera trajectory, `CalcV=1` activates the calculation of the relative speed of the platform during acquisition. `CalcV=1` will be used in case it's necessary to evaluate the delay in `CenterBascule` command later, which value will then be used as an optional argument to recalculate the orientation with `OriConvert`. Only in some cases can the delay be important: due to inappropriate extraction of the GPS position from the telemetry logs, due to high platform speed (or strong wind) or very small base (i.e., high overlap combined with low altitude).

Once the `FileImagesNeighbour.xml` file is obtained, the `Tapioca File` command can be run. Using the value `-1` as the image size is equivalent to using full resolution images. It is often advisable to reduce the resolution ratio (the size to be processed compared to the original size in pixels of the largest side of the image) to a value between 0.3 and 0.5 to make processing faster.

In cases where coordinates need to be transformed into a Euclidean reference system, the `ChSys` argument is called up, indicating the reference system chosen in the format as in the `proj4` library and present in the `Directory` in `.xml` format.

At the same command, it was considered appropriate to indicate:

- `ByP= 12`, indicates the number of processors that will be used to parallelise the process;
- `Detect=Digeo`, allows the user to select the algorithm for finding the matching points, passing from the default `Sift++` to `Digeo`, which is faster but has little documentation regarding its application;
- `Ratio=0.6`, to choose the ratio between the first- and second-best matching points. The default setting is `0.6`, a lower value indicates that less ambiguity and fewer points are desired.

Methods of filtering the tie points obtained from `Tapioca` were sought in order to strengthen the model by removing points of strong ambiguity. `Schnaps` cuts each image into a number of windows defined by the `NbWin` argument, then checks for the presence of homologous points and their correspondence with at least one other image in each of these windows. The remaining supernumerary parts in the windows are probably removed to produce a more uniform distribution of matches and thus promoting convergence when estimating camera calibration and orientations. The command is under development and does not have sufficient documentation to make it well-founded for the present pipeline.

At the end of the feature search processes and therefore of the correspondences between the various points of the images, it is necessary to introduce an orientation phase that sets preliminary geometries between all the points starting from a camera modelling and then passing through the relative geometries between the various shots.

The general tool for calculating image orientation is `Apero`. It is a relatively complex tool that has been broken down into several basic tools that offer a simplified interface to some functions:

- `Tapas` is a tool that offers most of `Apero`'s possibilities for calculating purely relative and IOs;
- `AperiCloud` generates a visualisation of the position of the cameras and the sparse points cloud;

- `Bascule` generates orientations consistent with some physical information in the scene;
- `Campari` is a tool for compensating heterogeneous measurements such as tie points and GCPs.

```
mm3d Tapas Brown ".*JPG" Out=BrownCal

mm3d CenterBascule ".*JPG" BrownCal rett rettCal

mm3d Campari ".*JPG" rettCal BrownCal-Campari-GPS EmGPS=[rett,0.02,0.05] All-
Free=1 GpsLa=[0,0,0.4]

mm3d AperiCloud ".*JPG" BrownCal-Campari-GPS Out=SparsePointsCloud.ply
SeuilEc=0.4 WithCam=0

meshlab {cloudcompare} SparsePointsCloud.ply
```

Figure 2.16. Example of application of the `Tapas`, `Bascule`, `AperiCloud` and `Campari` commands. Refer to the MicMac manual for more precise details of the arguments defined for each command.

With `Tapas` the user has very little control over the strategy used to calculate orientation. The default strategy used by `Tapas` is:

- initialise all intrinsic calibration using EXIF data (or via a pre-calculated calibration provided by existing data), then lock in any unknown parameters instead;
- choose a central image (usually the image with the highest number of matching points);
- calculate the orientation of the images using a "standard" strategy;
- and once all images have been sorted, release all intrinsic parameters in a predefined order.

In `Tapas`, the Calibration Mode of the cameras can be selected, i.e., the mathematical model of calibration chosen and then the relevant parameterisation. MicMac gives the possibility to choose different camera models, unlike the other software. A detailed description of the lens models will be given in section 4.2. In order, however, to

monitor possible variations and distinguish different behaviours between the software, it was preferred to set the Brown Model (Duane, 1971), known to have been adopted in the Agisoft Metashape software. The argument `Out=BrownCal` identifies the name of the output of this process.

When using `Tapas` an important part of the information is also displayed directly in the Command Prompt such as: the residues or the number of tie points used for the images. Care must be taken with residuals, which must be reduced to less than 0.5 pixels for good orientation. All this information is also stored in the `Residus.xml` file.

The `CenterBascule` tool allows to transform a purely relative orientation, as calculated with `Tapas`, into an absolute one. In particular, `CenterBascule` assigns a new `rettCal` orientation to a dataset of images with a centre orientation derived from the previous steps, taking into account the actual positioning of the photoshoot centres defined by the `rett` database processed in `OriConvert`.

At the end of this step, the `Campari` command is used to perform a least-squares compensation of the model orientation through heterogeneous measurements. Essentially starting from the `rettCal` orientation obtained in `CenterBascule`, `Campari` compensates the measurements assuming the coordinates of the `rett` database images with the relative plane and altitude accuracies. `GpsLa`, which identifies the initial lever-arm vector, and `AllFree` arguments, which enables the refinement of all camera calibration parameters, are introduced.

`AperiCloud` is used to generate a visualisation of the sparse point cloud and camera position, previously calculated by `Tapas`. This command does nothing more than transfer all the geometries estimated in the previous processes to the points, recording a `.ply` file in the root directory, named `AperiCloud_NameAssigned.ply`. The optional argument `SeuilEc=0.4` is introduced, with which all those points with a high residual value can be filtered out, i.e. tending to be those points classifiable as outliers eliminated in Agisoft Metashape through the Reprojection Accuracy filter. The argument `LimBsH=10`, i.e., a limit to the base-to-height ratio between adjacent points, as in the Reconstruction Uncertainty filtering method in Agisoft Metashape, was also tested in the test phase, but the point cloud was null at the end of the pro-

cesses. Often, some arguments need to be checked and, above all, the interpretations in the manuals need to be corrected. Finally, it was set `WithCam=0` (equal to 1 by default) to remove the graphic display of the cameras at the time of acquisition. Then, using software such as MeshLab or CloudCompare, it is possible to display the cloud obtained (Figure 2.17).

The processes seen so far have required a much longer processing time than those described in the other two paragraphs. Of the operations that have been carried out, the `Tapioca` command requires about 50% of the time taken in this first phase.

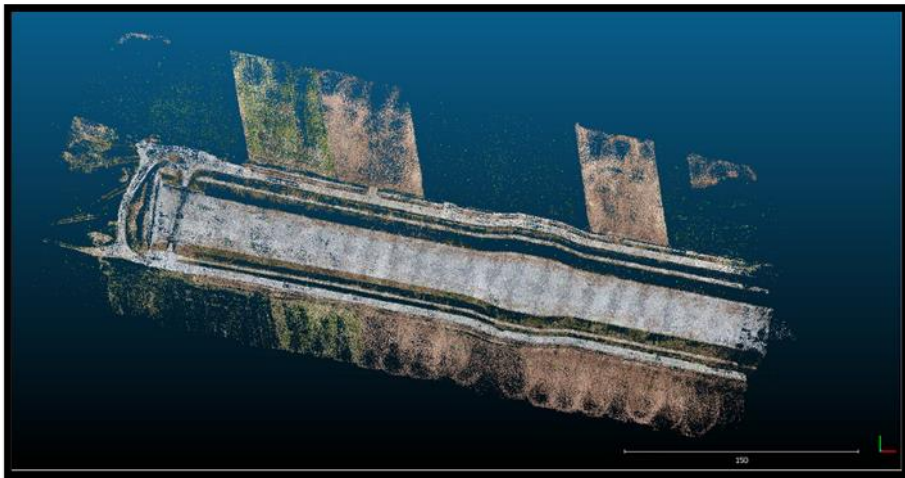


Figure 2.17. Sparse point cloud displayed in CloudCompare.

An optional iterative step is proposed, useful to compensate the whole photogrammetric block in the best way. Effectively, the `Campari` command also returns a compensated value of the lever-arm vector, which directly affects the positioning of the camera centres at the time of acquisition. In order to adjust their positioning to this estimated offset, the `CorrLA` command is introduced. It was set the mandatory `BrownCal-Campari-GPS` orientation and the value of the Lever-Arm extrapolated from the command prompt of the previous processing: the command will generate the `BrownCal-Campari-GPS-CorrLA` directory with the positions corrected by the lever-arm. The camera calibration corrections will be re-calculated in `Tapas`, setting `AutoCal` as the mode, assuming as starting parameters those already calculat-

ed `InCal=BrownCal` and considering the orientation of the cameras compensated `InOri=BrownCal-Campari-GPS-CorrLA`. Clearly, it is possible to go through this iterative phase also without considering the step linked to the Lever-Arm, therefore compensating the values of the camera calibration with the orientation obtained from the `Campari`, in the previous phase.

```
mm3d TestLib CorrLA ".*JPG" BrownCal-Campari-GPS [LA value obtained by Campari]

mm3d Tapas AutoCal ".*JPG" InCal=BrownCal InOri=BrownCal-Campari-GPS-CorrLA
Out=BrownCal2

mm3d CenterBascule ".*JPG" BrownCal2 rett rettCal2

mm3d Campari ".*JPG" rettCal2 BrownCal2-Campari-GPS EmGPS=[rett,0.02,0.05] All-
Free=1

mm3d AperiCloud ".*JPG" BrownCal2-Campari-GPS Out=SPC_CampariGPS2.ply
SeuilEc=0.4 WithCam=0
```

Figure 2.18. Example of application of the `CorrLA`, `Tapas`, `Bascule`, `AperiCloud` and `Campari` commands. Refer to the MicMac manual for more precise details of the arguments defined for each command.

The next step after the generation of the sparse point cloud is the collimation of the GCPs and CPs to transfer a robust and controlled IG to the model. In order to import the dataset of GCPs and CPs, measured in the field and recorded in a `.txt` file, a preliminary management of the positional information is required to obtain a `.xml` file readable by MicMac. To this end, the `GCPCovert` command is used to:

- transform a series of GCPs stored in a text format into `.xml` format;
- simultaneously transform the GCPs into a Euclidean coordinate system suitable for MicMac.

`GCPCovert` requires a specification of the format, which can be reported in the command line by `"#F= N X Y Z"` or by indicating a specific argument (e.g. `Ap-`

pInFile to read the format in the first line of the .txt file). Finally, the Out argument indicates the name of the .xml file resulting from the conversion.

In the following command lines, the SaisieAppuisPredicQT command is called up, which launches a graphical interface useful for collimating the points. Considering the orientation obtained in the previous BrownCal-Campari-GPS phases and loading the DatasetGCP.xml file of the GCP coordinates generated in GCPConvert, the SaisieAppuisPredicQT command is able to hypothesise the position of the GCPs in the images indicated in the command line that must be approved by the operator. The last mandatory argument is the name of a .xml file in which the image coordinates (X and Y in pixels) of the points are stored. By specifying MeasureInit.xml in this argument, two files will be created:

- GCP-S2D.xml, which stores the points in 2D coordinates for each image;
- GCP-S3D.xml, which stores points in 3D coordinates, calculated by spatial resection in relative coordinate systems given by the input orientation.

Considering the basic conversion for the success of the whole collimation phase of the GCPs, it is immediately obvious that the same steps must be performed for the CPs.

Indeed, SaisieAppuisPredicQT predicts the positioning of the GCPs in the images but it could happen that, due to the low accuracy of the GNSS metric information used in the first compensation, they are too out of phase for regular collimation. In these cases, it will be necessary to transfer a new temporary orientation to the model by locating at least three GCPs in the images using the SaisieAppuisInitQT command and then launch GCPBascule to settle the positioning on the collimated GCPs. The GCPBascule command allows to transform a purely relative orientation or one resulting from a previous orientation using CenterBascule, into an absolute orientation as soon as there are at least three GCPs whose projection is known in at least two images. In this new temporary orientation, the SaisieAppuisPredicQT command can be run to find the remaining GCPs. After all, the command SaisieAppuisPredicQT will be run again to collimate the CPs in the list.

```

mm3d GCPConvert "#F= N X Y Z" trincea_PC_rett_GCP.txt Out=DatasetGCP.xml
mm3d GCPConvert "#F= N X Y Z" trincea_PC_rett_CP.txt Out=DatasetCP.xml

mm3d SaisieAppuisPredicQT ".*JPG" BrownCal-Campari-GPS DatasetGCP.xml GCP.xml
mm3d SaisieAppuisPredicQT ".*JPG" BrownCal-Campari-GPS DatasetCP.xml CP.xml

mm3d GCPBascule ".*JPG" BrownCal-Campari-GPS BrownCal-GCP GCP-S3D.xml GCP-
S2D.xml

```

Figure 2.19. Example of application of the GCPConvert, SaisieAppuisPredicQT and GCPBascule commands. Refer to the MicMac manual for more precise details of the arguments defined for each command.

At the end of the process, it will be necessary to run the GCPBascule command to transfer the absolute orientation inherited from the collimated GCPs to the entire photogrammetric block.

Having transferred a robust absolute orientation to the sparse point cloud utilizing the GCPs, BA processing was started to correct and adjust the entire photogrammetric block. In particular, the Campari command was started introducing, as a useful measure for compensation, the database of implemented GCPs.

```

mm3d Campari ".*JPG" BrownCal-GCP BrownCal-Campari-GCP
GCP=[DatasetGCP.xml,0.02,GCP-S2D.xml,0.5] AllFree=1

mm3d AperiCloud ".*JPG" BrownCal-Campari-GCP Out=SPC_CampariGCP.ply SeuilEc=0.4
WithCam=0

mm3d GCPCtrl ".*JPG" BrownCal-Campari-GCP DatasetCP.xml CP-S2D.xml

cloudcompare SPC_CampariGCP.ply

```

Figure 2.20. Example of application of the Campari, AperiCloud and GCPCtrl commands. Refer to the MicMac manual for more precise details of the arguments defined for each command.

In the argument GCP= [DatasetGCP.xml,0.02, GCP-S2D.xml,0.5] it is defined the GCP database from the DatasetGCP.xml file returned by GCPConvert,

in which it is specified the accuracy in metres with which the points were measured, and the GCP-S2D.xml file with the relative accuracy in pixels with which these GCPs were collimated in the images.

The residuals on the CPs allow the accuracy of the georeferencing result to be qualified. The introduced command GCPCtrl allows us to quantify these residuals and thus return the degree of accuracy achieved in the processes seen. In particular, given the absolute orientation inherited from the GCPs and compensated in Campari, knowing the 2D coordinates of the CPs in the images resulting from the collimation phase, GCPCtrl returns the values of the residuals on all these points as displayed in the Figure 2.21.

```
Ctrl GPS0002 GCP-Bundle, D=0.137603 P=[0.00197353, -0.00109444, 0.137585]
Ctrl GPS0004 GCP-Bundle, D=0.0670823 P=[-0.00317237, 0.0089376, -0.0664085]
Ctrl GPS0008 GCP-Bundle, D=0.0338331 P=[0.00055252, -0.0294335, 0.0166747]
Ctrl GPS0011 GCP-Bundle, D=0.0257349 P=[0.00946808, 0.0014978, -0.023883]
Ctrl GPS0012 GCP-Bundle, D=0.0621692 P=[0.0140277, 0.00462618, -0.0603889]
Ctrl GPS0013 GCP-Bundle, D=0.0493462 P=[0.00822905, -0.001519, -0.0486315]
Ctrl GPS0016 GCP-Bundle, D=0.139053 P=[-0.0087034, 0.00828315, 0.138533]
Ctrl GPS0017 GCP-Bundle, D=0.0748879 P=[0.00904704, 0.00492412, 0.0741762]
Ctrl GPS0020 GCP-Bundle, D=0.134061 P=[-0.0208702, 0.0439593, 0.124917]
Ctrl GPS0021 GCP-Bundle, D=0.270654 P=[-0.00786254, 0.065908, 0.262389]

===== ERROR MAX PTS FL =====
|| Value=11.9332 for Cam=IMG_0342.JPG and Pt=GPS0021 ; MoyErr=7.26165
=====

=== GCP STAT === Dist, Moy=0.0994424 Max=0.270654
[X,Y,Z], MoyAbs=[0.00839065, 0.0170183, 0.0953586]
Max=[0.0208702, 0.065908, 0.262389] Bias=[0.000268949, 0.0106089, 0.0554962]
Rms=[0.0101163, 0.0270971, 0.118045]
[Plani,alti], Bias=[0.0106123, 0.0554962] RMS=[0.0289238, 0.118045]
Norm, Bias=0.0565018 RMS=0.121537
```

Figure 2.21. Example of GCPCtrl command results. Refer to the MicMac manual for more precise details of the arguments defined for each command.

The C3DC command starts the Dense Matching algorithms and calculates the coloured dense point cloud. It is possible to run C3DC in different modes.

The main modes are:

- QuickMac: multistereoscopic with ZoomF=8, i.e. the low preset 1pt/64px
- MicMac: multistereoscopic with ZoomF=4, i.e. medium preset 1pt/16px
- BigMac: multistereoscopic with ZoomF=2 i.e. preset high 1pt/4px

The MicMac mode works with scale-space pyramids. It starts the correlation on images with reduced resolution, and then successively improves the resolution. ZoomF argument is the final zoom: 1 is full resolution, 2 is half. Higher resolutions take much longer to process and do not necessarily improve the quality of the point cloud. C3DC computes depth maps which are raster images of the distances between the camera and image details.

When using PIMs2MNT command after C3DC, the DSM is produced by re-using these depth maps generated by this latter. PIMs2Mnt combines these individual depth maps into a global digital surface (or elevation) model. In the case of this tool, there is also the possibility of choosing the computation mode from the same ones seen in the C3DC tool. Indicating DoOrtho=1 enables the generation of the orthomosaic based on the DEM just processed. The other optional arguments are left in their default form.

```
mm3d C3DC MicMac ".*JPG" BrownCal-Campari-GCP Out=densepointscld.ply  
mm3d PIMs2MNT MicMac DoOrtho=1
```

Figure 2.22. Example of application of the C3DC and PIMs2MNT commands. Refer to the MicMac manual for more precise details of the arguments defined for each command.

In the entire pipeline presented, attention is given to the succession of processes to which the acquired data is to be submitted, leaving any appropriate parameterisation to the various cases under study and the commissioned requests.

The validation of the processing chains seen in this section is discussed in section 3.5.

3. GEOREFERENCING STRATEGIES IMPACTS

The production of geographic information is in the throes of progress thanks to the development of new sensors, tools, and algorithms, which are easy to implement and user friendly (Ma et al., 2015). However, the accuracy of photogrammetric results, obtained through automated software instructions and the use of cheap, non-metric, and roughly calibrated sensors, is often unsatisfactory (Green et al., 2019). Consequently, the accuracy of the results, the potential, and the repeatability of these procedures need a framework to circumscribe their limits and lay the fundamentals for a knowledgeable management (James et al., 2019). Several approaches to the correct and efficient reduction of geometric errors are available in the literature, although no exhaustive method has yet been defined (James et al., 2019, O'Connor et al., 2017). In fact, generalisation, standardisation and serialisation of data and processing across the entire RS landscape is an inevitable trend in the future development of the sector (Huang et al., 2018). On the other hand, it is the basis for solving the problem of inconsistent data and processing, and the possibility of extracting innovative information from the combination of several data and/or technologies.

The Geographic Information/Geomatics Technical Committee of the International Organization for Standardization (ISO/TC 211) (Kresse, 2004), the Defense Geospatial Information Working Group (DGIWC), the American National Standards Institute (ANSI), the Federal Geographic Data Committee (FGDC), and the German Institute for Standardization (DIN) have all established and published standards related to RS data. Examples are the ISO/TS 19101-2 Geographic information - Reference model - Part 2: Imagery, the ISO/TS 19131 Geographic information - Data product specifications, the ISO/DIS 19144-1 Geographic information - Classification systems - Part 1: Classification system structure, the ISO/ RS 19124 Geographic information - Image and

gridded data components, and the <<ISO 19115 Geographic information – Metadata (Kresse, 2008, Kresse, 2010). However, more standards are needed for consistent applications of RS data from multiple sources.

Basically, in the field of real long-range RS, all satellites have developed their product system standards (Kresse, 2010). On the contrary in the close-range products, in particular, those from UAVs, the lack of a unified product system standard has led to a misperception of the data and hampered the development of innovative applications (Cummings et al., 2017).

For example, while there is a large body of research work concerning the adoption of SfM-MVS workflows, the different levels of accuracy of the same end product resulting, however, from the adoption of different processing approaches in different software have not yet been fully understood (Saponaro et al., 2019b). No validation analysis has been conducted so far in the literature to consider these products as repeatable and reproducible, not even in relation to the use of workflows commonly accepted within the various software platforms (Benassi et al., 2017). On the other hand, in view of the geometric validation methods of the products, the dependency between the evaluations carried out and the repeatability and reproducibility of the results remain unexpressed since they are based on non-unambiguous standards, such as those of the American Society for Photogrammetry and Remote Sensing (ASPRS) (Photogrammetry and Sensing, 2015) or often of national regulations (Hendrickx et al., 2019). Moreover, the lack of detailed information about the algorithms implemented in commercial software platforms makes the whole interpretation even more complex.

The accuracy of the products derived from the SfM algorithm is highly variable and the causes are not yet fully understood (James et al., 2017b). Several factors can affect the accuracy of UAV-derived data, such as flight parameters, image quality, processing software, the morphology of the studied area and, most importantly, georeferencing methods. The regular use of GCPs significantly improves the accuracy of SfM products, but at the same time, their collection represents a laborious and time-consuming part of UAV campaigns (Manfreda et al., 2019). For this reason, several

works in the literature have focused on finding an effective and sustainable GCP detection strategy to limit costs and work time (Agüera-Vega et al., 2018, Rangel et al., 2018, Sanz-Ablanedo et al.). Developing a comprehensive understanding of the correlation between georeferencing and BA processes of 3D models seems crucial.

In view of the considerations just discussed, the research path devised in this phase of the thesis work concerned the in-depth study of georeferencing strategies that can be adopted in a chain of photogrammetric processes based on UAV data. It was analysed the applicable methodologies and their impact on the final accuracy of the products that can be returned. Subsequently, the validation methodologies of the final accuracies and the standards accepted by the scientific and professional community were discussed to make these results reproducible, repeatable, and consistent. Analyses were carried out in order to understand any existing relationships between the calculations dictated by the BA algorithms and the construction of the GCP networks, which are suitable for georeferencing and scaling the models. Finally, the processing chain described in paragraph 2.4.5 was validated and the results compared with the same ones obtained in other software platforms. These were compared with the previously defined standards to understand their correct utility in practical terms.

3.1 GEOREFERENCING METHODOLOGIES

It has already been discussed how the combination of the ability of UAVs to fly over difficult-to-access areas and reduce operational time and costs with improvements in SfM-MVS algorithms makes photogrammetry more competitive than traditional survey systems over small and medium-sized areas (Manfreda et al., 2018b). However, (James et al., 2017a) pointed out that a homogeneous quality of results is still difficult to achieve and, therefore, as proposed by (Manfreda et al., 2018b), the whole workflow should be critically checked to identify the best approach among the various possible methods.

One of the most critical phases of the entire processing structure analysed in paragraph 2.3.6 is that of georeferencing. According to the United States Geological Survey (USGS) definition:

"Georeferencing means that the internal coordinate system of a digital map or aerial photo can be related to a ground system of geographic coordinates. A georeferenced digital map or image has been tied to a known Earth coordinate system, so users can determine where every point on the map or aerial photo is located on the Earth's surface."

In other words, during the georeferencing phase, metric and spatial information is transferred to the SfM-MVS products so that they have a real and practical connotation. This step can be based on a multitude of methodologies and technologies, each of which brings with it a level of precision and accuracy. The choice of one methodology, or technology, over another will reflect the commissioned demands for accuracy and precision, but also the budget and time available (Padró et al., 2019).

From a review of current literature, the most widely employed technologies for georeferencing SfM-MVS products are GNSS receivers and TS. A comparison of the achievable results is proposed in section 3.3. To a large extent, GNSS receivers and related measurement techniques are the most widely used in UAV surveying, mainly due to their ease of use (Eltner and Sofia, 2020). The main methodologies that can be used for georeferencing are discussed below.

Currently, the most common UAVs are equipped with GNSS receivers (usually for GPS/GLONASS constellations, using the European Geostationary Navigation Overlay System (EGNOS) augmentation system) with C/A code assisted by IMU, in most cases with low accuracy. These are efficient for navigation and aircraft trajectory planning, while at the same time providing appreciable attitude stability and positional data are useful in the first steps of SfM alignment. On the other hand, this low equipment is not able to guarantee the achievement of the final accuracy requirements in the georeferencing steps (Padró et al., 2019).

In these cases, in fact, it is verified that the spatial resolution of the images is greater than the accuracy of the direct determination of the ExO parameters of the individual images at the time of sensor exposure, i.e., the positional accuracy (X, Y, Z) obtained directly from the GNSS receiver onboard the platform, and the sensor orientation (ω, ϕ, κ) obtained directly from the IMU device. This results in inaccurate georeferencing of the SfM-MVS product, or at least an error that largely exceeds the pixel size. This is caused by the low receiver rate in position measurements per second (Hz), which is crucial for sampling the position of a moving object.

As stated by (Colomina and Molina, 2014), the DG accuracy of a UAV-based products depends on the quality of the GNSS receiver. Indeed, a receiver can work in code or carrier phase mode, the latter usually providing higher range accuracy as the receiver can distinguish the sine wave oscillation where the signal code is located. This can be achieved conveniently by using a single-frequency L1 receiver.

The moderate code-based accuracy is acceptable in UAV campaigns that require only low-quality metrics (Benassi et al., 2017). The approximate economic cost of this GNSS device is less than 50 €. However, these images cannot be used to generate detailed cartography at large scales, such as 1:200 (Whitehead and Hugenholtz, 2015), nor can they be assumed to have reasonable pixel co-registration in multi-temporal studies using images with a spatial resolution below 0.1 m.

It seems trivial that the final accuracy can be improved by using a dual-frequency differential GNSS (DGNSS) receiver. A DGNSS can read two carrier phases at two wavelengths L1/L2 and take into account signal delays caused by atmospheric effects.

DG is a crucial step towards the automation of the whole procedure, however, as demonstrated in several papers (Daakir et al., 2017, Gabrlík et al., 2018, Grayson et al., 2018, Hu et al., 2017) but their results are not satisfactory compared to IG.

Given these latter considerations, UAV-based topographic processing is generally performed using a few known points, called GCPs. The accuracy of the output of these methods is a function of the number and precision of the GCPs engaged in the metric reconstruction. Clearly, operational costs and time increase proportionally to the GCPs acquired during field campaigns (Rangel et al., 2018, Sanz-Ablanedo et al.,

2018) and, consequently, optimisation of survey activities would improve the reliability and repeatability of UAV-derived products (Manfreda et al., 2018a).

IG, which is a well-known technique based on Aero-Triangulation (AT), provides a bundle block adapted to ground references, and can therefore determine the orientation of each image block indirectly. In practice, GCPs measured in the field are manually located in the corresponding images. Once a network of correspondences between images and terrain coordinates has been generated, block modifications are initiated.

Assuming an accessible region of interest, the economic costs of materialising GCPs, including the rental of a static DGNS and personnel costs amount to approximately €500. The time invested is approximately one hour per GCP to paint and materialise the points on the concrete platforms; obviously, the time duration would be reduced if mobile markers were used or if stable ground positions were painted. In addition to the measurement time, there will be time for post-processing of the static measurements and other processing to accurately locate the GCPs in the individual images.

The DGNS receiver can work with the information provided by a network of Permanent Reference Stations (PRS), but this infrastructure must be implemented in the region of the study area, as is the case with networks of permanent reference stations (EUREF-EPN) (Ihde et al., 2014) and Continuously Operating Reference Stations (CORS) (Snay and Soler, 2008). For example, the information from the Italian PRS National Dynamic Network (RDN2008), managed by the Istituto Geografico Militare (IGM), will be used in the work. DGNS measurements combined with PRS information allow the receiver position to be determined more accurately than RTK measurements.

Recently, the market offered DG Post-Processing Kinematic (PPK) solutions with devices light enough to be carried in UAV platforms <25 kg. This is an attractive option for users of environmental RS due to the accurate post-flight processing, thus not in real-time (Bisnath et al., 2004). However, it is important to achieve image positioning that is as accurate as possible. Although this method is not based on any GCP, it is still dependent on the base station located in the study area. The approximate cost of

these technologies varies from as little as €350 up to around €8500, highlighting how the costs become unaffordable for all users.

Reviewing the current literature, among the discussed methods, the IG method provides the highest accuracy overall (Padró et al., 2019). The DG-PPK methods prove to be very challenging and further developments are expected in the field. They show equal performance to the IG methods but with less effort in field activities. The basic DG and DGNS methods generally provide a systematic displacement due to the combined error sources of the lever arm offset and the lack of any ground reference point. However, the economic cost, time invested, and ground requirements of each method are different and may suit different RS purposes. In the case of both DGNS and PPK, the use of a station in the study area and a dual-frequency receiver allows a better correction of the satellite signal, the positional acquisition is optimal but at the same time, the instrumental expenses are quite high. At an approximate cost of €50, DG with GNSS navigation is the most cost-effective and user-friendly option and required no external or ground support. Therefore, in order to guarantee a high final geometric accuracy but at the same time accessibility in terms of cost and time for a large part of the users, combined solutions between DG and IG are investigated.

For example, it has already been shown that at least three GCPs, in addition to the geo-tags of each image, are required for the software platform to exploit this information for an effective BA. However, it is clear from the literature that the minimum number of GCPs needed to produce optimal quality is still uncertain. On this topic, (Manfreda et al., 2019) proposes a useful table to review the accuracy values obtained by varying the number of GCPs extrapolated from different UAV works. (James et al., 2017a) recommends a minimum of five GCPs, combined with accurate camera calibration, to obtain reliable results.

Therefore, the proposal of this research phase was to find an optimal combination between the georeferencing methodologies and the seen processing framework, in order to obtain cost-effective yet high accuracy SfM-MVS products.

3.2. TERMS OF GEOMETRIC ACCURACY STANDARDS

Although images acquired by UAVs typically have very high ground spatial resolutions, generally centimetres, these do not necessarily imply a correspondingly high geometric accuracy of the photogrammetric products that can be returned. Many UAV-based studies have been concerned with providing an overview of methodologies for estimating planimetric and vertical accuracies (Elkhrachy, 2021, Hugenholtz et al., 2016). These estimates are typically derived by comparing the surveyed and measured field positions of a number of control points in the various returned products. While such estimates can be useful in assessing the quality of the survey, checking accuracy is usually done on an ad-hoc basis, making it difficult to compare the accuracies of different surveys made by UAVs. This inconsistent approach can also cause problems when comparing results with those obtained from surveys carried out using other methods and can make it difficult to identify optimal processing methodologies.

This section discusses an initial assessment of UAV accuracy in the context of the mapping standards established by the ASPRS (Photogrammetry and Sensing, 2015). ASPRS is one of several organisations that rigorously define standards for positional accuracy on maps and geospatial data, and they are the most widely accepted and used standards internationally. Indeed, they have been rapidly accepted as the de facto standards for the industry. The ASPRS first released precision standards for large-scale mapping in 1990 (Accuracy, 1990), and in the March 2015 edition of Photogrammetric Engineering and Remote Sensing released an updated set of standards appropriate for mapping from digital imagery (Photogrammetry and Sensing, 2015). This version is fully designed for digital orthophotos and DEMs, and as such is independent of both map scale and contour interval. Positional accuracy standards are included for digital orthoimages, digital planimetric data, and digital elevation data. The accuracy classes, based on RMSE values, have been reviewed and updated from the 1990 standard to deal with the higher accuracies obtainable with new technologies (Smith and Heidemann, 2015). The standard is technology-independent and addresses a broad base while acknowledging the existence of application limitations. Specifi-

cally, UAV data have not been properly evaluated in the context of these latter standards, but several published works have been justified in validating them (Whitehead and Hugenholtz, 2015).

This standard addresses the geolocation accuracy of geospatial products and is not intended to cover the classification accuracy of thematic maps. The standard follows metric units of measure to be consistent with international standards and practices (although it does not refer to any of them) and does not specify the best methodology needed to achieve values above established thresholds. It will be the responsibility of the data provider to establish the control procedures and final quality of the geospatial product to be returned, along with the commissioned requirements.

Ground control and control point accuracies and processes should be established according to project requirements. Unless otherwise specified, all ground control and control points are normally expected to follow the network accuracy guidelines as detailed in Geospatial Positioning Accuracy Standards, Part 2: Standards for Geodetic Networks, Federal Geodetic Control Subcommittee, Federal Geographic Data Committee (FGDC-STD-007.2-1998) (Smith and Heidemann, 2015).

Horizontal accuracy shall be tested by comparing the planimetric coordinates of well-defined points in the data set with the coordinates determined by an independent source of higher accuracy. Vertical accuracy shall be tested by comparing the elevations of the surface represented by the data set with the elevations determined by an independent source of higher accuracy. The horizontal accuracy shall be evaluated using the RMSE statistics in the horizontal plane, i.e., $RMSE_x$, $RMSE_y$ and $RMSE_R$. Vertical accuracy is to be assessed in the z-dimension only. For the verification of vertical accuracy, different methods are used in non-vegetated soils (where errors typically follow a normal distribution suitable for RMSE statistical analysis) and vegetated soils (where errors do not necessarily follow a normal distribution). When the errors cannot be represented by a normal distribution, the 95th percentile value more correctly estimates the accuracy at a 95% confidence level. For these reasons, vertical accuracy must be assessed using $RMSE_z$ statistics in non-vegetated soils and 95th percentile statistics in vegetated soils.

Both $RMSE_z$ and 95th percentile methodologies specified above are currently widely accepted in standard practice and have been shown to work well for typical elevation datasets derived from current technologies. However, both methodologies have limitations, particularly when the number of control points is small.

Except for vertical data in vegetated terrain, the assessment methods outlined in this standard, and those related to the calculation of the National Standard for Spatial Data Accuracy (NSSDA) 95% confidence level estimates, assume that the errors in the dataset are normally distributed and that any significant systematic errors or biases have been removed. As a rule, these standards recommend that the average error should be less than 25% of the RMSE value specified for the project. In any case, average errors that are greater than 25% of the target RMSE, whether identified pre-delivery or post-delivery, should be examined to determine the cause of the error and to determine what action, if any, should be taken.

While older ASPRS standards used numerical ranks for discrete accuracy classes related to the map scale (i.e., Class 1, Class 2, etc.), many current approaches demand greater flexibility regarding these classes. In fact, many horizontal accuracy applications cannot be tied directly to compilation scale, source image resolution, or final pixel resolution. The latest standard, therefore, defines the horizontal and vertical accuracy classes in terms of $RMSE_x$, $RMSE_y$, $RMSE_z$ values and relates them to several parameters, including the GSD value of the product, which comes in handy in UAV-based work.

Accuracy standards for geospatial data have wide applications at national and/or international level, while specifications provide technical requirements/acceptance criteria that a geospatial product must conform to be considered acceptable for a specific use. Guidelines provide recommendations for the acquisition, processing, and/or analysis of geospatial data, normally intended to promote consistency and best practice in the industry. The current standard was developed in response to a pressing need in the GIS and mapping community for a new standard that embraces the digital nature of today's geospatial technologies.

Achieving the highest level of accuracy requires specific considerations of sensor type, ground control density, ground control accuracies, and overall project design. In many cases, this entails a higher cost. Consequently, the highest obtainable accuracies may not be suitable for all projects. Many geospatial mapping projects require high-resolution, high-quality imagery, but do not require the highest level of positional accuracy. This is particularly true for upgrades or similar projects where the intent is to improve image resolution, but still exploit existing elevation model data and terrain control data that may have originally been developed to a lower accuracy standard.

3.3. COMPARING GNSS AND TS TECHNOLOGIES

The achievement of the highest levels of accuracy, however, is certainly connected to the technology employed and the measurement technique pursued, and influenced by the chosen georeferencing methodology, as seen in paragraph 3.1. In a process of optimisation of the programming of the measurements and the restitution phase, it is evident that the user must examine the alternatives and then focus his attention on those that are most suitable to the project requirements. In other cases, it is necessary to adopt several measurement methodologies and implement several technologies. This gives rise to the need to analyse comparisons, investigate discrepancies and validate commutability. The objective of the analysis tackled at this stage of the research was essential to build general awareness of the origin of the errors underlying two measurement techniques, namely adopting GNSS and TS technologies, to weigh their effects on the reproducibility of the products in a multi-temporal survey.

A fortified watchtower, named Torre Zozzoli, in a state of abandonment and degradation, was chosen as a pilot area for the test. It is located between the municipalities of Lizzano and Pulsano, both small towns about 25 km south of Taranto (Region of Apulia, Italy) (Figure 3.1).

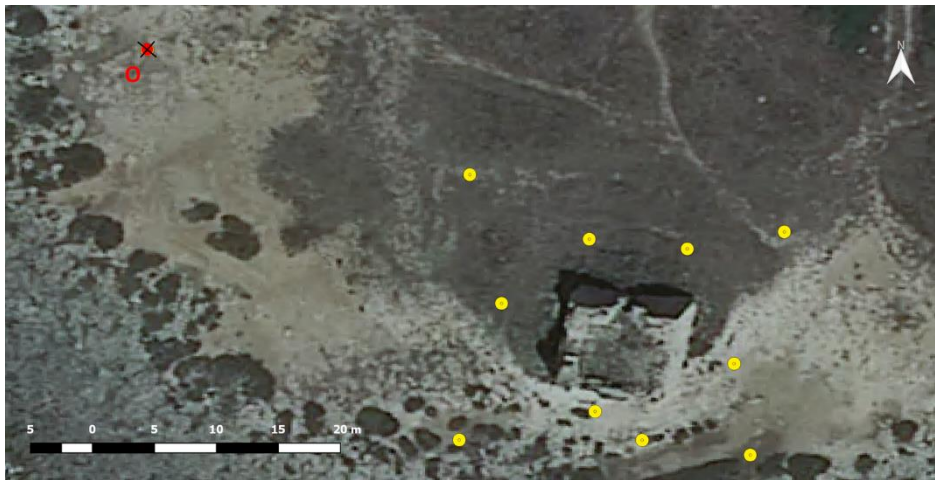


Figure 3.1. The study area and visualization of the disposition of the targets. In red the station O, origin of the network of vertices TS and useful for the conversion of points from the local reference system to the absolute.

A detailed description of the acquisition phase can be found in the work (Saponaro et al., 2020b). The acquired datasets were subjected to the photogrammetric processing chain analysed in the previous paragraphs.

The activities of the topographic measurements were carried out after careful planning and setting of the field operations. In order to generate a network of topographic vertices, two independent high-precision measurements of the same 11 ground truth points were performed. In particular, considering the small extension of the building under study, an arrangement of 10 targets was established in such a way as to homogeneously cover each side of the building but avoiding a condition of coplanarity between their support planes, the origin of complex dependencies between the vertices in the georeferencing phases. The eleventh target, identified by the label O, was instead positioned at about 20 metres from the structure, established as a specific reference station for the TS survey, and useful in the conversion phase between the reference systems of the two technologies (Figure 3.1). First, the points were measured with the Leica GS08plus receiver in Real-Time Kinematic (nRTK) network mode, achieving an average centimetre accuracy of 0.02 m along all three axes (WGS84/UTM zone 33N (EPSG:32633)).

Subsequently, the same points were acquired using the potential offered by the Trimble SX10 in TS mode. The network of stations was constructed by generating a closed traverse, clearly compensated by obtaining the coordinates of the vertices recorded in a local reference system, relative to the instrument. Two of the 11 points (stations O and GPS001) were assigned the coordinates measured in the GNSS survey, thus transferring a global reference system, the same as the GNSS survey, to the entire TS network.

After obtaining the coordinates of the targets distributed around the building through the two technologies described above, general statistics were examined to obtain the average systematic discrepancy and a predictive variance between the two types of positional measurements. In other words, the coordinates of the same points recorded by the two technologies were compared to take the relative mean error values of the supposed statistical distribution, according to each axis and absolute along the three axes. From this population of errors, their spatial planar distribution in the measured GCPs was also analysed. The values of the standard deviation (σ) and the RMSE were consequently estimated in the same way, according to each axis and in absolute form along the three axes.

Once the statistical distribution of deviations has been constructed, these indices configure how errors occur, explaining by comparing the mean and median errors on the possible systematic deviations between the two types of measurement. The standard deviations express how far these deviations deviate from the expected value, while the RMSE value takes into account possible sources of accidentality in the measurements, cumulated with systematic errors.

Based on a rough comparison of the technologies under study, positional measurements in nRTK-GNSS significantly reduce field efforts as there is no need to build a TS-compensated vertex network (30 min vs. 1.5 h). On the other hand, they require a fairly stable connection for instantaneous corrections and/or post-processing of the acquisitions to improve their accuracy, although still higher by an order of magnitude than that obtainable with TS (centimetres vs. millimetres).

Because of these premises on the measurement methods, in Table 3.1 it is possible to observe the values of the mean and median errors, of the standard deviation (σ) and the RMSE, considering both the contribution along each axis and in planar and 3D form. Figure 3.2 shows the frequency histogram of the deviations (Δ_{XYZ}) in ten classes in a range given by their maximum and minimum values.

Table 3.1. Average errors and RMSE values resulting from the comparison of positional measurement techniques from TS and nRTK-GNSS, in the same 10 targets homogeneously distributed in the investigated scene.

	X	Y	Z	XY	XYZ
Mean [m]	-0.008	-0.012	0.016	0.016	0.026
Median [m]	-0.009	-0.010	0.022	0.014	0.026
σ [m]	0.011	0.017	0.021	0.019	0.026
RMSE [m]	0.010	0.016	0.020	0.018	0.024

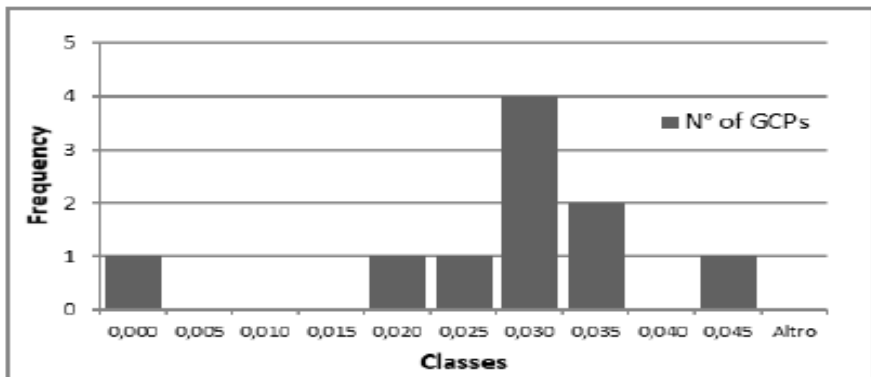


Figure 3.2. Frequency histogram of the deviations GCP(Δ_{XYZ}) between TLS and GNSS measurements.

A careful analysis of the results obtained comparing the two positional measurement techniques reveals a systematic deviation of the order of a centimetre intrinsic to the sensitivity of the GNSS survey mode chosen for this work. The greatest contribution to the errors is certainly more conveyed along the Z-axis, with a percentage of over 50% in the comparison between planar and 3D errors. However, the absence of targets strategically positioned on the building façades does not allow the evaluation of possible different behaviours when varying the laying plane. To demonstrate this and in order to identify the robustness of the measurements along each axis, Pearson's

coefficient R2 was estimated as a function of each axis of the measured points: the calculation returned the trio of values [0.9999998, 1.0, 0.9991070], showing effective linearity relationships between the two measurements, with the weakest values along the Z-axis.

On the other hand, the RMSE values show ranges that are almost comparable to the mean errors: since these are proportional to the square of the errors evaluated, any high value would produce considerable effects on the RMSE values themselves. This suggests that the measurements can be considered reliable and not affected by obvious anomalies. To confirm this, the distribution of the planar deviations in the GCPs was evaluated in order to possibly focus on where the major sources of error are concentrated (Figure 3.3).

GCP09 and GCP05 showed the most significant values when the contribution from errors along the Z-axis was removed. Since the operations in the field were uniform and given the spatial correlation between the above points, it is possible to attribute the error to the presence of obstacles, such as the tower itself.



Figure 3.3. Spatial Distribution of GCP planar deviations between TLS and GNSS measurements. Each circumference around each point represents the estimated average planar error. Circumferences have a scale factor 50 times the actual value.

Knowing the nature of the existing rejects as in Table 3.1, it is possible to cumulate a systematic contribution of 0.018 m to the RMSE values obtained in TS. Such contribution is the all-inclusive planar RMSE value of the systematic and accidental behaviours recorded by the statistics. The two technologies can thus be defined as interchangeable if the accuracy requirements for the geospatial products commissioned also include a quality equal to ASPRS Class II.

3.4. IMPROVEMENT OF THE GCP/CP NETWORK

The expanding demand for various applications requires further studies to explore ways to obtain more reliable information from UAV data derivatives. A number of studies have been conducted in determining different ways on how to improve the accuracy of outputs generated from UAV imagery: from environmental conditions and flight settings during image acquisition (Raczynski, 2017), attempting a minimum distance approach for GCPs (Pourali et al., 2014) and different spatial models of them (Ridolfi et al., 2017), evaluation of various positioning systems (Ruiz et al., 2013), to processing parameters such as feature extraction, image matching and BA (James et al., 2017a), to the algorithm for creating the dense point cloud (Rosnell and Honkavaara, 2012) and DEM (Ruiz et al., 2013) and polynomial transformation for image rectification using GCPs (Muhaisen, 2016). The pivotal factor that can significantly improve the quality of the data products is the use of an accurate and well-structured GCP network to correctly tie the model to the terrain values. It is clear from Section 3.2 that an organised and focused CP network is also fundamental to the validity of the accuracy checks. Therefore, to ensure both global and internal accuracy between datasets, the location, distribution, and number of GCPs/CPs should be taken into serious consideration when planning field operations. Since overuse of GCP/CP results in increased time and cost for an entire survey operation, a way must

be found to ensure the production of accurate and consistent data while minimising the time and cost of operations.

3.4.1. Optimize the Number of GCPs

One of the factors most analysed by the authors concerns the numerical optimisation of the GCPs to be implemented in the georeferencing step. A number such that it does not compromise the high final geometric accuracy required but at the same time efficient field and screen operations during marker collimation, both in terms of time and cost. The impact of the number of GCPs on the geometric quality of the derived photogrammetric products was thus studied (Awasthi et al., 2020, James et al., 2017a, Rangel et al., 2018, Siqueira et al., 2019, Villanueva and Blanco, 2019). As expressed by the ASPRS standards, the planimetric and altimetric accuracies are explained in terms of the RMSE recorded on the CPs or GCPs. The value of RMSE can be considered as the cumulative result of all errors, i.e., both random and systematic errors with a Gaussian distribution (Saponaro et al., 2018), and consequently representative of the absolute accuracy of each point.

For this study, a dataset of UAV images acquired at 70 m Above Ground Level (AGL) on an erosion-prone stretch of coastline, located in the southernmost part of the city of Bari (Apulia Region, Italy), was used. In the area, 30 GCPs were deployed and measured in nRTK mode using a Leica Viva CS10/GS10 receivers, achieving an average 3D accuracy of 0.02 m. More details on the SfM-MVS acquisition and processing phases can be found in (Saponaro et al., 2019c).

Figure 3.4 shows a complete view of the mean, max and min errors recorded in the CPs for each process. The mean error represents the actual systematic shift between the estimated points and the measured truth points: a stable and recognisable discrepancy. An RMSE value much higher than the mean error noted would suggest a predominance of accidental errors and therefore a clear instability of the results. Conversely, comparable RMSE and mean errors, verified by the bias values (min-max errors), clarify the statistical robustness of the results.

Figure 3.4 shows the $RMSE_{XYZ}$ values in CPs related to the 20 processed Chunks respectively, excluding the complete IG case: its results are reported in Table 3.2.

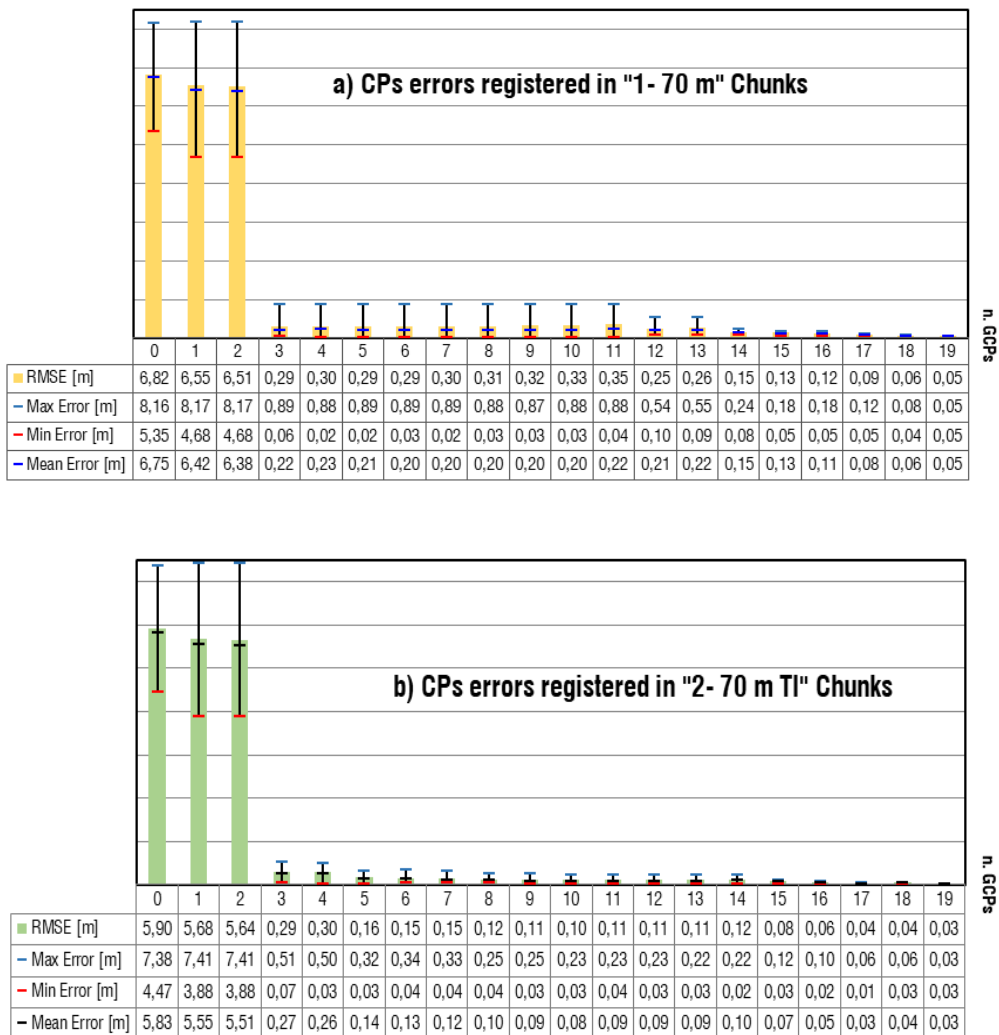


Figure 3.4. a) CPs errors registered in "1- 70 m" dataset varying the GCPs number implemented b) CPs errors registered in "2- 70 m TI" dataset varying the GCPs number implemented. TI: Treated Image.

Analysing the DG case, i.e., without the assistance of GCPs and using only the positional tags of the image checked in the box before starting the process, the accuracy

cies obtained show large gaps for possible use in the cartographic field. The low accuracy of the mounted sensors does not allow the achievement of high positional accuracy in DG, and, on the other hand, the lack of raw position data does not allow the identification of causes to improve the estimates.

It is also necessary to consider an efficient amount of GCP in the data georeferencing workflow to obtain highly accurate geospatial products. Overall, the two datasets show similar behaviour in terms of the number of GCPs implemented. There is a reduction in RMSE_{xyz} values when going from a number of GCPs used of 2 to 3, with an RMSE_{xyz} jump of about 5.5 m. The following configurations attest to the same order of magnitude achieved with slight centimetric fluctuations, related to the REs in the images of the implemented GCPs.

Table 3.2. Full description of the RMSE_{xyz} [m] values and the Error [pix] (i.e. RE) recorded in the 42 generated Chunks. The red box highlights the results considered as optimal for the model georeferencing. In the green box, the results obtained for the complete IG cases.

n.GCPs		1- 70 m		2 - 70 m TI	
		RMSE _{xyz} (m)	Error (pix)	RMSE _{xyz} (m)	Error (pix)
0	GCPs				
	CPs	6.822	2.466	5.904	0.481
1	GCPs	6.820	0.390	5.908	0.484
	CPs	6.552	2.536	5.682	0.480
2	GCPs	7.015	0.312	6.106	0.431
	CPs	6.514	2.656	5.645	0.487
3	GCPs	0.096	0.409	0.099	0.414
	CPs	0.297	2.800	0.299	0.498
4	GCPs	0.085	0.415	0.088	0.501
	CPs	0.305	2.894	0.301	0.475
5	GCPs	0.077	0.415	0.084	0.493
	CPs	0.299	2.986	0.166	0.480
6	GCPs	0.072	0.435	0.078	0.487
	CPs	0.299	3.047	0.156	0.484
7	GCPs	0.071	0.688	0.078	0.497
	CPs	0.307	3.168	0.153	0.477
8	GCPs	0.088	0.681	0.102	0.519
11	GCPs	0.076	0.639	0.088	0.487
	CPs	0.351	3.917	0.110	0.484
12	GCPs	0.244	2.990	0.087	0.507
	CPs	0.255	0.502	0.111	0.445
13	GCPs	0.236	2.888	0.084	0.504
	CPs	0.261	0.493	0.114	0.442
14	GCPs	0.263	2.835	0.081	0.502
	CPs	0.157	0.495	0.121	0.441
15	GCPs	0.256	2.752	0.089	0.513
	CPs	0.138	0.395	0.088	0.380
16	GCPs	0.249	2.706	0.087	0.507
	CPs	0.121	0.391	0.065	0.395
17	GCPs	0.245	2.689	0.087	0.503
	CPs	0.091	0.365	0.042	0.399
18	GCPs	0.239	2.605	0.084	0.493
	CPs	0.069	0.369	0.049	0.432
19	GCPs	0.234	2.558	0.082	0.494

	CPs	0.310	3.394	0.121	0.457		CPs	0.051	0.422	0.032	0.392
9	GCPs	0.084	0.668	0.099	0.508	20	GCPs	0.227	2.466	0.081	0.486
	CPs	0.321	3.470	0.113	0.464		CPs				
10	GCPs	0.080	0.662	0.093	0.506						
	CPs	0.332	3.572	0.106	0.465						

Optimal solutions were sought, based on the simultaneous occurrence of low RMSE values on both CPs and GCPs: a necessary condition to demonstrate the consistency of the RMSE values recorded on CPs. The values reported in Table 3.2 show optimal geometric accuracy achieved with 6-7 GCPs implemented for both Chunks, thus confirming the results obtained by (James et al. 2017). Focusing on the differences between the two processed Chunks, some considerations can be drawn. With reference to Table 4.2, the "2 - 70 m TI" Chunks show REs (pix), for both ground points, lower than the "1- 70 m" Chunks and, at the same time, these improve the geometric accuracy obtainable on the CPs. It can therefore be argued that masking and brightness adjustment techniques effectively improve the detection and matching of tie points, providing more robust results. On the other hand, however, these techniques can undermine the development of complete 3D models by not accurately masking particular areas.

3.4.2. Optimize the Distribution of GCPs

While the numerical optimisation of GCPs has greatly engaged the scientific community in deriving useful observations to facilitate work for users, on the other hand, it has become essential to investigate the influence of their dislocation in the surveyed area and the relative impacts on the achievable accuracies.

Indeed, an effective number of ground truths proves to be incidental to the amount of transferable information, neither insufficient nor redundant, such as to guarantee an accurate orientation and scaling of the photogrammetric products. The distribution of these ground truths turns out to be fundamental in the qualitative description of the morphology of the investigated area since the interpolations in the points where the spatial information will be computed depend on it.

It is evident that neither of the two strategies described in the last two paragraphs is more important than the other, but rather the GCP network needs careful and targeted planning.

Testing was carried out in a farmhouse known as “Casale di Pacciano”, located in the countryside of Bisceglie, 40 km far away from Bari (Apulia Region, Southern Italy) (Figure 3.5). A detailed description of the acquired datasets (UAV and GNSS campaigns) and SfM processing are given in (Saponaro et al., 2019a).



Figure 3.5. The test site and, in red, GCPs distributed in the area

The influence of the spatial distribution of GCPs on the implemented number was analysed. Seven copy sparse point clouds were generated, with a number of GCPs varying from 1 to 7, adopting a selection strategy that started from the GCPs on the borders towards the central ones. Subsequently, other seven point clouds were generated as copies of the original one and, in a similar way, GCPs were implemented by varying their number but adopting the opposite strategy to the first one described, i.e., from the centre towards the boundaries. Finally, other seven clouds were generated by adopting another strategy for choosing GCPs, i.e., balancing the distribution homogeneously. The BA algorithms were then started.

Figure 3.6 shows the statistical treatment for each model to examine the best GCP distribution strategy. The third selected spatial distribution returns better accuracy values. As discussed by (Rangel et al., 2018), the best results are obtained with a gradual distribution of GCPs to obtain a homogeneous density of points in the area, while maintaining a reasonable distance between points. Encouraging findings are also generated by the first spatial distribution, which involves marginal GCPs and central CPs, according to the literature (Rangel et al., 2018, Sanz-Ablanedo et al., 2018).

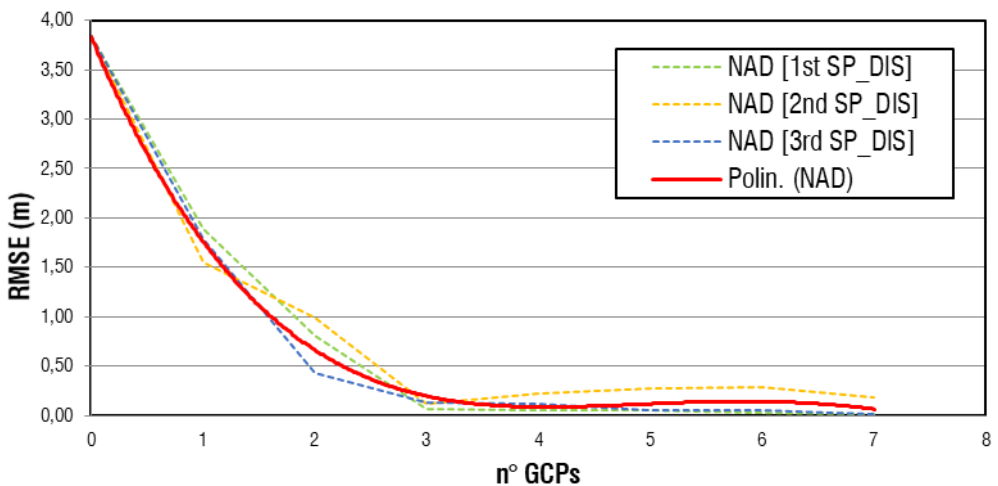


Figure 3.6. Impact of GCPs spatial distribution. NAD dataset developments and trend line by varying the spatial distribution: 1st SP_DIS: first distribution, 2nd SP_DIS: second distribution, 3rd SP_DIS: third distribution. The red line identifies a polynomial trend line that smooths out the effects of spatial distributions.

3.4.3. Suitable Allocation of Check Points

As explained several times in the preceding paragraphs, to provide a report on the geometric accuracy of the photogrammetric products generated, it is necessary to distribute check points (CP) in the investigated area, in addition to the GCPs from which to inherit the orientation and spatial scale. These points, measured topographically in the field in the same way as the GCPs, present themselves as an independent source useful for the subsequent verification of the coordinates estimated in the processes with those measured. In continuation of the concepts set out in Section 3.2 of

this research work, the ASPRS 2015 devotes ample space to the appropriate allocation of these CPs across the entire surveyed scene.

When geometric accuracy testing is to be performed, the distribution of control points will be project-specific and must be determined by mutual agreement between the data provider and the end-user.

A methodology to provide a quantitative characterisation and specification of the spatial distribution of control points across the project extent is required. Currently, there is no standardized methodology, indeed the ASPRS 2015 - Annex C promulgates only guidelines of it. The density and distribution of CPs are mainly based on empirical results and simplified area-based methods. The requirements of Annex C may be replaced and updated as new methods for determining the appropriate distribution of CPs are established and approved.

As in the case of ground truths analysed, the ASPRS proposes a strict distinction between control points intended for horizontal and vertical accuracy checks. The reader is referred to ASPRS 2015 Annex C for a detailed description of the two types of control points.

It is evident that by overlapping the requirements of both types of CPs, it is possible to identify points that are simultaneously useful for both accuracy checks. On the other hand, as specified in (James et al., 2017a), it is often convenient to place CPs in the vicinity of artefacts and/or natural features that are the focus of studies, avoiding more edge areas where sources of error may be concentrated due to the SfM technique itself.

The ASPRS recognises that some project areas may be unvegetated, while other areas are vegetated at the same time. For these reasons, the distribution of CPs may also vary according to the general proportion of vegetated and non-vegetated areas in the project. The CPs should generally be distributed proportionally between the different vegetated land cover types in the project.

3.5. ACCURACY ASSESSMENT AMONG DIFFERENT SOFTWARE PLATFORMS

Section 2.4 gave a brief overview of the numerous software platforms in continuous development in the field of UAV data processing for aerial photogrammetry (Cummings et al., 2017). Nevertheless, while these software are very efficient in the various processing phases, the different levels of accuracy of the final product resulting from the adoption of different processing approaches in the various software have not yet been fully understood (Flores-de-Santiago et al., 2020). There is no validation dissertation in the literature to consider these products as repeatable and reproducible, not even in relation to the use of workflows commonly accepted within the various software platforms. In fact, in view of the methods of geometric validation of the products, as seen in section 3.2 and drawn up by the ASPRS (Photogrammetry and Sensing, 2015) (or often by national standards), the dependence between the evaluations carried out and the repeatability and reproducibility of the results remain unexpressed (Benassi et al., 2017, Hendrickx et al., 2019). On the other hand, the lack of detailed information about the algorithms implemented in commercial platforms makes the whole interpretation even more complex.

Starting from the flow chains expressed in paragraphs 2.4. and 2.5, in the present research phase of the thesis work, the aim was, therefore, to provide a comparative evaluation of the three most used photogrammetric software in the industrial field, to obtain consistently, if not congruent, results. In particular, the three processing chains were started in parallel in Agisoft Metashape, Pix4D Mapper, and MicMac on a dataset of images relating to the excavation area of a road section in the trench of the Pedemontana Veneta (Figure 3.7). The reader is referred to (Saponaro et al., 2020c) for a detailed description of the acquisition campaigns carried out and the SfM-MVS processing.

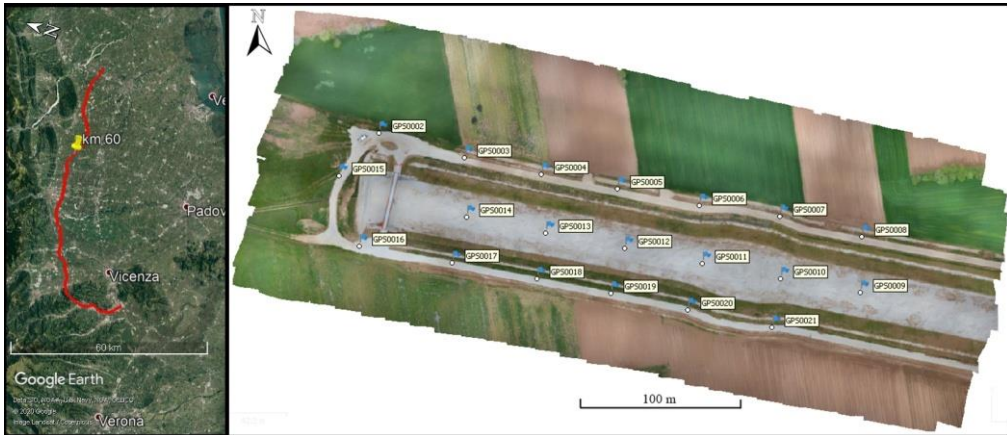


Figure 3.7. On the left, in red, the road axis of the Pedemontana Veneta Highway in its extension. On the right, a detail of the road section under excavation, object of study, near km 60, and the distribution of the GCP/CP targets in the overflow area. Image based on (Saponaro et al., 2020c).

As already explained in the above paragraphs, the processing pipelines were carefully parameterised to make them comparable in both licensed and open-source software. For a better interpretation of the results derived from the generation of point clouds processed from the same set of image data, through statistical inference, the influence on the accuracy of the final product of the number of GCP implemented in the georeferencing was then analysed (Meinen and Robinson, 2020, Siqueira et al., 2019).

In the georeferencing phase, the leave-one-out technique was adopted regarding the number of GCPs implemented: starting from the complete case of IG, implementing 20 GCPs, the number of GCPs was reduced by one unit each time, and these were incorporated into the set of CPs. At the end of the process, the DG case with 0 GCPs and 20 CPs was obtained.

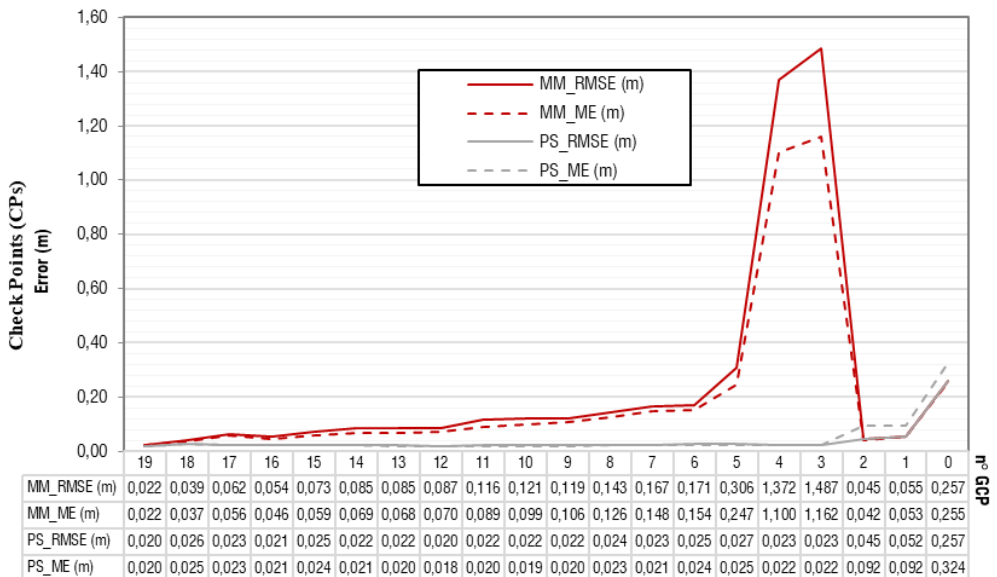
The values obtained from the 21 GCPs and CPs management cases implemented for each software, and thus from the related BA processes, were analysed and compared with the geometric standards widely accepted by the scientific community, as updated by ASPRS in 2015.

As defined in Section 3.2, the ASPRS defines accuracy classes based on RMSE thresholds evaluated on CPs for digital orthomosaics, digital planimetric data, and

digital elevation data (Photogrammetry and Sensing, 2015). At the same time, the mean absolute errors (ME) obtained along the three axes were analysed, looking for possible systematic errors. Instead, a check of the same error values on the GCPs accredits the robustness and consistency of the georeferencing steps in the photogrammetric blocks.

Figure 3.8 shows the trend of $RMSE_{XYZ}$ values and mean errors recorded in the various georeferencing cases in the Agisoft Metashape and MicMac software. In this comparison, the results obtained by not implementing image geotags in the various BA processes were analysed.

Analysing the values returned in the CPs, completely equal values are presented for the cases in which the number of GCPs implemented is less than 3, being characterised by the positional information of the geo-tags that therefore reduce the contribution of the tie points in the BA processes. This is indeed evident in the following cases where the BA processes within MicMac do not support a reduced number of GCPs and reveal much higher $RMSE_{XYZ}$ values than those derived from Agisoft Metashape.



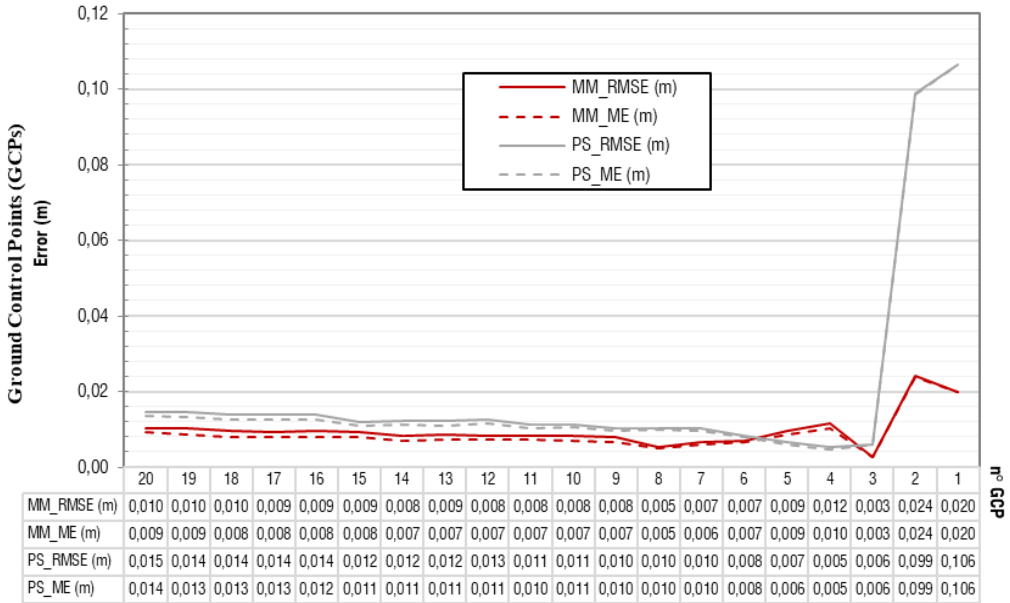


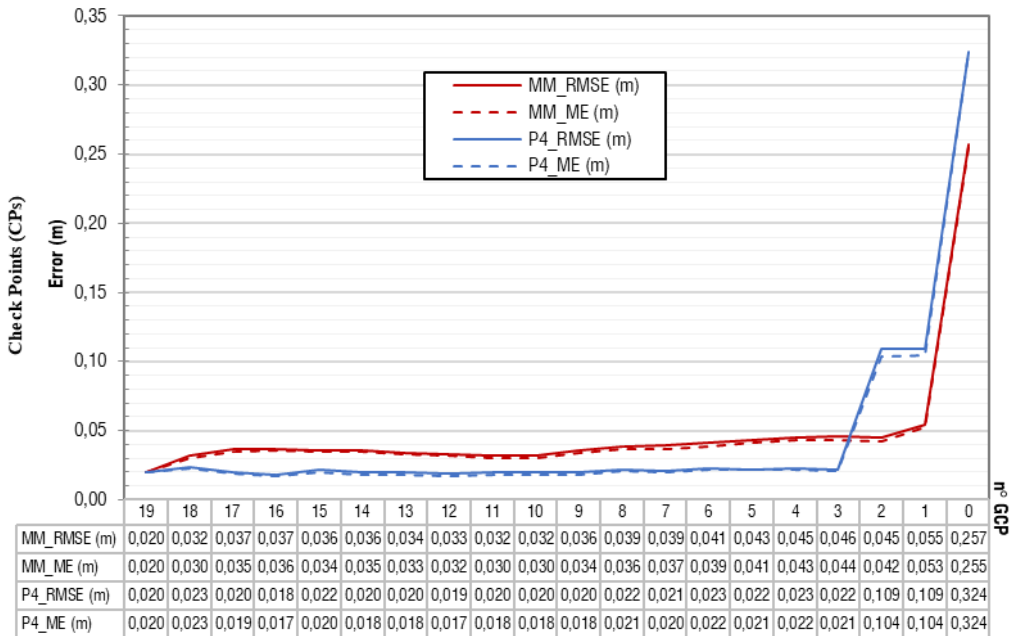
Figure 3.8. Comparison of RMSEXYZ and Mean Error (ME) values obtained on CPs and GCPs from MicMac (MM) and Agisoft Photoscan (PS) processes.

While in Agisoft Metashape the values can be considered constant for all cases, in MicMac there is a downward trend towards a minimum value in the georeferencing condition with 19 GCPs. The average errors follow the same trends, except for the cases in MicMac that fall within the range of 3-5 GCPs implemented, where the deviation shows lower systematic errors than accidental ones.

On the other hand, in Metashape, although there are slight deviations between the mean errors and RMSE below the implemented 3 GCPs, the values recorded in the GCPs show reduced robustness of the georeferencing, which then remains constant for all the other cases analysed. MicMac, on the other hand, produces more robust georeferencing than Metashape, showing lower RMSE values and average errors from the 6th GCP implemented onwards.

Figure 3.9 reveals the trend of $RMSE_{XYZ}$ values and mean errors recorded in the different georeferencing cases in Pix4D Mapper and MicMac software. In this comparison, the BA processes are considered to be complemented by the positional information of the images.

The first graph of Figure 3.9 shows a decreasing step behaviour of the Pix4D Mapper software for less than 3 GCPs implemented, in contrast to MicMac where, from the first implementation onwards, RMSE values and mean errors are almost constant. The precariousness of georeferencing below 3 implemented GCPs is indeed reflected in the error values recorded in second graph of Figure 3.9 in the GCPs about the performance in Pix4D. In MicMac, on the other hand, the variability is negligible, showing uniform robustness in each georeferencing case even if with higher values than those obtained in Pix4D. The BA procedures in Pix4D, therefore, benefit from a higher number of 3 GCPs, giving accuracy values on CPs better than an average deviation of about 1.5 cm up to the extreme case of 19 GCPs where the results between the two software converge.



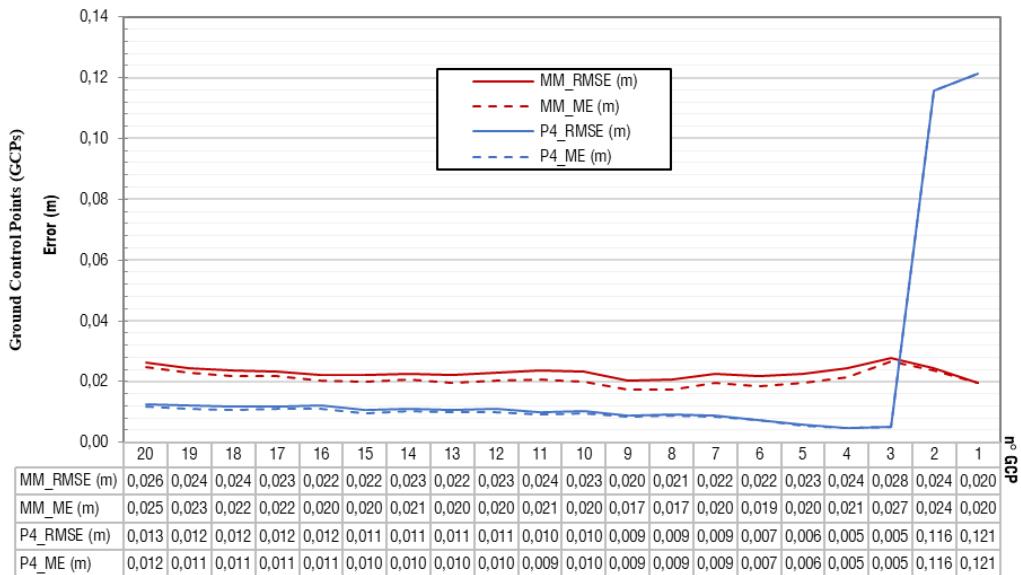


Figure 3.9. Comparison of RMSEXYZ and Mean Error (ME) values obtained on CPs and GCPs from MicMac (MM) and Pix4D Mapper (P4) processes

As can be seen in Figures 3.8-3.9 on the estimated values on the CPs, regardless of the assumptions made and the software used, the maximum accuracy limit reached of 0.02 m was inherited from the measurements on the implemented GCPs. More accurate results could only be obtained by adopting more accurate GNSS measurement modes, as seen in Section 3.1.

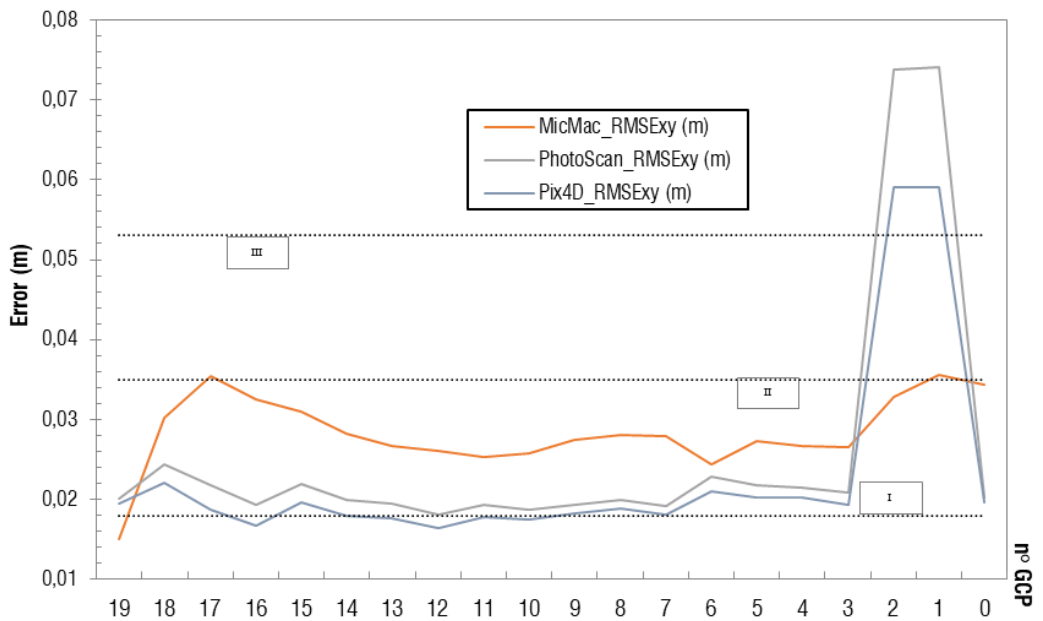
Lastly, the $RMSE_{XY}$ and $RMSE_Z$ values are evaluated in a unified analysis of the three software, comparing them with the thresholds set by the ASPRS standards.

The first graph of Figure 3.10 integrates the planar RMSE ($RMSE_{XY}$) values obtained in the three software and compares them with the thresholds set by ASPRS for digital planimetric data. The second one shows the comparison between the RMSE values along the Z-axis for each georeferencing case and the ASPRS standards for vertical data. In this comparison, the RMSE values obtained in MicMac by integrating the positional image information into the BA processes were considered.

The obtained results can be considered in line with those already discussed in previous works (Saponaro et al., 2019a, Saponaro et al., 2019c) and Section 3.4.1, where it was possible to see a consistent trend of RMSE values for DG and full IG cases,

especially regarding the elbow point of the statistical curve in a range of implemented GCPs equal to 5-7. On the other hand, observing the results obtained by Benassi et al. (Benassi et al., 2017), comparing the processes in the three software analysed within the scope of this study, as in Figure 3.10, MicMac offers a constancy of the planar RMSE values as the implemented GCPs vary, while, at the same time, Pix4D also shows a behaviour comparable to those obtained in Metashape even if considered better.

From a summary analysis of the generated examination, it is fundamental to see that the elaborations in the different software, being carried out according to a common workflow, generate results that are not congruent but, in most cases, consistent and comparable. In fact, as can be seen, both planar and vertical RMSE values assume comparable trends, maintaining, in most of the implemented georeferencing cases, the same class of accuracy provided by the ASPRS standards.



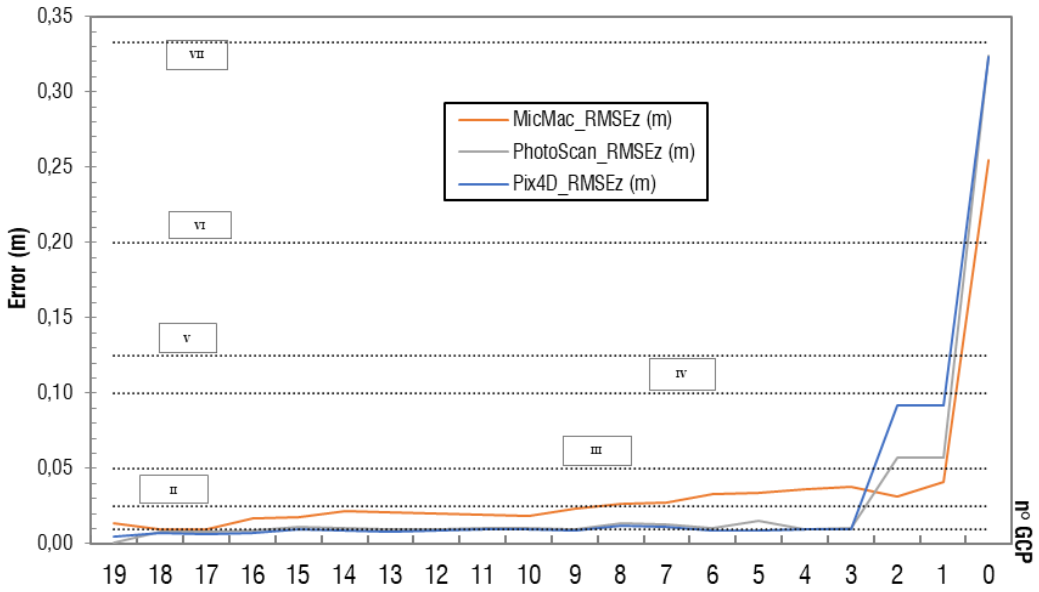


Figure 3.10. Assessment of the $RMSE_{xy}$ and $RMSE_z$ values obtained in the three software, as the GCPs implemented vary, with the threshold values published by ASPRS for Digital Planimetric Data and Vertical Data, respectively.

4. GEOMETRIC PRE-PROCESSING OF CAMERAS

Over the years, several approaches have been proposed to improve the accuracy of 3D models and the level of detail of the survey. The data processing techniques are continuously refined: in particular, the SfM-MVS algorithms are constantly updated to enhance the photogrammetric workflow. These algorithms are now enabled to automatically and simultaneously retrieve all unknown parameters of the camera poses and to interpret characteristic points in the images. Thus, in contrast to conventional aero-triangulation methods, SfM techniques retrieve an estimate of the IO and relative ExO of UAV images without a priori knowledge of the camera poses (Jiang et al., 2020, Schonberger and Frahm, 2016, Xu et al., 2016). The process of identifying the IO of each camera is technically referred to as geometric camera calibration.

In general, camera calibration can be performed with two strategies: it can be performed independently of aerial acquisitions with a pre-calibration or be included in the adjustment of the BA, referred to as self-calibration. Pre-calibration is often performed in the laboratory using converging images and varying the depth of the scene. (Lichti et al., 2002) indicated that laboratory camera calibration still presents problems in the context of aerial photogrammetry because the depth of the calibration scene and the acquisition setting do not change within the same scale. Self-calibration benefits precisely from the progress made in recent years in identifying and matching automated features. However, there is a risk that the distortion parameters derived in this way are dataset-specific and may not be applicable to other datasets.

On the other hand, all RS data need pre-processing before they can be used. In general, it is not suggested to use raw images directly acquired from sensors because the data need to be corrected geometrically, but also radiometrically and spectrally,

due to deformations caused by interactions between sensors, atmospheric conditions, and terrain profiles. For example, in optical data, the spectral signature of each material is unique in a laboratory measurement while the spectral signatures of field data are changeable due to material variation, environmental effects, surface contaminants, adjacency effects of nearby objects, seasonal changes, and so on. This can lead to the phenomenon that similar signatures might denote different objects, while different signatures might denote the same object.

Moreover, recent technological advances have made it possible to reduce the weight and size of the sensors, making them on the one hand suitable for small flight platforms such as UAVs, but on the other hand forcing the integrity and robustness of the optical-mechanical-digital components. The majority of manufacturers have put cheaper but not entirely profitable sensors on the market for metric work.

Only a few dedicated aerial camera systems for UAVs have been presented that meet the main criteria of conventional aerial mapping cameras (Kraft et al., 2016). Thus, the need for a new image processing environment for camera calibration equipped on UAVs has been highlighted (Lim et al., 2019).

Many scholars have focused on the factors that influence the final accuracy of UAV measurements. The flight height and the technical characteristics of the sensor (pixel size, focal length, sensor size, etc.) which together with the modelling of the IO of the sensor can strongly influence the final results (Cramer et al., 2017, Luhmann et al., 2016, Pérez et al., 2012).

The complexity of modelling can result in an over-parametrisation of the camera calibration environment and a deviation from the optimisation requirements of photogrammetric processes. For this reason, several aspects for the optimisation of the parameterisation during the BA phase are considered in the chapter, in particular the influence of the flight plan geometry. The necessary requirements during UAV missions are described by (Przybilla et al., 2015) as well as (Gerke and Przybilla, 2016). The remaining optical and mechanical inadequacies of the cameras, as well as user errors during operation, however, cannot be modelled in the evaluation process and may impose additional accuracy losses.

The estimation of calibration coefficients is essential to generate accurate measurements but, when using SfM, they show a strong geometric instability that depends on the low photogrammetric quality of the camera (Salvi et al., 2002). Much research has explored the impact of camera calibration parameters on the final results, but without attempting to model the existing relationships (Capolupo et al., 2020c). Reliable calibration is only possible with a proper image acquisition setup (Przybilla et al., 2015). Reliable calibration means that the camera parameters are determined to be physically correct, i.e., decoupled as best as possible from the remaining unknowns of the ExO parameters. This is particularly important when calibrations have to be transferred to other mission sites (Cramer et al., 2017).

This research chapter has been useful to fill existing gaps in this regard, firstly exploring the potential of camera self-calibration methodologies, how to optimise processes, and finally investigating simplified relationships between IO parameter estimates and accuracy predictive function modelling. Finally, a new approach, based on the combination of uni- and multivariate statistics, was drafted to predict the error components affecting the final 3D models.

As classical photogrammetry focuses on the precise geometric modelling of 3D objects, geometric calibration and stability are an important part of the process flow.

4.1. CAMERA CALIBRATION METHODOLOGIES

Camera calibration is an important process in photogrammetry. Calibration refers to the estimation of the corrections necessary to make the acquisitions, and consequently the subsequent extractable information, somewhat reproducible, repeatable, and consistent.

The corrections typically include radiometric and geometric corrections. A complete radiometric correction is related to the sensitivity of the remote sensor, the topography and angle of the sun, dispersion, and atmospheric absorption. In the next chapter, some useful procedures for the radiometric treatment of photogrammetric products will be analysed.

Geometric correction, on the other hand, aims to correct for the flattening, twisting, stretching, and displacement of RS image pixels relative to their actual position on the ground.

Geometric camera calibration plays an important role in photogrammetry, which determines the projection from 3D point coordinates to 2D image coordinates. Accurate camera calibration and rigorous orientation procedures, in fact, are necessary for the extraction of accurate and reliable 3D metric information from images (Remondino and Fraser, 2006). For this reason, camera calibration and the evaluation of high-quality IO parameters have been a major topic in photogrammetry research and development for decades (Remondino and Fraser, 2006). Many camera calibration techniques have been developed in recent years.

In traditional photogrammetry, cameras are rigorously calibrated in the laboratory. Calibration parameters are determined by analysing photos captured on accurately measured targets located at certain calibration sites.

According to the literature (Cramer et al., 2017, Han et al., 2016, Remondino and Fraser, 2006, Zhou et al., 2020), in digital photogrammetry, however, camera calibration can be achieved using different strategies:

- Calibration is performed using a gridded panel, usually with black and white checkerboard patterns, with well-known coordinates or distances. The procedure follows the classical rules of close-range photogrammetry: first, the panel images have to be collected from different positions, after that the checkerboard has to cover the whole sensor format and, finally, an adequate transverse and longitudinal overlap between sequential images have to be guaranteed (Cramer et al., 2017, Salvi et al., 2002). An appropriate acquisition geometry is important to avoid unwanted correlations between parameters. After image collection, semi-automatic or automatic procedures are used to detect model angles. Generally, this method is used when the camera has to be calibrated separately from the 3D reconstruction of the object. In these cases, the mechanical stability of the camera itself directly determines the validity of the calculated parameters and, consequently, wear and tear over time

of the components may lead to inevitable changes in the estimated parameters.

- Calibration in a high-precision 3D calibration field, i.e., using a series of images of the survey object but following the laboratory rules, described in the previous point. Appropriate 3D grid structures are often used on which the control points are placed.
- Self-calibration simultaneously returns both the calibration parameters and the reconstruction of the model using the images. Self-calibration is performed in the field directly using the images in which the GCP projections are present. In this case, the object itself replaces the calibration panel. An expected shortcoming is that recognising targets together with their coordinates could be ambiguous because these targets would not have the same shape and could encounter blurring due to remote observation. The convenience of using this approach is that the IO parameters are determined simultaneously with the object survey. All the observations on the images, collected with different perspectives, and the redundancy of the GCPs contribute to the estimation of the unknown parameters.

Laboratory self-calibration uses photos of targets in close proximity which may result in better target recognition and is expected to cover the defects expected in situ self-calibration. However, laboratory self-calibration has the problem that the shooting distance (or acquisition) is limited by the size of the targets displayed on the digital panels and targets are acquired nearby, unlike conventional laboratory calibration. Small calibration errors estimated in a close model may not be critical in close-range photogrammetry (Han et al., 2016).

In a non-rigorous approach, however, calibration is based on SfM algorithms alone and feature extraction using tie-points. It is worth noting that the focal length cannot be estimated in this case, like all metric information in the 3D model. An alternative, however, is to equip the aircraft with a GNSS receiver capable of transferring the metric information to the camera calibration phase.

Clearly, self-calibration is popular because it does not depend on strict calibration benchmarks. It only uses the relationships between targets in images taken in different locations and unstructured. Camera self-calibration has been widely implemented by modern SfM solutions.

It is therefore evident that in UAV photogrammetry the IO of the camera system, its stability during image acquisition and flight, as well as its calibration options and consideration in BA, are limiting factors for the level of accuracy of the processing chain. In general, consumer cameras provide automatic zoom, image stabilisation and limited options in manual modes. These problems lead to a lower accuracy potential due to the lack of stability and long-term validity of the IO parameters. In addition to the use of hardware components that limit the accuracy, the application of different software packages for UAV photogrammetry could significantly influence processing results. In addition, UAV images are highly influenced by dynamics during flight and cause unstructured image blocks and subsequent processing difficulties. On the contrary, a self-calibration can be considered versatile and flexible to the different acquisition conditions that arise.

On the other hand, the camera instability to be expected when using consumer cameras causes a loss of accuracy of at least 200%. If self-calibration is used with UAV flights one should be aware of the quality and significance of parameter estimation. A pre-calibration should be introduced if possible (Hastedt and Luhmann, 2015). The consideration of pre-calibrated fixed IO parameters is therefore possible. However, this usually does not guarantee consistency with standard processing within the UAV software, which does however give the possibility to apply or not necessarily self-calibration corrections for the final camera parameters.

There are three types of errors that can be distinguished and used to characterise the behaviour of instruments such as UAV cameras, namely random errors, systematic errors, and errors (Pfeifer et al., 2013).

Random errors are independent of each other. When the random error optimisation technique is applied, the camera parameters can be estimated and the errors between the measurement and the scene model can be minimised. Accuracy is improved by

increasing the number of measurements both spatially and temporally in the mediation process. However, the averaging step does not necessarily lead to more accurate values, mainly due to the existence of systematic errors.

A systematic error may remain constant during the repetition of an experiment or may vary slowly, for example, due to the temperature of the physical component. However, these errors can also be modelled. Systematic errors can be calibrated or reduced by following special data acquisition procedures (Chow and Lichti, 2013). In (Yusoff et al., 2017), a list of such errors related to camera operation, or errors related to scene structure, is proposed. Finally, coarse error, or also called blunder error, is defined as errors that are not part of the measurement process at all (Yusoff et al., 2017).

4.2. CAMERA LENS MODELS

In summary, geometric calibration is a process that relates the world's coordinate points to their corresponding image positions (Cramer et al., 2017). This means knowing the internal geometry of the camera from which the estimation of IO parameters can be discerned.

The geometry cannot be assumed to be unique and not even constant over time. A variety of cameras can be used in UAV-based scenarios, the majority of which are included in the so-called consumer segment: compact cameras, mirrorless systems and/or bridge cameras (Digital Single Lens Mirrorless) as well as the classic Digital Single Lens Reflex (DSLR) cameras. These are common to the general (mass) photographer market where stable and reproducible camera geometry is not the primary goal in development (Przybilla et al., 2019). It becomes necessary to consider the geometries of these lenses and to structure a tool that can control the accuracy of the estimates.

As seen in the previous section, software tools based on SfM algorithms can be used to perform the calibration. Most of them use planar configuration models and these toolboxes contain different algorithms for the camera frame, spherical, cylindrical, or

fish-eye lens model. Several papers in the literature however state how the use in photogrammetry of non-frame lenses, can abuse the camera calibration algorithms by adding complexity in estimating the correct parameters (Hastedt et al., 2016).

An ideal lens would represent straight lines present in the examined scene as straight lines also in the image. However, most lenses are subject to imperfections that cause straight lines to be represented as curves in the image. Such distortions are dominated by radial effects, which increase with distance from the centre of the lens and are therefore greater in the corners of the image. Lenses with short focal lengths tend to exhibit barrel distortion, which is due to the fact that magnification is greater at the centre than at the edges of an image, resulting in straight lines being bent towards the edges of the image.

Pincushion distortion is the opposite of barrel distortion and is typical of telephoto lenses (very long focal lengths). Magnification increases at the outer edges of an image, which creates a curvature of the lines and an apparent expansion of the features away from the optical axis.

The description of the lens geometry will necessarily have to be modelled in order to generate a mathematical simulation of their behaviour. Over the years, various alternatives have been proposed in the scientific literature and (Luhmann et al., 2016) propose a discussion of them. For the purposes of this paper, a detailed discussion is not essential.

The functional model in photogrammetric reconstruction is based on the central projection model, respectively. Often the same functional description is applied for IO, based on (Duane, 1971). In general, while the photogrammetric approach is structured on nonlinear inverse modelling in 3D space (Luhmann et al., 2016), Planar calibration models, as defined in the previous section, implement a two-step method based on linear descriptions according to (Zhang, 2000) and subsequent nonlinear adjustments.

Schematically, camera parameters commonly discovered through calibration procedures include the calculated principal distance or focal length (f) of the lens, parameters (x_p, y_p) denoting the coordinates of the centre of image projection (principal

point), and the lens distortion coefficients ($k_1, k_2, k_3, k_4, p_1, p_2, p_3, p_4$) where the k_i terms represent the radial lens distortion coefficients and the p_i terms represent the decentred distortion coefficients caused by a lack of centration of the lens elements. Radial and decentration distortions include aberrations that affect image position (Pérez et al., 2012).

As seen in sections 2.4 and 2.5, most photogrammetric software provides the 10 parameters of Brown's model (Capolupo et al., 2020c, Duane, 1971, Eltner and Sofia, 2020) (Equations 5.1-5.2), or possibly the relationships between the parameters of different lens models are provided in order to use conversions.

$$\Delta x = -\frac{\Delta f}{c} + \bar{x}r^2 K_1 + \bar{x}r^4 K_2 + \bar{x}r^6 K_3 + \bar{x}r^8 K_4 + [(2\bar{x}^2 + r^2)P_1 + 2P_2\bar{x}\bar{y}](1 + P_3r^2 + P_4r^4) + B_1\bar{x} + B_2\bar{y} \quad (4.1)$$

$$\Delta y = -\frac{\Delta f}{c} + \bar{y}r^2 K_1 + \bar{y}r^4 K_2 + \bar{y}r^6 K_3 + \bar{y}r^8 K_4 + [2P_1\bar{x}\bar{y} + (2\bar{y}^2 + r^2)P_2](1 + P_3r^2 + P_4r^4) \quad (4.2)$$

where f is the focal length, Δx and Δy are the image corrections, Δf is the correction to the initial value of the principal distance, \bar{x} and \bar{y} are the coordinates of a general point, K_i are the radial distortion coefficients, P_i are the tangential distortion coefficients, B_i are the in-plane correction parameters for differential scaling between horizontal and vertical pixel spacing and non-orthogonality (axial skew) between x and y axes, r is the radial image distance estimated using Equation 4.3:

$$r^2 = \bar{x}^2 + \bar{y}^2 = (x - x_p)^2 + (y - y_p)^2 \quad (4.3)$$

where x_p and y_p are the coordinates of the principal point.

Usually, the internal camera parameters are set constants for all images in a photogrammetric project. The distortion parameters are defined with respect to the principal point.

4.3. INFLUENCE OF UAV FLIGHT PLANNING ON CAMERA CALIBRATION

Although there has been substantial consideration of UAV performance and image processing approaches, sensor specifications, and optimal image acquisition parameters have been less widely discussed.

Primarily, sharpness and exposure have a direct impact on the usefulness of the data collected, and camera settings, optimal or otherwise, are underestimated within the literature (Lucieer et al., 2014). GSD is often the only metric reported even in the professional field (D'Oleire-Oltmanns et al., 2012).

Flight mission planning should include a rational examination of the imaging configuration (pixel size, focal length, sensor size, and flight height) and exposure settings (ISO, aperture, shutter speed, focus, and flight speed) due to their impact on image sharpness and GSD (O'Connor et al., 2017). Indeed, as demonstrated in (Saponaro et al., 2019a), this information is crucial to ascertain the quality of the input image data which, fundamentally, represents the basic raw data, and can have an impact on the effectiveness of the derived outputs.

To be precise, (O'Connor et al., 2017) review the principles behind digital image capture and consider their influence on the necessary camera characteristics and capture settings to ensure sharp, well-exposed images.

Towards capture a digital image, light reflected or emitted from a scene is collected by a sensor and converted into electrical signals that are measured and stored. The area captured, referred to as the IFOV, is a function of the focal length f of the camera lens and the size of the sensor onto which the image is projected. The point of convergence of these light rays is where the sharpest view is formed. The sharpness of the image is influenced by both the aperture and the focus of the lens. In an idealised system, a perfectly sharp image is produced when the lens is positioned so that the light from the object being imaged is focused on the sensor - that is, the light rays from a point source intersect exactly in the plane of the sensor. In real systems, lens imperfections prevent the rays from intersecting perfectly on the sensor, resulting in convergence in a small region known as the "circle of confusion". Nevertheless, as long as the circle of confusion is not appreciably large, the entity seems to be in focus. For photogrammetric purposes and consistent estimation of IO parameters across the entire dataset, it is, therefore, advisable to set a narrow focal aperture and constant focus ideally at infinity, removing any auto-focus options that would differentiate the parameters for each shot.

As an output, cameras typically produce a RAW image file, which contains all the digital data read from the sensor. In addition, the camera produces a processed version of the RAW file that is saved in the 8-bit Tagged Image File Format (TIFF) and/or Joint Photographic Experts Group (JPEG) file format. JPEG files are much smaller than their RAW equivalents due to the data compression applied during processing. TIFF files are a good compromise as they safeguard the integrity of the data. (Cramer et al., 2017) recommends the use of uncompressed raw images: in fact, the JPG format is designed to be pre-configured at the factory and does not record actual image errors, in addition to compression effects.

The issue that is not sufficiently addressed by many users are the special requirements on the geometry underneath the photogrammetric block when auto-calibration is chosen from the dataset itself.

As has been described above, in laboratory calibration scenarios, special configurations and camera tilt are implemented to achieve these decoupled parameters, which is not possible in real flight scenarios. However, since the angles of the nadir in UAV applications tend to become larger than in classical in-flight photogrammetric imaging, this already supports block geometry and calibration. Camera calibration with in-situ or purely self-calibration methods are sufficient but only work if the block has sufficiently good geometry.

All photogrammetric blocks consisting of parallel flight lines or 360° circular image blocks with a large image overlap should meet the prerequisites. According to (Cramer et al., 2017), the combination of two nadir blocks in a cross-flight configuration, with slightly different flight heights, provides the best results. An additional oblique block added does not significantly affect the accuracy. This is contrary to expectations but could be expected if the different blocks are not connected correctly through the tie point correspondences. Due to the use of convergent images, however, the correlation between IO parameters could be minimised. Oblique image flights facilitate camera calibration due to the greater depth of the images. Secondly, the focal length is likely to vary during acquisitions due to the temperature variation of the camera. When this variation is not taken into account and camera calibration is pro-

vided for the entire dataset, a major degradation of accuracy can occur, mainly in altimetry. When only nadir images are present, a 1-pixel variation in focal length can reduce 3D accuracy by 1 cm. The inclusion of oblique images brings a significant improvement, which is a good solution to the problem. (Meinen and Robinson, 2020) additionally recommends performing oblique flights before nadir flights.

Perhaps it is useful not to start the in-situ calibration from zero values, but to use the previous calibration as an approximation. Especially the distortion of the camera system can change little. Should the case occur in a non-conventional block geometry, an optimal pre-calibration of the camera is necessary. Ideally, the camera should be calibrated in a temporal and spatial context close to the mission area (i.e., using a test area) and these parameters can then be adopted. However, the camera pre-calibration performed in a close-up scenario may be inaccurate for aerial scenarios due to the different depths of the scene (Sanz-Ablanedo et al., 2020).

If the area of interest should be very flat, the estimation of the main distance may be inaccurate due to the high correlation of the Z-component and the focal length in the viewing geometry at the nadir. The literature suggests that so-called cross-flight patterns and different flight heights could make the self-calibration process more reliable (Flores-de-Santiago et al., 2020, Gerke and Przybilla, 2016). The different flight directions contribute to a more accurate estimate of the principal point.

The self-calibration of the camera improves and/or residual errors are better compensated through ExO, respectively, when more GCPs are provided. Although the applied software does not provide statistical measurements on the adjusted unknowns, it is likely that the external and IO parameters are highly correlated. Hence, it is tricky to operate self-calibration if the landscape is not undulating or if cross-flights at different altitudes are not feasible. The absolute accuracy of block orientation can be significantly improved by using the onboard RTK solution.

For example, block deformation, defined as a central dome (Sanz-Ablanedo et al., 2020), is a typical problem with UAV image blocks, especially when the block is not supported by well-distributed GCPs. According to (James and Robson, 2014), these errors can be significantly reduced by acquiring convergent images, or by the inclu-

sion of uniformly distributed GCPs. The use of oblique perspectives, although more challenging to perform, has been proven to be an efficient way of mitigating systematic errors (Zhou et al., 2020). The integration of RTK-based image positional observations into the UAV processing workflow has also been found to have a strong positive impact, particularly on the height component (Gerke and Przybilla, 2016).

Finally, the damper effect is a common problem when performing aerial acquisitions with consumer-grade UAV platforms. With multiple flight configurations (oblique images, nadir images at multiple heights), the degradation induced by the rotational motion of the camera can be significantly reduced. Mounting the camera on a stabiliser is also a good practice to minimise the influence of camera shake. The translational movement of the camera affects the final accuracy in a more complicated way. Some commercial software offers solutions to correct this impact by estimating the camera movement when adjusting the BA (Zhou et al., 2020, Eltner and Sofia, 2020). Performing the acquisition in stop-and-go mode may be an easier way to overcome the impact of the shutter effect.

In summary, it is recommended to perform camera recalibration when good flight geometry is available, and it is always advantageous to diversify the flight geometry.

For a given camera calibration, the focal length error can be corrected during BA with a good acquisition configuration. When an incorrect focal length is given and not recalculated during BA, the camera heights will deviate from the theoretical values to compensate for the incorrect focal length.

4.4. CAMERA CALIBRATION OVER-PARAMETRISATION ISSUE

Deciding which parameters should be considered during BA, and with which weights, is essential for robust model reconstruction from overlapping images. (James et al., 2017a) have shown that estimating too many camera model parameters during BA can lead to over-parameterization and thus errors in the final model. For example, in many applications, two radial distortion parameters are sufficient even though more values could be implemented. (Remondino et al., 2012) previously dis-

cussed the importance of choosing the correct number of parameters. They observed some effects for SfM software tools that estimated the internal camera geometry for each image and suggested using only one internal camera model if one camera was used to capture images. Similar conclusions were also supported by (Rosnell and Honkavaara, 2012). A potential approach to control overparameterization is to consult the correlation values between the estimated camera parameters: they should be low. In addition, the significance of each estimated parameter can be consulted to check for over-fitting (James et al., 2017b).

Modelling the camera with variable image parameters causes three more parameters per image to be estimated within the BA. Thus, the number of unknowns grows to nine per image. These parameters describe the variation of the main distance and the displacement of the main point.

According to (Przybilla et al., 2020) the full 13-parameter set of Brown's model should be routinely applied. In truth, the 10-parameter model, as expressed in Equations (4.1-4.3), is adopted by default in most work when using the fully automatic camera calibration procedure. Although practically, it might appear as the best and most convenient choice, from the accuracy point of view, in many cases, it does not represent the optimal solution, due to the different role and meaning of those parameters within the BA numerical solution (James et al., 2017a). In (Capolupo et al., 2020c), a high correlation was found between the coefficients P_i and the coordinates of the principal points. Thus, once removing P_i from the unknowns, x_p and y_p in some way can absorb its correlated variation. In other words, users do not get an exhaustive overview of the geometry and the errors embedded in each parameter.

A prior analysis was carried out to understand any correlations that may exist between the IO parameters, looking for ways to minimise them. Based on the IO parameter estimates and cross-validation tests, the Pearson's Coefficient (R) was calculated separately for each dataset to test the correlation between the IO parameters. The R coefficient was interpreted according to (Fryer, 1996, Medjkane et al., 2018): $R > 0.7$ means strong correlation; $0.5 < R < 0.7$ means moderate correlation; $R < 0.5$

means weak correlation. A statistical analysis (handled by R, (Chambers, 2008)) was then performed to analyse the error components and identify any outliers.

Subsequently, an attempt was made to model statistically significant relationships by structuring a Principal Component Analysis (PCA) between IO estimates and measurement errors. This allows for a judicious and reduced parameterisation of the lens model, consisting of parameters that tend to be uncorrelated. Finally, a potentially useful methodology for predicting final errors was developed, once the IOs are known.

4.4.1 Preliminary Correlation Analysis

Five flights were scheduled and performed in December 2018, January 2019, February 2019, March 2019, and October 2019, respectively (Table 4.1). The stretch of coastline discussed in section 3.4.1 located in Bari (Apulia Region) was selected as the pilot site. Considering the same 30 points measured with GNSS, a cross-validation was performed in a progressive mode.

Table 4.1. Photogrammetric datasets acquired during the five UAV campaigns and related GSD values.

Acquisition date	#N Images	GSD (m/pix)
December 12th, 2018	77	0.041
January 8th, 2019	77	0.047
February 19th, 2019	77	0.048
March 16th, 2019	77	0.041
October 16th, 2019	77	0.042

Following the processing framework discussed in Chapter 2, the sub-datasets, for each month of acquisition, were processed. In particular, the BA algorithms were started for each structured geo-referencing setting, which, at the same time, define the camera calibration estimates. The results of these were collected and analysed as follows.

IO parameters are independent of the spatial orientation of the image and, consequently, do not depend on the position and attitude of the camera (Gruen and Beyer, 2001). Table 4.2 shows the main statistics calculated for all estimated IO parameters concerning all processed datasets. These parameters can be clustered into two

groups: one including x_p , y_p , B1, B2, P3 and P4 is distinguished by a large variability; another one, involving the remaining parameters, shows quite similar values for all computed metrics. Since all tests generated similar estimates of the radial and tangential distortion parameters, these can be considered strictly camera-dependent without any influence from other factors. Furthermore, Pi coefficients are known to be less significant than radial coefficients (one or two orders of magnitude smaller (Smith and Heidemann, 2015)). The boxplots in Figures 5.2-5.6 confirm this fact.

Table 4.2. Statistics of I.O. parameter evaluations calculated with respect to the 31 replications for the 5 processed datasets (December 2018, January 2019, February 2019, March 2019, October 2019); Stat—statistic; Max—maximum; Min—minimum; SD—standard deviation; f—focal length; x_p and y_p coordinates of principal point; B1; B2—skew coefficients; K1, K2, K3, K4 —radial distortion coefficients; P1, P2, P3, P4—decentering distortion coefficients.

Survey	Stat.	F (pix)	X_p (pix)	Y_p (pix)	B1	B2	K1	K2	K3	K4	P1	P2	P3	P4
Dec.	Max	2366.21	-0.19	6.85	2.72	0.16	-0.130	0.140	-0.030	0.014	0.0004	-0.0002	-0.0900	0.3100
	Min	2221.83	-3.20	3.48	-0.73	-0.96	-0.140	0.110	-0.050	0.008	-0.0004	-0.0008	-0.4900	0.1900
	Mean	2285.31	-2.31	4.88	0.80	-0.44	-0.140	0.120	-0.040	0.011	0.0003	-0.0005	-0.3700	0.2700
	SD	31.57	0.82	0.77	0.99	0.31	0.000	0.010	0.003	0.001	0.0002	0.0001	0.0800	0.0400
Jan.	Max	2358.48	-1.47	5.82	2.69	1.21	-0.130	0.140	-0.037	0.014	0.0007	-0.0003	-0.0018	0.3300
	Min	2262.76	-4.66	4.35	-0.03	-1.27	-0.140	0.120	-0.049	0.010	-0.0001	-0.0006	-0.5856	-0.030
	Mean	2319.96	-3.68	5.18	0.93	-0.54	-0.140	0.130	-0.043	0.012	0.0005	-0.0005	-0.4703	0.2700
	SD	18.79	0.93	0.34	0.85	0.53	0.000	0.000	0.002	0.001	0.0002	0.0001	0.1548	0.0900
Feb.	Max	2366.49	-1.59	4.45	3.25	0.01	-0.140	0.140	-0.040	0.010	0.0004	-0.0002	0.1900	0.3300
	Min	2310.47	-2.83	3.46	0.13	-1.16	-0.150	0.120	-0.050	0.010	-0.0001	-0.0004	-0.3900	-0.040
	Mean	2339.33	-2.19	3.78	1.15	-0.48	-0.140	0.130	-0.040	0.010	0.0003	-0.0003	-0.2500	0.2300
	SD	11.71	0.30	0.20	0.87	0.28	0.000	0.003	0.001	0.001	0.0001	0.0001	0.1550	0.0940
Mar.	Max	2320.640	2.730	7.040	2.040	1.300	-0.130	0.130	-0.040	0.010	0.0002	-0.0001	0.3600	0.5100
	Min	2267.75	-1.55	1.96	-2.69	-1.42	-0.140	0.120	-0.0400	0.010	-0.0007	-0.0006	-0.4800	0.0100
	Mean	2305.52	-0.07	3.29	0.45	-0.59	-0.140	0.130	-0.0400	0.010	0.0000	-0.0002	0.0300	0.3300
	SD	16.80	1.07	1.66	1.38	0.79	0.000	0.000	0.0016	0.001	0.0003	0.0001	0.2300	0.1700
Oct.	Max	2363.46	-0.49	4.76	1.68	0.18	-0.140	0.140	-0.0400	0.015	0.0003	-0.0003	-0.1860	0.2910
	Min	2275.08	-2.45	2.94	-1.22	-2.04	-0.160	0.120	-0.0500	0.011	-0.0003	-0.0007	-0.4720	0.1190
	Mean	2338.25	-1.65	3.79	0.22	-0.99	-0.140	0.134	-0.0470	0.014	0.0002	-0.0004	-0.3010	0.2260
	SD	26.29	0.53	0.52	0.75	0.57	0.000	0.006	0.0030	0.001	0.0002	0.0001	0.0830	0.0630

A further outline analysis come up from the coefficient of variation ($C_v = \text{standard deviation/average, } 100.0 \%$) of the IO parameter estimates. The results are shown in Figure 4.1. The focal length f and the K_i coefficients are the most balanced parameters. On the contrary, the coefficients x_p , y_p , B_i and P_i show a large irregularity depending on the operational conditions.

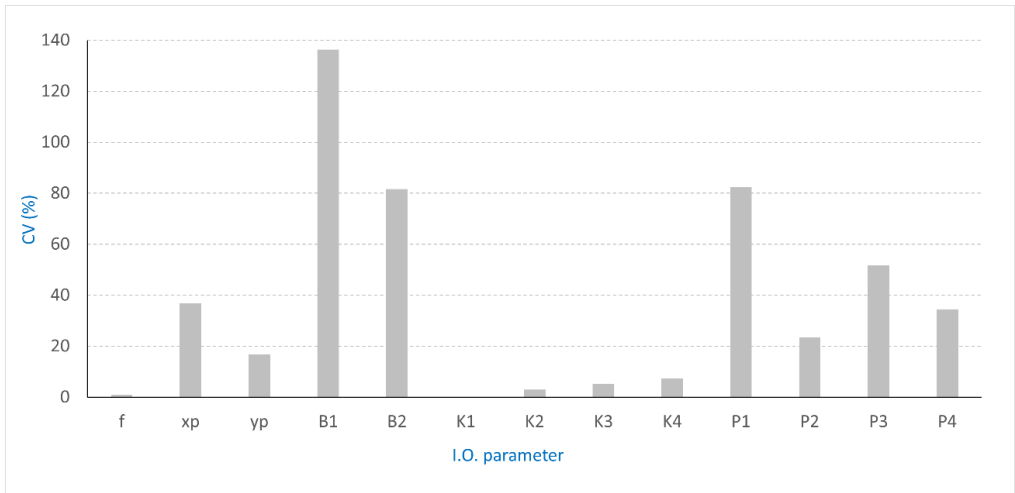


Figure 4.1. Coefficients of variation (C_v , %) computed for all IO parameters for all the processed datasets.

According to the boxplots in Figures 4.2-4.6, one can recognize a similar trend affecting all IO parameters. In particular, the October dataset (Figure 4.6) looks to contain no outliers for most of the parameters (f , K_1 - K_2 - K_3 - K_4 - P_3 - P_4). On the contrary, in the other datasets, no outliers were noticed for B_1 , P_1 , P_2 in the December dataset (Figure 4.2); y_p and x_p did not present outliers in the January and February datasets (Figures 4.3 and 4.4); f , P_4 and K_2 had no outliers in the March dataset (Figure 4.5).

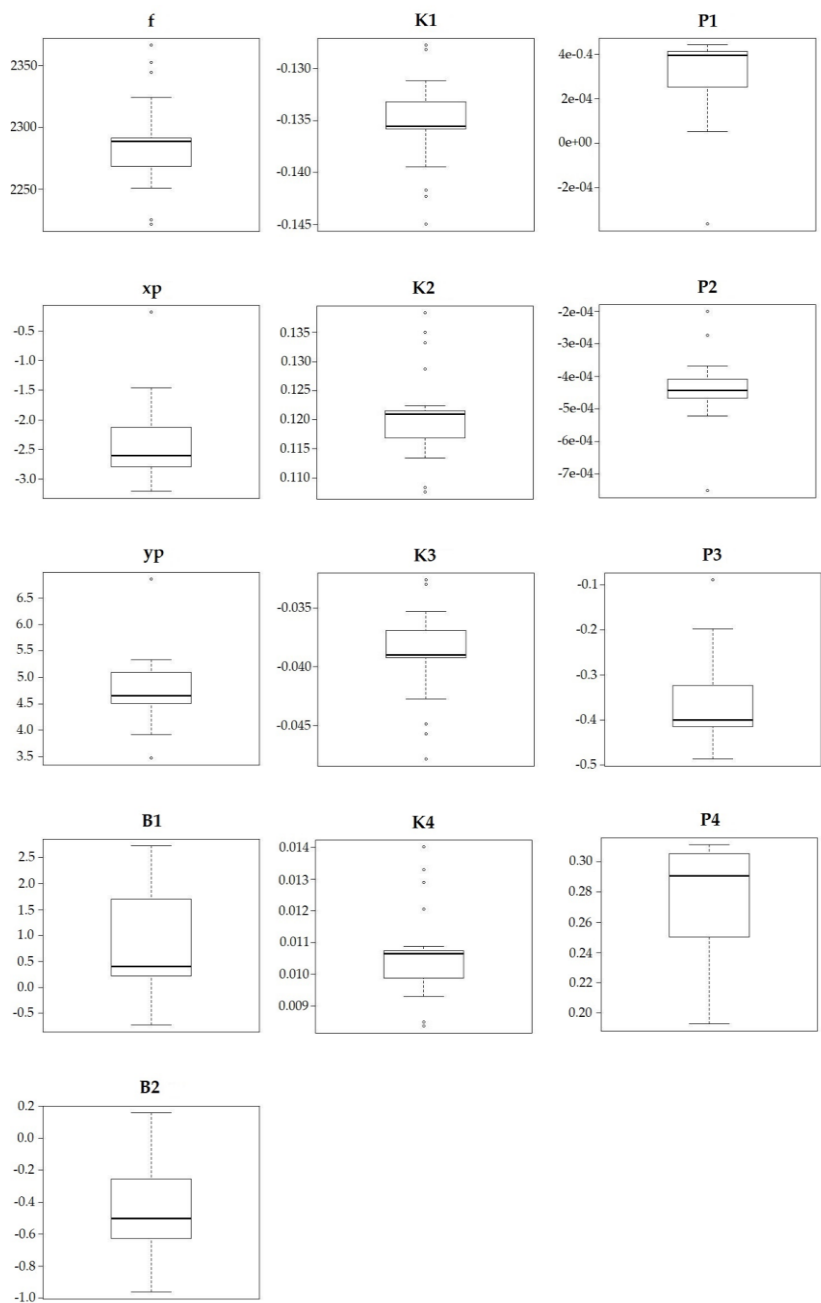


Figure 4.2. Boxplot of IO parameters from the December dataset. f —focal length; x_p and y_p coordinates of the principal point offset; $B1$, $B2$ —skew parameters; $K1$, $K2$, $K3$, $K4$ —radial distortions; $P1$, $P2$, $P3$, $P4$ —components of the decentering distortions.

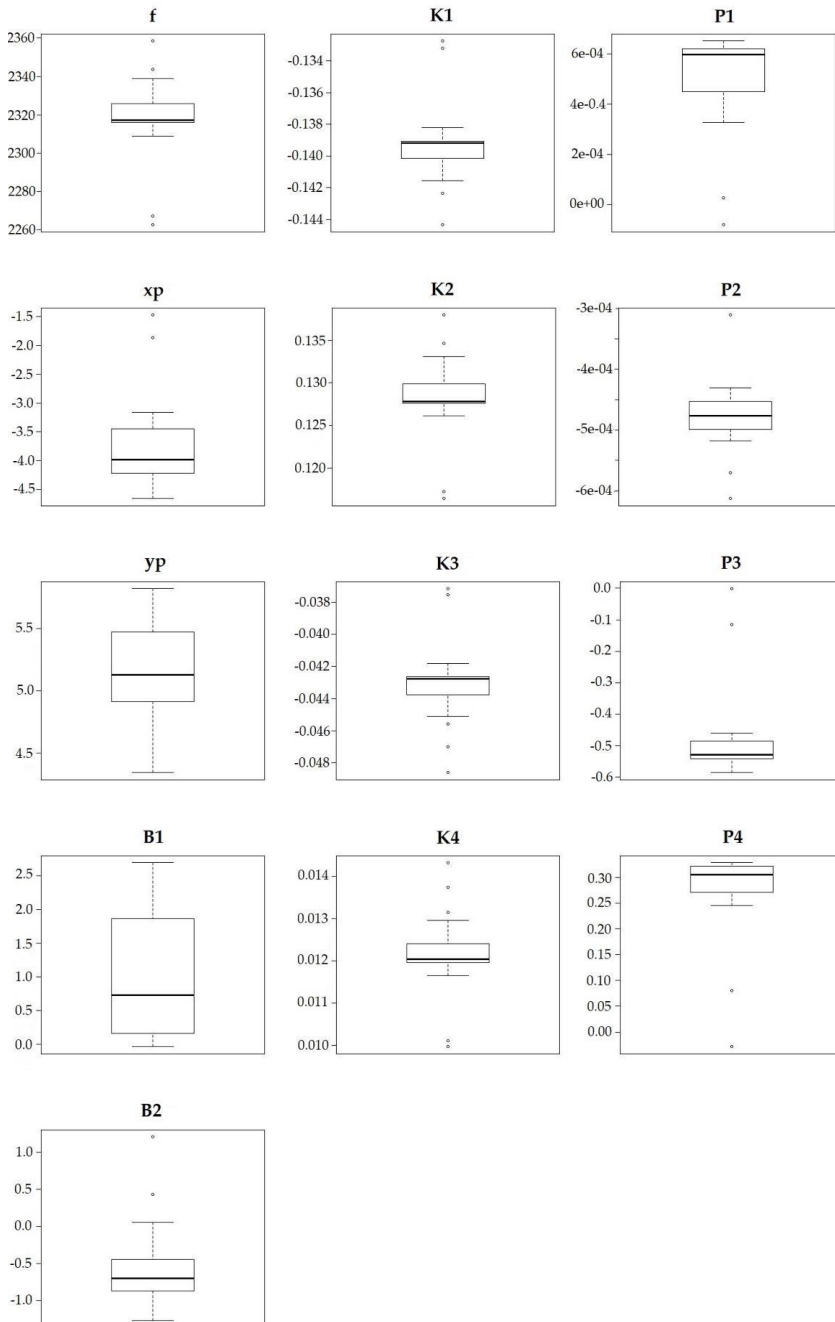


Figure 4.3. Boxplot of IO parameters from the January dataset. f —focal length; x_p and y_p coordinates of the principal point offset; B_1 , B_2 —skew parameters; K_1 , K_2 , K_3 , K_4 —radial distortions; P_1 , P_2 , P_3 , P_4 —components of the decentering distortions.

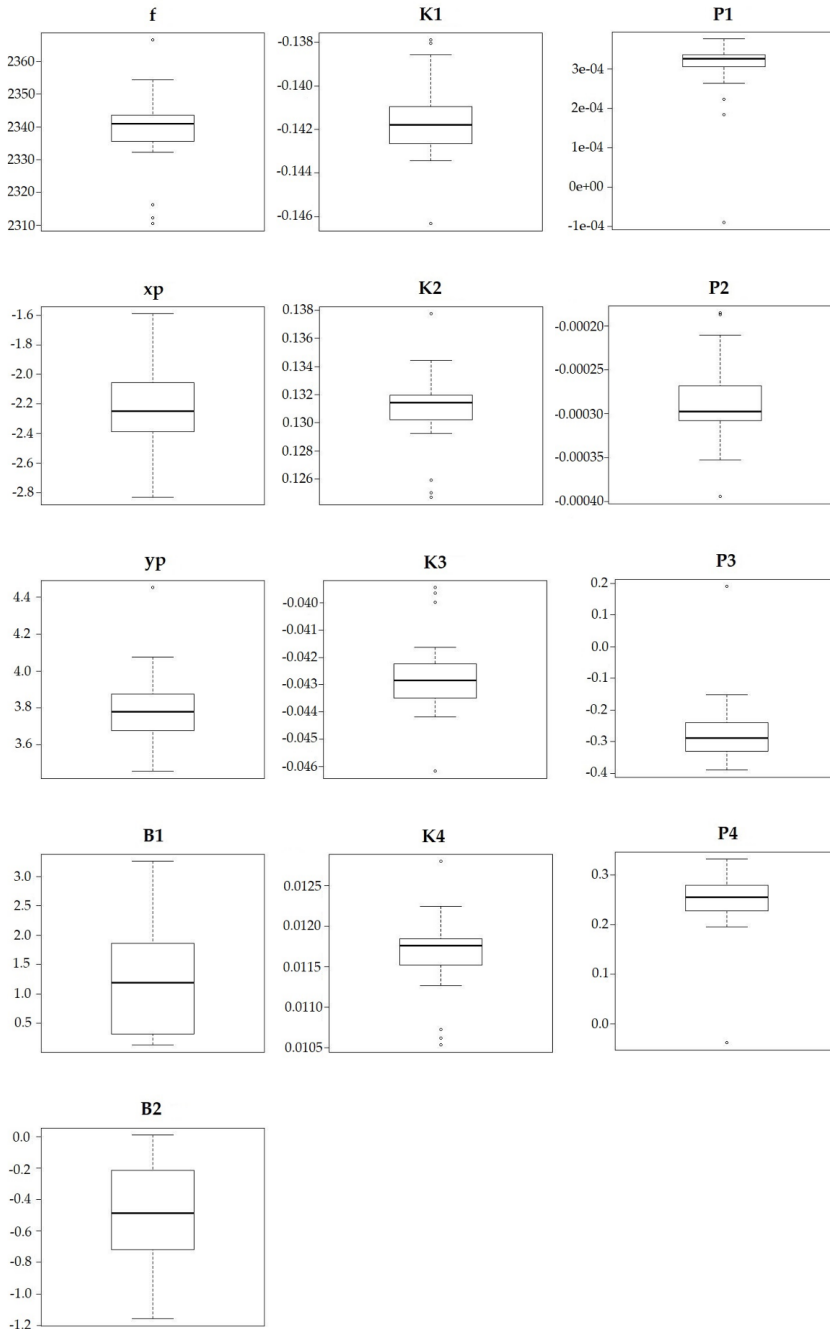


Figure 4.4. Boxplot of IO parameters from the February dataset. f —focal length; x_p and y_p coordinates of the principal point offset; B_1 , B_2 —skew parameters; K_1 , K_2 , K_3 , K_4 —radial distortions; P_1 , P_2 , P_3 , P_4 —components of the decentering distortions.

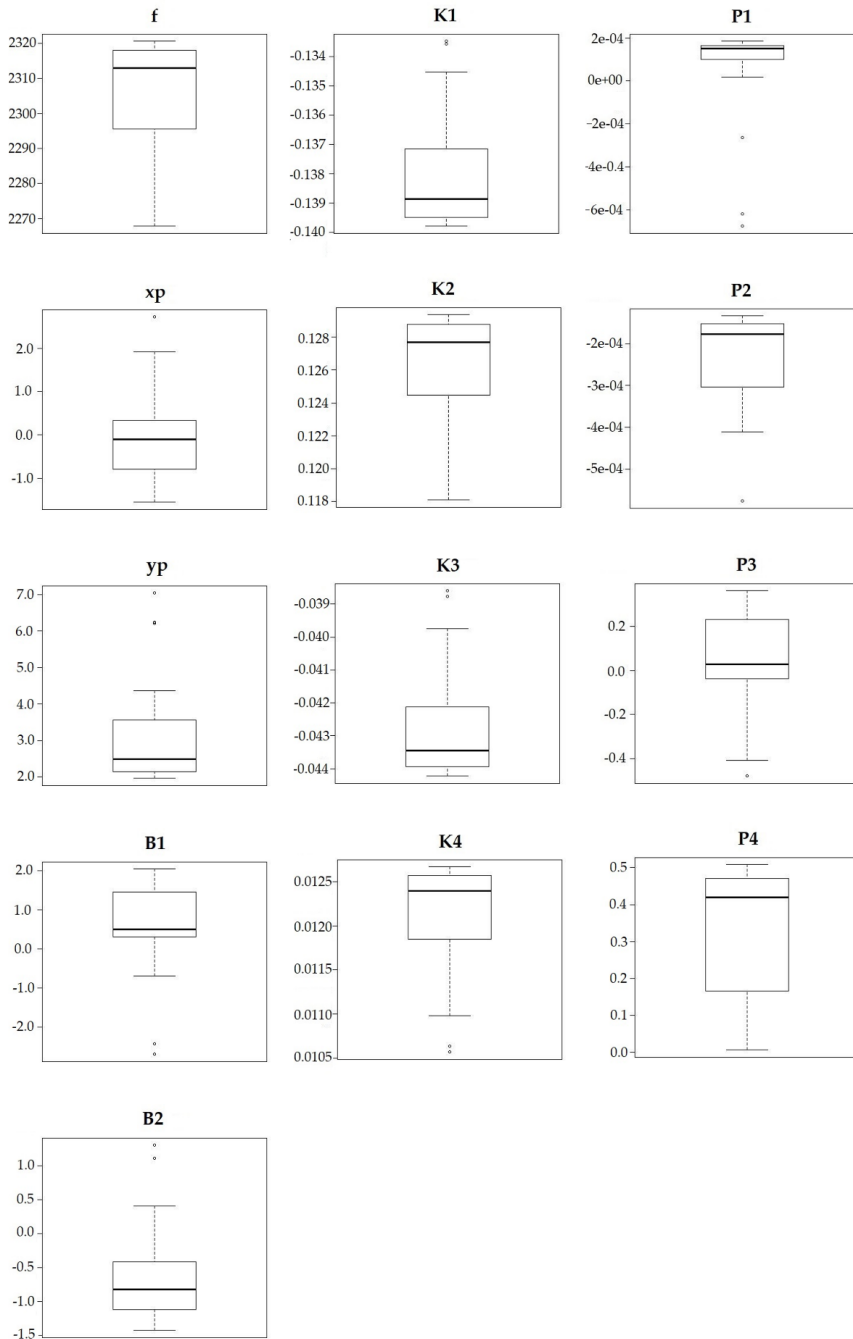


Figure 4.5. Boxplot of IO parameters from the March dataset. f —focal length; x_p and y_p coordinates of the principal point offset; B_1 , B_2 —skew parameters; K_1 , K_2 , K_3 , K_4 —radial distortions; P_1 , P_2 , P_3 , P_4 —components of the decentering distortions.

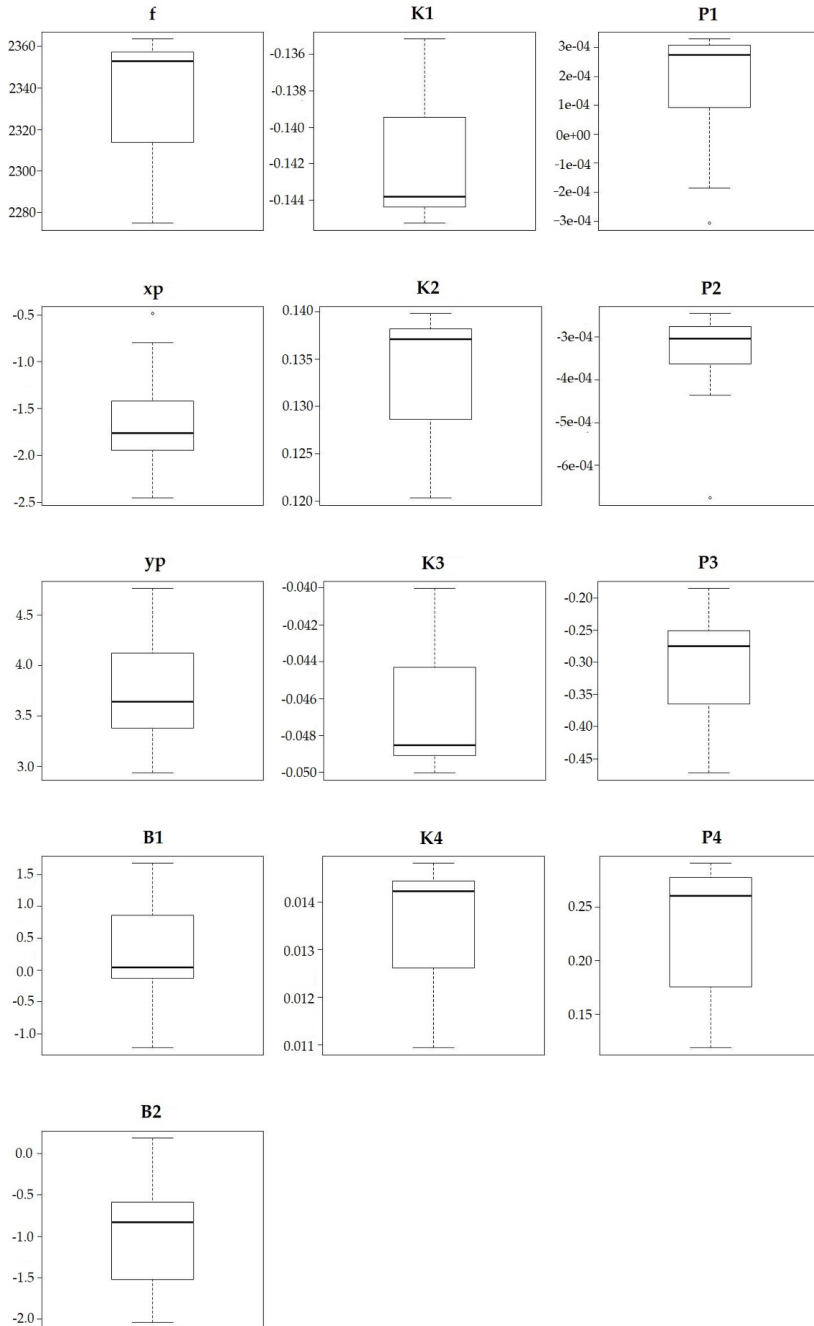


Figure 4.6. Boxplot of IO parameters from the October dataset. **f**—focal length; **xp** and **yp** coordinates of the principal point offset; **B1**, **B2**—skew parameters; **K1**, **K2**, **K3**, **K4**—radial distortions; **P1**, **P2**, **P3**, **P4**—components of the decentering distortions.

The relationships between the IO parameters were investigated by estimating correlation matrices for all datasets. The results are shown in Tables 4.3-4.7. The correlation matrix contains positive and negative values in the range $[-1, +1]$. Positive values mean that a direct relationship between the variables is present, while negative values indicate an inverse relationship. The higher the values, the stronger the correlation.

All data sets showed fairly similar values, which can be summarised as follows: the focal length was highly correlated with the coefficients of radial aberrations; xp was moderately correlated with yp and, in most cases, with Pi coefficients; yp was poorly/moderately correlated with all other parameters (March dataset excluded); skew parameters (B1, B2) were poorly/moderately correlated with the other parameters (March dataset excluded); Ki coefficients showed to be internally correlated with each other and externally with focal length; a moderate correlation was found between yp and P2. January and February showed a low correlation of Ki with yp and P2.

Table 4.3. Correlation matrix of camera IO parameters as estimated from the December 2018 dataset (f= focal length (pix); xp and yp coordinates of the principal point offset; B1, B2 = Skew parameters; K1, K2, K3, K4= radial distortions; P1, P2, P3, P4= components of the decentering distortions).

	f	xp	yp	B1	B2	K1	K2	K3	K4	P1	P2	P3	P4
f	1	-0.15	-0.56	0.10	0.03	-1.00	1.00	-1.00	0.99	0.27	0.51	0.37	0.44
xp	-0.15	1	0.51	-0.26	-0.04	0.12	-0.12	0.08	-0.07	-0.96	-0.58	0.43	-0.73
yp	-0.56	0.51	1	-0.49	0.29	0.54	-0.55	0.53	-0.53	-0.69	-0.91	-0.48	-0.43
B1	0.10	-0.26	-0.49	1	-0.59	-0.06	0.12	-0.08	0.10	0.35	0.20	0.44	-0.17
B2	0.03	-0.04	0.29	-0.59	1	-0.04	0.02	-0.04	0.03	-0.12	-0.02	-0.37	0.12
K1	-1.00	0.12	0.54	-0.06	-0.04	1	-1.00	1.00	-1.00	-0.23	-0.51	-0.38	-0.42
K2	1.00	-0.12	-0.55	0.12	0.02	-1.00	1	-1.00	1.00	0.24	0.50	0.40	0.41
K3	-1.00	0.08	0.53	-0.08	-0.04	1.00	-1.00	1	-1.00	-0.20	-0.49	-0.42	-0.38
K4	0.99	-0.07	-0.53	0.10	0.03	-1.00	1.00	-1.00	1	0.19	0.48	0.43	0.37
P1	0.27	-0.96	-0.69	0.35	-0.12	-0.23	0.24	-0.20	0.19	1	0.68	-0.26	0.78
P2	0.51	-0.58	-0.91	0.20	-0.02	-0.51	0.50	-0.49	0.48	0.68	1	0.31	0.49
P3	0.37	0.43	-0.48	0.44	-0.37	-0.38	0.40	-0.42	0.43	-0.26	0.31	1	-0.46
P4	0.44	-0.73	-0.43	-0.17	0.12	-0.42	0.41	-0.38	0.37	0.78	0.49	-0.46	1

Table 4.4. Correlation matrix of camera IO parameters as estimated from the January 2019 dataset (f= focal length (pix); xp and yp coordinates of the principal point offset (pix); B1, B2 = Skew parameters; K1, K2, K3, K4= radial distortions; P1, P2, P3, P4= components of the decentering distortions).

	f	xp	yp	B1	B2	K1	K2	K3	K4	P1	P2	P3	P4
f	1	0.51	-0.30	-0.27	0.59	-1.00	1.00	-0.99	0.98	-0.52	-0.17	0.55	-0.52
xp	0.51	1	-0.46	-0.02	0.72	-0.52	0.57	-0.63	0.65	-0.98	-0.36	0.95	-0.92
yp	-0.30	-0.46	1	0.43	-0.25	0.32	-0.30	0.32	-0.32	0.35	-0.37	-0.55	0.44
B1	-0.27	-0.02	0.43	1	-0.39	0.27	-0.25	0.29	-0.29	0.08	0.04	-0.24	0.18
B2	0.59	0.72	-0.25	-0.39	1	-0.60	0.64	-0.70	0.72	-0.81	-0.21	0.83	-0.87
K1	-1.00	-0.52	0.32	0.27	-0.60	1	-1.00	0.99	-0.98	0.54	0.15	-0.57	0.54
K2	1.00	0.57	-0.30	-0.25	0.64	-1.00	1	-0.99	0.99	-0.58	-0.19	0.60	-0.58
K3	-0.99	-0.63	0.32	0.29	-0.70	0.99	-0.99	1	-1.00	0.65	0.23	-0.67	0.65
K4	0.98	0.65	-0.32	-0.29	0.72	-0.98	0.99	-1.00	1	-0.67	-0.25	0.69	-0.67
P1	-0.52	-0.98	0.35	0.08	-0.81	0.54	-0.58	0.65	-0.67	1	0.43	-0.95	0.95
P2	-0.17	-0.36	-0.37	0.04	-0.21	0.15	-0.19	0.23	-0.25	0.43	1	-0.24	0.22
P3	0.55	0.95	-0.55	-0.24	0.83	-0.57	0.60	-0.67	0.69	-0.95	-0.24	1	-0.98
P4	-0.52	-0.92	0.44	0.18	-0.87	0.54	-0.58	0.65	-0.67	0.95	0.22	-0.98	1

Table 4.5. Correlation matrix of camera IO parameters as estimated from the February 2019 dataset (f= focal length (pix); xp and yp coordinates of the principal point offset (pix); B1, B2 = Skew parameters; K1, K2, K3, K4= radial distortions; P1, P2, P3, P4= components of the decentering distortions).

	f	xp	yp	B1	B2	K1	K2	K3	K4	P1	P2	P3	P4
f	1	0.008	0.18	0.16	-0.16	-0.88	0.99	-0.93	0.97	0.14	-0.15	-0.12	0.19
xp	0.01	1	-0.51	0.18	-0.34	-0.35	0.12	-0.27	0.20	-0.77	0.26	0.74	-0.56
yp	0.18	-0.51	1	0.48	0.08	-0.09	0.18	-0.14	0.18	0.18	-0.40	-0.33	0.19
B1	0.16	0.18	0.48	1	-0.32	-0.14	0.20	-0.16	0.19	-0.04	0.16	-0.17	0.22
B2	-0.16	-0.34	0.08	-0.32	1	0.15	-0.18	0.18	-0.20	0.05	-0.01	-0.01	-0.03
K1	-0.88	-0.35	-0.09	-0.14	0.15	1	-0.93	0.99	-0.95	0.27	0.09	-0.27	0.17
K2	0.99	0.12	0.18	0.20	-0.18	-0.93	1	-0.97	0.99	0.01	-0.14	-0.01	0.08
K3	-0.93	-0.27	-0.14	-0.16	0.18	0.99	-0.97	1	-0.99	0.19	0.14	-0.18	0.10

K4	0.97	0.20	0.18	0.19	-0.20	-0.95	0.99	-0.99	1	-0.09	-0.16	0.08	-0.01
P1	0.14	-0.77	0.18	-0.04	0.05	0.27	0.01	0.19	-0.09	1	0.11	-0.94	0.90
P2	-0.15	0.26	-0.40	0.16	-0.01	0.09	-0.14	0.14	-0.16	0.11	1	-0.27	0.43
P3	-0.12	0.74	-0.33	-0.17	-0.01	-0.27	-0.01	-0.18	0.08	-0.94	-0.27	1	-0.97
P4	0.19	-0.56	0.19	0.22	-0.03	0.17	0.08	0.10	-0.01	0.90	0.43	-0.97	1

Table 4.6. Correlation matrix of camera IO parameters as estimated from the March 2019 dataset (f= focal length (pix); xp and yp coordinates of the principal point offset (pix); B1, B2 = Skew parameters; K1, K2, K3, K4= radial distortions; P1, P2, P3, P4= components of the decentering distortions).

	f	xp	yp	B1	B2	K1	K2	K3	K4	P1	P2	P3	P4
f	1	0.04	-0.70	0.13	-0.40	-0.95	1.00	-0.94	0.96	0.53	0.77	0.66	0.78
xp	0.04	1	0.49	-0.94	0.76	-0.31	0.10	-0.32	0.28	-0.73	-0.30	-0.38	0.06
yp	-0.70	0.49	1	-0.66	0.85	0.46	-0.64	0.43	-0.47	-0.94	-0.93	-0.93	-0.81
B1	0.13	-0.94	-0.66	1	-0.90	0.16	0.06	0.18	-0.13	0.85	0.50	0.58	0.12
B2	-0.40	0.76	0.85	-0.90	1	0.14	-0.34	0.10	-0.14	-0.91	-0.70	-0.78	-0.45
K1	-0.95	-0.31	0.46	0.16	0.14	1	-0.97	1.00	-0.99	-0.25	-0.60	-0.45	-0.69
K2	1.00	0.10	-0.64	0.06	-0.34	-0.97	1	-0.97	0.98	0.46	0.73	0.61	0.75
K3	-0.94	-0.32	0.43	0.18	0.10	1.00	-0.97	1	-1.00	-0.22	-0.57	-0.42	-0.65
K4	0.96	0.28	-0.47	-0.13	-0.14	-0.99	0.98	-1.00	1	0.27	0.60	0.46	0.67
P1	0.53	-0.73	-0.94	0.85	-0.91	-0.25	0.46	-0.22	0.27	1	0.85	0.84	0.61
P2	0.77	-0.30	-0.93	0.50	-0.70	-0.60	0.73	-0.57	0.60	0.85	1	0.85	0.81
P3	0.66	-0.38	-0.93	0.58	-0.78	-0.45	0.61	-0.42	0.46	0.84	0.85	1	0.78
P4	0.78	0.06	-0.81	0.12	-0.45	-0.69	0.75	-0.65	0.67	0.61	0.81	0.78	1

Table 4.7. Correlation matrix of camera IO parameters as estimated from the October 2019 dataset (f= focal length (pix); xp and yp coordinates of the principal point offset (pix); B1, B2 = Skew parameters; K1, K2, K3, K4= radial distortions; P1, P2, P3, P4= components of the decentering distortions).

	f	xp	yp	B1	B2	K1	K2	K3	K4	P1	P2	P3	P4
f	1	-0.63	-0.50	-0.26	-0.26	-1.00	1.00	-1.00	1.00	0.70	0.51	-0.54	0.83
xp	-0.63	1	0.28	-0.28	0.30	0.58	-0.63	0.60	-0.62	-0.91	-0.66	0.73	-0.65
yp	-0.50	0.28	1	0.01	0.13	0.46	-0.49	0.47	-0.48	-0.63	-0.77	-0.28	-0.43

B1	-0.26	-0.28	0.01	1	-0.64	0.31	-0.26	0.28	-0.27	0.27	0.42	0.12	-0.41
B2	-0.26	0.30	0.13	-0.64	1	0.23	-0.27	0.25	-0.26	-0.35	-0.38	0.10	0.04
K1	-1.00	0.58	0.46	0.31	0.23	1	-1.00	1.00	-1.00	-0.65	-0.46	0.53	-0.81
K2	1.00	-0.63	-0.49	-0.26	-0.27	-1.00	1	-1.00	1.00	0.70	0.50	-0.54	0.82
K3	-1.00	0.60	0.47	0.28	0.25	1.00	-1.00	1	-1.00	-0.67	-0.48	0.54	-0.82
K4	1.00	-0.62	-0.48	-0.27	-0.26	-1.00	1.00	-1.00	1	0.69	0.49	-0.55	0.82
P1	0.70	-0.91	-0.63	0.27	-0.35	-0.65	0.70	-0.67	0.69	1	0.83	-0.47	0.71
P2	0.51	-0.66	-0.77	0.42	-0.38	-0.46	0.50	-0.48	0.49	0.83	1	-0.04	0.32
P3	-0.54	0.73	-0.28	0.12	0.10	0.53	-0.54	0.54	-0.55	-0.47	-0.04	1	-0.65
P4	0.83	-0.65	-0.43	-0.41	0.04	-0.81	0.82	-0.82	0.82	0.71	0.32	-0.65	1

Despite all the specific circumstances, these findings suggested that the IO parameters contain redundant information. Consequently, a PCA could show that most of the decorrelated information can be explained by a few PCs, whose detection was carried out with the Kaiser criterion.

4.4.2. PCA and Synthetic Indexes Definition

The IO values and the errors calculated during the BA were compared to assess their mutual relationship. In this respect, all values were pre-processed by an R-routine developed in-house to extract the most meaningful information through Principal Component Analysis (PCA), based on the principle of variance maximisation (Abdi and Williams, 2010). PCA, probably the most popular multivariate statistical method, is dedicated to dimensionality reduction and works by removing redundant information from a multivariate dataset in which variables may be intercorrelated (Wold et al., 1987). After identifying the components of the most relevant variables, it converts the original dataset into a new one composed of independent and orthogonal vectors, called Principal Components (PC) (Abdi and Williams, 2010). The first component provides most of the information, describing most of the inertia of the input data, resolving most of the variance of the data; the second component is orthogonal to the first and absorbs most of the remaining variance (Wold et al., 1987). The same principle is used to find all the other components that, essentially, will represent a dimin-

ishing level of information as to their position within the transformation increases (Abdi and Williams, 2010). As a result, the first components compress most of the original information making it possible to drastically reduce the dimensionality of the data by eliminating redundant content (Griffiths and Burningham, 2019).

In this research work, the Singular Value Decomposition (SVD) approach (Abdi, 2007) was applied to obtain the calculation of PCs. The number of outstanding PC was selected by Kaiser's criterion (Kaiser, 1960) which suggests setting a threshold of eigenvalue = 1.0.

Subsequently, the selected PC components were weighted and linearly combined into a synthetic index (hereafter called SI). The SI was obtained as a weighted average of all significant components as presented in Equation 4.4. The weights were extracted directly from the PCA procedure.

$$SI = \frac{\sum w_i * Dim_i}{\sum w_i} \quad (4.1)$$

where w_i and Dim_i are the weights and principal components respectively.

The December, January, February, and October blocks were processed separately to identify those PCs that, for each dataset, could synthesise most of the original information. This was done with reference to the correlation graphs in Figure 4.7 that relate the IO parameters to the PCs.

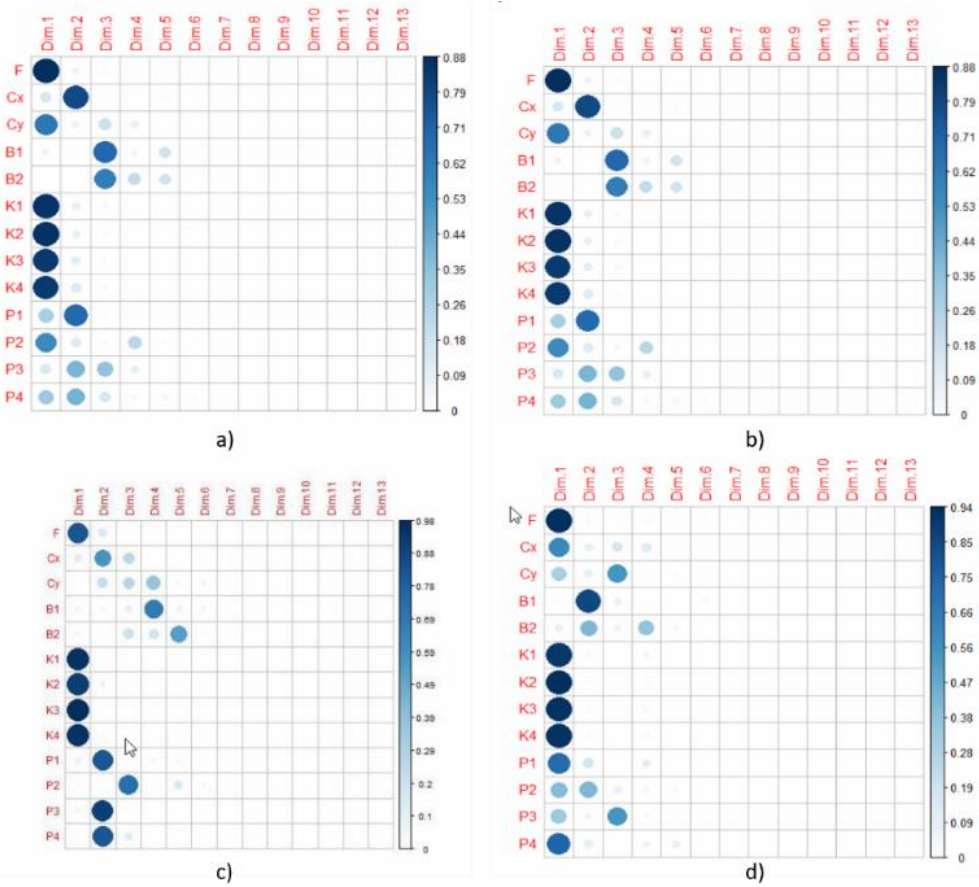


Figure 4.7. Correlation plot between IO parameters and PC (Dim). a) December; b) January; c) February; d) October. (f= focal length; xp and yp coordinates of the principal point offset; B1, B2 = Skew parameters; K1, K2, K3, K4= radial distortions; P1, P2, P3, P4= components of the decentering distortions).

Application of Kaiser's criterion showed that the three strongest PCs were sufficient to describe most of the variance of the IO parameters for the December (Figure 4.7a), January (Figure 4.7b) and October (Figure 4.7d) datasets. In contrast, five PCs were needed to explain most of the information residing in IO parameter estimates from the February dataset (Figure 4.7c). These results confirmed what the basic statistics in Tables 4.3-4.7 had already demonstrated: the IO parameters are indeed highly intra-correlated.

4.4.3. Predictive Function Detection

Once the SIs were calculated (Table 4.8), the R coefficient was calculated between them and the RMSE_i error components affecting the final measurements of the oriented blocks, resulting in both GCPs and CPs (Table 4.9). The starting hypothesis was that SI could be a predictor of the error components. Therefore, based on the values of the R coefficients obtained, an interpolation function was calibrated to predict the following errors:

- East coordinate error (RMSE_E),
- North coordinate error (RMSE_N),
- Horizontal Coordinate Error (RMSE_H),
- Total Error (3D) (RMSE_T),
- Image positioning error (RMSE_I).

SI was taken as the independent variable of the calibrated functions and the unknown x as the predictor.

Table 4.8. Synthetic index (SI) as computed by eq. 4.4 for the December, January, February and October datasets.

Variable	December	January	February	October
SI	1.42	1.85	1.08	1.79

Table 4.9. Correlation coefficient between RMSE_i and SI computed for each dataset (GCPs=Ground control Points; CPs=Check points; E= East coordinate; N=North coordinate; H= height coordinate; T=3D error; I=positioning error in the image space).

	GCPs					CPs				
	RMSE _E	RMSE _N	RMSE _H	RMSE _T	RMSE _I	RMSE _E	RMSE _N	RMSE _H	RMSE _T	RMSE _I
Pearson's R	0.5	-0.8	-0.10	-0.12	-0.11	0.28	-0.80	-0.50	-0.49	0.67

Only situations showing a moderate ($0.5 < R < 0.7$) or high Pearson's coefficient (>0.7) were modelled in the next step (Mutanga et al., 2005). Consequently, since SI showed moderate and high correlation with the RMSE_E and RMSE_N GCPs, respective-

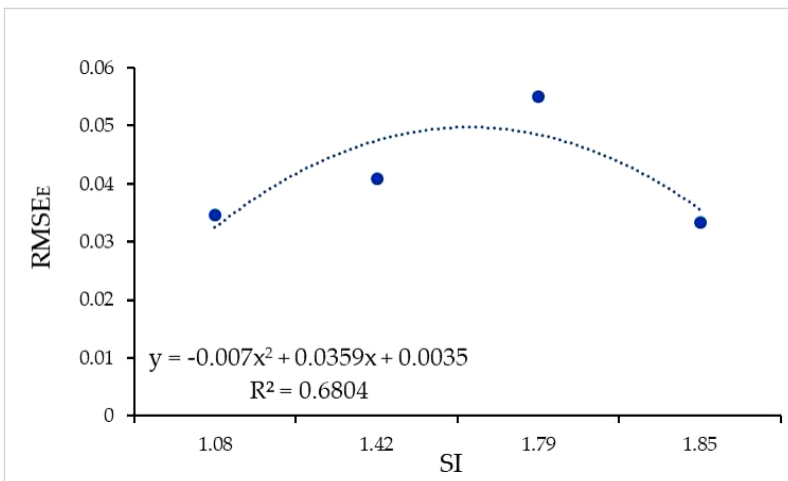
ly, these relationships were modelled. Conversely, since the $RMSE_E$ CPs showed low correlation with SI it was excluded from the modelling.

A 2nd order polynomial (Equation 4.5) was found to fit all significant relationships well. The model parameters (a, b, and c) as estimated by Ordinary Least Squares for each error studied (y) are given in Table 4.10. The goodness of fit was tested with reference to the coefficient of determination (R^2).

$$y = ax^2 + bx + c \quad (4.2)$$

The reliability and accuracy of the proposed predictive method were tested by applying the calibrated models to all available datasets, including March. The results for GCP and CP are shown in Figures 4.8 and 4.9, respectively. The graphs also show the coefficient of determination (R^2). For GCP, the lowest R^2 value was 0.68 ($RMSE_E$), while $RMSE_N$ CPs showed the highest R^2 (0.99).

Concerning the March dataset, in particular, PCA analysis was applied to recognise significant CPs that could explain most of the IO variance parameters. Two PCs were found to satisfy Kaiser's criterion and, consequently, were used to calculate the SI of March (3.060). The March SI value was then used to predict $RMSE_i$, according to Equation 4.5 applied using the coefficients in Table 4.10.



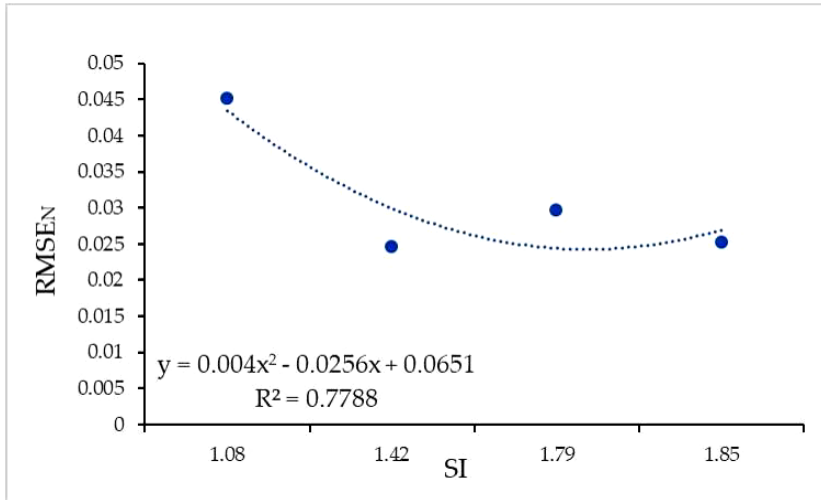
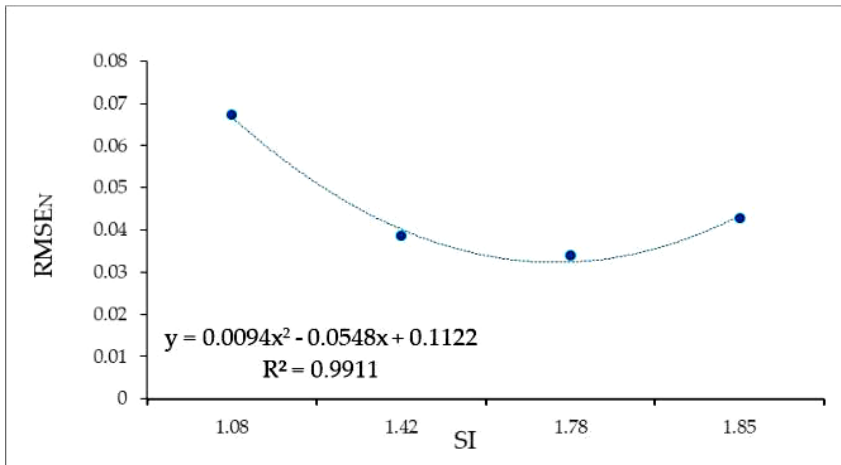


Figure 4.8. Significant predictive functions of RMSEE, RMSEN calculated on GCPs. R2 is the coefficient of determination.

Table 4.10. Coefficients of the calibrated predictive functions (E = East coordinate; N= North coordinate; H= height coordinate; T= total (3D) error; I= positioning error in the image space)

	RMSE _E (m) – GCPs	RMSE _N (m) – GCPs	RMSE _N (m) - CPs	RMSE _H (m) - CPs	RMSE _T (pix) - CPs
a	-0.0070	0.0040	0.0094	-0.0166	-0.0166
b	0.0359	-0.0256	-0.0548	0.0696	0.0696
c	0.0035	0.0651	0.1122	0.0535	0.0881



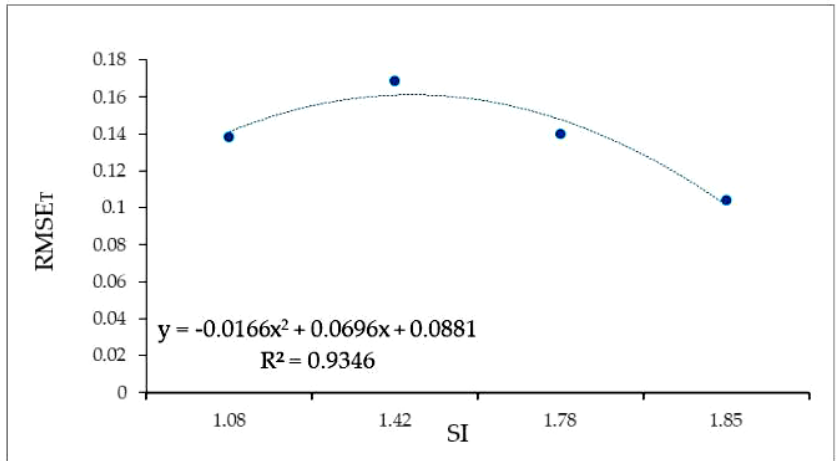
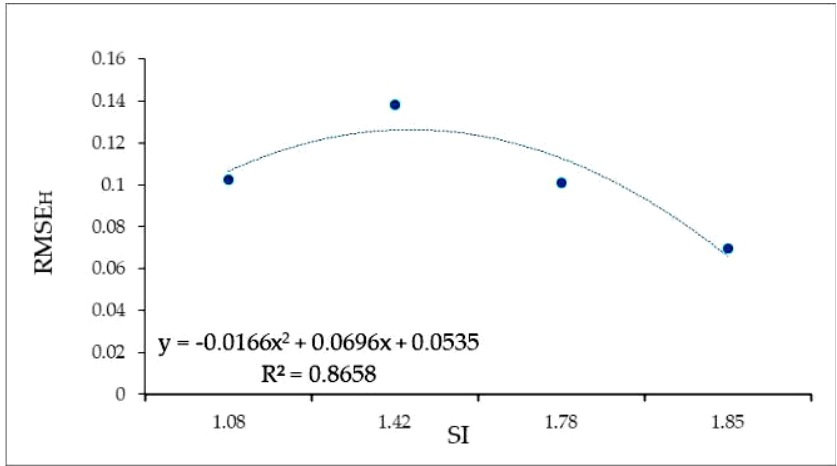


Figure 4.9. Significant predictive functions of RMSE_N, RMSE_H, RMSE_T calculated on CPs. R² is the coefficient of determination.

To summarise the performance of the models, all RMSE_j estimates were compared, by differentiation, with the corresponding values of the BA solutions (the reference ones). The RMSE was then calculated for all tested differences and the RMSE_j estimated. The results are shown in Table 4.11.

Table 4.11. Differences between RMSE_j values as estimated by the calibrated predictive models and the correspondent ones from BBA for the March dataset.

Errors	March dataset difference (m)
RMSE _E (GCPs)	0.0024

RMSE _N (GCPs)	0.0047
RMSE _N (CPs)	0.0110
RMSE _H (CPs)	0.0039
RMSE _I (CPs)	0.0014

4.4.4. Discussion

This research intended to look at the dependence of the accuracy of measurements from UAV-based SfM models on the IO parameter estimations of the camera model. Several researchers have examined this issue, noting the strong influence of camera parameters on the final accuracy of reachable measurements.

Nevertheless, no operational procedure had ever been suggested that was able to predict the potential accuracy obtainable once the camera parameters were established. At this stage of the research, a simple method was pursued which, in their preliminary tests, provided encouraging results. The proposed method integrates uni- and multivariate statistics to investigate and remove the correlated information residing in the IO parameters of the camera as estimated during the BA.

After this preliminary study that ensured the comparability of the processed datasets, a more in-depth investigation looked separately at the error components (RMSE_i). Some fundamental statistics (e.g., maximum, minimum, mean, and standard deviation) of the IO parameter estimates were also calculated for each processed data set (Table 4.2). All showed similar statistics. The results confirmed photogrammetric software, in general, cannot estimate stable IO parameters while the initial conditions (e.g., the number of GCPs) change (Smith and Heidemann, 2015, Zhang, 2000). Indeed, the statistics showed a high variability of the solutions.

However, the order of magnitude remained the same in all datasets (Figure 4.1) and a similar trend, as shown in the boxplots of Figures 4.2-4.6. Furthermore, the order of magnitude obtained is consistent with that obtained by other researchers (Smith and Heidemann, 2015); they showed that Pi parameters are smaller by one or two orders of magnitude than radial parameters and that Ki has the most significant deviations.

The correlations between the IO parameters were then studied, finding a high degree of intracorrelation. The correlation values were found to be consistent with those re-

ported in the literature (Tables 4.3-4.7, (Smith and Heidemann, 2015)). The correlated information was aggregated using PCA (Fraser, 2013); it was found that two to five PCs are generally sufficient to explain most of the variance in IO parameter estimates. With these assumptions, an index (SI) was defined to summarise the decorrelated information that the first PCs were able to aggregate. The SI was taken as a predictor of RMSE_j, and the corresponding predictive function calibrated (Figures 4.8 and 4.9). Model calibration was obtained concerning the December, January, February, and October datasets. The March dataset was used differently to validate predictive models. Despite the few observations used for calibration, the proposed predictive functions showed satisfactory results when applied to the validation set, generating RMSE_j estimates very close to the actual values calculated during the BA by the software.

5. PIXEL-BASED ANALYSIS

Several key developments achieved in the last decade show enormous potential in generating characterising information, in a radically new way, based merely on images and their pixels (Hamylton et al., 2020). As seen in previous chapters, computational advances have increased the accessibility of low-cost machines with fast arithmetic units, opening the possibility of undertaking machine learning-oriented numerical approaches. Even today, the variability and richness of natural features represented as raster images and the relatively coarse resolution of EO satellite images pose a challenge to pattern recognition algorithms. However, the substantial increase in spatial resolution that has been introduced through the operation of UAV platforms at much lower altitudes, reducing the size of ground pixel projections by three orders of magnitude, has made machine learning perform well for even the smallest scenario properties. Even in the case of dynamic environments, i.e., subject to natural or anthropogenic change, deep learning techniques have enhanced the identification of features of interest and also track how they evolve over time.

Machine learning from these images essentially translates into automatically categorising pixels based on their values and transforming them into a form of final component or group of objects in the raster (Alif et al., 2018). In other words, classification in RS involves categorising the response functions recorded in the images, i.e., the light reflected from the Earth's surface and recorded in the pixels by the sensors, as “virtual” representations of real-world objects. This process can be achieved simply by manually viewing, interpreting, and annotating aerial images through digitisation, or the application of a variety of machine learning approaches. Each of these approaches is subject to advantages and disadvantages. Visual interpretation and digitisation of images yield highly reliable mapping results, such approaches however are shown to

be both time consuming and susceptible to interpreter bias, not to mention errors in manually digitising features (Barlow, 2018). At the same time, basic machine learning offers a fundamentally different approach by relying on programmed algorithms to classify input image data into an output map based on the relative statistical reflectance properties of their composite pixels. In the advanced conceptual view of Machine Learning, the data and the desired output are provided to a learning algorithm, called a learner, which then generates the algorithm that transforms one into the other. In a more complex and evolved stage, deep neural networks (DNNs) are composed of multiple layers between the input and output layers that collectively define the correct mathematical manipulation that generates the output from the input through a series of convolutions (LeCun et al., 2015).

These algorithms are finding increasing use in RS applications and the scientific community is deeply engaged in investigating their performance. In the case of feature detection from RS images, one of the key challenges is to agree on the most appropriate approach to reliably recognise real-world objects from a large number of pixels. So far, this has mainly been accomplished by using statistical classifiers that distinguish features or land cover based on several reflectance values across different wavebands that compose an image or by employing predefined rule sets to classify logically segmented objects from an image (Xie et al., 2008). A distinction is therefore made between pixel-based and object-based approaches to image analysis. Further, in a supervised approach, given an input image and a predefined training set of categories, a detection algorithm can identify all instances of pixels and/or objects that fall into these categories in an image. In practice, supervised decision rules use training areas to determine a priori class membership probabilities. Quantitative classification methods applied to digital images include unsupervised pixel-based clustering (Keyport et al., 2018). In general, unsupervised clustering is a good first step in digital image analysis to reveal patterns and possible distinguishing features for use in more structured classification methods. Supervised classification produces higher overall classification accuracies, commonly never less than 55%. Clearly, differences in flight altitude, illumination, shadows, partial occlusions, low sun angles and weather varia-

bility will lower image quality and thus both visual interpretation and digital classifier performance (Keyport et al., 2018). Finally, parametric and non-parametric classifications and a wide range of combinations and permutations of these different approaches are identified (Franklin, 2018).

Pixel-based image classification is based on the assumption that the spectral response patterns of individual pixels and the textures associated with the classes of interest can be statistically grouped into an appropriate set of informative classes. Classes are determined by their statistical separability with certain assumptions on class structure, or with non-parametric decision rules.

Object-based methods, on the other hand, attempt to simplify the image before classification by using coherent segments and/or objects that correspond to the targets of the individual classes. For very high-resolution images, object-based image classification techniques have shown better performance than the pixel-based approach (Chen and Wang, 2018). The first and critical step in object-based image classification is segmentation, which involves grouping similar pixels, according to a certain similarity threshold, into homogeneous objects (Keyport et al., 2018). Therefore, object-based image analysis (OBIA) techniques not only allow for the consideration of spectral information but also contextual, textural, shape and spatial relationships in image objects with respect to individual pixels (Mafanya et al., 2017).

However, the aim of this research is to create a validated and robust classification procedure that will subsequently result in an automated method that is simple to apply, especially for end-users with limited knowledge of spatial data processing, and that is low cost in terms of the tools required.

Given the considerations discussed above, a pixel-based approach to testing performance was deemed more effective by adopting photogrammetric products based on UAV acquisitions, as reviewed in previous chapters.

In most cases, UAVs are equipped with inexpensive cameras capable of acquiring only the visible RGB bands. These consumer cameras often have the problem of not being radiometrically calibrated (Haghighattalab et al., 2016, Wang and Myint, 2015). As seen in chapter 4, in order to provide RS data with a quantitative value, it is neces-

sary to calibrate them both geometrically and radiometrically, while performing an absolute atmospheric correction (Pompilio et al., 2018). Specifically, calibration allows the recovery of the relationship between the position and radiance pairs on the ground and the coordinates and brightness of the image, respectively.

Despite the advantages of using UAVs and low-cost cameras, it is also necessary to address their limitations and to analyse their impacts in the data post-processing stages. While the objectives of the work dictate the selection between satellites and UAVs or between different types of UAVs and sensors, the validity and commensurability of the different results obtainable will need to be verified. In order to do so, it is necessary, once again, to validate the processing procedure so as to fully define their comparability and, in some cases, their interchangeability.

5.1. RADIOMETRIC CALIBRATION OF IMAGES

In general, radiometric calibration of a sensor is achieved by using known gain and offset coefficients to convert DN into sensor radiance and then, after normalisation, into sensor reflectance.

Several methods have considered the effects of illumination and atmosphere on sensor radiance, including normalisation to a spectrally flat target or image average, radiative transfer models that simulate the interaction between radiation and the atmosphere, and empirical surface relationships between sensor radiance and ground reflectance (Pompilio et al., 2018). Due to the technical limitations of these calibration methods, there is a need to identify a feasible and convenient radiometric calibration method when processing images collected by commercial digital cameras using UAVs (Wang and Myint, 2015).

As in the case of geometric calibration, several strategies can be identified for full radiometric calibration: in the laboratory, on-board, in a test field (vicarious) and by self-calibration (on-the-job). The main difference between the methods is the conditions under which the calibration takes place. Consequently, this influences the equipment to be used and the level of accuracy achievable.

- Calibration in the laboratory: This is performed indoors, typically using spheres or integrating hemispheres as light sources. This procedure can be carried out periodically, at the same time as the spectral calibration. In detail, the sensor is exposed to a homogeneously illuminated target to normalise the inhomogeneous illumination of the chip due to the optical path of the system and the differences in the radiometric response function of the individual chip elements. The result is a correction function that transforms the DN_s recorded by the chip into linear radiometric coefficients. In addition, it is possible to identify the sensor's radiance response when the light source is known.
- On-board calibration: is carried out under working conditions using various on-board calibrators or natural light sources (the Sun, the Moon).
- Vicarious methods: system calibration is carried out under flight conditions using artificial targets present in the scene, or natural targets, such as desert sand or salt flats. An alternative to the reference target is the use of incident radiation. The vicarious calibration can be either the radiance-based or the reflectance-based method. In the first case, a well-calibrated radiometer measures the radiance of the ground target. In the case of the reflectance-based method, accurate information about the atmospheric conditions and the reflectance of the object must be available.
- Self-calibration also called block radiometric adjustment: as in the case of geometric calibration, it is performed using the actual mapping data. The procedure uses some optimisation techniques that exploit redundant information from several overlapping images to model the function between the DN and the reflectance of the object. In the process, matching points are identified in several images and radiometric control points, e.g., a reference panel, can be included. The outputs are the parameters of the radiometric model that can be applied to produce radiometrically correct images. This is the procedure most implemented in SfM-MVS software.

Among radiometric methods, laboratory calibration is the most rigorous due to the stationary and controlled conditions under which operations are performed. The use

of UAVs, compared to airborne or satellite platforms, has as the main advantage in radiometric measurements the possibility to fly under clouds and neglect atmospheric corrections. However, cloud movement can cause problems, as well as unstable atmospheric conditions and irradiance stability can affect in-flight calibration. For low-altitude RS, however, vicarious calibration, in particular reflectance-based methods, and the self-calibration approach are the most widely used. According to (Aasen et al., 2015), self-calibration is the technique that performs best in unstable atmospheric and radiation conditions. In contrast, the accuracy of vicariant methods suffers from unstable irradiance.

As a basis of these strategies (Aasen et al., 2018), in general, to generate reflectance images from radiance images, two approaches can be defined:

- irradiance measurements, based on a second sensor (or optical pathway) that measures the spectrally resolved downwelling illumination;
- radiometric reference targets. These targets present a uniform intensity and approach Lambertian reflectance characteristic. Generally flat and level, without obstructions, they should be large enough, preferably more than five times the GSD of the image, to reduce adjacency effects by selecting only the central part of the panel. The incident irradiance can be estimated using atmospheric radiative transfer models (ARTM) or measured using an irradiance spectrometer. As an alternative, a stationary or mobile irradiance sensor with cosine receiver optics can be used. The former sensor can collect consecutive measurements of the Lambertian reference panel on the ground; the latter can continuously measure irradiance in flight or during ground operations. The incident light sensor (ILS) is also mounted on UAV platforms at a reciprocal angle to the sensor's measurement geometry. In short, if a sensor should face nadir, the radiation sensor should face zenith.

Successful quantitative image classification requires a shrewd interest in the radiometric concerns of the image during data acquisition (Mafanya et al., 2018). The influence of target-dependent bidirectional reflectance distribution function (BRDF) effects, acquisition variability (e.g., illumination conditions and 'hot spots', flight opera-

tions, variable calibration target performance), geometric errors in the image and field data (including IFOV variance), can have a significant impact on the quality and utility of the resulting images.

Pseudo-invariant targets within the imaging area (often located near take-off and landing sites), used to establish relationships between spectral reflectance and radiance of the detected image, will vary radiometrically and geometrically with illumination and sensor view angles. The rapidly and intermittently interacting solar and cloud irradiance during even a short-term acquisition mission can bring about significant radiometric variability. The temporal characteristics of the image (e.g., season, time of day) will dictate some mission planning considerations, and thus influence the information content of the images, which in turn, will help guide the choice of effective image classification methods.

Low flight altitudes, generally below 150 m, above the ground, due to regulatory restrictions on flight rules, result in a larger number of images being collected than those acquired from a satellite platform or piloted aircraft over the same area (Dainelli et al., 2021). This leads to the difficulty of performing in situ reflectance calibration measurements on the surface for all images acquired by UAVs (Olsson et al., 2021). Thus, this requires the positioning of several calibration targets in the field that homogeneously cover the area. This results in longer field activity times and significant effort in the field, considering the difficulties encountered in more inaccessible scenarios (Mafanya et al., 2018).

Estimation and, when possible, normalisation of these effects is a requirement for defining the reliable signature of an object. Radiometric calibration not only has the main function of characterising the sensors but also allows eliminating all aberrations of the radiometric signal related to environmental conditions.

The basic principle is the evaluation of the DN response of systems using a reference with well-known radiance at various intensity levels to estimate the radiometric calibration parameters and the reflectance of the object.

Therefore, the whole procedure can be identified in few steps: (1) radiometric characterisation of the sensor, (2) generation of the reflectance factor, (3) radiometric nor-

malisation of the scene, (4) radiometric validation. Thus, firstly, the radiometric characterisation of the sensor allows the transformation of the sensor digital numbers into normalised, and a further step can be performed to generate the radiance at the sensor. Then, the data are converted into reflectance factors using support devices hypothetically calibrated in radiometric terms. At that point, the image can be used as it is, and the reflectance factors can be converted into reflectance quantities. Finally, the radiometry results will have to be validated.

Having discussed a pre-processing and processing framework for UAV data, it is essential to perform a radiometric calibration of the photogrammetrically returnable orthomosaics to be considered quantitatively and qualitatively comparable, and useful for subsequent quantitative classifications.

To this end, in order to perform a radiometric calibration of the generated orthomosaics, the variability of the results obtained by applying the ELM (Smith and Milton, 1999) with different spatial resolutions for three different scenarios was compared. Calibration validations were attested by comparing the extractable spectral signatures on targets in vegetated, asphalt and bare soil areas with those found in the literature. This allowed us to assess the accuracy of the calibration process and, therefore, the level of confidence in the interpretation of the derived products.

5.1.1. Pilot Sites and Materials

For the requirements of the current testing, three different datasets were selected, based on the following criteria: (1) have a different context, (2) captured by different UAV/camera sensors, (3) have a different georeferencing strategy, and (4) capture by different altitude AGL and (5) different GSD. A preview of these pilot site can be noticed in Figure 5.1. A detailed description of the areas is given in (Saponaro et al., 2021). Table 5.1 shows the characteristics and technologies used for each dataset.

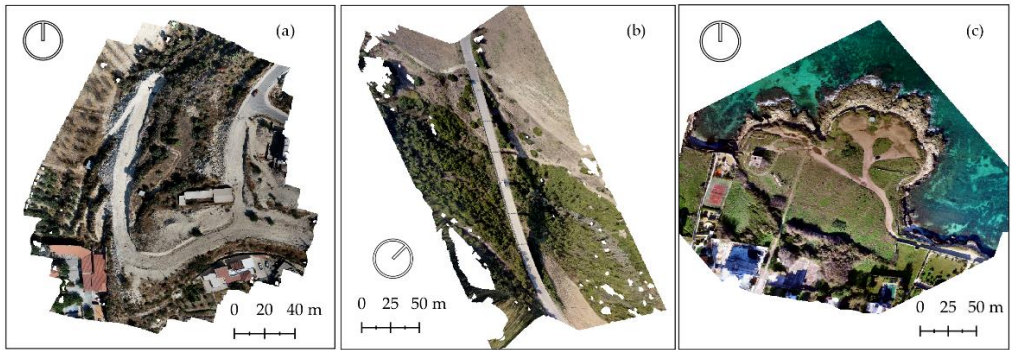


Figure 5.1. Pilot sites: (a) a construction site located in Fasoula (EL), Cyprus, (b) an out-of-town viaduct in Grottole (MT), Italy, (c) an abandoned archaeological area in Bari (BA), Italy. The icon to the left of the reader identifies the north orientation of the areas.

Table 5.1. Summary of surveyed scenarios adopted technologies and acquired datasets.

	Case Study (a)	Case Study (b)	Case Study (c)
Location	Fasoula (EL), Cyprus	Grottole (MT), Italy	Bari (BA), Italy
Equipment	DJI Phantom 4 Pro RTK RGB f-8.8, Model FC6310S	DJI Mavic 2 Zoom RGB f-4.386, Model FC2204	DJI Inspire 1 v.2 ZenMuse X3 RGB f-3.61, Model FC350
Images	174 images (5472x3648 pix)	287 images (4000x3000 pix)	87 images (4000x3000 pix)
AGL/GSD	50 [m]/9.7 [mm/pix]	30 [m]/1.3 [cm/pix]	90 [m]/3.9 [cm/pix]
Georeferencing Strategy	DG with RTK on-board	IG with 11 GCPs in nRTK	DG with low-cost GNSS receiver

Four orthomosaics were exported for each examined scenario: starting from the highest resolution and then doubling, tripling, and quadrupling the resolution, resampling each time by bilinear interpolation (Table 5.2).

Table 5.2. List of spatial resolution solutions generated per scenario. The GSD values below represent an approximation to the nearest millimetre of the effective values.

	Case Study (a)	Case Study (b)	Case Study (c)
Orthomosaic [m/pix]	{1} 0,001	{1} 0,017	{1} 0,036
{1} <i>min.res.</i>	{2} 0,019	{2} 0,035	{2} 0,071
{2} <i>min.res.x2</i>	{3} 0,029	{3} 0,052	{3} 0,107
{3} <i>min.res.x3</i>	{4} 0,039	{4} 0,070	{4} 0,142
{4} <i>min.res.x4</i>			

5.2. EMPIRICAL LINE METHOD (ELM)

The ELM is a non-strict but basic approach to calibrate image DNs to approximate units of surface reflectance. The ELM for data collected from RGB UAVs sensors could be estimated using the following linear equation (5.1):

$$\rho(\lambda) = A * DN + B \quad (5.1)$$

where $\rho(\lambda)$ is the reflectance value for a specific band (range 0%-100%), DN is the raw digital numbers of the orthophotos, and A and B are terms that can be determined using the least-squares fitting approach (Agapiou, 2020b). Although it is widely used with reasonable results, radiometric corrections with ELM can introduce noise, and its application should be done with great caution. In fact, most digital cameras have built-in algorithms that use a curvilinear function to transform electromagnetic radiation into digital signals to simulate the way human eyes perceive grey. Therefore, consumer cameras are designed to take good-looking pictures, not to capture scientific data for research. Therefore, the relationship between surface reflectance and raw image DNs remains poorly decipherable for these cameras (Wang and Myint, 2015). In the more general case, even when irradiance measurement is not available, by distributing several (quasi) Lambertian lenses with a known spectral reflectance, ELM is commonly used to calculate reflectance factors. The procedure allows generating reflectance and normalising the signal for different illumination conditions between flights and atmospheric effects. The ELM can also be useful when spectroscopic in-

formation on the ground is not available (Smith and Heidemann, 2015). Using the raw DN values per band extrapolated from "virtual" targets distributed in the investigated scenarios, a linear relationship is constructed by empirically associating to the DN the extreme percentage values (range 0%-100%) of the reflectance, respectively low and high. Thus, a relation between the sensor radiance and the surface reflectance is constructed by calculating those non-varying spectral targets and comparing these measurements with the respective DNs of the images (Wang and Myint, 2015). Thus, prediction equations are developed that can ponder changes in illumination and atmospheric effects. Due to the low altitude at which UAV measurements are taken and the lack of precise information, the impact of atmospheric effects can be deliberately ignored (Agapiou, 2020b). It is suitable for detection times of less than 30 minutes under stable meteorological conditions (clear skies) and coverage of the reflectance range of interest must be ensured with a minimum of two reference targets. This is possible when the distribution of DN to reflectance within an image can be considered linear.

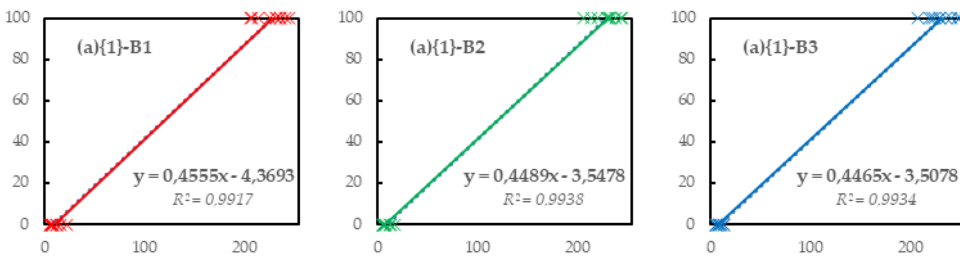
The orthomosaics were imported into the open-source software QGIS (3.16.5 'Hannover') (Team, 2021). The suitability of the target sites to the criteria proposed in (Pompilio et al., 2018) was considered: (a) high spatial homogeneity, concerning the spatial resolution of the image dataset, i.e. ideally, each target should cover an area of about 5x5 pixels in the reference images; (b) representativeness of the dynamic range of the radiance in the region; (c) low adjacency effects of targets positioned at a suitable distance from other scattering volumetric disturbances; (d) low slope effects, i.e., targets with flat or Lambertian surfaces; (e) low temporal irregularity of the spectral response, i.e., targets with steady spectral response that do not exhibit rapid changes due to short-term dynamic phenomena. Following the procedures adopted in (Agapiou, 2020b), high and low reflectance targets were manually identified as depicted in Figure 5.2, avoiding points with equivocal exposure.

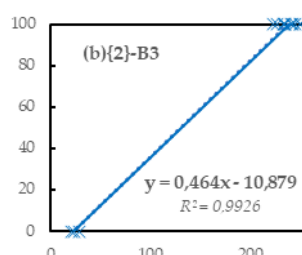
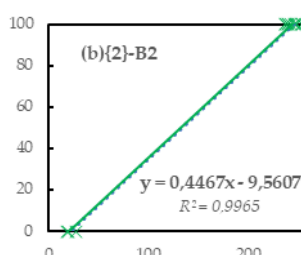
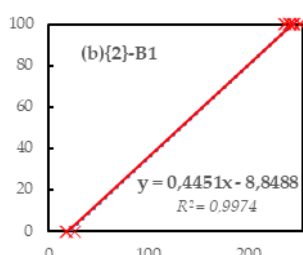
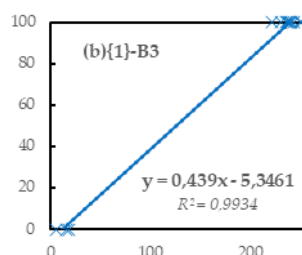
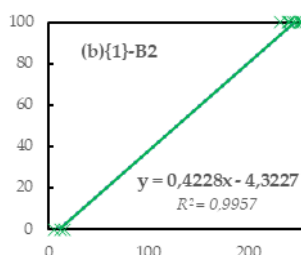
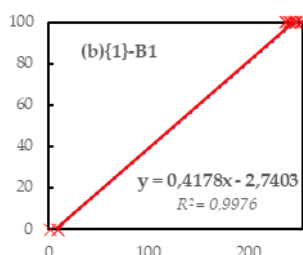
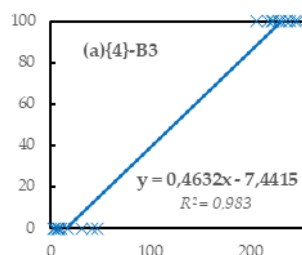
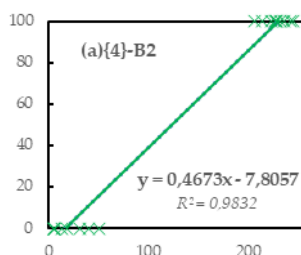
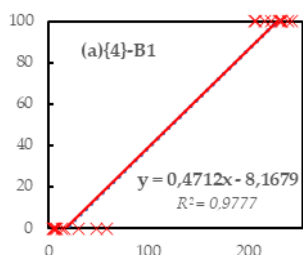
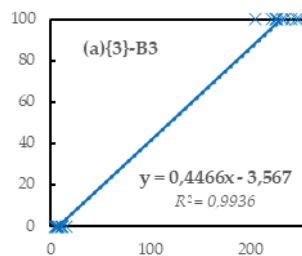
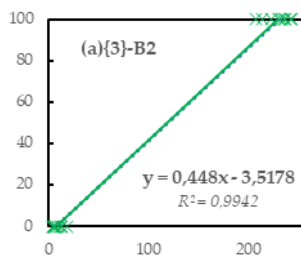
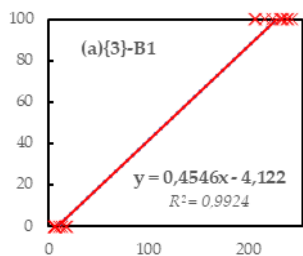
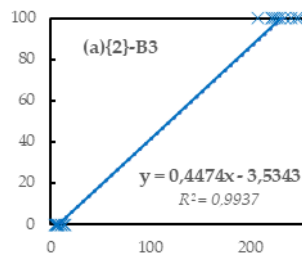
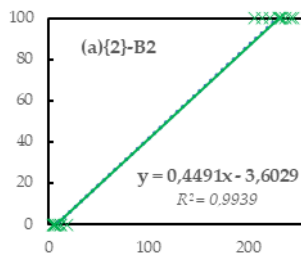
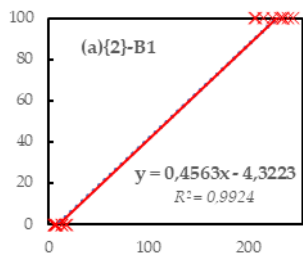


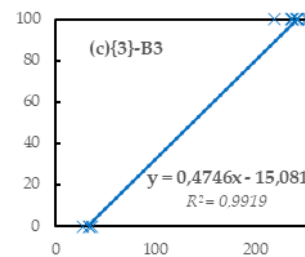
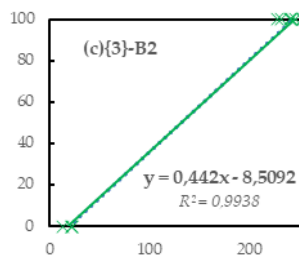
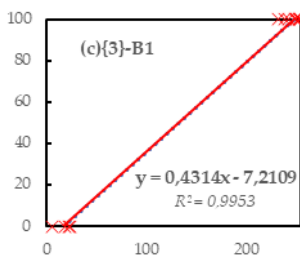
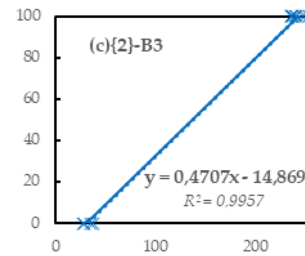
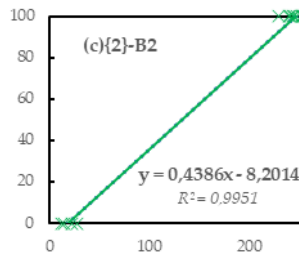
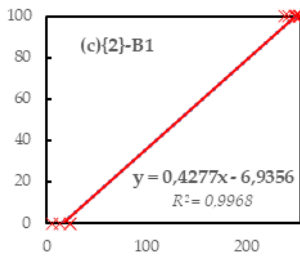
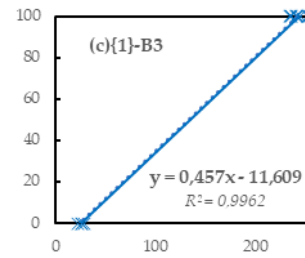
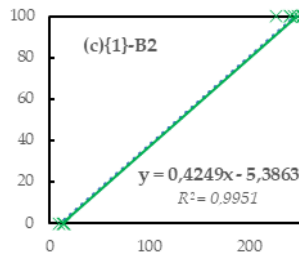
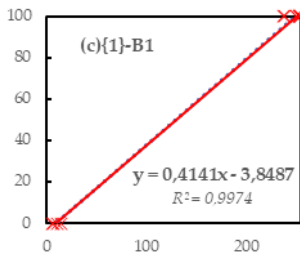
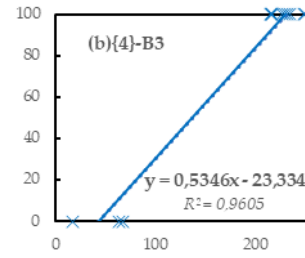
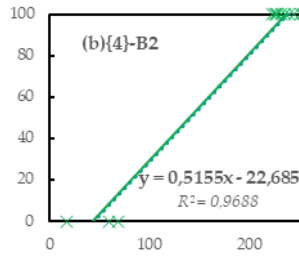
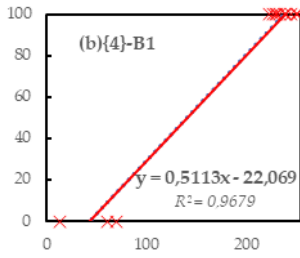
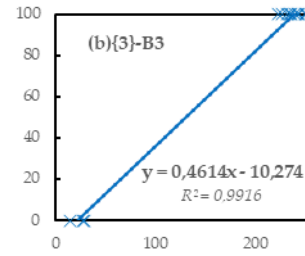
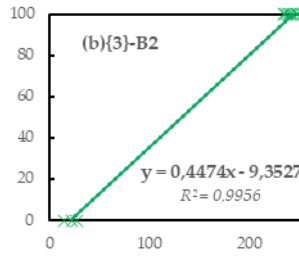
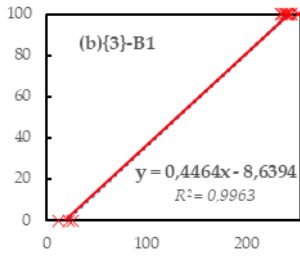
Figure 5.2. Example of high (top) and low (bottom) reflectance targets selected for each case study.

5.2.1. Extract Regression Lines

The A and B values of equation (5.1) were assessed and applied in the Raster Calculator of the QGIS software to carry out the radiometric calibration of each band. Goodness-of-fit measures, such as the coefficient of determination (R^2), are employed to appraise the accuracy of the ELM correction so that the appropriateness of the regression can be quantitatively demonstrated (Pompilio et al., 2018).







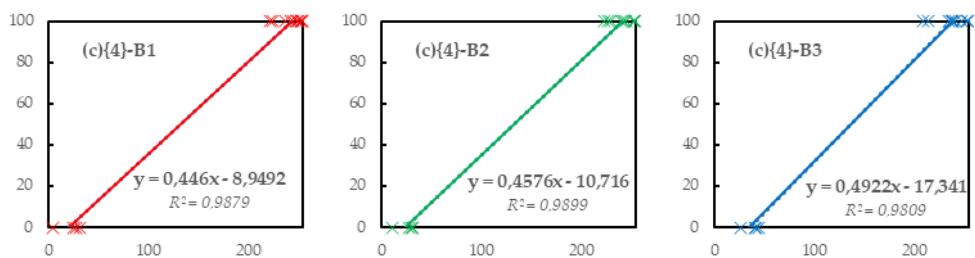
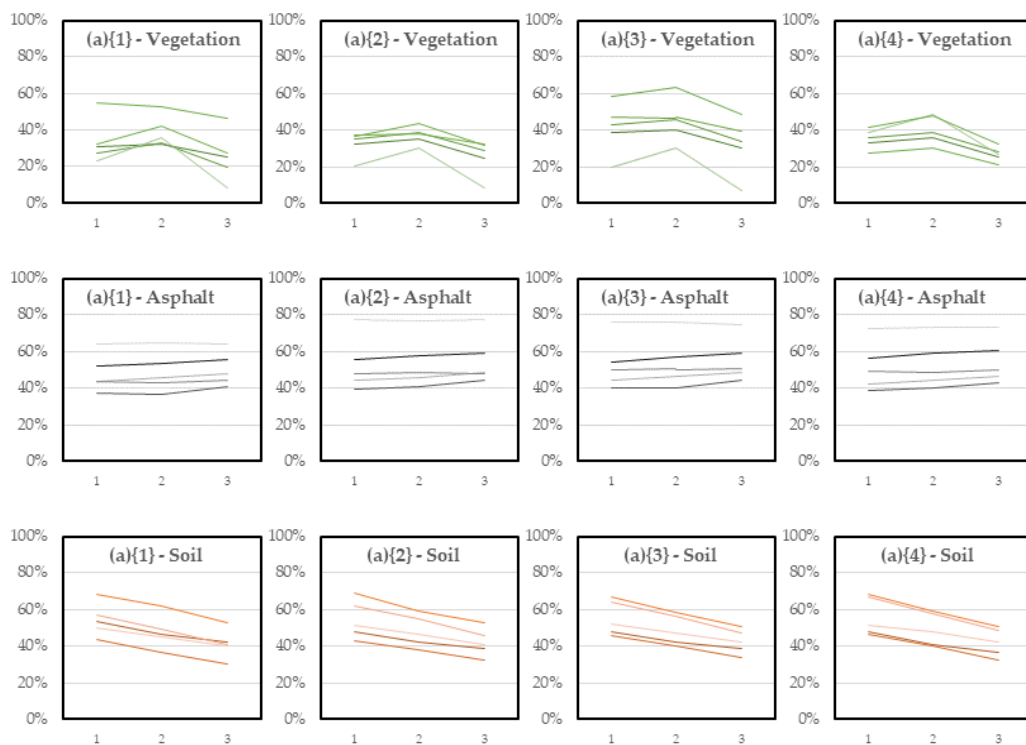
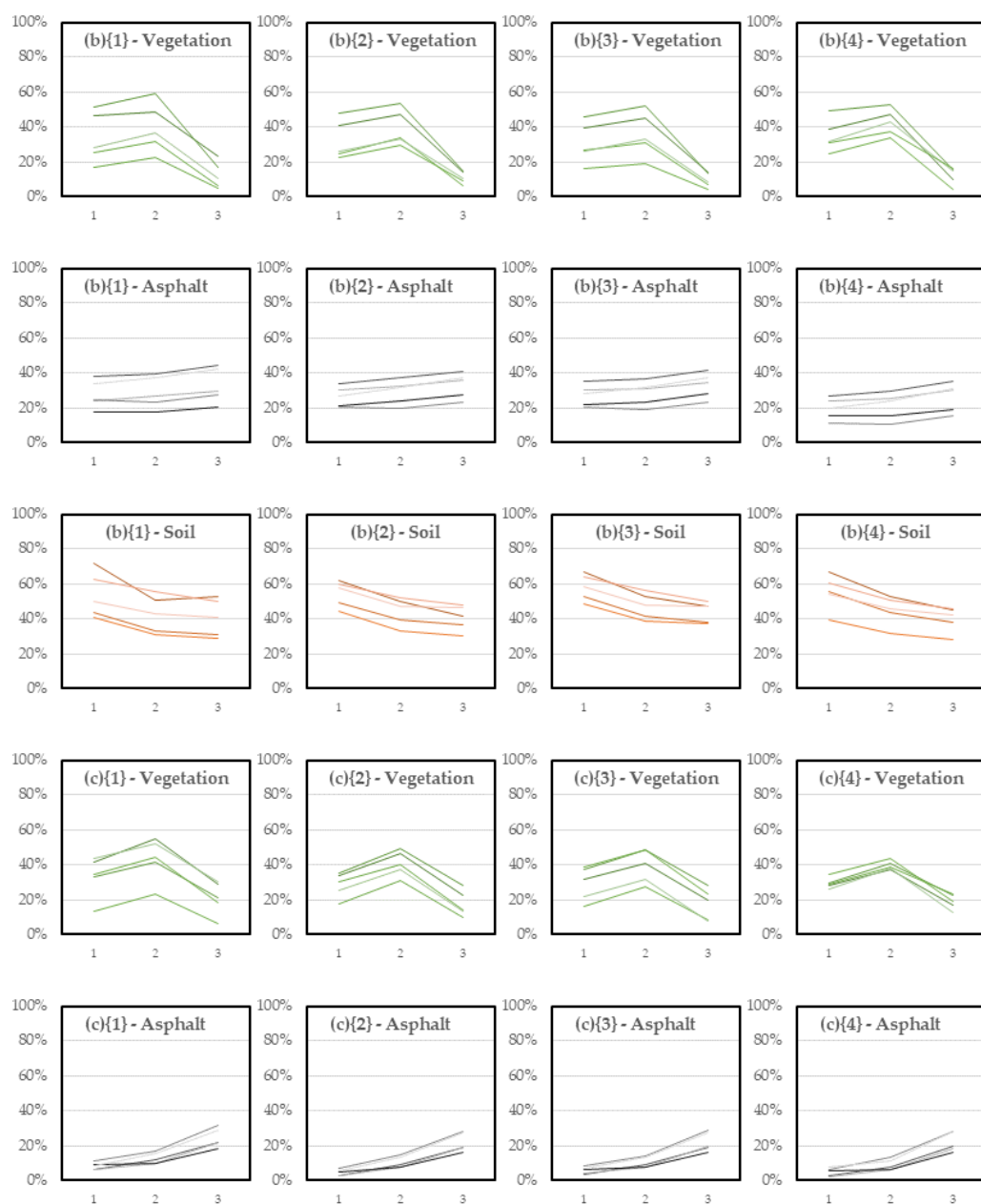


Figure 5.3. Regression lines obtained by applying ELM: DNs values in abscissa related to percentage reflectance values in ordinate. Scenarios (a), (b) and (c) are represented in spatial resolutions {1}, {2}, {3} and {4} in the three bands (B1, B2, B3), red, green and blue respectively. In each graph, the regression equation and the coefficient of determination R2 can be observed.

5.2.2. Radiometric Validation

To confirm the consistency of the calibrations performed, 15 points per scenario were manually detected among vegetation, bare soil and asphalt. Their spectral signatures were matched with those commonly agreed upon in the literature.





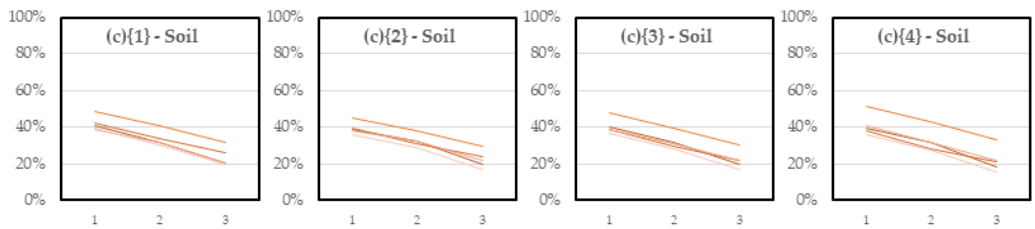


Figure 5.4. Spectral signatures of 15 control points were manually caught from radiometrically calibrated rasters. The points are scattered among 5 points in vegetated areas, 5 in asphalt areas, and 5 in bare soil areas. The results are shown in scenarios (a), (b) and (c) in spatial resolutions {1}, {2}, {3} and {4}. In abscissa the band number, in ordinate the percentage reflectance value recorded.

5.3. VEGETATION HEALTH MONITORING

The integration of UAV data, GIS development and geospatial technologies have supplied new insights into the application for detection and feature extraction of targeted objects and Land Use/Land Cover (LULC) monitoring (Comert et al., 2018, Comert and Kaplan, 2018, Lv et al., 2017).

The most revolutionised area concerns the monitoring of vegetation status and the dynamics affecting it (Al-Ali et al., 2020). For example, the extraction of vegetation information is considered an essential step in environmental restoration strategies to identify degraded areas in the early stages of degradation or those already under stress (Lima-Cueto et al., 2019). Other research works test these methodologies to optimise agricultural and forestry processes. (Tmušić et al., 2020) provides an extensive description of current and developing applications. In fact, RS provides a synoptic view, covering a large area and extracting accurate information on current phenomena or preventing others, at an acceptable economic cost (He and Weng, 2018). Many scientists are using spectral measurements derived from numerous satellite sensors, such as vegetation indices (VI), to monitor, for example, the seasonal dynamics of vegetation and assess the impact of drought on vegetation. Around the world, several studies have used RS for mapping and monitoring vegetation cover at local and regional scales, depending on the different sensors (Aasen et al., 2015,

Candiago et al., 2015, Capolupo et al., 2020d, Fuentes-Peailillo et al., 2018, Räsänen and Virtanen, 2019, Xie et al., 2008).

Several comparative analyses between object-based and pixel-based classification techniques for LULC feature extraction can be found in the literature (Shukla and Jain, 2020). The result of the analyses describes the superiority of object-based classification but also the relative complexity in achieving such results.

At the same time, several image classification methods have been developed that have improved landscape mapping capabilities in the multi-temporal perspective. However, several studies have mainly examined classifiers to classify vegetation cover in ecosystems and observed that classification methods may have different performances depending on landscape classes (Capolupo et al., 2020b, De Luca et al., 2019, Gašparović et al., 2020, Yano et al., 2016). Some classifiers have illustrated that they may over- or under- estimate vegetation cover due to the structural characteristics of plants, which cannot be easily detected at satellite image resolutions. New research efforts are focusing on exploring classification methods using ultra-high-resolution imagery captured by UAVs.

UAV images and photogrammetric results allow us to obtain many precise measurements of vegetation quickly and easily, define any feature, extract it from the whole product and manage it for other purposes (Candiago et al., 2015). For example, for the generation of DEMs, it is necessary to exclude vegetated areas through masking operations; in other cases, it is considered useful to monitor any temporal changes, such as crop yield estimation, land cover monitoring, urban growth monitoring, drought monitoring, etc. (Candiago et al., 2015, Kwan et al., 2020, Nhamo et al., 2020). Numerous VIs are formulated based on different mathematical equations that can detect healthy vegetation, taking into account atmospheric effects and soil refraction noise (Mesas-Carrascosa et al., 2020, Wan et al., 2018). One of the most well-known and widely used vegetation indices is the so-called normalized difference vegetation index (NDVI). The NDVI is determined take advantage of the near-infrared and red-band reflectance values of multispectral images (Kwan et al., 2020). Although several VIs are available for vegetation extraction, it remains a challenge to select the

most appropriate one for specific applications. This, of course, depends mainly on the scenario under study (Agapiou, 2020b).

In various application areas, the extraction of vegetated areas can be easily achieved using professional multi-band sensors that include a band dedicated to the NIR part of the spectrum (approximately between 760-900 nm), which commercial RGB cameras cannot capture. Typically, spectral radiances in the red and NIR wavelength regions of the electromagnetic spectrum detect photosynthetically active radiation and are most useful for reliably distinguishing vegetation from other types of ground cover. In addition, the use of these sophisticated but mainly expensive sensors compared to commercial RGB cameras makes operations unprofitable and limited. RGB cameras are often preferred among different sensors due to their low-cost availability, low power requirements, ease of use and flexibility in implementation (Ocampo et al., 2019). It is clear that the absence of an infrared band potentially limits the ability to distinguish vegetation from other non-vegetative terrain based on their spectral reflectance. This suggests that these RGB aerial photographs, lacking the NIR band but with very high spatial resolution, may be considered at least suitable in the coarse distinction between vegetation types.

Several authors have proposed to study the advantages of using common sensors in the visible bands and then evaluate their performance compared to previous sensors (Costa et al., 2020, Zhang et al., 2019a). Thus, the need emerged to structure pre-processing and post-processing methodologies for geometric and radiometric contents to make them at least comparable with more sophisticated sensors (Fuentes-Peailillo et al., 2018).

Therefore, the idea that emerged for this study concerns the investigation of VIs generated from visible bands, i.e., taken from sensors that are accessible by a wide pool of users and especially easy to use (Hunt et al., 2013, Jiang et al., 2019).

In this study, after examining the performance of different VIs in the visible band in various environments using different UAV technologies, the impacts of spatial resolution and possible image pre-processing, such as area masking, in the extraction of visible-VI vegetation were evaluated. As stated by (Agapiou, 2020a) and (Niederheiser

et al., 2021), spatial resolution was a key characteristic for mapping vegetation in RS imagery of heterogeneous environments. In this regard, (Räsänen and Virtanen, 2019) compared multi-sensor and multi-resolution products and explored their vegetation mapping proficiency in terms of classification performance. As evidenced by (Kwan et al., 2020), the very high spatial resolution of UAV images often produces noise effects due to the growth of visible targets, so it is crucial to investigate the optimal resolution in each scenario and possible pre-processing actions to efficiently map vegetation.

5.4. RGB-BASED VEGETATION INDICES

Given the radiometric band calibration procedures seen in Section 5.2.1 for each orthomosaic in Table 5.2, various vegetation indices were calculated in the visible bands. The ten (10) equations implemented are shown below. Referring to the study carried out in (Agapiou, 2020b), the following vegetation indices were evaluated for all case studies:

- Normalized Green–Red Difference Index (NGRDI)

$$(\rho_G - \rho_R) / (\rho_G + \rho_R) \quad (5.1)$$

- Green Leaf Index (GLI)

$$(2 * \rho_G - \rho_R - \rho_B) / (2 * \rho_G + \rho_R + \rho_B) \quad (5.2)$$

- Visible Atmospherically Resistant Index (VARI)

$$(\rho_G - \rho_R) / (\rho_G + \rho_R - \rho_B) \quad (5.3)$$

- Triangular Greenness Index (TGI)

$$0.5 * [(\lambda_R - \lambda_B)(\rho_R - \rho_G) - (\lambda_R - \lambda_G)(\rho_R - \rho_B)] \quad (5.4)$$

- Red–Green Ratio Index (IRG)

$$\rho_R - \rho_G \quad (5.5)$$

- Red–Green–Blue Vegetation Index (RGBVI)

$$(\rho_G * \rho_G) - (\rho_R * \rho_B) / (\rho_G * \rho_G) + (\rho_R * \rho_B) \quad (5.6)$$

- Red–Green ratio Index (RGRI)

$$\rho_R / \rho_G \quad (5.7)$$

- Modified Green–Red Vegetation Index (MGRVI)

$$(\rho_G^2 - \rho_R^2) / (\rho_G^2 + \rho_R^2) \quad (5.8)$$

- Excess Green Index (ExG)

$$2 * \rho_G - \rho_R - \rho_B \quad (5.9)$$

- Color Index of Vegetation (CIVE)

$$0.441 * \rho_R - 0.881 * \rho_G + 0.385 * \rho_B + 18.787 \quad (5.10)$$

where ρ_B is the reflectance in the blue band, ρ_G is the reflectance in the green band, ρ_R is the reflectance in the red band, λ_B is the wavelength of the blue band, λ_G is the wavelength of the green band and λ_R is the wavelength of the red band. As can be noticed in equation (5.5) to determine the TGI index, the peak wavelength sensitivity of the RGB camera was mandatory. Hence, the index calculation still depends on the hypothesis that the user gets the peak wavelength sensitivity of the used camera. Low-cost RGB cameras were not supplied with the specifications of the mounted CMOS sensors, as in these cases under study (Ocampo et al., 2019). It was thus chosen to set default values for all cases of $\lambda_B = 480$ nm, $\lambda_G = 560$ nm, and $\lambda_R = 655$ nm. The results were then analysed and compared using 150 random points automatically identified in the orthomosaics (Figures 5.5-5.6).

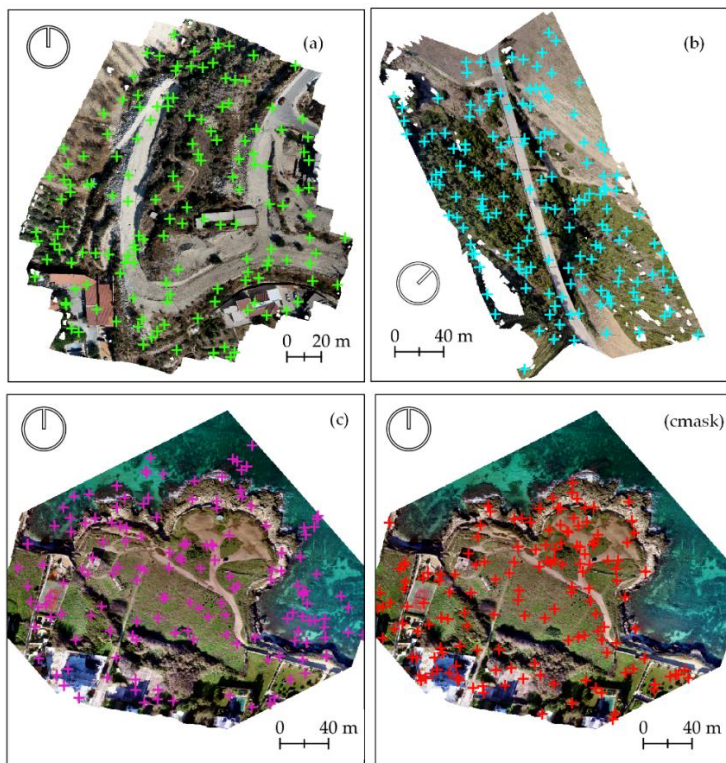


Figure 5.5. Distribution of random points analysed for examining the yields of vegetation indices in scenarios (a), (b) and (c). The distribution for scenario (c) subjected to the masking operation of the water zones, called (cmask), was also represented.

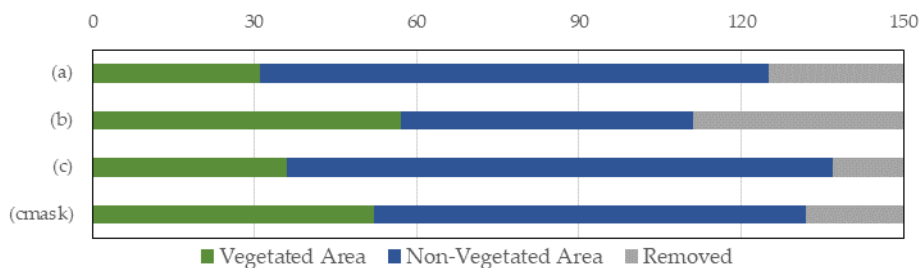


Figure 5.6. Counting of points in vegetated and non-vegetated areas. Points removed due to incorrect reflectance values were shaded in grey.

5.4.1. Separability Capabilities

Prearranged the division between points in vegetated and non-vegetated areas (Figure 5.6), the two statistical populations for each VI, for each resolution solution and scenario, were tested in the T-test with a 95% confidence level to cross-examine their significance for successive statistical inferences. Therefore, the latter proposes acceptable and unacceptable results in terms of significance with respect to the chosen confidence level. In particular, the non-acceptable results already attest to a complete inability to separate vegetated and non-vegetated areas, since the mean values of the indices cannot be defined as independent.

The normalised difference between the mean value \overline{VI} for each index over vegetated areas and non-vegetated areas:

$$\frac{\overline{VI}_{Vegetated} - \overline{VI}_{Non\ Vegetated}}{\max(VI_{Vegetated})} \quad (5.11)$$

represents the adopted descriptor of the propensity of each vegetation index to attesting separability in the extraction of the above classes.

A comparison of performance between the indices, i.e. a normalised difference for all case studies between all vegetation indices referring to the NGRDI, was set up based on the results in Table 5.3. The normalised difference indicated the percentage difference between:

$$\frac{\overline{VI}_{Vegetated\ i} - \overline{NGRDI}_{Vegetated}}{\overline{NGRDI}_{Vegetated}} \quad (5.12)$$

where each mean value was normalised to the maximum value of each index among vegetated points.

The statistics presented were examined for the three scenarios investigated, in the four spatial resolution solutions and for all vegetation indices computed to investigate possible relationships regarding their efficiency in relation to the spatial resolution adopted. Finally, a masking of the areas where water is present was tested for scenario (c). In fact, aware of the noise and distortions that can be derived photogram-

metrically in these areas, the possible behaviour of vegetation indices and their ability to distinguish vegetation was examined, removing these sources of ambiguity.

5.4.2. Influences of Spatial Resolution and Masking

The results were presented in Table 5.3. Blue colour indicates negative normalised difference value, while red colour, positive value per vegetation index for each spatial resolution. Lighter colours thus indicate a low degree of separability. The acronym NA identifies Not Acceptable results, defined above, due to differences between the means of the indices that are not significant for the 95% confidence level adopted in the T-test.

Overall, the limit values of the normalized difference range from a minimum of -675.3% to 304.9% for all indices in solution {1}, from -482.1% to 3123.2% in {2}, from -350% to 6337.3% in {3} and finally from -654.8% to 595.3% in solution {4}. The extreme values of these ranges were found in the TGI index in all analysed resolutions. In general, the remainder were more moderate values. In the complete evaluation of the ratio between not acceptable and acceptable values resumed by the T-test was 0.45 in case {1}, 0.40 in {2}, 0.325 in {3} and 0.35 in {4}. The optimal resolution for obtaining a greater number of vegetation indices at a 95% confidence level of the T-test was identified in {3}.

The results achieved in the (a) case showed a higher mean acceptability ratio in the T-test equal to 0.175. Usual surfaces, low vegetation, and discernible feature point definitely make orthomosaics more workable for vegetation indices. Subsequently, a somewhat comparable average acceptability ratio was found in the scenario (c_{mask}). In this case, a ratio of 0.2 was noted between acceptable and not acceptable values in all resolutions. In particular, the masking of the water areas from the orthomosaic improves their interpretability by the indices, returning acceptable values of separability between the classes investigated. Case (c) showed a mean ratio of 0.65 between the analysed resolutions. Particularly noteworthy were the values achieved by the IRG index (c_{mask}), compared with the corresponding NA results in case (c). For the following statistics, it was therefore preferred to focus on the (c_{mask}) case.

Last, case (b) was distinguished by an average acceptability ratio of 0.5. Only the latter scenario revealed a linear improvement in the acceptability ratio as the spatial resolution diminishes.

The highest magnitude was noted in case (c){3}, so with no masking, regarding the TGI index with a rate of 6337.3%. Furthermore, this index showed the acceptability ratio equal to 0, indicating to be functional in all cases and getting on very consistent values.

The ExG index appeared functional in each scenario (ratio equal to 0) and at each resolution solution: the most meaningful scores were produced in scenarios (b) and (c_{mask}). Stated a percentage deviation of more than 20% between scenarios (c) and (c_{mask}).

The VARI index was not acceptable for all cases examined, excluding case (b) at resolution {4}, thus showing the highest ratio of 0.9375 among the indices. Moreover, it was not rated high enough to be considered functional for separability between classes. As already seen in (Agapiou, 2020b), the CIVE (ratio 0.0625) index achieved the lowest score for all the resolution solutions in each scenario; among them, the scenario (c_{mask}) is the most reactive. The NGRDI performed similarly to the VARI index and was only adequate in solutions {2} and {3} of scenarios (a) and (c), with irrelevant scores below 15%. Its acceptability ratio was 0.75.

Scenario (c) did not react to the MGRVI (ratio 0.4375), RGRI (r. 0.4375), RGBVI (r. 0.375), IRG (r. 0.3125), and GLI (r. 0.4375) indices, while significant scores were scored in both (c_{mask}) and (a), excluding the RGRI index in the latter scenario. Remarkable values were documented in scenario (c_{mask}) for the IRG index.

Table 5.3. The normalised difference (%) between the mean value \bar{VI} for each index over vegetated areas and non-vegetated areas. Blue colour indicates negative normalised difference value, while red colour, positive value per vegetation index for each spatial resolution. Lighter colours thus indicate a low degree of separability, while the acronym NA identifies Not Acceptable values due to failure of the T-test.

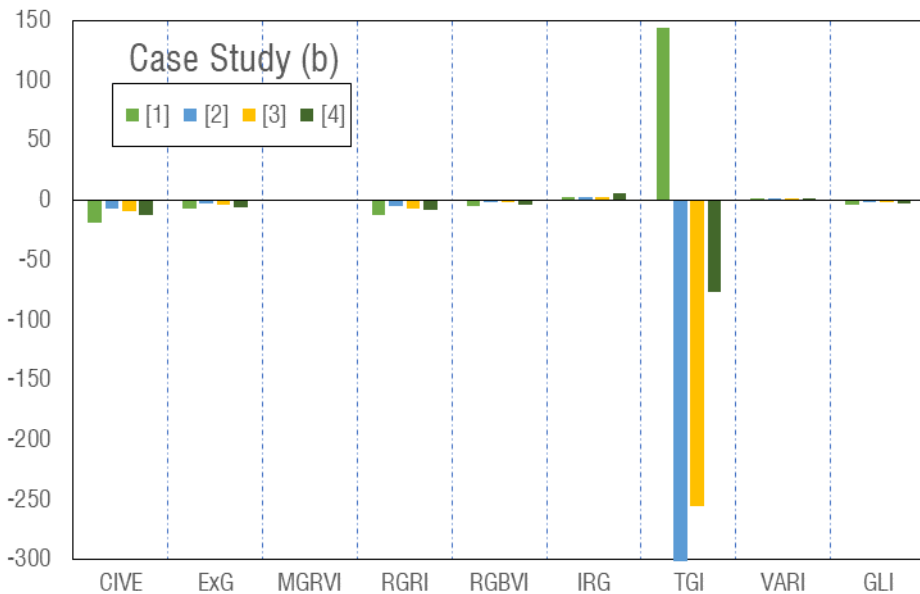
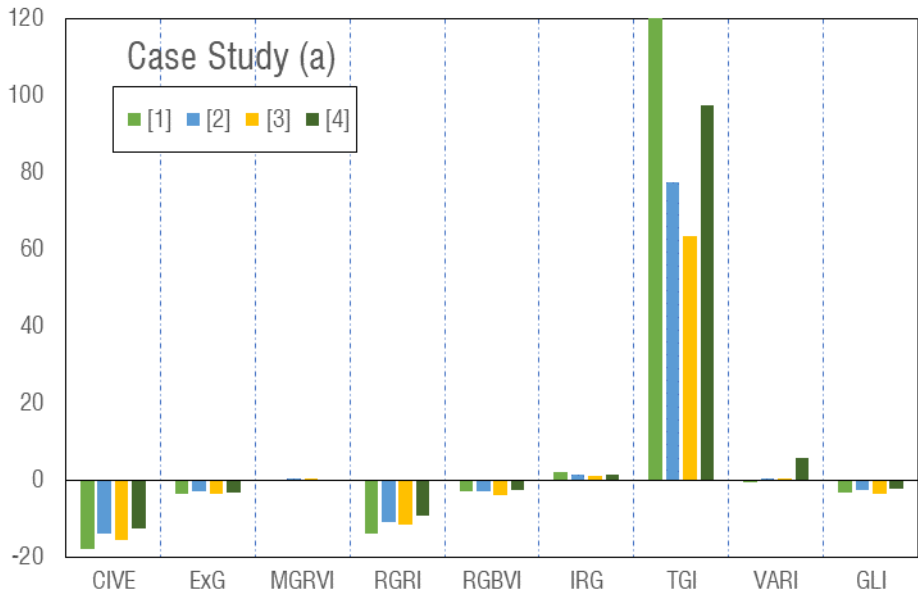
[%]		CIVE	ExG	MGRVI	RGRI	RGBVI	IRG	TGI	VARI	GLI	NGRDI
{1}	(a)	NA	21.7	12.1	-6.0	19.7	-42.4	-564.1	NA	22.5	NA

	(b)	-0.3	40.0	NA	NA	NA	-63.1	-675.3	NA	NA	NA
	(c)	-0.1	16.3	NA	NA	NA	NA	304.7	NA	NA	NA
	(c _{mask})	-0.5	47.3	21.3	-18.5	36.8	-207.2	304.9	NA	32.6	NA
{2}	(a)	-0.1	26.7	14.2	-6.2	26.6	-39.4	-482.1	NA	24.7	13.7
	(b)	-0.3	46.3	NA	NA	NA	NA	3123.2	NA	NA	NA
	(c)	-0.1	15.6	NA	NA	NA	NA	137.1	NA	NA	-12.3
	(c _{mask})	-0.5	44.0	23.3	-19.6	41.5	-316.1	282.0	NA	38.3	NA
{3}	(a)	-0.1	27.9	14.7	-5.4	29.8	-40.1	-350.0	NA	28.3	14.1
	(b)	-0.3	43.7	NA	NA	26.3	-101.5	2201.4	NA	25.9	NA
	(c)	-0.1	14.4	NA	NA	NA	NA	6337.3	NA	NA	-13.8
	(c _{mask})	-0.6	45.5	21.8	-19.6	34.5	-310.4	326.7	NA	27.9	NA
{4}	(a)	-0.1	31.4	11.8	-7.1	25.2	-46.7	-654.8	NA	23.9	NA
	(b)	-0.3	48.9	17.4	NA	32.7	-100.7	531.1	5.7	NA	NA
	(c)	-0.1	14.1	NA	NA	NA	NA	398.5	NA	NA	NA
	(c _{mask})	-0.6	47.2	26.1	-17.9	48.4	-190.4	595.3	NA	47.9	NA

In general, the case study (c_{mask}) tended to give high differences between vegetated and non-vegetated areas regardless of the applied vegetation index, indicating that post-processing of the images by removing areas of ambiguity, such as water, optimises interpretability in the analysis. It was not possible to identify the most challenging environment to work with and try to discriminate vegetation from other areas at any resolution solution. The general trend suggested that as the sampling frequency increases, lower resolutions reduce ambiguities or noise in vegetated areas, thus improving discriminability. From Table 5.3, it can be deduced that within the same trend, some resolutions work better than other lower resolutions and are therefore optimal in describing the radiometric information.

The results of this analysis were shown in Figure 5.7 for each scenario in the various spatial resolution solutions. In Figure 5.7, high values imply that the VI_i index performed better than the NGRDI index; on the contrary, negative values suggest that the

specific index performed worse. Trivially, vegetation indices around zero have comparable performance with the reference index.



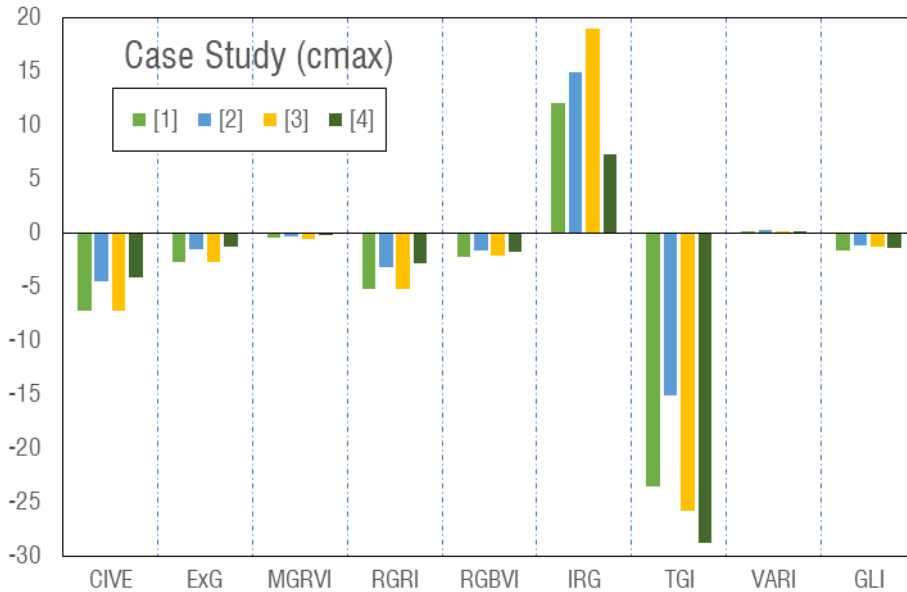


Figure 5.7. Normalised difference (%) for all case studies among all vegetation indices concerning the NGRDI index is considered the reference.

From the results in Figure 5.7, it was observed that the IRG index performed positively in comparison to the NGRDI index for all case studies in any resolution solution. In most cases, the VARI index also exhibited positive behaviour relative to the reference index, except for scenario (a) in resolution {1} in which it takes on a negative but near-zero value of -0.48%. Nevertheless, the IRG and VARI performance did not exhibit efficacies of more than 10%, and in the case of the VARI index, this is almost as good as the NGRDI index. On the other hand, given the considerations from Table 5.3, the VARI index cannot be considered completely efficient. With its acceptability ratio of 0.3125, the IRG index was shown to be non-functional in scenario (c). Therefore, it is based on Figure 5.7, efficient for this work. The latter gives a faintly diminishing efficiency in the case study (a), rising in case (b) and peaking at resolution {3} in case (c_{mask}).

An irregular performance was that of the TGI vegetation index as it provided for case (a) yields of over 60%, up to a maximum of 121% in the different resolutions, while for cases (b) and (c_{mask}) very negative values, excluding case study (c_{mask}) at the first resolution {1} where it even reached a value of 144%.

The rest of the computed vegetation indices, on the other hand, show negative yields compared to the reference index: not extremely high values of less than -20%. It was not feasible to explain a normal behavior of the efficacy of the indices as the implemented resolution varies. In this regard, (Agapiou, 2020b) asserted that for each case study, the optimal index is not unique, which is also in line with the aforementioned results in Table 5.3. Thus, it is not possible to presume an explicit relationship between the resolution of the orthomosaic and the index resumed.

5.4.3. Analysis of Results

The results revealed in the previous paragraph provide some useful matters for arranging an interesting discussion on vegetation extraction in orthomosaics, in various scenarios and at various spatial resolution solutions.

The application of vegetation indices based on visible bands, perhaps from a non-metric camera, emphasizes the potential for discriminating diffuse and routine vegetated areas. Therefore, in order to recognize their limitations and efficiencies, the results presented in Table 5.3 indicated the behaviour of different indices in making high or low separability between vegetated and non-vegetated areas. In several cases, even some indices could not gain significant values and therefore not acceptable at the 95% confidence level of the T-test. As already known in other recent works (Agapiou, 2020b, Jiang et al., 2019, Kwan et al., 2020), it was shown that there cannot be a single index that performs in the same way for the various case studies. Accordingly, it was obvious that each index is appropriate for particular environmental contexts. Therefore, there is a demand to generate an abundant collection of cases to statistically comprehend any similarities between the various indices and the contexts examined.

In this regard, the values of the average acceptability indices allowed us to deduce some issues. The background of some orthomosaics can be extremely complex, such as the case study (c). The results learned in Table 5.3 showed that the masking of highly ambiguous areas, such as areas with the presence of water, completely improves the interpretability of the images. Masking leads to the exclusion of false-

positive points. Discrepancies in the sensitivity of cameras to catch backscattered reflection values at specific wavelengths can be considerable, as has been demonstrated in the past by other studies (Mafanya et al., 2018). In addition to spectral complexity and scenario heterogeneity, some other factors can affect the overall performance of the indices: for example, uneven illumination (low cloud effect), sun exposure (shaded and partially sunny areas) and the presence of dense vegetation. In scenario (b), the SfM-MVS processing of densely vegetated areas produced many noisy and distorted areas. In general, these areas appeared to be a constant source of reconstruction errors due to the low efficiency of SfM techniques in defining unambiguous points. Matching algorithms are weak in identifying stable matching points in vegetated areas, which generates artefacts and distortions that are difficult to resolve (Ludwig et al., 2020). As shown in Table 5.3, this resulted in a loss of efficiency of extraction techniques in vegetated areas. Scenario (a) showed to be more valuable in the application of vegetation indices as it is characterised, even though with a heterogeneous context, by numerous points and areas not subject to high noise. On the other hand, only in this scenario is the TGI index considered to be very effective, given the objections deduced from Table 5.3 and Figure 5.7. This confirms what has already been established: the effectiveness of one vegetation index less than another is linked to the context detected. Another important finding in this matter was that in cases where a ratio of visible band combinations was included in the formulation of the indices (Equations (5.2), (5.3), (5.4), (5.7), (5.8), (5.9)), these did not produce acceptable results in scenarios (b) and (c).

Recent studies (Agapiou, 2020a) showed that the optimal resolution for RS applications was related to the spatial characteristics of the targets under consideration and their spectral properties. Indeed, in (Agapiou, 2020a) the high resolution of an orthomosaic was not always optimal for a given vegetation index in the various case studies. Using low-cost camera sensors, it is assumed that there are overlaps between channels that cannot independently record distinct ranges of wavelengths. As no information is available on this aspect, it is not possible to measure its significance. This problem was first passed on to the radiometric information recorded in the pixels

and then to the formulation of the indices, whose components thus become correlated, as actually observed.

Contemplating Table 5.3, the resolution solution {3} presented a reasonable acceptability ratio for all scenarios. This was not consistent with the magnitude of separability of the examined indices and the efficiency regarding the reference index NGRDI (Figure 5.7). In fact, a reduction in spatial resolution smoothes out the noise or distortion caused in the photogrammetric generation of the ortho-mosaics or resulting from the poor quality of the source images. On the contrary, observing Figure 5.7, it was then evident that each vegetation index does not have a unique behaviour when varying the resolution: each of them has an optimal resolution for each context analysed, thus deducing the complexity of extrapolating a direct relationship between these parameters.

Comparing the observations in Table 5.3 and Figure 5.7, only the IRG index presents advantageous characteristics for all scenarios in each resolution solution. Although its efficiency compared to the NGRDI was less than -5%, a wide use of the ExG index cannot be excluded. This was certainly reliable in discerning vegetated areas in any environment and any resolution solution.

In summary, from the partial results of these tests, the following aspects can be highlighted:

- The performance of each index varies for each case study, as already observed in other works. Therefore, in order to estimate the performance of the indices in general, it is essential to construct a large case study covering as many contexts as possible.
- The TGI index, able to return very significant and functional values in terms of separability between vegetated and non-vegetated areas, performs better than the NGRDI index, taken as a reference, only in a regular context without ambiguous areas. The IRG index, on the other hand, performs well in all scenarios but with moderate performance.

- The high resolution of an orthomosaic was often not optimal for the vegetation indices in the various case studies; by reducing the resolution, the noise in each pixel is smoothed out, improving the radiometric information.
- The masking of areas that are strongly characterised by ambiguity, such as those in the presence of water, improves their interpretability by the indices and increases their performance.
- In areas with dense vegetation, the reduced ability of SfM-MVS techniques to establish and triangulate unambiguous junction points produces obvious artefacts or distortions that compromise the performance of vegetation indices in extracting correct information.

The results of these tests can be applied to any RGB orthomosaic, taken from a low-altitude system or aerial imagery.

5.5. Classification Algorithms Impacts

After examining the statistical comebacks regarding the performance of vegetation indices in terms of separability between vegetated and non-vegetated areas, the impact of the most significant indices in the application of pixel-based classification algorithms was assessed. In particular, taking advantage of radiometrically calibrated RGB orthomosaics and vegetation indices that are performance-qualified in distinguishing different classes, supervised and unsupervised classification approaches were adopted in this research step in order to identify the advantages and disadvantages of each.

As already discussed in the introduction of this chapter, the scientific literature presents a multitude of classification methodologies and the choice, in this research work, fell on pixel-based image analysis algorithms. Pixel-based methods use the red, green and blue bands without any image pre-processing, whereas object-based methods require clustering of what is present in the scene. In object-based image analysis, the analyst is faced with an unavoidable challenge: the determination of the segmentation parameters, in particular the segmentation scale, is often very complex

and, if not supported by certain expertise, is bypassed by a default parameterisation. Since the segmentation parameters depend both on the image resolution and on the objects of interest to be mapped, one often incurs in numerous attempts, in overparameterisation and inevitable errors, as well as in visual analysis, to find acceptable values (Safonova et al., 2021, Shukla and Jain, 2020).

With a view to the democratisation of processes and the definition of a framework, also for photogrammetric post-processing, accessible to end-users with a high degree of comparability, interchangeability and repeatability, the results of pixel-based classifications were tested and analysed.

As described in detail in the following paragraphs, in the same macro-category, supervised and unsupervised classification algorithms are distinguished for the creation of a set of training or non-training pixels to be used in the next step.

Among the former, a distinction is made between automatic and manual classification methods. Automatic classification methods are based on an automated chain of procedures on the input data, including the calculation of spectral indices, their threshold for binary raster classification, the generation of random points and the merging of the training data of the various classes. Manual classification methods, on the other hand, use a conventional polygon created by an expert based on ground truth identification. Precisely, the signature area or training area is created employing an area of interest (AOI) through which class signatures are collected and then applied as seeds for the extraction of the signature used in classification. More than one training area is considered for a class and then merged to overcome the inhomogeneity of the AOIs selected as sample data for the respective class. Fusing the sample data results in a single sample with a wider range of statistics for class discrimination and/or clustering. This establishes the statistical basis for the software to recognise existing classes in a raster file.

At this point, the chosen AOIs may or may not be converted into parametric data representing the spectral properties of the area of interest in the image according to the classification methodology. Parametric classification algorithms assume statistical distributions of any class. A common choice is a normal distribution, which requires

a covariance matrix or mean vector, while non-parametric methods make no assumption of the probability distribution. The parametric signature method includes image classification algorithms such as maximum likelihood, Mahalanobis distance, minimum distance, spectral angle mapping and spectral correlation mapping, while the commonly applied non-parametric signature methods are parallelepiped and feature space. Since the non-parametric method is applied over a wide distribution of class members in a raster file, they are typically considered robust. However, this does not necessarily imply that the accuracy is superior to parametric approaches (Franklin, 2018, Räsänen and Virtanen, 2019).

The time invested in carrying out this step is then spent on training the algorithm, i.e., calibrating it and making it work automatically in the detection of the various features. Once trained, such algorithms on the other hand have usefulness that goes beyond the object of a single work, as they can be applied to other images, thus increasing their practical value for vegetation management (Hamylton et al., 2020).

Manual classification methods produce accurate results for vegetation and bare soil classification limited to narrow spectral cases. The automatic pixel-based method has a specific disadvantage regarding the time efficiency of the algorithm, as the time required for its completion is strongly influenced by the separate polygons created by the threshold of the values of the vegetation indices used, which depends on the level of noise in the UAV images.

Unsupervised classification is considered an iterative procedure with no need for prior information (Gašparović et al., 2020). In general, these methods are considered as clustering algorithms, which calculate distance functions and group similar pixel values into a spectral class. In the final step, the generated classes are recognised and labelled based on the colour composition of the image and field observations. Finally, these classes can be divided into the desired classes. The output classes, however, may not correspond to any of the classes of interest, as they represent spectral classes.

At the end of each classification procedure, sets of test samples must be considered to verify the accuracy and precision of the classification. In the supervised cases, the

data vectorized as AOIs are divided randomly, with 30% of the data being added to a training set for classification and 70% for evaluating the accuracy of the classification results. In general, however, two different sets can be constructed so that the test samples can be considered independent and can also be used in cases of unsupervised classification. At the end of the comparison between the assigned classification and that estimated by the algorithm, a confusion matrix is extracted from which the robustness and accuracy of the process can be deduced.

The automatic classification algorithm could potentially be improved by adding data from any NIR and/or Red-Edge bands to the simple RGB bands, due to the known limitations of vegetation analysis using data from the visible part of the spectrum. In other cases, one could combine data from the digital orthomosaic with height data from a DEM, created photogrammetrically using the same inputs. In this research step, however, information obtained from the calculation of the vegetation indices in the previous paragraphs were used. Considering the asserted evaluations of their ability to separate vegetated and non-vegetated areas, the best performing vegetation indices were used for each case under study to assess possible improvements in classification results.

Orthomosaics in the radiometrically calibrated visible bands and vegetation maps in the TGI and IRG indices were exported from QGIS software and uploaded to the open-source Sentinel Application Platform (SNAP) developed by Brockmann Consult, Skywatch, Sensar and CS and provided free of charge by ESA/ESRIN. The SNAP design is ideal for EO processing and analysis due to these technological advances: extensibility, portability, modular rich client platform, generic EO data abstraction, tiled memory management and graphics processing framework. Created essentially for the Sentinel Toolboxes, the platform and the various integrated tools support numerous sensors other than Sentinel sensors. In this work, photogrammetric products derived from UAV technologies were used.

SNAP provides several supervised and unsupervised raster image classification algorithms. For this tests, the processing chains concerning classifications with super-

vised Random Forest (RF) (Breiman, 2001) and unsupervised K-Means Clustering (Jung et al., 2014) algorithms were adopted.

5.5.1. Supervised Random Forest Algorithm

A fast and objective tool for feature selection is a decision tree, as it is a non-parametric statistical technique that is not affected by outliers and correlations, can reveal interactions between variables and is also an excellent data reduction tool. In a decision tree, a set of data is successively subdivided into increasingly homogeneous subsets until terminal nodes are determined. For example, a common partitioning rule in decision trees is the Gini index, which returns a measure of heterogeneity: zero if all observations in a node belong to the same class; vice versa, 1 when the different class sizes in the node are equal. The results of the decision trees can be used by applying derived class prediction rules or by using the decision trees as a feature selection tool. The prediction success, the cross-validated error rate of the tree and the purity of the terminal nodes, together with the separability of the classes and the accuracy of the additional analyses, serve as an indication of the efficiency of the processes. A single decision tree is not performance-adequate to undertake highly complex feature classification and multi-class dimension prediction.

The Random Forest, on the other hand, is a tree-based machine learning algorithm that utilizes the power of multiple decision trees to get predictions.

The decision tree classifier is still a pixel-based classification method that executes multi-stage classifications employing a series of binary decisions to separate pixels into different classes. Each decision divides the pixels of an image (or several images) into two classes on the basis of an expression. This large number of entities, relatively uncorrelated decision trees essentially operate as a committee to outperform the individual constituent models. Each individual tree in the random forest makes a class prediction and the class with the most votes become the model prediction.

The low correlation among the models is the key to the proficiency of the whole. In this sense, the trees protect each other from their individual errors, as long as they are not all consistently in the same direction. While some trees may be wrong, many

others can move as a group in the correct direction. For the random forest to work, the predictions and thus the errors made by individual trees must have low correlations with each other.

To this end, the algorithm requires that among the plotted training areas there are actual signals of the features sought so that the models generated using these features perform better than the random hypotheses screened at some nodes. In addition, the algorithm makes use of the method of Bootstrap Aggregation. In practice, decision trees are very sensitive to the data on which they are trained: small changes to the training set can result in significantly different tree structures. However, the random forest takes advantage of this by allowing each individual tree to randomly sample from the data set with replacement, resulting in different trees. This process is known as bagging. This imposes even more variation between trees in the model and eventually results in less correlation between trees and more diversification. Thus, in Random Forest algorithms, decision trees are not only trained on different datasets through bagging but also use different features to make decisions.

Machine learning algorithms have been increasingly used to classify large amounts of complex data, especially high-resolution UAV images. These algorithms are superior to conventional supervised classification algorithms in terms of classification accuracy and time efficiency (Belgiu and Stein, 2019, Gašparović et al., 2020). (De Castro et al., 2018) suggested that the random forest (RF) machine learning algorithm was the best for classification automation, as it requires far fewer classification parameters than similar machine learning techniques.

Orthomosaics in the radiometrically calibrated RGB bands of the three scenarios and the four spatial resolution solutions were uploaded into SNAP. Given the observations discussed in Section 5.4.3, vegetation maps of the TGI and IRG indices were exported from QGIS software and loaded into the SNAP workspace for the spatial resolution solutions of each scenario, respectively.

The blue, green and red spectral channels of each subset served as input in plotting the AOIs of three classes: vegetation, asphalt, and bare soil. Areas were identified on

the visual basis of RGB orthomosaics displayed in the workspace. These areas were collected in vector bins, which could be retrieved by the RF classification algorithms. The collection was organised in such a way as to consider it balanced by classes, following the recommendations of (Belgiu and Stein, 2019) and (Gašparović et al., 2020). Due to the low flight height, UAV images cover a relatively small footprint on the ground, but the number of pixels in the image is relatively high due to the high resolution. Therefore, the analysis of UAV images can be even more intensive than the analysis of traditional aerial and satellite images. Therefore, 10 AOIs per class were plotted, attempting to collect within them the spectral variability and texture of each class (Figure 6.8). The methodology used to create a training dataset for the automatic methods ensures that the training data always covers the same percentage of area for each class, which guarantees the usability and robustness of the algorithm.





Figure 5.8. Example of AOI vectors identified in scenario (a). In fuchsia AOIs concerning asphalt, in blue those concerning bare soil and in green those concerning vegetation.

In the case of parametric files, AOIs are converted into statistical parameters. In order to generate input class parameters for each AOI, the signature editor is required, and this tool is useful for analysing the distribution of signatures in the containers of AOI vectors. The distributions of the AOI vector bins (vegetation, asphalt, and bare ground) for the investigated scenarios and the adopted spatial resolutions are analysed below (Figures 5.9-5.13).

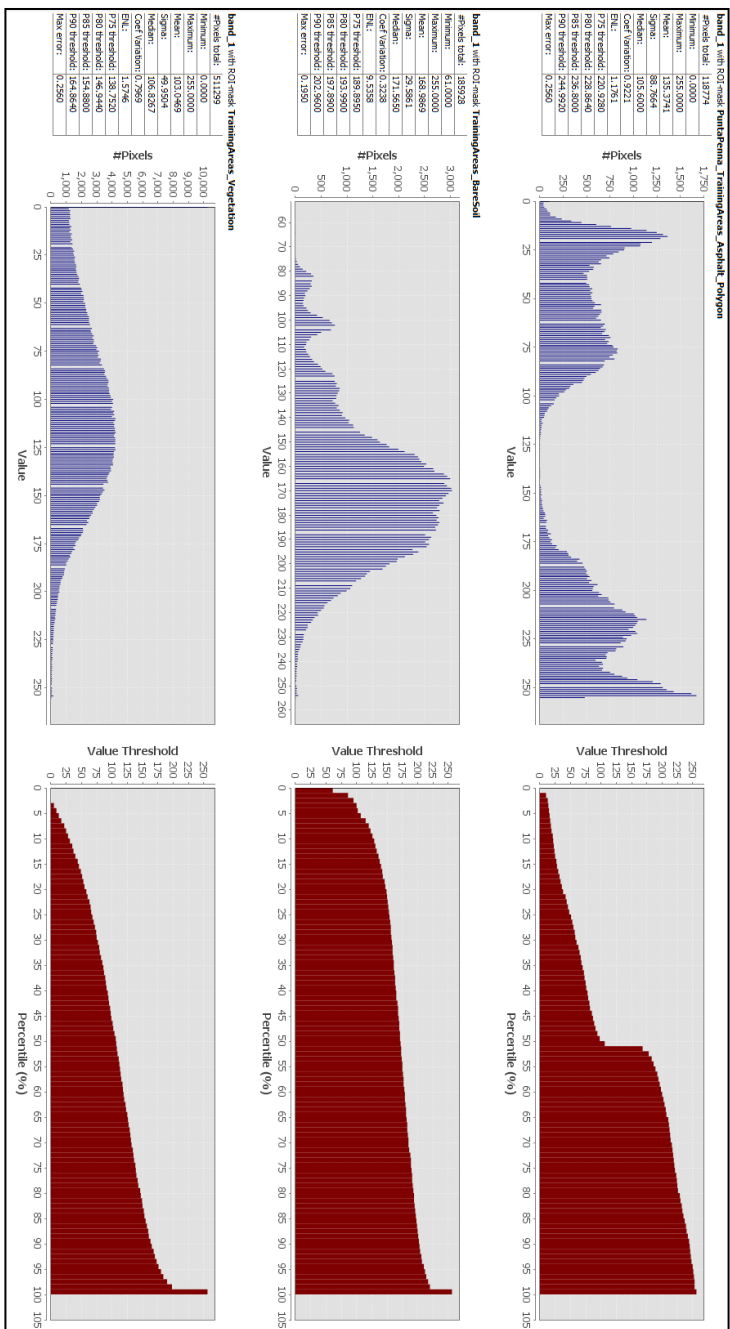


Figure 5.9. Statistical distribution of signatures in the containers of AOI vectors regarding Band 1 for asphalt, bare soil and vegetation.

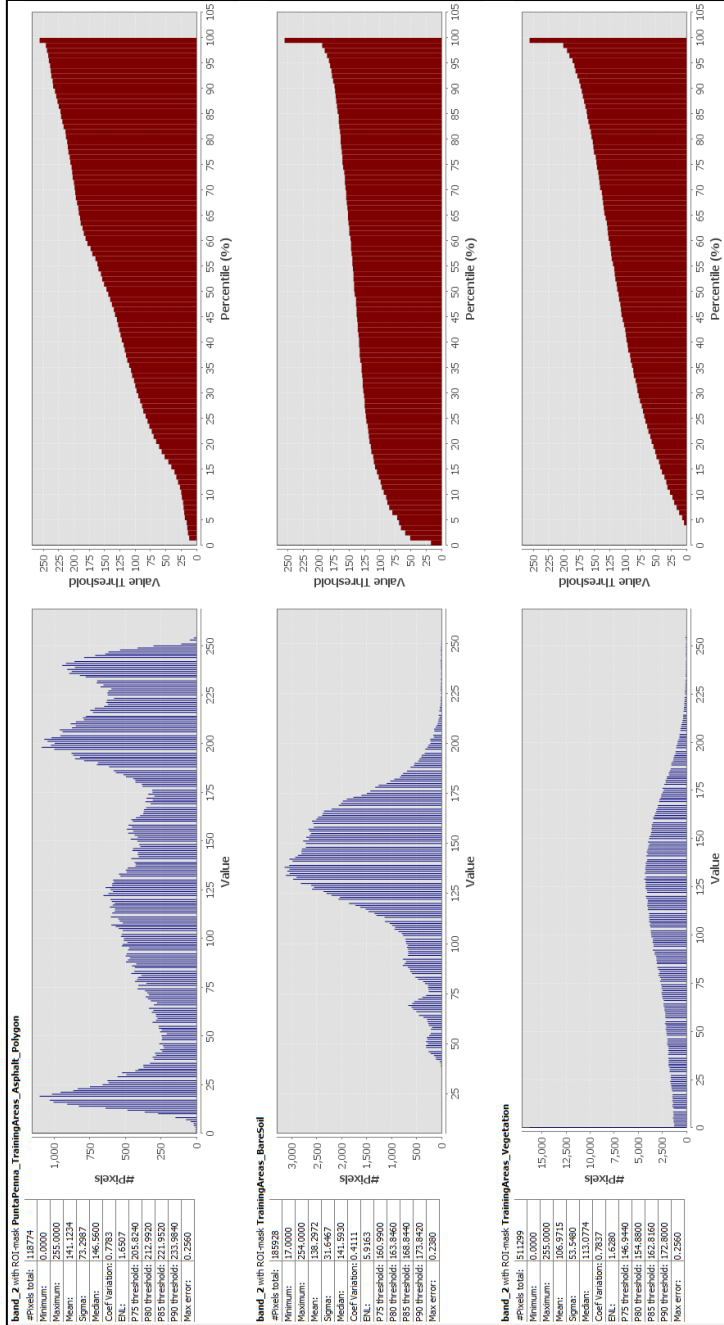


Figure 5.10. Statistical distribution of signatures in the containers of AOI vectors regarding Band 2 for asphalt, bare soil and vegetation.

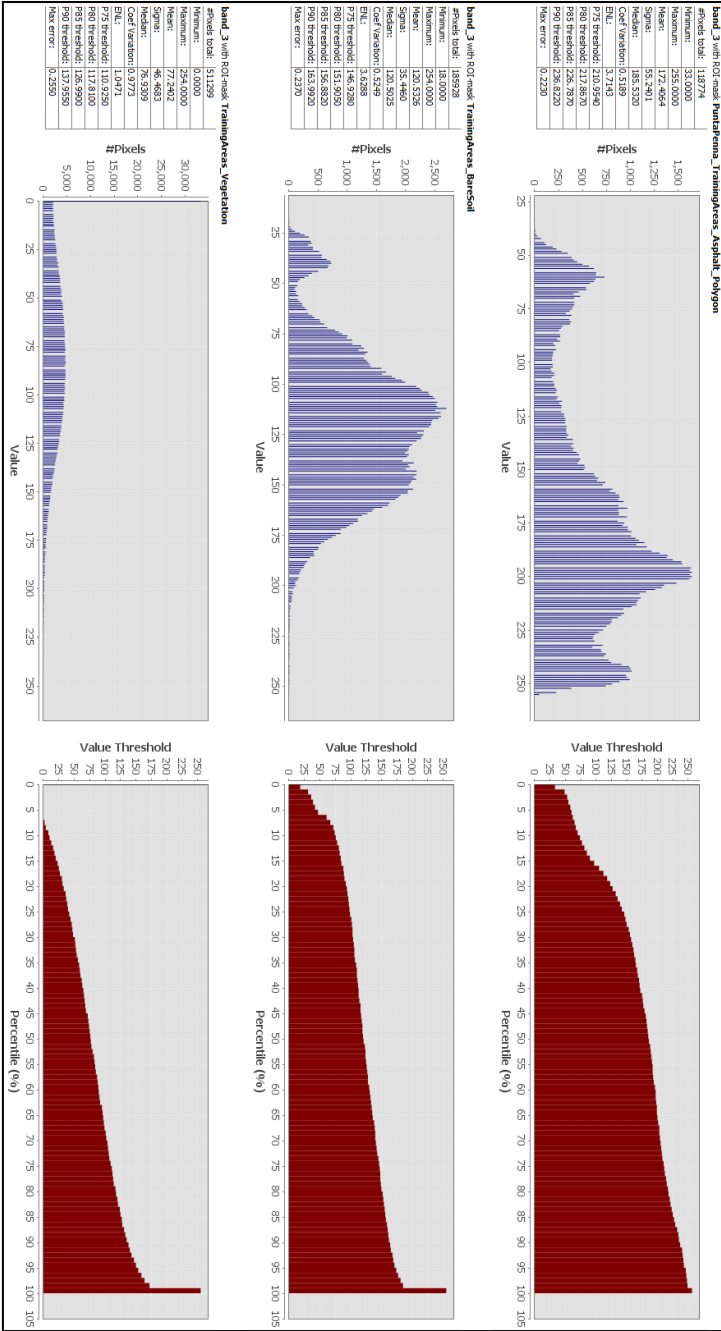


Figure 5.11. Statistical distribution of signatures in the containers of AOI vectors regarding Band 3 for asphalt, bare soil and vegetation.

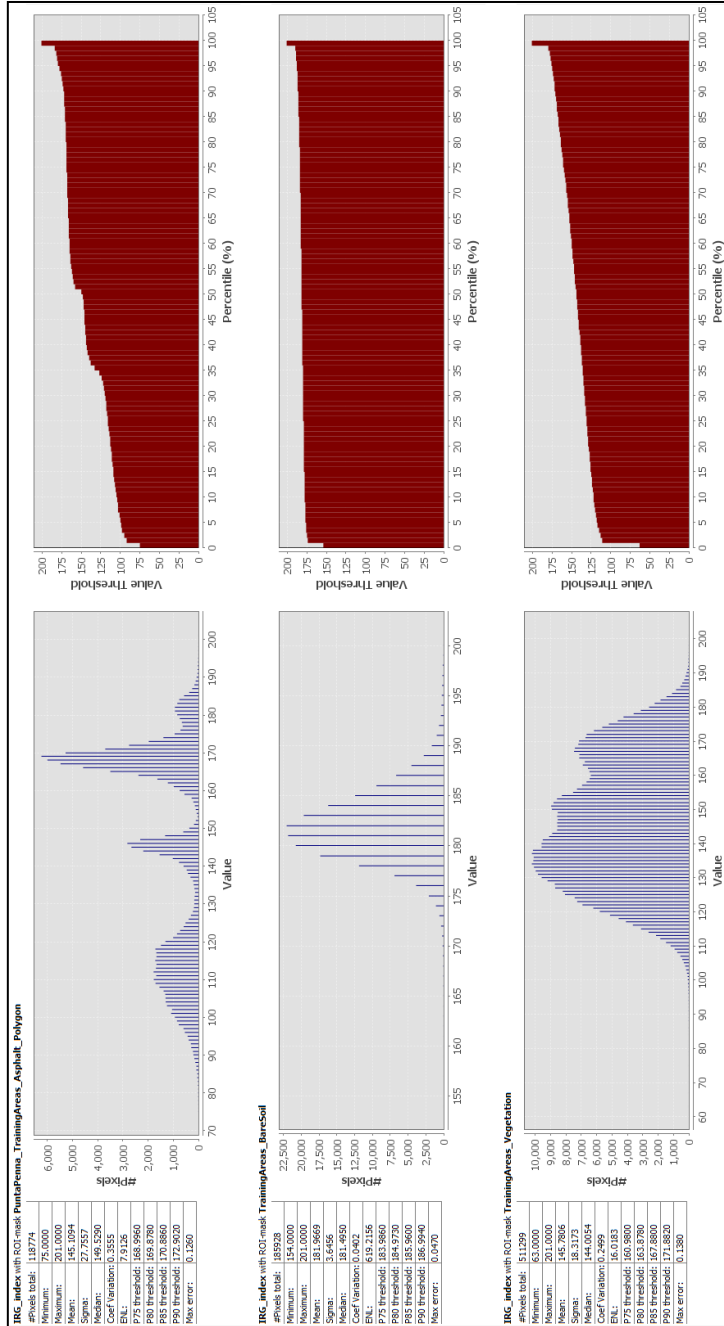


Figure 5.12. Statistical distribution of signatures in the containers of AOI vectors regarding Band IRG index for asphalt, bare soil and vegetation.

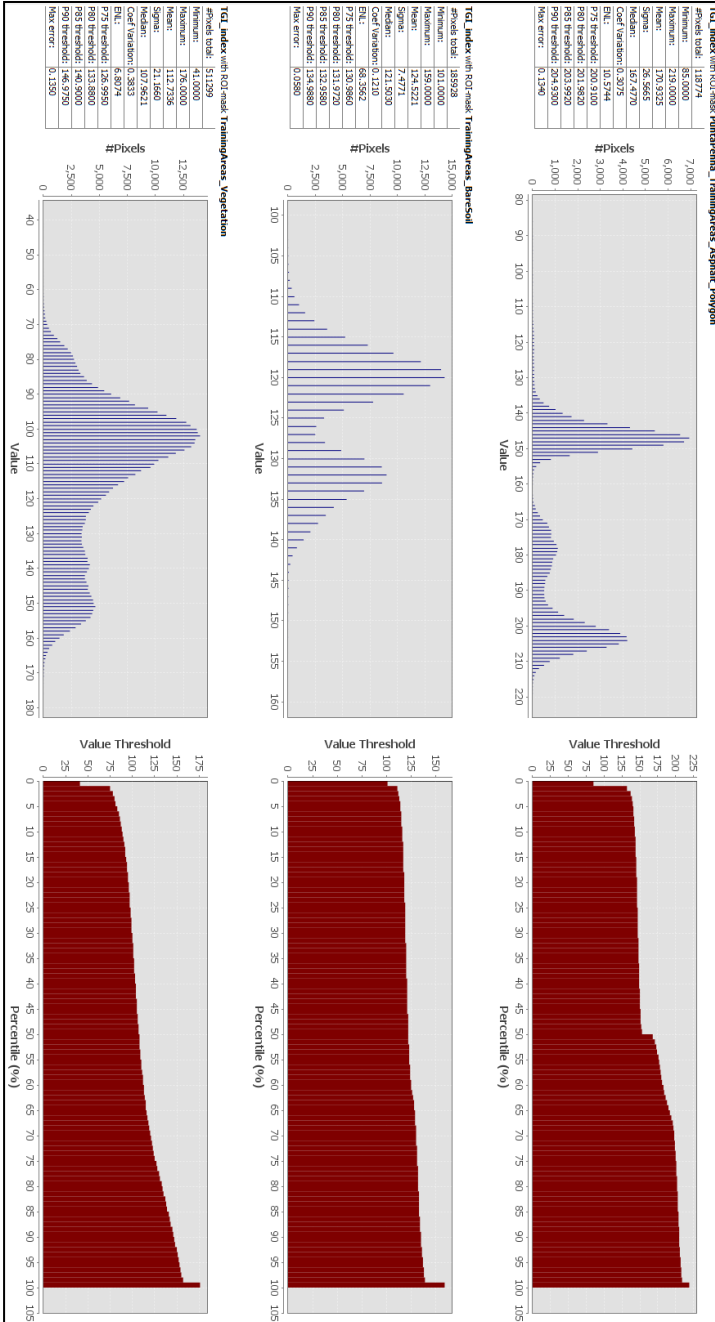
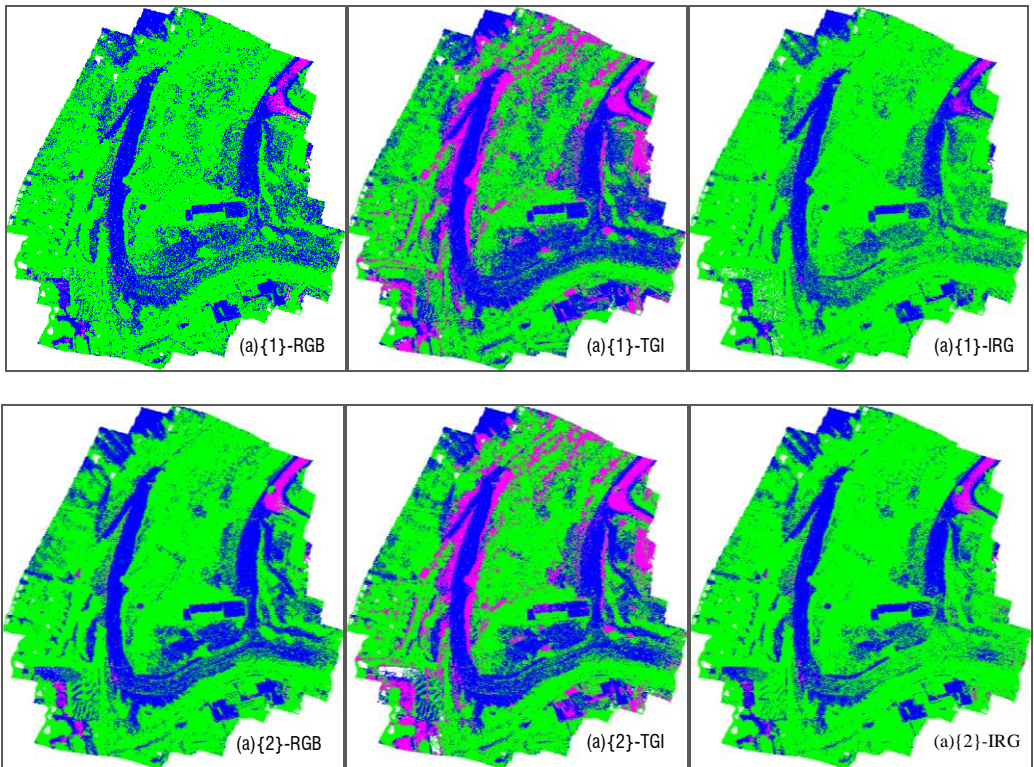
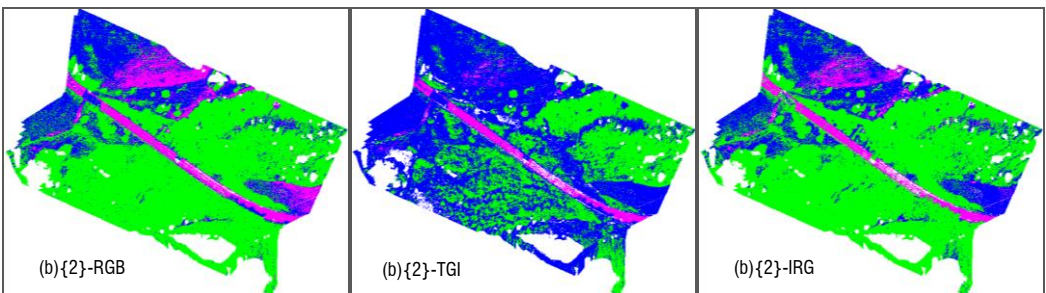
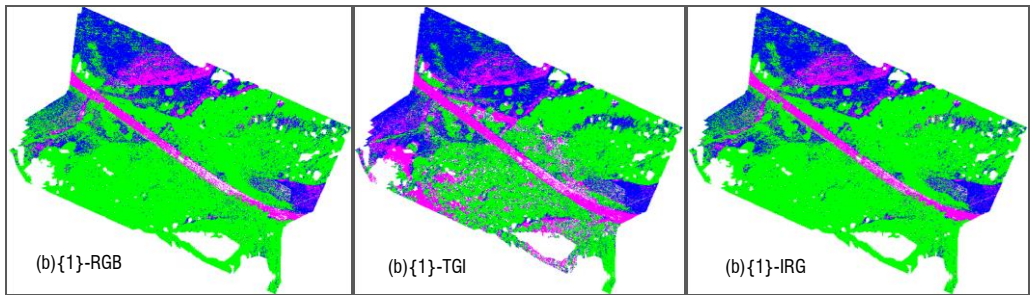
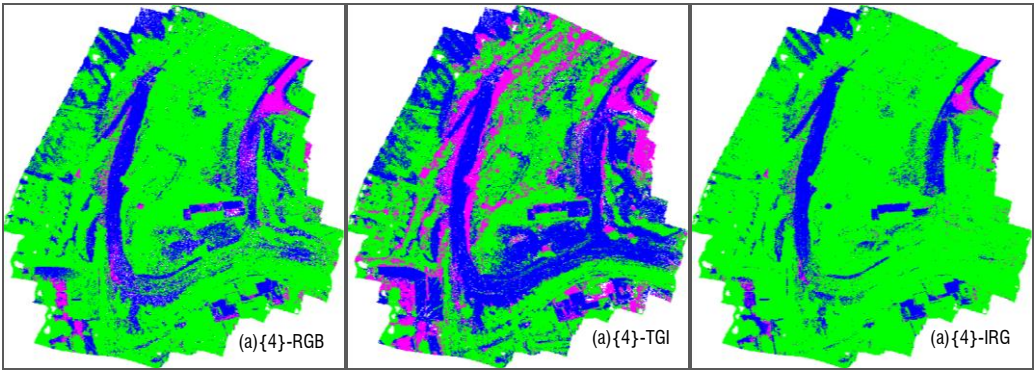
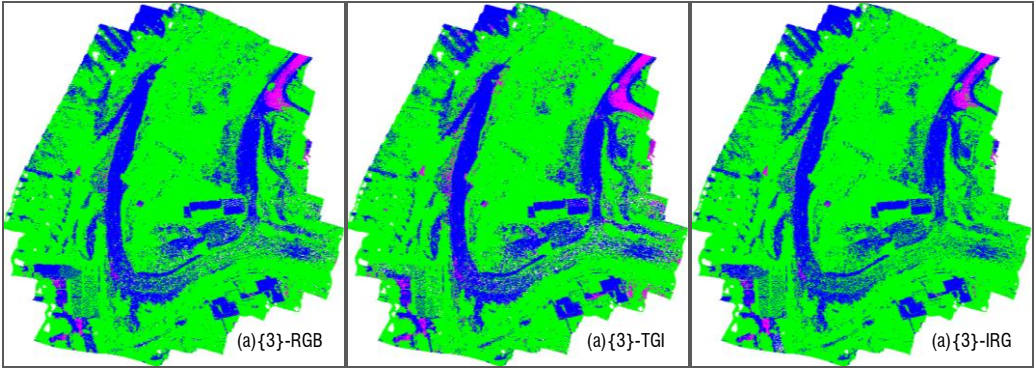
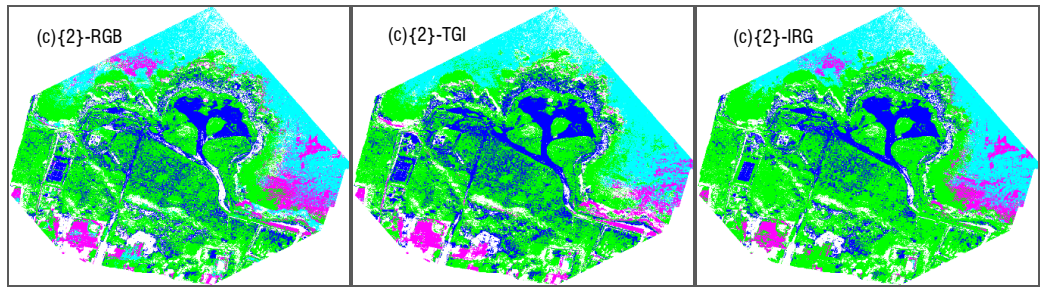
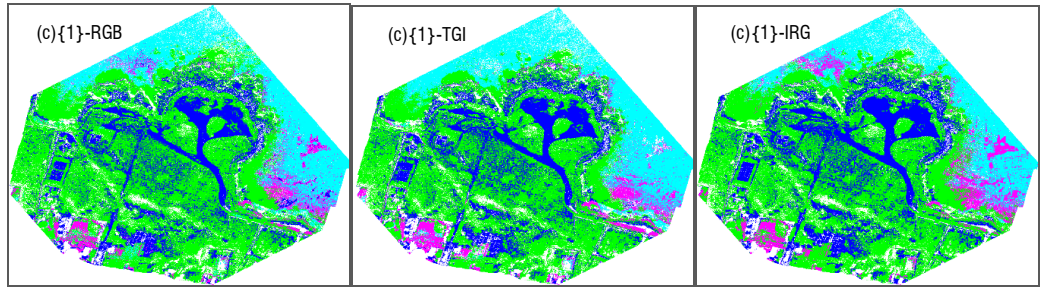
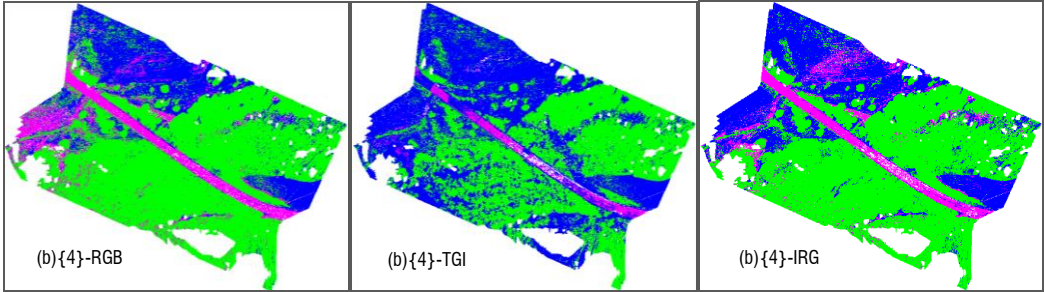
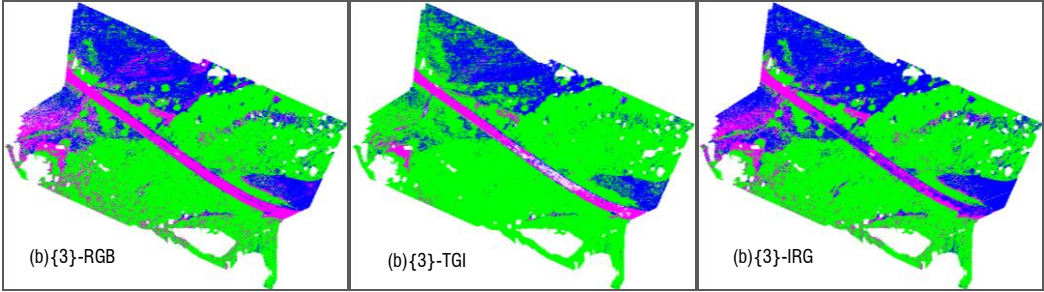


Figure 5.13. Statistical distribution of signatures in the containers of AOI vectors regarding Band TGI index for asphalt, bare soil and vegetation.

In order to verify and validate the classification results, 30 pins for each prediction class were distributed in each investigated scenario to perform the bootstrapping method. These pins represent ground truths digitally identified by the orthomosaics themselves and assigned to a certain class. Once the classification processes are complete, the predictions of the classes in the pins can be compared with the previously assigned classes and confusion matrices can be constructed. After the processes were completed, the supervised Random Forest algorithms were started.







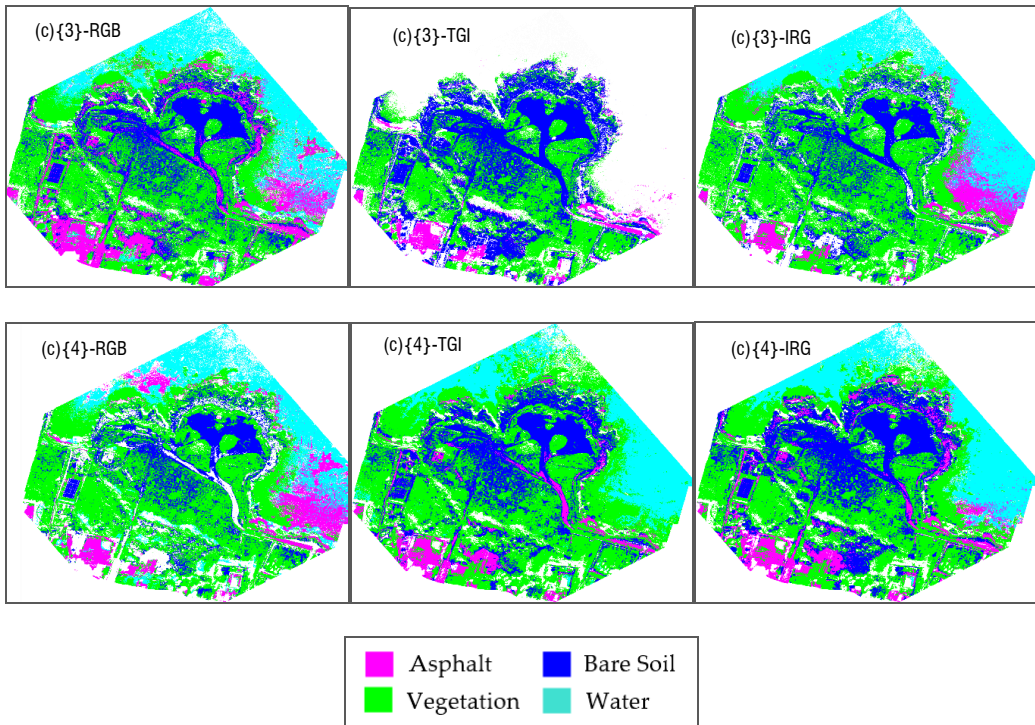


Figure 5.14. RF maps for all cases analysed.

5.5.2. Unsupervised K-Means Cluster Algorithm

Clustering is an important means in general of data mining, but also of algorithms capable of separating data of a similar nature. Unlike the classification algorithm discussed in Section 5.5.1, clustering belongs to the type of unsupervised algorithms. Clustering involves dividing a large dataset into a multiplicity of data clusters, which reveal some characteristics of each subset. It is accomplished by estimating similarity or closeness based on the distance measurement method and intends to find a structure (intrinsic clustering) in an unlabelled collection of data. A cluster is thus an assortment of objects that are similar to each other and are “dissimilar” to objects belonging to other clusters.

One of the most characteristic and commonly used clustering algorithms for performing unsupervised classifications of rasters got from RS is the so-called K-means Algorithm. (Tang et al., 2017) effectively integrated a K-means method with a machine

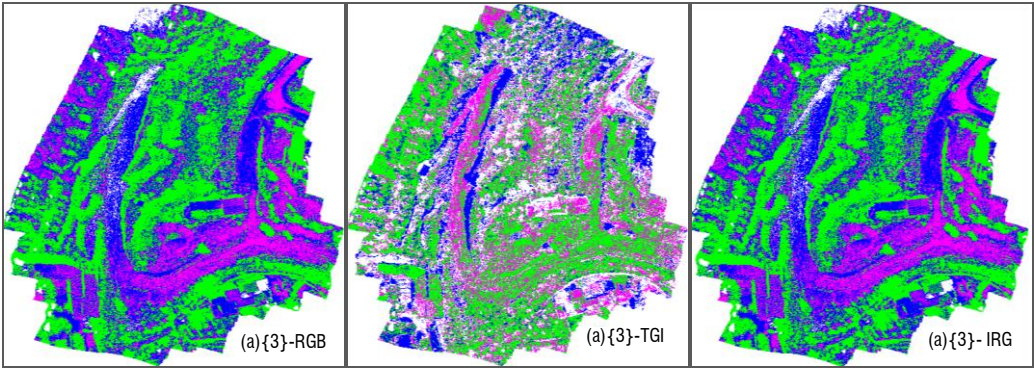
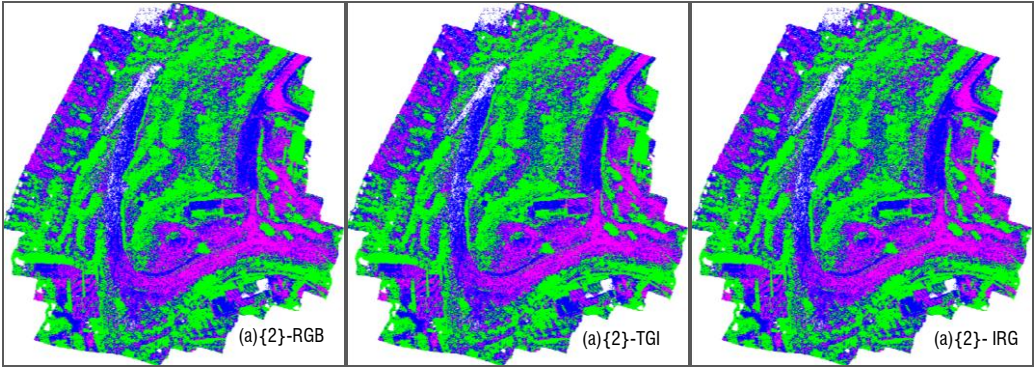
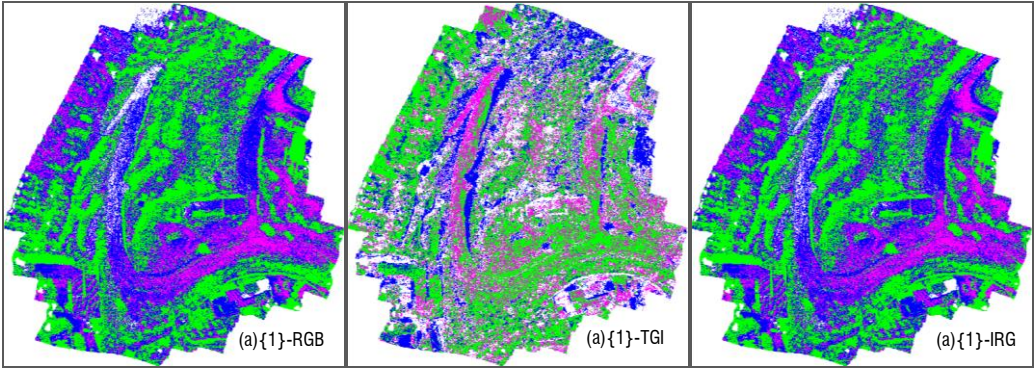
learning algorithm for weed detection. (Vrindts et al., 2005) used revised K-means clustering to determine management zone gradation using soil and crop data.

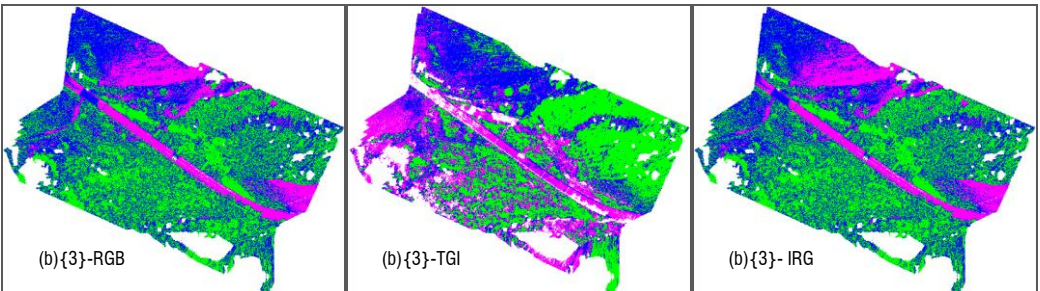
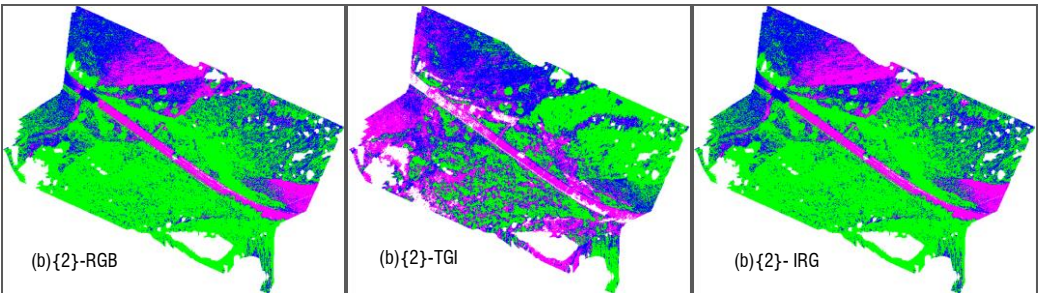
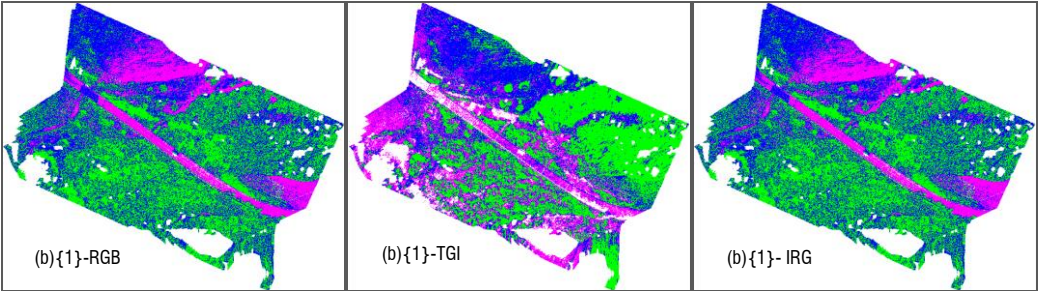
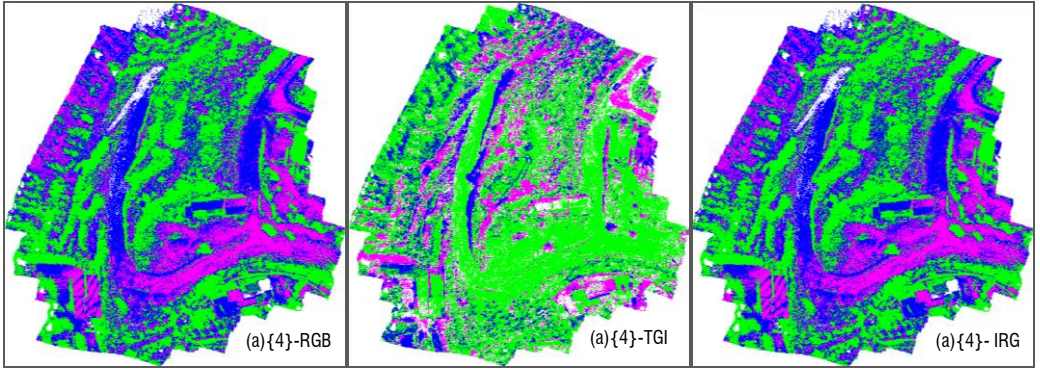
The latter is presented as a structured iterative process to refine the cluster modelling and thus find the best congestion. The cluster analysis procedure is analysed to determine the properties of the dataset and the target variable and is typically used to determine how to measure the similarity distance.

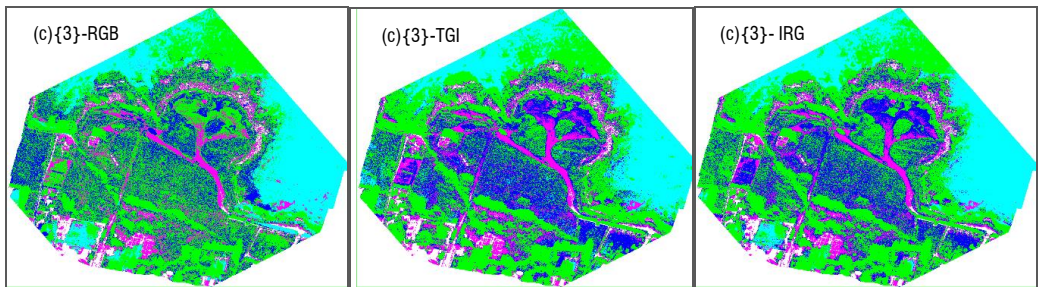
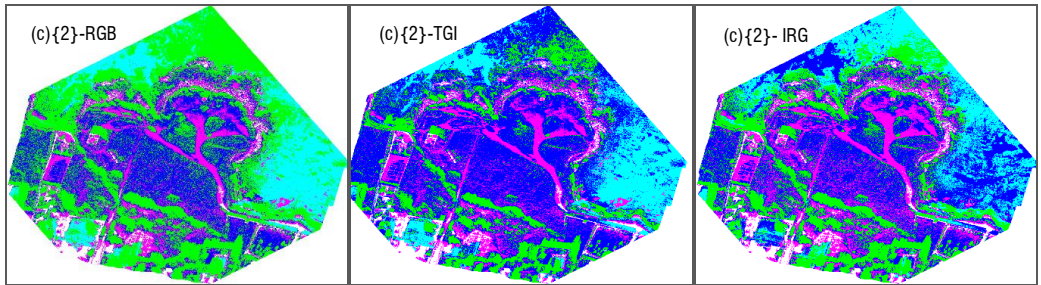
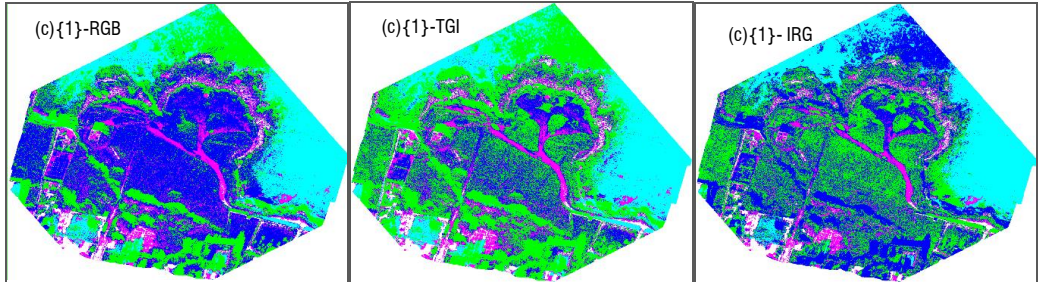
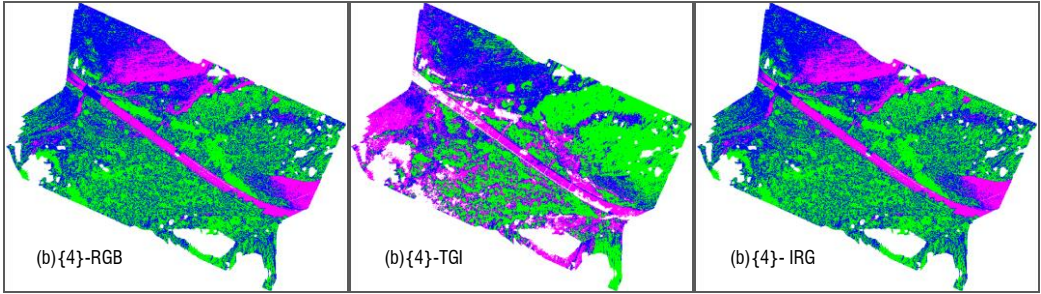
As described in (Jung et al., 2014), the algorithm requires as input the number of k centroids for each cluster and a database containing n data items, representing the set of all instances analysed by the algorithm. The centroids are imaginary or real points at the centre of a cluster from which the Euclidean distances to other data will be evaluated. Iteratively the algorithm evaluates these data distances from the centroids, and each is reassigned to the cluster to which the object is most similar based on the average value of the objects in the cluster. As the average value is updated, iteratively re-assignments occur until no more changes occur, i.e., a point of convergence is reached where no more cluster changes occur.

The k-means algorithm has the advantage of being quite fast, as few calculations and consequently, little computer processing time is required to calculate the distances between the data and the centroids at each iteration. On the other hand, k-means has a couple of disadvantages. Firstly, it is necessary to select how many k groups you wish to visualise. This is not always trivial as it is not always possible to do this, especially for problems of higher complexity. In addition, K-means also starts with a random choice of centroids and therefore may produce different clustering results on different sequences of the algorithm. Consequently, the outcomes may not be repeatable and lack consistency.

In the SNAP software, the unsupervised K-Means classification algorithms were started and using the pins already identified in the previous paragraph, the accuracy of this classification methodology was evaluated with the relative Confusion Matrix metrics.







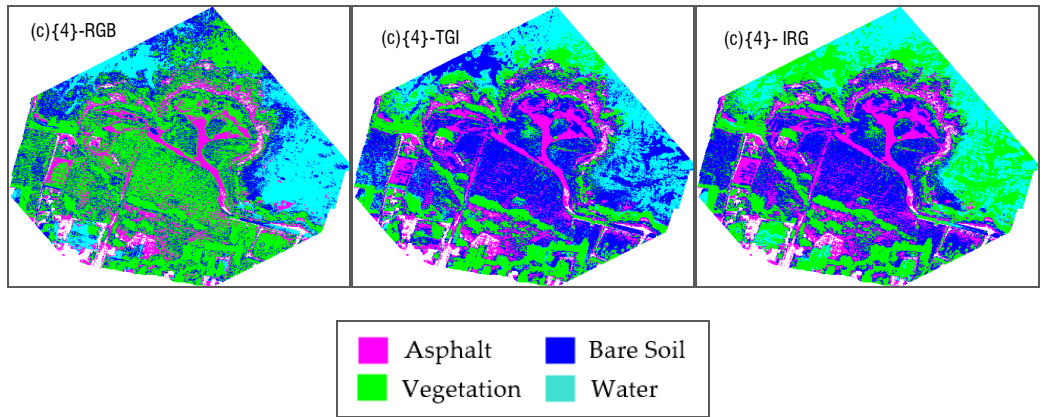


Figure 5.15. K-Means algorithm results for all cases analysed

5.5.3. Confusion Matrix Metrics

After the algorithms have been successfully executed, the classification results are evaluated for accuracy based on truth data. The bootstrapping method was adopted to allow a formal statistical comparison of the accuracy of the classification approaches adopted.

Adopting the guidance given in (Hossin and Sulaiman, 2015), the following metrics are computed to quantify the accuracy of the extracted features:

- Error Rate (ERR) is calculated as the number of all incorrect predictions divided by the total number of the dataset. The best error rate is 0 and the worst is 1.

$$ERR = \frac{FP+FN}{TN+FP+FN+TP} \quad (5.1)$$

- Accuracy indicates the accuracy of the model as the name implies. Therefore, the best accuracy is 1, while the worst is 0.

$$Accuracy = \frac{TP+TN}{TN+FP+FN+TP} \quad (5.2)$$

- Precision is the ability of a classifier not to label a positive instance that is negative. For each class, it is defined as the ratio of true positives to the sum of true and false positives.

$$Precision = \frac{TP}{TP+FP} \quad (5.3)$$

- Recall: also called sensitivity, is the ability of a classifier to find all positive instances. For each class, it is defined as the ratio between true positives and the sum of true positives and false negatives.

$$Recall = \frac{TP}{TP+FN} \quad (5.4)$$

- Specificity (SP): is calculated as the number of correct negative predictions divided by the total number of negatives (N). It is also called true negative rate (TNR). The best specificity is 1, while the worst is 0. This formula can be used for the calculation:

$$SP = \frac{TN}{TN+FP} = \frac{TN}{N} \quad (5.5)$$

- False-positive rate: The false-positive rate (FPR) is calculated as the number of incorrect positive predictions divided by the total number of negatives. The best false positive rate is 0 while the worst is 1.

$$FPR = \frac{FP}{TN+FP} = 1 - SP \quad (5.6)$$

- F-Score: is a weighted harmonic average of the Precision and Recall metrics such that the best score is 1 and the worst is 0.

$$F - Score = \frac{2 * Recall * Precision}{Recall + Precision} \quad (5.7)$$

For this purpose, True Positives (TP), True Negatives (TN), False Positives (FP) and False Negatives (FN) are estimated for the vegetation, asphalt and bare soil classes based on ground truth data. TP represents the correctly classified objects for the given class among all extracted objects, FP represents the falsely classified objects among the extracted objects, and FN is the missed or not extracted objects. Finally, TN represents the objects correctly classified among all extracted objects but not within the class in question.

Confusion matrices are thus constructed for each spatial resolution of each scenario for three cases of classification, both supervised and unsupervised: using only the

visible (RGB) bands, adding to these the vegetation map of the TGI index and, finally, adding to the RGB bands the information of the IRG index. From these matrices, the metrics proposed in Tables 5.4 and 5.5 are extrapolated.

Table 5.4. Confusion matrices and related metrics for the analysed cases of RF supervised classification.

(a): Supervised RF Classification - RGB

	{1}			{2}			{3}			{4}		
	V	A	B	V	A	B	V	A	B	V	A	B
<i>Error Rate</i>	0.23	0.26	0.17	0.18	0.19	0.27	0.31	0.22	0.28	0.26	0.14	0.24
<i>Accuracy</i>	0.78	0.74	0.83	0.82	0.81	0.73	0.69	0.78	0.73	0.74	0.86	0.76
<i>Precision</i>	0.63	0.57	1.00	0.90	1.00	0.63	0.54	0.94	0.72	0.58	0.88	0.91
<i>Recall</i>	1.00	1.00	0.57	0.60	0.50	0.57	1.00	0.50	0.43	1.00	0.77	0.34
<i>Specificity</i>	0.64	0.60	1.00	0.96	1.00	0.82	0.52	0.98	0.90	0.60	0.93	0.98
<i>False Positive Rate</i>	0.36	0.40	0.00	0.04	0.00	0.18	0.48	0.02	0.10	0.40	0.07	0.02
<i>F-Score</i>	0.77	0.72	0.72	0.72	0.67	0.60	0.70	0.65	0.54	0.73	0.82	0.50
Mean F-Score	0.68			0.72			0.63			0.68		

(a): Supervised RF Classification - TGI

	{1}			{2}			{3}			{4}		
	V	A	B	V	A	B	V	A	B	V	A	B
<i>Error Rate</i>	0.11	0.06	0.16	0.13	0.04	0.13	0.20	0.13	0.24	0.11	0.06	0.16
<i>Accuracy</i>	0.89	0.94	0.84	0.88	0.96	0.87	0.80	0.87	0.76	0.89	0.94	0.84
<i>Precision</i>	0.77	0.96	0.83	0.73	0.97	0.95	0.64	0.92	0.74	0.77	0.93	0.86
<i>Recall</i>	1.00	0.87	0.67	1.00	0.93	0.63	1.00	0.73	0.47	1.00	0.90	0.63

<i>Specificity</i>	0.84	0.98	0.93	0.81	0.98	0.98	0.68	0.96	0.91	0.84	0.96	0.95
<i>False Positive Rate</i>	0.16	0.02	0.07	0.19	0.02	0.02	0.32	0.04	0.09	0.16	0.04	0.05
<i>F-Score</i>	0.87	0.91	0.74	0.85	0.95	0.76	0.78	0.81	0.57	0.87	0.92	0.73
Mean F-Score	0.84			0.85			0.72			0.84		

(a): Supervised RF Classification - IRG

	{1}			{2}			{3}			{4}		
	V	A	B	V	A	B	V	A	B	V	A	B
<i>Error Rate</i>	0.33	0.26	0.35	0.33	0.22	0.30	0.31	0.22	0.28	0.33	0.16	0.29
<i>Accuracy</i>	0.67	0.74	0.65	0.67	0.78	0.70	0.69	0.78	0.73	0.67	0.84	0.71
<i>Precision</i>	0.54	1.00	0.52	0.52	1.00	0.67	0.54	0.94	0.72	0.51	0.95	0.80
<i>Recall</i>	1.00	0.37	0.40	1.00	0.47	0.40	1.00	0.50	0.43	1.00	0.67	0.27
<i>Specificity</i>	0.47	1.00	0.79	0.48	1.00	0.88	0.52	0.98	0.90	0.49	0.97	0.96
<i>False Positive Rate</i>	0.53	0.00	0.21	0.52	0.00	0.12	0.48	0.02	0.10	0.51	0.03	0.04
<i>F-Score</i>	0.70	0.54	0.45	0.68	0.64	0.50	0.70	0.65	0.54	0.67	0.78	0.40
Mean F-Score	0.56			0.61			0.63			0.62		

b): Supervised RF Classification - RGB

	{1}			{2}			{3}			{4}		
	V	A	B	V	A	B	V	A	B	V	A	B
<i>Error Rate</i>	0.13	0.14	0.16	0.06	0.20	0.24	0.03	0.05	0.08	0.06	0.06	0.11
<i>Accuracy</i>	0.87	0.86	0.84	0.94	0.80	0.76	0.97	0.95	0.92	0.94	0.94	0.89
<i>Precision</i>	0.76	0.80	0.87	0.88	0.69	0.68	0.91	0.88	1.00	0.88	0.75	1.00

<i>Recall</i>	0.97	0.77	0.67	1.00	0.71	0.57	1.00	1.00	0.77	1.00	1.00	0.73
<i>Specificity</i>	0.82	0.91	0.94	0.90	0.84	0.86	0.95	0.93	1.00	0.89	0.93	1.00
<i>False Positive Rate</i>	0.18	0.09	0.06	0.10	0.16	0.14	0.05	0.07	0.00	0.11	0.07	0.00
<i>F-Score</i>	0.85	0.78	0.75	0.94	0.70	0.62	0.95	0.94	0.87	0.94	0.86	0.85
<i>Mean F-Score</i>	0.80			0.75			0.92			0.88		

(b): Supervised RF Classification - TGI

	{1}			{2}			{3}			{4}		
	V	A	B	V	A	B	V	A	B	V	A	B
<i>Error Rate</i>	0.04	0.08	0.11	0.01	0.10	0.11	0.13	0.03	0.15	0.01	0.03	0.04
<i>Accuracy</i>	0.96	0.92	0.89	0.99	0.90	0.89	0.87	0.97	0.85	0.99	0.97	0.96
<i>Precision</i>	0.91	0.87	0.88	0.97	1.00	0.76	0.73	1.00	0.90	0.97	0.85	1.00
<i>Recall</i>	1.00	0.90	0.77	1.00	0.68	0.97	1.00	0.92	0.63	1.00	1.00	0.90
<i>Specificity</i>	0.94	0.93	0.95	0.98	1.00	0.84	0.79	1.00	0.96	0.97	0.97	1.00
<i>False Positive Rate</i>	0.06	0.07	0.05	0.02	0.00	0.16	0.21	0.00	0.04	0.03	0.03	0.00
<i>F-Score</i>	0.95	0.88	0.82	0.98	0.81	0.85	0.85	0.96	0.75	0.98	0.92	0.95
<i>Mean F-Score</i>	0.89			0.88			0.85			0.95		

(b): Supervised RF Classification - IRG

	{1}			{2}			{3}			{4}		
	V	A	B	V	A	B	V	A	B	V	A	B
<i>Error Rate</i>	0.09	0.13	0.12	0.11	0.15	0.12	0.01	0.13	0.14	0.01	0.02	0.03
<i>Accuracy</i>	0.91	0.87	0.88	0.89	0.85	0.88	0.99	0.87	0.86	0.99	0.98	0.97

<i>Precision</i>	0.81	0.81	0.92	0.77	0.82	0.88	0.97	0.85	0.76	0.97	0.94	1.00
<i>Recall</i>	1.00	0.78	0.73	1.00	0.67	0.77	1.00	0.73	0.83	1.00	1.00	0.90
<i>Specificity</i>	0.86	0.91	0.96	0.82	0.93	0.94	0.98	0.93	0.87	0.98	0.97	1.00
<i>False Positive Rate</i>	0.14	0.09	0.04	0.18	0.07	0.06	0.02	0.07	0.13	0.02	0.03	0.00
<i>F-Score</i>	0.90	0.79	0.81	0.87	0.73	0.82	0.98	0.79	0.79	0.01	0.02	0.03
Mean F-Score	0.83			0.81			0.85			0.97		

(c): Supervised RF Classification - RGB

	{1}			{2}			{3}			{4}		
	V	A	B	V	A	B	V	A	B	V	A	B
<i>Error Rate</i>	0.20	0.25	0.30	0.17	0.07	0.16	0.10	0.10	0.10	0.19	0.06	0.15
<i>Accuracy</i>	0.80	0.75	0.70	0.83	0.93	0.84	0.90	0.90	0.90	0.81	0.94	0.85
<i>Precision</i>	0.71	1.00	0.56	0.74	1.00	0.79	0.87	0.88	0.84	0.72	0.91	0.88
<i>Recall</i>	0.90	0.27	0.77	0.87	0.75	0.79	0.87	0.81	0.90	0.87	0.77	0.76
<i>Specificity</i>	0.73	1.00	0.65	0.81	1.00	0.87	0.92	0.95	0.90	0.76	0.98	0.92
<i>False Positive Rate</i>	0.27	0.00	0.35	0.19	0.00	0.13	0.08	0.05	0.10	0.24	0.02	0.08
<i>F-Score</i>	0.79	0.42	0.65	0.80	0.86	0.79	0.87	0.84	0.87	0.79	0.83	0.81
Mean F-Score	0.62			0.82			0.86			0.81		

(c): Supervised RF Classification - TGI

	{1}			{2}			{3}			{4}		
	V	A	B	V	A	B	V	A	B	V	A	B
<i>Error Rate</i>	0.17	0.22	0.28	0.11	0.07	0.17	0.05	0.16	0.20	0.17	0.17	0.13

<i>Accuracy</i>	0.83	0.78	0.72	0.89	0.93	0.83	0.95	0.84	0.80	0.83	0.83	0.87
<i>Precision</i>	0.75	1.00	0.59	0.87	1.00	0.74	0.96	1.00	0.63	0.69	0.86	0.83
<i>Recall</i>	0.90	0.35	0.80	0.87	0.72	0.86	0.90	0.53	0.97	0.89	0.62	0.83
<i>Specificity</i>	0.79	1.00	0.68	0.90	1.00	0.81	0.98	1.00	0.72	0.80	0.94	0.89
<i>False Positive Rate</i>	0.21	0.00	0.32	0.10	0.00	0.19	0.02	0.00	0.28	0.20	0.06	0.11
<i>F-Score</i>	0.82	0.51	0.68	0.87	0.84	0.79	0.93	0.70	0.76	0.77	0.72	0.83
Mean F-Score	0.67			0.83			0.80			0.78		

(c): Supervised RF Classification - IRG

	{1}			{2}			{3}			{4}		
	V	A	B	V	A	B	V	A	B	V	A	B
<i>Error Rate</i>	0.30	0.28	0.37	0.19	0.16	0.15	0.15	0.16	0.15	0.14	0.15	0.04
<i>Accuracy</i>	0.70	0.72	0.63	0.81	0.84	0.85	0.85	0.84	0.85	0.86	0.85	0.96
<i>Precision</i>	0.62	0.64	0.50	0.68	1.00	0.80	0.74	1.00	0.77	0.75	0.83	0.97
<i>Recall</i>	0.70	0.59	0.47	0.93	0.50	0.83	0.97	0.43	0.86	0.90	0.69	0.93
<i>Specificity</i>	0.70	0.80	0.73	0.73	1.00	0.87	0.77	1.00	0.84	0.84	0.93	0.98
<i>False Positive Rate</i>	0.30	0.20	0.27	0.27	0.00	0.13	0.23	0.00	0.16	0.16	0.07	0.02
<i>F-Score</i>	0.66	0.62	0.48	0.79	0.67	0.81	0.84	0.60	0.81	0.82	0.75	0.95
Mean F-Score	0.58			0.76			0.75			0.84		

Table 5.5. Confusion matrices and related metrics for analysed cases of unsupervised classification with K-Means algorithms.

(a): Unsupervised K-Means Classification - RGB

	{1}			{2}			{3}			{4}		
	V	A	B	V	A	B	V	A	B	V	A	B
<i>Error Rate</i>	0.30	0.42	0.46	0.27	0.35	0.41	0.27	0.35	0.43	0.27	0.41	0.46
<i>Accuracy</i>	0.70	0.58	0.54	0.73	0.65	0.59	0.73	0.65	0.57	0.73	0.59	0.54
<i>Precision</i>	0.80	0.48	0.35	0.77	0.56	0.39	0.83	0.56	0.38	0.84	0.49	0.35
<i>Recall</i>	0.53	0.47	0.50	0.57	0.63	0.44	0.50	0.67	0.46	0.53	0.57	0.43
<i>Specificity</i>	0.87	0.66	0.56	0.86	0.66	0.65	0.92	0.64	0.63	0.91	0.61	0.60
<i>False Positive Rate</i>	0.13	0.34	0.44	0.14	0.34	0.35	0.08	0.36	0.38	0.09	0.39	0.40
<i>F-Score</i>	0.64	0.47	0.41	0.65	0.59	0.41	0.63	0.61	0.42	0.65	0.52	0.39
Mean F-Score	0.51			0.55			0.55			0.52		

(a): Unsupervised K-Means Classification - TGI

	{1}			{2}			{3}			{4}		
	V	A	B	V	A	B	V	A	B	V	A	B
<i>Error Rate</i>	0.56	0.49	0.62	0.27	0.35	0.41	0.58	0.58	0.67	0.67	0.69	0.63
<i>Accuracy</i>	0.44	0.51	0.38	0.73	0.65	0.59	0.42	0.42	0.33	0.33	0.31	0.37
<i>Precision</i>	0.52	0.23	0.14	0.77	0.56	0.39	0.58	0.09	0.13	0.35	0.13	0.25
<i>Recall</i>	0.53	0.50	0.07	0.57	0.63	0.44	0.50	0.25	0.08	0.45	0.18	0.11
<i>Specificity</i>	0.32	0.51	0.64	0.86	0.66	0.65	0.27	0.46	0.55	0.23	0.38	0.65
<i>False Positive Rate</i>	0.68	0.49	0.36	0.14	0.34	0.35	0.73	0.54	0.45	0.77	0.62	0.35
<i>F-Score</i>	0.52	0.31	0.10	0.65	0.59	0.41	0.54	0.13	0.10	0.39	0.15	0.15
Mean F-Score	0.31			0.55			0.25			0.23		

(a): Unsupervised K-Means Classification - IRG

	{1}			{2}			{3}			{4}		
	V	A	B	V	A	B	V	A	B	V	A	B
<i>Error Rate</i>	0.28	0.41	0.45	0.27	0.35	0.41	0.26	0.35	0.42	0.27	0.41	0.46
<i>Accuracy</i>	0.72	0.59	0.55	0.73	0.65	0.59	0.74	0.65	0.58	0.73	0.59	0.54
<i>Precision</i>	0.81	0.48	0.36	0.77	0.56	0.39	0.84	0.56	0.39	0.84	0.49	0.35
<i>Recall</i>	0.57	0.47	0.50	0.57	0.63	0.44	0.53	0.67	0.46	0.53	0.57	0.43
<i>Specificity</i>	0.87	0.67	0.57	0.86	0.66	0.65	0.92	0.64	0.64	0.91	0.61	0.60
<i>False Positive Rate</i>	0.13	0.33	0.43	0.14	0.34	0.35	0.08	0.36	0.36	0.09	0.39	0.40
<i>F-Score</i>	0.67	0.47	0.42	0.65	0.59	0.41	0.65	0.61	0.43	0.65	0.52	0.39
Mean F-Score	0.52			0.55			0.56			0.52		

(b): Unsupervised K-Means Classification - RGB

	{1}			{2}			{3}			{4}		
	V	A	B	V	A	B	V	A	B	V	A	B
<i>Error Rate</i>	0.30	0.27	0.40	0.18	0.25	0.31	0.23	0.25	0.34	0.22	0.25	0.33
<i>Accuracy</i>	0.70	0.73	0.60	0.82	0.75	0.69	0.77	0.75	0.66	0.78	0.75	0.67
<i>Precision</i>	0.70	0.65	0.42	0.76	0.66	0.56	0.72	0.66	0.50	0.77	0.67	0.52
<i>Recall</i>	0.47	0.80	0.47	0.83	0.70	0.47	0.70	0.77	0.43	0.67	0.73	0.53
<i>Specificity</i>	0.86	0.68	0.67	0.81	0.78	0.81	0.82	0.74	0.77	0.86	0.77	0.74
<i>False Positive Rate</i>	0.14	0.32	0.33	0.19	0.22	0.19	0.18	0.26	0.23	0.14	0.23	0.26
<i>F-Score</i>	0.56	0.72	0.44	0.79	0.68	0.51	0.71	0.71	0.46	0.71	0.70	0.52
Mean F-Score	0.57			0.66			0.63			0.65		

(b): Unsupervised K-Means Classification - TGI

	{1}			{2}			{3}			{4}		
	V	A	B	V	A	B	V	A	B	V	A	B
<i>Error Rate</i>	0.07	0.11	0.16	0.04	0.09	0.12	0.07	0.12	0.17	0.04	0.08	0.12
<i>Accuracy</i>	0.93	0.89	0.84	0.96	0.91	0.88	0.93	0.88	0.83	0.96	0.92	0.88
<i>Precision</i>	0.86	0.82	0.81	0.91	0.78	0.95	0.88	0.73	0.86	0.91	0.77	0.96
<i>Recall</i>	1.00	0.74	0.73	1.00	0.95	0.70	0.97	0.90	0.63	1.00	0.94	0.73
<i>Specificity</i>	0.88	0.95	0.90	0.93	0.89	0.98	0.90	0.87	0.94	0.93	0.91	0.98
<i>False Positive Rate</i>	0.12	0.05	0.10	0.07	0.11	0.02	0.10	0.13	0.06	0.07	0.09	0.02
<i>F-Score</i>	0.92	0.78	0.77	0.95	0.86	0.81	0.92	0.81	0.73	0.95	0.85	0.83
Mean F-Score	0.82			0.87			0.82			0.88		

(b): Unsupervised K-Means Classification - IRG

	{1}			{2}			{3}			{4}		
	V	A	B	V	A	B	V	A	B	V	A	B
<i>Error Rate</i>	0.30	0.27	0.40	0.19	0.25	0.30	0.23	0.25	0.34	0.20	0.24	0.32
<i>Accuracy</i>	0.70	0.73	0.60	0.81	0.75	0.70	0.77	0.75	0.66	0.80	0.76	0.68
<i>Precision</i>	0.70	0.65	0.42	0.74	0.66	0.58	0.72	0.66	0.50	0.78	0.67	0.53
<i>Recall</i>	0.47	0.80	0.47	0.83	0.70	0.47	0.70	0.77	0.43	0.70	0.73	0.53
<i>Specificity</i>	0.86	0.68	0.67	0.80	0.78	0.82	0.82	0.74	0.77	0.86	0.77	0.75
<i>False Positive Rate</i>	0.14	0.32	0.33	0.20	0.22	0.18	0.18	0.26	0.23	0.14	0.23	0.25
<i>F-Score</i>	0.56	0.72	0.44	0.78	0.68	0.52	0.71	0.71	0.46	0.74	0.70	0.53

Mean F-Score	0.57	0.66	0.63	0.66
---------------------	-------------	-------------	-------------	-------------

(c): Unsupervised K-Means Classification - RGB

	{1}			{2}			{3}			{4}		
	V	A	B	V	A	B	V	A	B	V	A	B
<i>Error Rate</i>	0.33	0.29	0.35	0.41	0.47	0.54	0.49	0.34	0.50	0.47	0.42	0.53
<i>Accuracy</i>	0.67	0.71	0.65	0.59	0.53	0.46	0.51	0.66	0.50	0.53	0.58	0.47
<i>Precision</i>	0.60	0.57	0.58	0.59	0.42	0.16	0.42	0.57	0.32	0.47	0.48	0.19
<i>Recall</i>	0.60	0.67	0.50	0.57	0.62	0.10	0.50	0.70	0.20	0.57	0.64	0.10
<i>Specificity</i>	0.72	0.73	0.76	0.61	0.48	0.67	0.51	0.64	0.70	0.50	0.54	0.72
<i>False Positive Rate</i>	0.28	0.27	0.24	0.39	0.52	0.33	0.49	0.36	0.30	0.50	0.46	0.28
<i>F-Score</i>	0.60	0.62	0.54	0.58	0.50	0.12	0.45	0.63	0.24	0.52	0.55	0.13
Mean F-Score	0.58			0.40			0.44			0.40		

(c): Unsupervised K-Means Classification - TGI

	{1}			{2}			{3}			{4}		
	V	A	B	V	A	B	V	A	B	V	A	B
<i>Error Rate</i>	0.27	0.21	0.36	0.38	0.45	0.51	0.46	0.42	0.46	0.48	0.50	0.53
<i>Accuracy</i>	0.73	0.79	0.64	0.62	0.55	0.49	0.54	0.58	0.54	0.52	0.50	0.47
<i>Precision</i>	0.68	0.70	0.52	0.61	0.42	0.19	0.35	0.53	0.44	0.31	0.45	0.37
<i>Recall</i>	0.70	0.70	0.50	0.63	0.64	0.10	0.36	0.57	0.40	0.19	0.60	0.37
<i>Specificity</i>	0.76	0.84	0.73	0.61	0.50	0.73	0.63	0.58	0.63	0.73	0.42	0.55
<i>False Positive Rate</i>	0.24	0.16	0.27	0.39	0.50	0.27	0.37	0.42	0.37	0.28	0.58	0.45

<i>F-Score</i>	0.69	0.70	0.51	0.62	0.51	0.13	0.35	0.55	0.42	0.24	0.51	0.37
Mean F-Score	0.63			0.42			0.44			0.37		

(c): Unsupervised K-Means Classification - IRG

	{1}			{2}			{3}			{4}		
	V	A	B	V	A	B	V	A	B	V	A	B
<i>Error Rate</i>	0.21	0.29	0.25	0.30	0.25	0.42	0.39	0.32	0.40	0.55	0.51	0.58
<i>Accuracy</i>	0.79	0.71	0.75	0.70	0.75	0.58	0.61	0.68	0.60	0.45	0.49	0.42
<i>Precision</i>	0.68	1.00	0.61	0.65	1.00	0.44	0.52	0.57	0.50	0.18	0.42	0.33
<i>Recall</i>	0.90	0.20	0.90	0.67	0.36	0.67	0.47	0.64	0.50	0.07	0.64	0.40
<i>Specificity</i>	0.72	1.00	0.66	0.73	1.00	0.54	0.70	0.71	0.67	0.76	0.39	0.43
<i>False Positive Rate</i>	0.28	0.00	0.34	0.28	0.00	0.46	0.30	0.29	0.33	0.24	0.61	0.57
<i>F-Score</i>	0.77	0.33	0.73	0.66	0.53	0.53	0.49	0.60	0.50	0.10	0.51	0.36
Mean F-Score	0.61			0.57			0.53			0.32		

5.5.4. Discussion

After performing the supervised and unsupervised classification procedures using the RF and K-Means algorithms, respectively, the validation metrics were extracted. Considering the comparison between the labelling assigned and that predicted by the software in the 90 pins placed, for each scenario, at each resolution and for each classification mode (RGB bands, adding the TGI band, adding the IRG band), the confusion matrices were extracted and from these the relative metrics were computed. In Tables 5.4 and 5.5, the metrics were summarised for each class: vegetation (V), asphalt (A) and bare soil (B). In the present examination of the third scenario, the

unmasked data (c) was preferred to analyse the performance of the classification algorithms at a basic level of image processing, i.e., only radiometrically corrected.

A coarse radiometric calibration such as ELM does not allow a clear distinction to be made between and in the image components. This results in a reduction in the ability to distinguish classes such as asphalt and bare ground, which in several cases may have spectral similarities (e.g., as in the case of highly weathered asphalt). In fact, as can be seen from Figures 5.14 and 5.15, in all the cases analysed, regardless of the classification methods used, the greatest diatribe emerges precisely between the two classes asphalt and bare ground. As far as the classification with the RF algorithms is concerned, in Tables 5.4, the low F-score values (minimum case of 0.33 for A in (c), {1}, + IRG band) are attributable to these two classes, while the class concerning the vegetation presents values always higher than the minimum of 0.67, found in case (a), spatial resolution {4}, +IRG band mode. The highest F-score value of 0.98 was calculated for four vegetation cases at resolutions {2}, {3}, {4} in the vegetation index classifications and all in scenario (b). While the algorithms are facilitated in this scenario by the high presence of vegetation, resolution {1} is less effective due to the presence of noise and distortions in the pixels.

On the other hand, looking at the F-score values in the unsupervised classification cases in Tables 5.5, a drastic reduction of the values is found. While on the one hand, the highest values of 0.95 are recorded for scenario (b), both in the vegetation for resolutions {2} and {4} in the +TGI mode, on the other hand, a minimum value of 0.10 is reached in the discrimination of bare ground, at resolution {3} in scenario (a) of the +TGI case.

In order to better synthesise the functionalities, the average F-score is proposed to give a more focused overview of the efficiency of each case analysed. From the comparison of these values in the two Tables 5.4 and 5.5, for the values obtained by the unsupervised classification a general reduction of about 30% from those obtained by the supervised classification emerges. This is also confirmed by the remaining part of the calculated metrics, in particular Accuracy and Precision. Among the analysed values, except for case (b) +TGI where the values are very functional, all scenarios

where the classification used IRG maps had a slight improvement. On the other hand, analysing the average F-score values for the supervised mode, the results tend to be better for all the cases where TGI information was used, but also IRG compared to the simple RGB cases. This shows how the VI improve the ability to separate the classes, as already shown in paragraph 5.4.1 but in view of the automation of processes, then using unsupervised modes, it is necessary to have a more incisive radiometric information such as that retrievable from the NIR bands.

By comparing the trends of the F-score values with respect to the spatial resolutions at which they are calculated, it is not possible to extrapolate a certain regularity.

Looking at Figures 5.14-15 and Table 5.4-5, the best-fitting results in the case of supervised classifications result for the scenarios: (a), spatial resolution {2}, classification mode with vegetative index TGI; (b), spatial resolution {4}, classification mode with vegetative index IRG; (c), spatial resolution {3}, basic classification mode with RGB bands.

In the unsupervised modes, however, they result for the scenarios: (a), resolution {3}, classification mode with vegetative index IRG; (b), spatial resolution {4}, classification mode with vegetative index TGI; (c), spatial resolution {1}, classification mode with vegetative index TGI. This demonstrates once again how the various datasets react unevenly to the algorithms used.

6. POINT-BASED ANALYSIS

The growth of techniques and technologies, as seen in Section 2, to collect huge point clouds has made it inevitable to channel energies towards the study of methodologies oriented to an automated interpretation of these data, usable in any engineering application. As pointed out by (Weidner et al., 2021), this route represents an interesting challenge since today the most critical phases of the management and processing of these Big Spatial Data are still usually carried out manually. The manual analysis of these huge masses of points is long and laborious and could never guarantee explicit and exclusive information, since it is conditioned by the subjectivity of the operator, thus highlighting the need for efficient techniques able to identify objective characteristics (Jafari et al., 2017). (Blomley et al., 2014) stated that being able to extract reliable geometric features from these point clouds is crucial to fully exploit the potential of these data, for example, for structural analysis or object detection (Nettis et al., 2020). Indeed, starting from point distribution characteristics such as smoothness, regularity and vertical dispersion, these favours the distinction between points of the type of surface or object they represent (Kim et al., 2013). The fully automated analysis of point clouds acquired by the most established technologies, such as those recorded by laser scanners (Chehata et al., 2009, Mallet et al., 2011), and those obtained by UAV-based photogrammetry, terrestrial or traditional aerial photogrammetry, has therefore become a topic of great involvement (Farella et al., 2019a, Karantanellis et al., 2020, Weinmann et al., 2015).

In order to describe the local 3D geometry at a given point, in a logical sense, the spatial distribution of the other points within a reasonable local neighbourhood will have to be taken into account. The identification of the best neighbourhood for each point is a pivotal problem for a wide variety of works in the literature: data down-

sampling, template fitting, feature detection and computation, interpolation, registration, segmentation, filtering, or modelling purposes (Brodu and Lague, 2012, Demantké et al., 2011, Farella et al., 2019b, Weidner et al., 2019). Precisely, an optimal neighbourhood can be defined as the largest set of spatially close points that belong to the same object, thus able to express some 1D, 2D or 3D features (Brodu and Lague, 2012, Demantké et al., 2011, Farella et al., 2019b, Farella et al., 2019a, Karantanellis et al., 2020). For example, (Weinmann et al., 2014) considered the optimal neighbourhood of each individual 3D point focusing on extracting relevant, but not redundant, features able to increase their distinctiveness. While it is already difficult to identify a reasonable local neighbourhood, on the other hand dealing with the complexity of 3D scenes, caused on the one hand by irregular sampling and on the other hand by the heterogeneity of objects, implies a considerable computational capacity and detects a variety of available geometric features, often also marginal or poorly weighted. In addition, neighbourhood parameterization is often typically prepared based on empirical or a priori heuristic knowledge of the study environment. Several works have therefore focused on improving these methodologies for automatic interpretation and learning of some useful features, such as geometric ones (Weinmann et al., 2014).

Based on established image-based techniques, as seen in Chapter 4, the idea of analysing invariant moments was also found to be valid for observing the geometric properties of point clouds. In fact, from the analysis of the covariance matrix or the structure tensor computed within the local neighbourhood, one proceeds to the extraction of their geometric characteristics (Blomley et al., 2014). The eigenvalues obtained have been understood as neighbourhood features that provide additional information useful to discriminate planes, edges, corners, lines and volumes. Trivially, these features then describe the local spatial distribution of 3D points (Chehata et al., 2009). Moreover, the use of such features ensures their feasibility for heterogeneous and unstructured data and at the same time no a-priori knowledge of the scene is required (Farella et al., 2019b).

In general, the local neighbourhood for each point can be defined by a spherical or cylindrical neighbourhood with a fixed radius r (Thomas et al., 2018). Alternatively, it could be identified by setting a fixed number $k \in \mathbb{N}$ of nearest neighbours to the point of interest. Regardless of the definition mode, both are based on a scale parameter that is either a radius or k , which is commonly selected to be identical for all points in the cloud but, ideally, it would be optimal to obtain a variable scale parameter dependent on the local 3D structure as well as the local density of the points. Calculating these features at multiple scales reveals itself in higher accuracy than at a single scale, precisely because objects can have different properties at different scales of analysis (Blomley et al., 2014). However, multiscale approaches lead to larger feature spaces where it will be necessary to use feature selection schemes appropriate for the scope of work and at the same time reduce the computational load. A multiscale approach would reduce the accessibility to a wide range of users, disincentivising them due to the complex parameter management and multifaceted correlation between inferable features. Deducing features on a single scale, on the other hand, means that a scale must be considered to describe some features better than others and will have to be chosen carefully (Weinmann et al., 2015). Therefore, a suitable scalar dimensionality approach can be used as an alternative to define a targeted geometric behaviour of points. Understandably, the dimensionality of an object depends on the spatial scale at which it is examined. An object that appears planar up close (at a smaller spatial scale) may be 3D at a larger spatial scale. For example, in (Kim et al., 2013) at various spatial scales, considering a histogrammetric distribution of features, the selection of the most useful features was done by observing in which attributes the mean distance between the averages exceeds the mean standard deviation. The creation of a representative inventory is also a function of the size of the smallest event that can be detected. In particular, (Williams et al., 2018) suggested that the smallest detectable movement, or Level of Detection (LoD), is a key parameter, firstly, for delineating the dimensionality of the model and subsequently for calculating erosion or rockfall volumes. It involves masking out regions of change that ex-

ceed a narrow threshold at the LoD. This leads to an approach in which it is the end that resolves the optimal spatial scale.

In the geometric analysis of point clouds, every single observation can only be interpreted based on its relations with other elements and its probability of belonging to a certain class of objects (Farella et al., 2019b). Each class of objects shows a characteristic coherence at different spatial scales, so it is crucial to establish invariable features that can represent structural information that is not observable at other scales. Consequently, a suitable scale may depend on the type of feature chosen. (Blomley et al., 2014) therefore deduced that when pursuing a covariance approach, the same homogeneous environment at a smaller scale may define more distinctive features, while the distribution of shapes may be significant at a larger scale.

This research phase is proposed to analyse the behaviour of the scalar dimensional approach when varying the geometric resolution, i.e., the GSD, of point clouds from UAVs of the same scenario acquired at two different altitudes. Given the above considerations, it has been fundamental to verify if the deducible spatial characteristics (1D, 2D and 3D) of the same scenario can be considered comparable when varying the acquisition strategy, considering the other conditions fixed.

Given the considerations about the possibility of extracting geometric features based on point-based analysis, the study focused on the optimisation of multi-temporal and multi-sensor cloud-to-cloud comparison operations using the powerful M3C2 algorithm implemented in the open-source CloudCompare suite (Lague et al., 2013a). This algorithm, if properly parameterized and thus predisposed to the observation of a targeted dimensionality of the models, provides useful information of the variations existing between co-registered clouds, useful for example in cases of environmental monitoring.

Finally, to automate the point-based processing and comparison of data from multi-epoch UAVs, an innovative way of co-registering clouds, called "co-alignment", was analysed and proposed.

In the final section of this study phase, the potential of this approach to extract geometries from point clouds when harmonised with developments in Building Information Modelling (BIM) architectures was analysed.

6.1. PCA FEATURE EXTRACTION

Recent approaches to find characteristics of 3D geometries are based on features derived from the local covariance matrix indicative of the invariant second-order moments within point positions (Blomley et al., 2014). Through statistical principal component analysis (PCA) it is possible to extract three eigenvalues ($\lambda_1 > \lambda_2 > \lambda_3$) from the covariance matrix. These represent the local 3D structure at the location of the analysed point and each eigenvalue measures the variation of the set of local points along the direction of the corresponding eigenvector. Briefly, PCA defines the principal directions in three orthogonal vectors and the respective magnitude of variation of the points distribution around the centre of the defined neighbourhood, called centroid, in the eigenvalues (Farella et al., 2019b). The proportions of the variance explained by each eigenvalue are defined as:

$$PCA(1) = \lambda_1 / (\lambda_1 + \lambda_2 + \lambda_3) \quad (6.1)$$

$$PCA(2) = \lambda_2 / (\lambda_1 + \lambda_2 + \lambda_3) \quad (6.2)$$

$$PCA(3) = \lambda_3 / (\lambda_1 + \lambda_2 + \lambda_3) \quad (6.3)$$

As explained in Figure 6.1 of (Brodu and Lague, 2012), the triangular domain of all possible proportions works well in representing the dimensionality cases of the model as the weight of each eigenvalue varies.

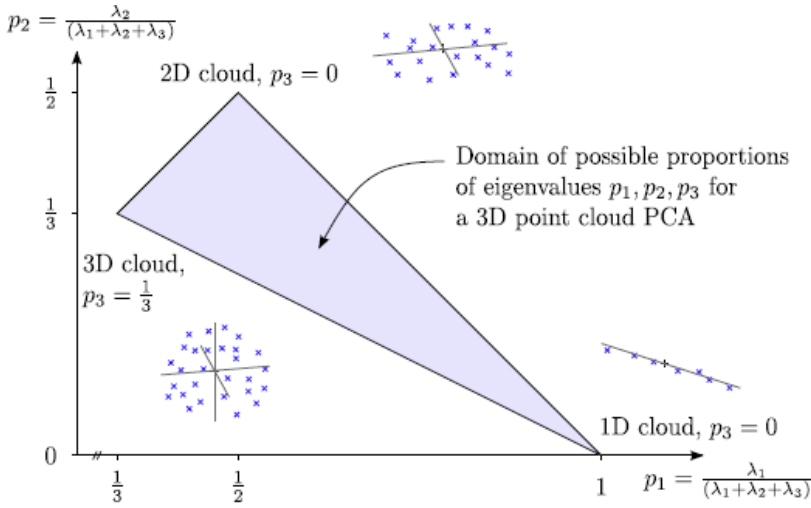


Figure 6.1. Triangular domain of possible proportions of eigenvalues (Brodu and Lague, 2012)

Given the constraint:

$$PCA(1) + PCA(2) + PCA(3) = 1 \quad (6.4)$$

when only a single eigenvalue λ_1 accounts for the total variance in the neighbourhood sphere the points are oriented along one dimension. Alternatively, when two eigenvalues were necessary to account for the variance but the third one does not contribute the cloud is locally mostly planar. Conversely, a fully 3D cloud is one where all three eigenvalues have the same magnitude. The proportions of eigenvalues thus identify a rate of how much 1D, 2D or 3D the cloud looks locally at a given scale (Figure 6.2).

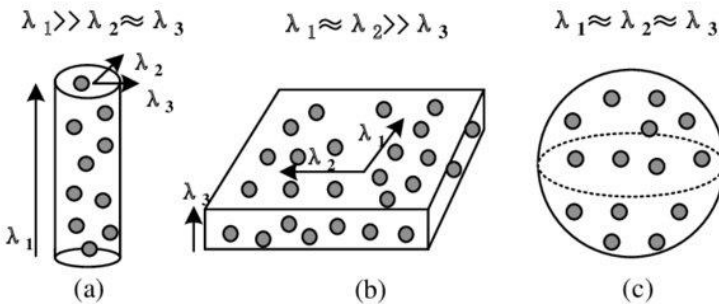


Figure 6.2. Trends in the spatial orientation of point clouds (Qin et al., 2018).

Nevertheless, the combination of these eigenvalues generates some shape descriptors, designed to highlight a predominantly linear, planar, or scattering behaviour of the neighbourhood, otherwise also other measures such as omnivariance, anisotropy and eigenentropy. These local 3D shape features are formally called eigen-features.

The feature of linearity is employed to examine whether a set of points can be modelled by a 3D line (Waldhauser et al., 2014):

$$L = (\lambda_1 - \lambda_2)/\lambda_1 \quad (6.5)$$

The planarity feature is used to describe the smoothness of a surface:

$$P = (\lambda_2 - \lambda_3)/\lambda_1 \quad (6.6)$$

The feature of sphericity investigates the scattering of a neighbourhood:

$$S = \lambda_3/\lambda_1 \quad (6.7)$$

Next, the feature of omnivariance explains how a neighbourhood of points were distributed inhomogeneously across a 3D volume:

$$O = (\lambda_1 * \lambda_2 * \lambda_3)^{\frac{1}{3}} \quad (6.8)$$

Anisotropy is a measure that is higher if the eigenvectors differ a lot. These measures have the potential to discriminate between orientated and non-orientated objects, as oriented objects have a higher anisotropy (Elberink and Maas, 2000):

$$A = (\lambda_1 - \lambda_3)/\lambda_1 \quad (6.9)$$

Last of all, the feature of eigenentropy gives a measure of the order or disorder of 3D points within the covariance ellipsoid (Weinmann et al., 2014):

$$E_\lambda = -(\lambda_1 * \ln \lambda_1 - \lambda_2 * \ln \lambda_2 + \lambda_3 * \ln \lambda_3) \quad (6.10)$$

Eigenentropy values tending towards 1 identify disturbances within the ellipsoid, thus highlighting the presence of points with 3D behaviour. Vice versa, values up to 0 detect an increasing order, passing from planar to linear dimensionality.

One of the proposals indicated by (Weinmann et al., 2014), for the identification of a suitable scaling parameter for the dimensional analysis of models, consists in analysing the curvature variation through the value of PCA (3). The curvature using PCA (3) should then be calculated as seen in equation (6.3) from the ratio of the minimum eigenvalue to the sum of the eigenvalues. Indeed, PCA (3) approximates the change in curvature in the vicinity of a given point. If the presence of accretion jumps can be translated into strong deviations in the normal directions, an appropriate value of the scaling parameter would identify concordant values of PCA (3) and thus it would be this parameter that would be able to describe various coherent levels of curvature. However, this approach proves not to be intuitive and expeditious enough.

The most common approach to defining a local neighbourhood depends on a user-defined radial distance r or a fixed value k of neighbourhood points. In this research work, the radius approach was adopted. The radius defines a spherical or cylindrical volume within which the neighbourhood of points is incorporated (Figure 6.3). The radius must be large enough to incorporate enough points to calculate meaningful statistics, but not so large as to lose spatial detail (Kim et al., 2013).

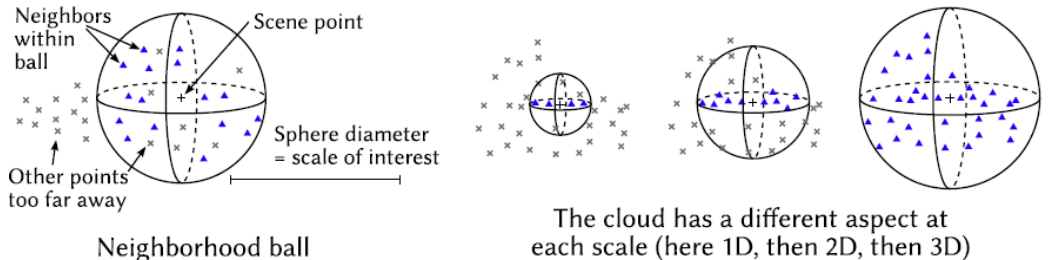


Figure 6.3. Local neighbourhood approach based on a radial distance r (Brodu and Lague, 2012).

The geometric features that can be formulated will therefore be influenced by the search radius, which determines the size of the neighbourhood over which these features will be quantified. Moreover, autocorrelation and other features might be tracked only at some scales less than at others (Blomley et al., 2014). Thus, different authors have organised different approaches to identify the most suitable search parameter r for the most diverse purposes. In one of the approaches, the conceptual basis for the search parameter r is defined. Considering, for example, the nature of second-order

moments, since in their computation the distance of an element from the mean participates quadratically, it follows those elements in the vicinity are less important than those further away and this becomes useful in extracting the geometric behaviours of the model (Blomley et al., 2014). At the same time, since PCA is an orthogonal transformation and therefore unitary, the resulting eigenvalues are sensitive to the original scale. It remains to be shown whether this optimal proximity dimension for the covariance characteristics corresponds to the characteristic scale of any structure. The approach used in this research step is referred to as scale-based dimensionality. The dimensional scale-based approach discovers, for each 3D point, the optimal search radius by determining the neighbourhood at various and increasing radii (between a minimum and a maximum value) and choosing the one that minimises a rate of unpredictability of the set of points.

The same portion of the waterfront analysed in section 3.4.1 was chosen as the study area. More details about the technologies used and the acquisition phases are reported in (Saponaro et al., 2019a). For the examinations concerning this research phase, two flight missions carried out on 15 and 16 March 2019 were used, characterized by two different flight altitudes of 70 m and 100 m AGL.

Framing the same area but at two different elevations resulted in two GSD values of 0.03 m/pix and 0.043 m/pix, respectively. Considering the results obtained in Section 3.4.1, the 30 targets in the two datasets were marked, and 14 GCPs were chosen for model georeferencing. The remaining part of the markers was then considered as CPs of the models.

The obtained dense point clouds were then imported into the open-source software CloudCompare. The following features were computed using the Computes Geometries tool:

- 1st, 2nd and 3rd Eigenvalues ($\lambda_1, \lambda_2, \lambda_3$)
- PCA (1), PCA (2) and PCA (3)
- Anisotropy and Omnivariance
- Linearity, Planarity and Sphericity
- Eigenentropy.

These were computed for ten values of the scale parameter r of a sphere, varying the latter from a minimum equal to the value of the GSD of each dataset and from time to time multiplying it up to 10. Table 6.1 summarizes the values of r for the two cases under study.

Table 6.1. Summary of the used scale parameters r .

r	[70 m]	[100 m]
GSD * 1	0.030 m	0.043 m
GSD * 2	0.060 m	0.086 m
GSD * 3	0.090 m	0.129 m
GSD * 4	0.120 m	0.172 m
GSD * 5	0.150 m	0.215 m
GSD * 6	0.180 m	0.258 m
GSD * 7	0.210 m	0.301 m
GSD * 8	0.240 m	0.344 m
GSD * 9	0.270 m	0.387 m
GSD * 10	0.300 m	0.43 m

This CloudCompare tool allows to obtain scalar fields in raster format (Figure 6.4), from which it's possible to extrapolate statistics on the computed geometric characteristics. The behaviours of these characteristics were analysed and finally, the most significant dimensionality behaviours were identified by observing the Eigenentropy trends.

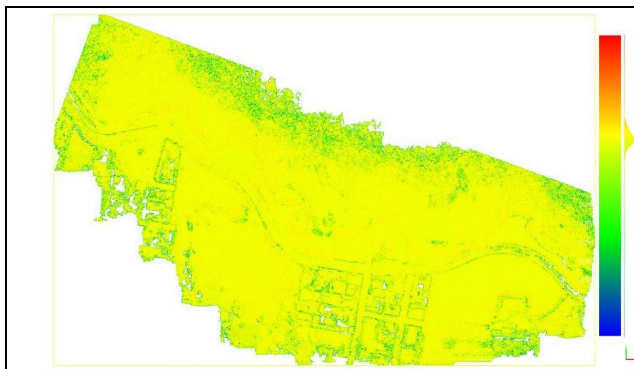


Figure 6.4. Example of Scalar Fields obtained for [100 m] Eigenvalues and scale parameter r equal to 0.215

6.1.1. Eigenvalues and PCA results

The recorded trends of the eigenvalues as the scale parameter r changes in the two dense point clouds obtained from images acquired at 70 m and 100 m AGL have been analysed below. Figure 6.5 shows the behaviour recorded for the two cases at different altitudes and how they can be considered completely comparable also when the scale parameter r varies. The values of the eigenvalues have undergone only a reportioning, about double, passing from the [70 m] to the [100 m] case. This suggests that the magnitude of the eigenvalues becomes proportional to the UAV acquisition altitude and that, as the GSD value increases, the PCA approach reiterates the dimensional traces already deduced at the lower altitude.

Analysing the behaviour as r varies in the 1st Eigenvalues, decreasing peaks were observed for r values starting from 0.030 m and 0.060 m. The remaining part of the cases is positioned on magnitudes equal to about 0.024 for the [70 m] case and 0.049 for [100 m]. Amongst these, the r -scale parameters of 0.387 m and 0.430 m show more pronounced peaks around those values. The first eigenvalue can be considered fundamental to discriminate those scaling parameters that are efficient in the calculation of the dimensionality of the point clouds. As in fact already discussed by (Brodu and Lague, 2012), null values of the 1st eigenvalue would void the triangular domain hypothesis while a very low magnitude would detect a weak orientation along the respective eigenvector, making the measurement unreliable. It was therefore clear that for scale parameters below 0.090 m [70 m] and 0.129 m [100 m], the PCA approach fails to accurately describe the geometric behaviour of the clouds.

On the other hand, analysing the 2nd Eigenvalues, for r values lower than 0.172 m the points fell mainly around 0, while for the remaining scale parameters distributions between 0.018-0.024 in the case of [70 m] and 0.038-0.050 in the case of [100 m] were observed. In the 3rd Eigenvalues cases, it is evident that they assumed values around 0, thus highlighting already in this first step a non-3D behaviour of both photogrammetric reconstructions.

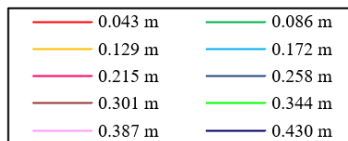
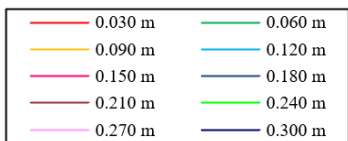
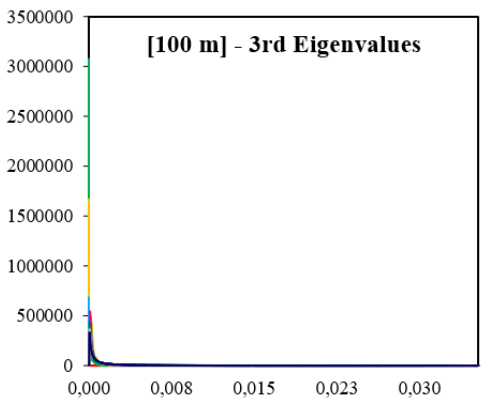
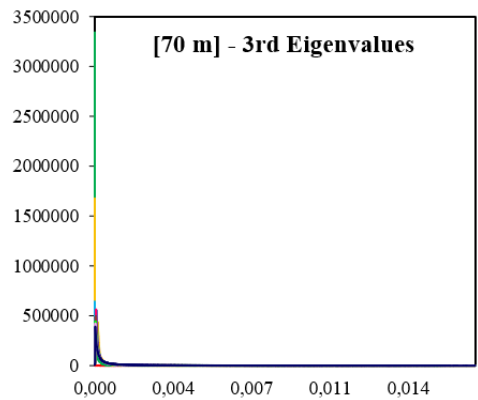
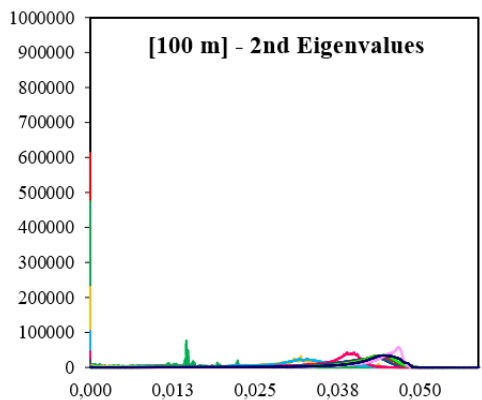
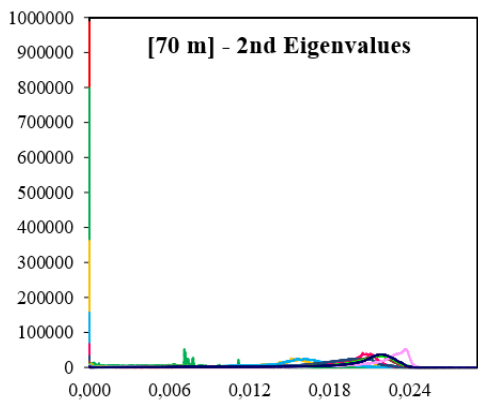
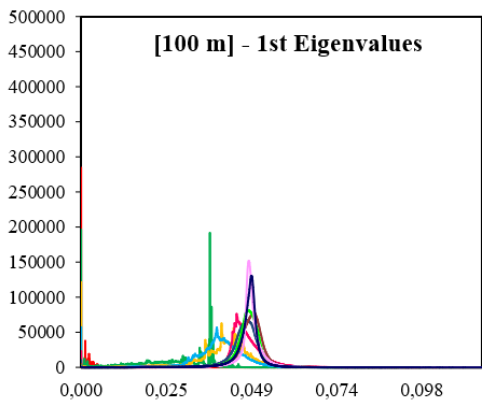
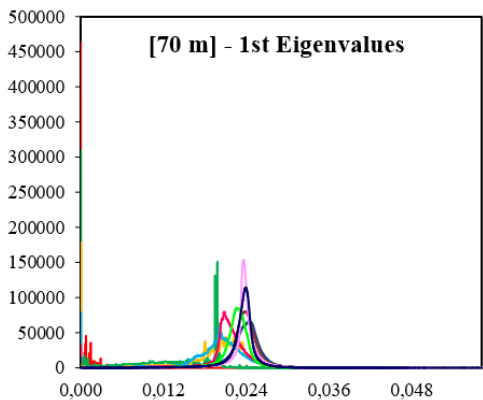
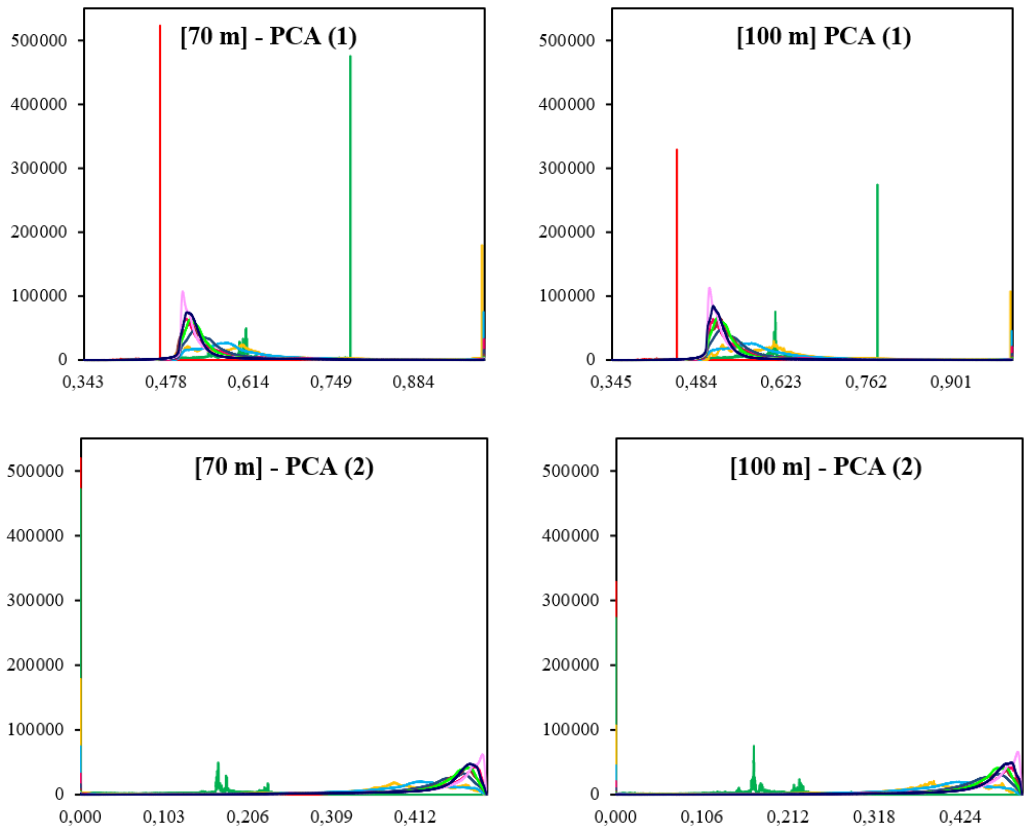


Figure 6.5. Histograms of the three eigenvalues as the scale parameter r changes. The abscissae show the values of the eigenvalues, the ordinates the number of points in each class. Below is the legend with the colour scale for each scale parameter r .

The trends recorded in the PCA (1,2,3) variance proportions as the scale parameter r changes in the two dense point clouds obtained from images acquired at 70 m and 100 m AGL were analysed below (Figure 6.6).



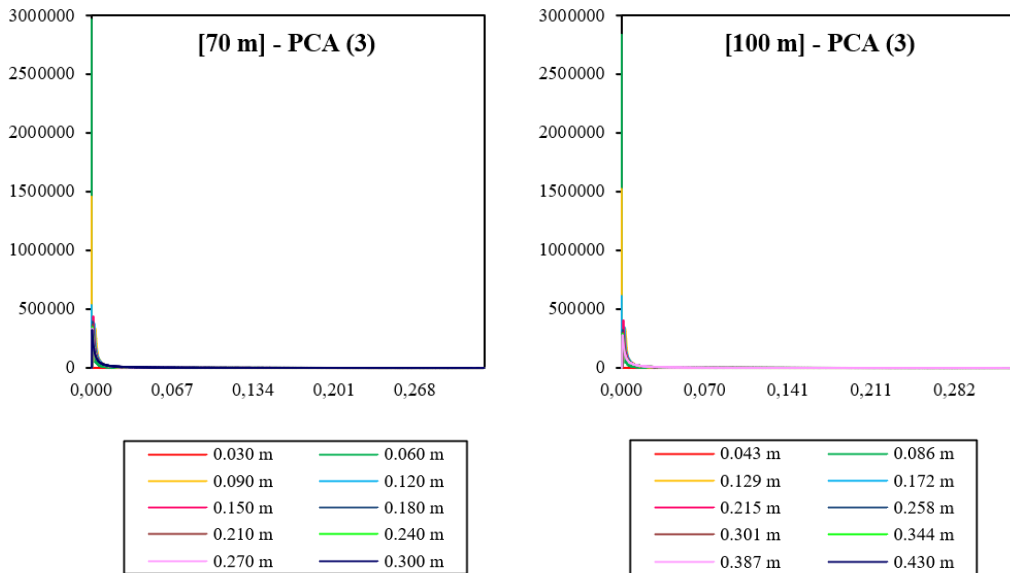


Figure 6.6. Histograms of the three eigenvalues as the scale parameter r changes. The abscissae show the values of the eigenvalues, the ordinates the number of points in each class.

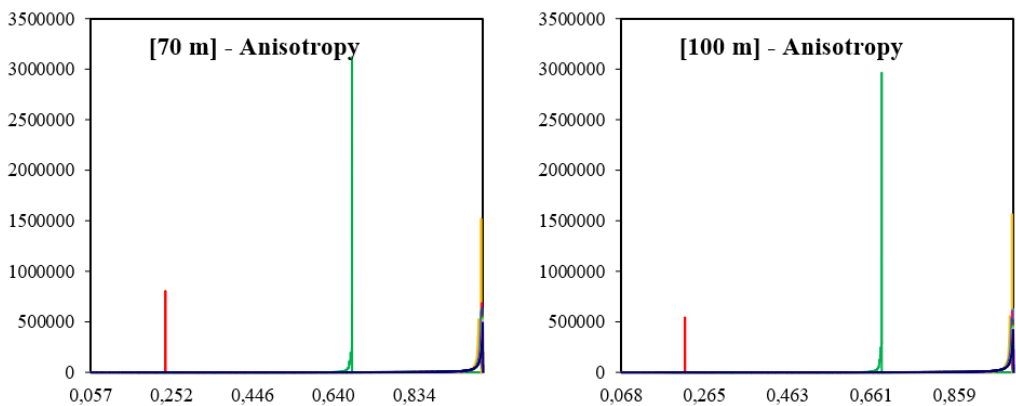
The histograms presented in Figure 6.6 confirmed what had already been observed in the previous analyses, i.e., given comparable behaviour, a slight increase in the magnitude of each variance proportion is observed in the [100 m] case.

In the first two histograms increasing peaks in the PCA (1) value for scale parameters r lower than 0.120 m [70 m] and 0.129 m [100 m] were observed, passing from a predominantly planar behaviour (greater than 0.33, the threshold of three-dimensionality) to a linear one when it assumed a value equal to 1. In the remaining part of the cases, this settles at around a PCA (1) value of 0.500, identifying predominantly planar behaviour. The considerations were confirmed by observing the PCA (2) histograms, in which the same scale parameters mentioned above assume a value of 0, while in the remaining part of the cases it tends to 0.500. Lastly, for the PCA (3) cases, as already stated in the previous paragraph, these assumed values predominantly equal to 0, ascertaining that the PCA approach failed in identifying 3D behaviour.

6.1.2. Anisotropy and Omnivariance

Figure 6.7 analysed the trends of the Geometric Features Anisotropy and Omnivariance as the scale parameter r changes in the two dense point clouds obtained from images acquired at 70 m and 100 m AGL.

Higher values of anisotropy identify the presence of eigenvalues (λ_1, λ_3) on eigenvectors that differ greatly. This, however, leads to discriminate oriented objects (high anisotropy) from non-oriented objects, and therefore to discriminate possible dimensionality: in particular, a value of 0 defines isotropy, i.e. a 3D behaviour, vice versa for values equal to 1 the behaviour will be 1D. The histograms obtained confirmed what has already been discussed, i.e. absent 3D behaviours, while on the one hand, the prevalence of r -radius describe 1D behaviours, on the other hand for the 0.030 m and 0.060 m [70 m] and 0.043 m and 0.086 m [100 m] the behaviours can be considered planar.



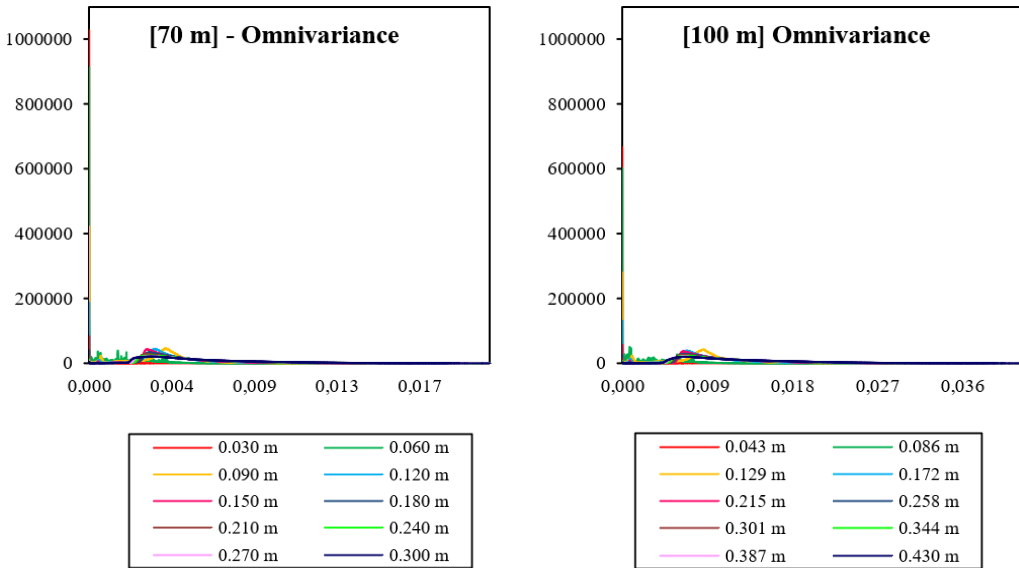


Figure 6.7. Histograms of the Anisotropy and Omnivariance as the scale parameter r changes. The abscissae show the values of the eigen-features, the ordinates the number of points in each class.

The values of Omnivariance tending to 0.33 identify 3D behaviour, while at 0 a linear attitude. It was evident how these were concentrated for values equal to 0.004 and 0.009 for the cases [70 m] and [100 m], respectively: therefore a planar behaviour, but it is clear that there is a strong presence in the analysed clouds of elements with linear behaviour that push the point distributions towards values of 0.

6.1.3. Linearity and Planarity

Figure 6.8 analyses the trends of the geometric characteristics Linearity and Planarity as the scale parameter r changes in the two dense point clouds obtained from images acquired at 70 m and 100 m AGL. It has been chosen not to propose the histograms related to Sphericity as they were not significant by proposing values equal to 0, showing nothing more than what has already been discussed.

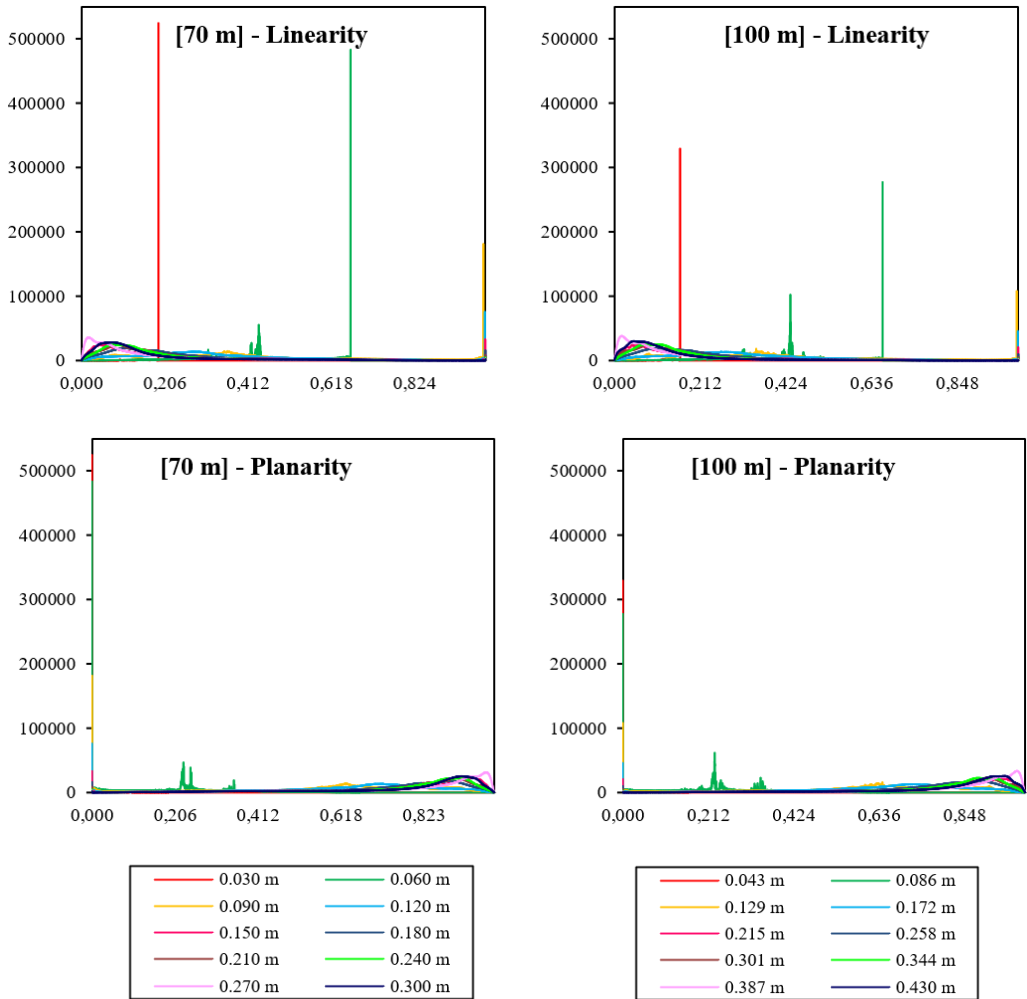


Figure 6.8. Histograms of Linearity and Planarity as the scale parameter r changes. The abscissae show the values of the eigen-features, the ordinates the number of points in each class.

The histograms complete the discussion undertaken so far, giving greater significance to the results learned. Since there are no significant 3D behaviours, the two geometric features represented can be considered almost complementary. They show how certain cases of the scale parameter r assume zero values in the histograms of Planarity and at the same time assume values equal to 1 in those of Linearity, and vice versa. The behaviours at radius 0.030 m and 0.060 m [70 m] and 0.043 m and 0.086 m [100 m], as already highlighted in the previous paragraphs, are significant

since they attest to the presence of both linearity and planarity in the description of the point clouds.

6.1.4. Eigenentropy Values

The entropy function provides for each reconstructed 3D point a measure of the probability of belonging to a part of the scene with specific geometric behaviour. High entropy values, i.e., tending to 1, indicate a disordered geometric behaviour of the neighbouring point and, most likely, the non-planar nature of these points. On the contrary, values lower than about 0.7 identify first a planar behaviour, then a linear one until they cancel out.

Since the discussed eigenvalues (λ_1 , λ_2 , λ_3) were values obtained from the minimization for each point of the Eigenentropy value of the ellipsoid, the histograms in Figure 6.9 represented the distribution of the significant features in the investigated area. Very spanned distributions of the latter identified a non-univocal behaviour of all points and therefore the chosen scaling parameter r was not sufficiently uniform and descriptive of the whole scenario. Peak distributions, on the other hand, showed that the scaling parameter r can be considered optimal, i.e., it can best explain the prevailing dimensionalities of the scenario. Therefore, from a general survey, histograms with scale parameter r obtained by multiplying the GSD value by 9 and 10 were the most efficient. Thus, r -scale parameters one order higher than the GSD value were able to qualitatively and quantitatively better identify the dimensionality of the survey carried out, regardless of the used acquisition strategy.

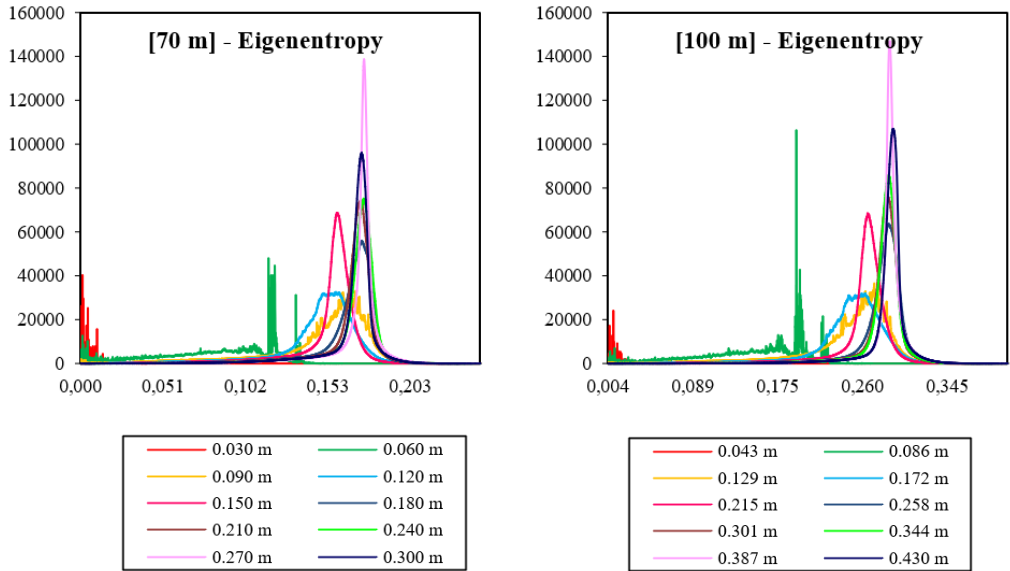


Figure 6.9. Histograms of Eigenentropy as the scale parameter r changes. The abscissae show the values of the eigen-feature, the ordinates the number of points in each class.

To summarise, the results achieved demonstrate how this field of application can advance new point-based learning methodologies useful for the extraction of valid morphological information. In general, the behaviours recorded for the two different flight height cases were completely comparable even if the scale parameter r varies. The values of geometric features undergone a reportioning passing from the [70 m] to the [100 m] case. This suggests that the magnitude of the eigenvalues was proportional to the UAV acquisition altitude and that, as the GSD value increases, the PCA approach reiterates the dimensional traces already inferred at the lower altitude. At last, r -scale parameters one order higher than the GSD value were able to qualitatively and quantitatively better identify the dimensionality of the survey carried out, regardless of the acquisition strategy used.

6.2. M3C2 ALGORITHM ENHANCEMENTS

The rise of high-density and accurate point clouds based on technological developments in the geomatics field, mainly related to the rise of UAVs, has favoured the definition of fully automated cloud-to-cloud comparison and analysis methods.

Several methods exist to compare point cloud data and estimate, for example, the topographic change of the surveyed area or object. The simplest Cloud to Cloud (C2C) methodology is identified, passing through Cloud to Mesh (C2M), the calculation of the DEM of Difference (DoD) and lastly the more refined Multiscale Model-to-Model Cloud Comparison (M3C2) methodology (Lague et al., 2013b). (Shirowzhan et al., 2019) introduce the various change detection algorithms and describe their differences in detail. These methods can be used in the open-source CloudCompare platform and allow the estimation of topographic changes between two successive reconstructions of the same features in a 3D environment. The C2C and M3C2 methods compare two-point clouds, C2M analyses the differences in elevation of a cloud compared to a facet of a triangulated surface model of the reference cloud, while DoD compares precisely the derived DEMs. C2C is the simplest and fastest method of comparing point clouds, as it does not require a grid or triangulation of data. For each point in the second point cloud, the nearest point is defined in the first point cloud and the surface variation is estimated as the vertical distance between the two points. The technique is suitable for detecting rapid changes in very dense point clouds. However, it is not an accurate method for measuring horizontal changes or the distance between vertical surfaces. The C2M method evaluates the change in surface elevation. The vertical distance between data points within a point cloud (or surface mesh) and a 3D reference mesh defines the surface change. Nevertheless, interpolating absent data creates uncertainties that are tricky to quantify.

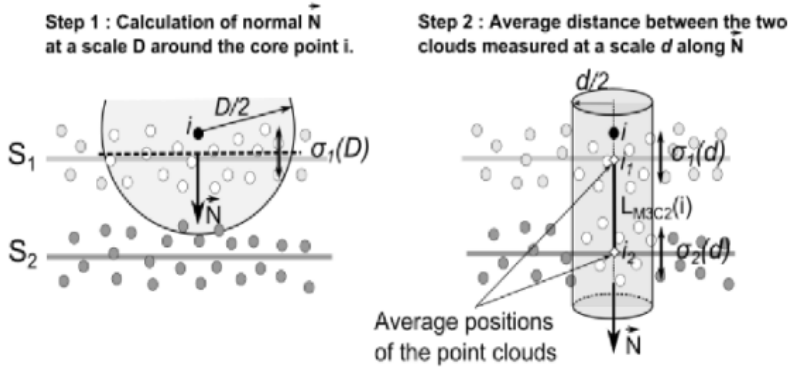
When point clouds are oriented and projected onto the XY plane, they are rasterized into DEMs. The subtraction of two DEMs produces a DoD, which highlights the change in one direction along the z-axis (Wheaton et al., 2010). This method results in simple and fast calculations, although for accuracy it relies on the DEMs' ability to accurately model the terrain geometry; oriented terrain surfaces should be relatively

orthogonal to the z-axis. A further consideration is that DEMs cannot model protruding features in the terrain and the grid size may reduce the level of detail that can be captured by DoD change detection (Wheaton et al., 2010). Therefore, the DoD method is not very suitable for change detection on geometrically complex terrains with protruding features and large sets of surface orientations. In order to improve the accuracy of DoD in a difficult site, segments with similar orientations can be grouped for separate analysis, although this may complicate data processing and interpretation.

The M3C2 algorithm measures the local distance between two-point clouds in the direction normal to the surface, operating directly on point clouds without triangulation or gridding. The plugin can compare two-point clouds derived from different types of acquisition and returns scalar fields that explain the differences in shape and uncertainties in their computation. It can be understood in two stages: in the first, the algorithm proceeds to estimate the normal of the points and then calculates the differences along with them.

First, the roles for the clouds to be compared are identified: one will be referred to as the reference, while the other will be understood as the one to be compared. For the calculation of the normals, at each core point i , a normal vector N is defined to a plane interpolating the neighbouring points of the reference cloud that lie within a radius $D/2$ from i (Figure 6.10). Each normal is positively oriented towards the nearest of a set of user-defined "orientation" points, e.g., the various scan positions in TLS acquisitions or GCPs in the remaining cases. The standard deviation of the distance of the neighbouring points from the best-fit plane is recorded and used as a measure of the cloud roughness $\sigma_i(D)$ on the D scale near i . This is also known as reduced roughness (Lague et al., 2013b).

a Principle of the Multiscale Model to Model Cloud Comparison M3C2



b M3C2 on complex topography

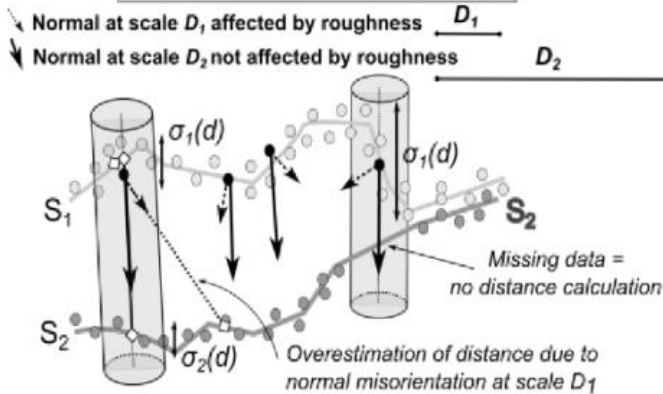


Figure 6.10. Representation of the functioning of the M3C2 algorithm (Lague et al., 2013b).

Once the normal for the central point i has been defined, it is used to project i onto the cloud to be compared. In this cloud, the user sets a diameter d , called the projection scale, so as to generate a cylinder whose axis passes through i and within which the intercept of the normal N will be sought. A maximum length of the cylinder is set to speed up the calculation. The intercept of each cloud with the cylinder defines two subsets of points of dimension n_1 and n_2 . Projecting each of the subsets onto the axis of the cylinder provides two distributions of distances (with an origin on i). The mean of the distribution indicates the average position of the cloud along the normal direction, i_1 and i_2 , and the two standard deviations are the local estimates of the rough-

ness of the point cloud $\sigma_1(d)$ and $\sigma_2(d)$ on the d scale along the normal direction. If outliers are expected in the data (such as vegetation), i_1 and i_2 can be defined as the median of the distance distribution and roughness is measured by the quartile interval. The local distance between the two LM3C2_(i) clouds is then given by the distance between i_1 and i_2 (Figure 6.10a). Figure 6.10b illustrates a case where the orientation of the cloud at the d scale is not orthogonal to the previously estimated normal at the d scale. The “apparent” roughness $\sigma_1(d)$ will be higher than the “true” localised roughness. This will generate a larger confidence interval coherent with the greater uncertainty related with a measurement where the surface orientation is not locally reliable with the normal direction. It should also be noted that the case where no intercept is detected with the compared cloud due to missing data or changes in surface visibility is also represented. In these cases, the algorithm does not return any calculation (Figure 6.10b).

For each estimated distance, the M3C2 algorithm also calculates the distance uncertainty (95% detection level or $LoD_{95\%}$), using the following equation:

$$LoD_{95\%} = \pm 1.96 \left(\sqrt{\frac{\sigma_1(d)^2}{n_1} + \frac{\sigma_2(d)^2}{n_2}} + reg \right) \quad (6.1)$$

where:

- $\sigma_1(d)^2$ and $\sigma_2(d)^2$ represent independent variances of the positions of the sub-cloud,
- n_1 and n_2 are the numbers of points of the subsampled clouds
- *reg* is the co-registration error between the two corresponding multitemporal clouds.

In this way, a distance can only be considered statistically significant when it is greater than the $LoD_{95\%}$ value. The algorithm automatically verifies this condition for each estimated distance.

The entire reference cloud can be defined as either central points or a subsampled set of the reference cloud. The original resolution of both point clouds is used in M3C2 calculations regardless of whether the data is subsampled in the process. In the present research work, priority was given to the original reference cloud without sub-

sampling it. In summary, the information that the algorithm extracts and associates with each point in the cloud are:

- Distance to the closest corresponding point in the compared cloud;
- The uncertainty associated with the distance value;
- Significant change.

The geometry of the search cylinder is defined by the user, who controls the degree of spatial averaging that occurs. The size of the scale and projection diameters are chosen based on the application, point spacing and surface complexity.

(DiFrancesco et al., 2020) deduce two general observations useful for the choice:

- Smaller projection diameters result in more detailed delineated edit objects, at the cost of accepting more random noise in the calculated distances.
- A large projection diameter relative to the footprint of the analysed event reduces the probability that the phenomenon can be extracted. Spatial averaging causes the M3C2 distances of the outer boundary of the variable feature to fall below $LoD_{95\%}$.

The choice of a correct parameterization that can be valid for point clouds that differ in terms of acquisition technology, the scenario being investigated, and the phenomenon being analysed is therefore complicated and efficient.

In the following paragraph, some variants of M3C2 in the literature were discussed and lastly, given the observations made in the previous paragraphs, an alternative methodology was proposed that is functional to the significant geometric characteristics of the analysed clouds.

6.2.1. Algorithm Parametrisation Performance

From a survey of the literature concerning implementations of the M3C2 algorithm, several new variants have been published to address some of the shortcomings of the native algorithm.

(James et al., 2017b) described a new method for full 3-D change detection between SfM-MVS surveys essentially based on the M3C2 algorithm but incorporating SfM-MVS-specific uncertainty estimates. In particular, the authors state how the original

M3C2 algorithm is functional for point clouds obtained by TLS technology, where the acquisition methodology itself guarantees regularity in the spacing between points and homogeneity in point density (James et al., 2017b). In the case of clouds obtained by SfM-MVS techniques, these characteristics lose their robustness, and it is essential to incorporate the SfM-MVS point cloud precision maps in the comparison calculation. These maps are computed by running Monte Carlo tests that return all the detailed metrics characteristic of rigorous photogrammetry. Individual estimates of coordinate accuracy in X, Y and Z are thus provided for all scattered points. These estimates are then interpolated onto dense point clouds in CloudCompare software. The resulting 2D or 3D accuracy maps can be used to identify weak areas in surveys and to assess survey limiting factors such as georeferencing. Subsequently, the change between the resulting point clouds is quantified, identifying where 3D differences exceed a locally derived confidence limit detection. In summary, the resulting M3C2-PM variant enables confidence-limited change detection that adequately considers photogrammetric and georeferencing considerations that are specific to photogrammetric surveys (James et al., 2017).

M3C2-EP variant extends the well-established algorithm of (Lague et al., 2013b) by introducing error propagation for statistical signal-to-noise separation. According to (Winiwarter et al., 2021), the separation of change signal from noise proves to be crucial for topographic change detection. The amount of change (i.e., LoD) that must occur before it can be reliably quantified depends on several factors, including:

- The type of sensors used to map the topography, in particular, the sensor configuration and its uncertainties
- The way the data is processed
- The properties of the surface (material and geometry).

Knowledge of these factors would allow statistically valid statements to be made about the change that is occurring. The M3C2-EP algorithm simply incorporates this knowledge into the framework for detecting changes in multi-temporal point clouds (Winiwarter et al., 2021).

Despite the considerable added value of these implementations, no structured methodologies for setting a functional parameterization are found in the scientific literature. As discussed in Section 6.2, surface roughness does the orientation of the surface normal dependent on the scale D at which it is estimated. Finding a criterion that ensures that the scale set by the user produces a normal orientation that is not affected by lower scale roughness is essential. At the same time, it is important to indicate an optimal projection scale d in order not to lose information on the compared point cloud. In many works, it was, therefore, crucial to analyse the point clouds in their geometric characteristics before comparing them. In order to find an ideal scaling parameter, one proceeds iteratively by calculating the roughness and the average density by varying r . This parameter represents the radius of a sphere within which, point by point, the following will be evaluated: the number N of neighbouring points, thus giving the density of the points, and the roughness expressed as the distance between the kernel point and the best fitting plane calculated in the sphere. These scalar fields help in understanding the texture of the point cloud and thus choose the parameter r that simultaneously presents a density of points around the point such that it can best represent the local roughness. While on the one hand, the computation of roughness and point density characteristics at various scales can return a rough statistical survey useful for the identification of functional M3C2 scale parameters, on the other hand, the observations deduced in Section 6.1 lead to the conclusion that different scale parameters can describe different geometric behaviours (1D, 2D, 3D). As in fact observed in the tests of paragraphs 6.1.1-4, there is more than one scale parameter r to demonstrate a similar geometric behaviour of the point cloud and among these some succeed in expressing the behaviour itself in the best way. It seems therefore evident that in the planning of the chain of processing oriented to the comparison between point clouds, it must be previously chosen the geometric behaviour to investigate (1D, 2D, 3D). Subsequently, the most functional and efficient scale parameter r can be identified, both for the commissioned investigation scale and in terms of roughness and point density.

6.3. MULTI-EPOCH CLOUD-TO-CLOUD

Accurate high-resolution mapping of the Earth's surface is substantial for documenting its morphology and understanding the processes that govern the environment (Carvalho et al., 2020, Peppas et al., 2019). Planning becomes more complicated in cases where accessibility may be dangerous or inconvenient due to the direct influence of weather, especially in the case of large events, and the impracticability of places such as, for example, along cliffs. These requirements, therefore, exclude or influence many of the conventional surveying techniques. Functional change detection requires repeated surveys of the area of interest at the relevant geomorphic time scale, sufficient accuracy, and precision to correctly interpret changes and their significance (James et al., 2019). Furthermore, consistent co-registration between products for any accurate comparison becomes crucial (de Haas et al., 2020, Saponaro et al., 2020a, Saponaro et al., 2020b). It is of paramount importance that time-differentiated SfM products are accurate and spatially consistent. Hence, there is a growing need to establish proper management of SfM-clouds starting from their generation to the identification of a valid co-registration approach for a proper comparison between them (Coulter et al., 2019) but which is both versatile and automated.

Current methodologies applied for co-registration between point clouds were explored and finally, considering a multi-temporal case study, the impacts of a co-alignment approach were analysed in comparison to more established co-registration methods. Interesting observations were deduced and the basis for the standardisation of this innovative approach was laid.

6.3.1. Co-Registration Methods

In a more traditional approach, co-registration between point clouds, covering the same survey area but taken at different times, is inherited from the georeferencing itself. The point clouds are adjusted by the same number of GCPs in the same targets for each dataset acquired, to equalize the georeferencing conditions. In most cases, the targets measured in the field represent natural physical points that may change or

be removed over time due to the multi-temporality of the surveys. On the other hand, in monitoring cases where the required accuracy is high, the co-registration between these clouds is directly influenced by the accuracy of the field measurements and the operator's accuracy in the marking phase. The georeferencing errors of each cloud would propagate into the co-registrations, generating accumulated errors often larger than the set LoD.

Alternatively, the co-registration can be set manually by taking one cloud as a reference and overlaying the others in at least 4 reference points. In practice, manual alignment tools are used that require the search for homologous points in the distributed GCPs between photogrammetric models. In these cases, however, it is essential that the clouds have at least comparable curvatures and scales, otherwise subsequent adjustments are unmanageable.

These approaches are time-consuming and therefore do not sufficiently account for geometric errors on the models (Cucchiario et al., 2020b). On the other hand, the lack of a priori knowledge of the investigated area and the optimal conditions for it makes it difficult to identify a precise number of GCPs, valid in different scenarios in terms of shape and size. As also seen in Chapter 3, at most, on a comparable basis of scenario, technology and adopted methodology, results from the USGS suggest that only a number greater than 10 and with high accuracy of less than 3 cm makes co-registration between models sufficiently accurate (Kasprak et al., 2019). In practice, the co-registration procedure proceeds iteratively to reduce the registration RMSE from time to time, which significantly lengthens the operational time, in addition to the time required for marking GCPs.

In order to overcome the extended operating time, an automated procedure of the various steps can be considered. Automated registration tools, such as CloudCompare's Iterative Closest Point algorithm (Cucchiario et al., 2020b, Peppia et al., 2019), have often been used to automatically search and match thousands of points and to reduce the registration RMSE below a certain threshold. As in manual co-registration, one point cloud, the reference, is kept fixed while the other, the source, is transformed to best match the reference.

The algorithm iteratively revises the transformation, i.e., combining translation and rotation, which is necessary to always minimise the RMSE of the distance from the source to the reference point cloud, given by the sum of the squares of the differences between the coordinates of the matched pairs.

On the other hand, while co-registration can be considered improved, errors can be exaggerated. The automatic procedure generates bias by exaggerating the fit of the clouds to the reference cloud, particularly in cases where the distribution of GCPs is not well dispersed. In short, this bias causes the automatic registration to adjust the clouds to have a lower RMSE, but at the same time gives them a false shape that can cause incorrect changes detection in multi-epoch monitoring.

6.3.2. Co-Alignment Approach

More recently, (Feurer and Vinatier, 2018) first and (Cook and Dietze, 2019) later demonstrated that processing multi-epoch datasets as a single block in the alignment phase of SfM processing allows for the computation of coherent multi-temporal point clouds. Referred to as "Co-Alignment" (Cook and Dietze, 2019), this methodology requires the alignment of a much larger number of images, especially when combining multiple surveys. This certainly leads to a non-linear increase in processing time and requires more hardware capacity, but with an increase in computational capacity helped by the strong parallelisation of SfM methods (de Haas et al., 2020). (Cook and Dietze, 2019) showed that co-alignment of UAV-derived images by DG generates blocks for each dataset characterised by orientations comparable to those obtained with the classical approach by IG.

In multi-epoch scenarios, the individual epochs are processed and combined into a common framework, initially using the poses of the various images (Zhang et al., 2020). Subsequently, the blocks are optimised using GCPs, collimated into a single solution, or by DG. Compared to the classical approach, co-alignment improves the accuracy of topographic change detection by a factor of 4 in the case of IG and by a factor of 3 with DG (de Haas et al., 2020). As this topic has only recently become the subject of study, the supporting literature is very scarce.

The aim of this research step is therefore to investigate the co-alignment of sparse point clouds as an alternative co-registration method. Given multi-epoch datasets processed individually or co-aligned, the MEs and RMSEs on well-distributed CPs were evaluated by adopting different georeferencing strategies. Then, by performing dense matching algorithms, DEMs were calculated from their outputs. Output performance was evaluated by calculating the DoD, which can detect any discrepancies between vertical estimates (Wheaton et al., 2010), and cloud-to-cloud comparisons were obtained using the M3C2 algorithm (Lague et al., 2013b), aimed at extrapolating the local deviation between models.

A processing workflow, consistent with the results of the previous paragraphs, was performed by generating accurate point clouds and DEM of the coastal area located in Torre a Mare-Bari (Italy), subject to multi-epoch monitoring, as discussed in other paragraph of this thesis. The processing flow was performed independently in three separate chunks (DEC, MAR, OCT), each created for the specific datasets (77 images) acquired in December 2018, March 2019 and October 2019. A final fourth chunk (CO) was also generated to deal with the total dataset acquired in all campaigns (231 images) simultaneously (Figure 6.11).

Georeferencing strategies were implemented. Three different setups were performed for each chunk, based on the adoption of i) 20 GCPs, ii) 10 GCPs, iii) 0 GCPs (DG) case (James et al., 2017a, Padró et al., 2019). The selected CPs (10) were not changed in the three examined setups.

Once the BA phase was completed, the fourth chunk, related to the co-alignment case, was duplicated into three sub-chunks. These CO sub-chunks were subjected to a split-phase: precisely, in each of them, the images referring to the acquisitions of (March, October), (December, October) and (December, March) respectively were removed. In this way, the first sub-chunks involved only the images acquired in December, the second only the images collected in March and the third only the images collected in October. This operation does not affect the orientation of the blocks calculated in the previous step as the software maintains the weighted estimates during the Co-Alignment and BA phase.

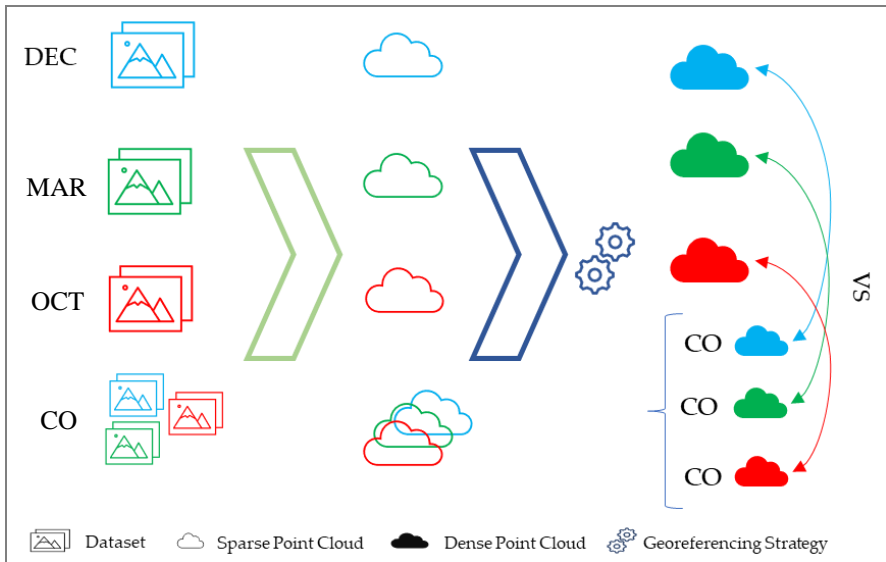


Figure 6.11. Schematisation of the operations carried out for the planned tests.

6.3.3. Improvements of Co-Registration Step

The results obtained in the same epochs are compared to extrapolate possible improvements and validate this innovative and automated co-registration methodology.

Table 6.2 shows the characteristics of the generated point clouds, showing that, in terms of numerical entity, the co-alignment procedures do not disturb the coherence of the photogrammetric procedures. Given the impossibility of detecting a precise systematicity between the dataset behaviours and taking into account the considerations reported by (Coulter et al., 2019), it is evident that these low numerical ΔN variations are attributable to the light conditions at the time of the field data campaigns. Furthermore, Table 6.2 also allows us to detect the influence of georeferencing strategies on the consistency of the final point clouds, showing comparable results for the three setups. These results are also supported by the statistics (ME and RMSE) reported in Table 6.3. Although suffering from the increased computational effort with reduced manual operations, the co-alignment procedure returns geometrically robust products. The planar RMSEs were in a range from +2.47% for the CO-MAR case in DG to -7.44% for the CO-OCT case in IG (20 GCP). The $RMSE_{30}$ on the other hand all

obtained better values than the non-coaligned cases, in particular, the best result was obtained in the CO-OCT case with a value of -6.84%. The systematic errors are spatially consistent over time, aided by the search for paired matching points over multiple timestamps, and thus can be discriminating for change detection tasks.

Table 6.2. Summary of points included in the Sparse Point Clouds (SPC) and Dense Point clouds (DPC) for the three different setups (0, 10 and 20 GCPs) per each analysed sub-chunk. Percentage rate (ΔN) between the amount of points contained in the co-aligned clouds and the original ones. The labels DEC, MAR, OCT indicate respectively the datasets of December, March, October; the labels preceded by the prefix CO are the ones obtained by Co-Split.

ID	GCPs	SPC	DPC	ΔN [%]
DEC	0	111,985	4,736,385	
	10		4,718,898	
	20		4,744,114	
MAR	0	131,265	5,166,324	
	10		5,151,581	
	20		5,163,812	
OCT	0	94,550	4,720,623	
	10		4,693,732	
	20		4,714,341	
CO-DEC	0	113,602	4,720,623	-0.33
	10		4,693,732	-0.53
	20		4,714,314	-0.63
CO-MAR	0	133,494	4,969,606	-3.81
	10		4,950,451	-3.90
	20		4,968,757	-3.78
CO-OCT	0	98,860	4,787,687	+1.42
	10		4,767,307	+1.57
	20		4,782,280	+1.44

On the contrary, when comparing the percentage changes between $RMSE_p$ and $RMSE_{3D}$, it is evident that planar components affect the final error more than the vertical one as $RMSE_{3D}$ is slightly higher in all the examined scenarios. However, georeferencing strategies affect the results as their values improve as the number of GCPs increases, as discussed by (Capolupo et al., 2020c, Saponaro et al., 2020c).

Appreciable improvements, however, can be observed in DG cases by adopting the co-alignment methodology.

Table 6.3. Summary of statistics measured on the 10 CPs distributed in the investigated scene. For each variable, the comparison between the models obtained from conventional and co-aligned procedures is presented in terms of percentage (Δ).

ID	GCPs	ME [m]	Δ ME [%]	RMSEP [m]	Δ RMSEP [%]	RMSE3D [m]	Δ RMSE3D [%]
DEC	0	2.008		1.437		2.047	
	10	0.095		0.098		0.108	
	20	0.056		0.047		0.059	
MAR	0	1.856		1.510		1.907	
	10	0.096		0.098		0.109	
	20	0.057		0.047		0.059	
OCT	0	3.599		1.281		3.758	
	10	0.095		0.099		0.108	
	20	0.059		0.047		0.061	
CO-DEC	0	1.981	-1,35	1.430	-0,49	2.015	-1,57
	10	0.094	-0,71	0.096	-2,10	0.107	-1,25
	20	0.055	-1,59	0.046	-3,51	0.058	-1,35
CO-MAR	0	1.800	-3,02	1.548	2,47	1.830	-4,05
	10	0.096	-0,33	0.097	-1,22	0.108	-0,39
	20	0.056	-0,98	0.046	-2,81	0.059	-0,65
CO-OCT	0	3.418	-5,03	1.306	1,90	3.575	-4,87
	10	0.093	-2,26	0.094	-5,56	0.104	-3,92
	20	0.055	-6,49	0.043	-7,44	0.057	-6,84

From the DEMs computed in each modelling, the DoD was extrapolated. The DoDs is a 2.5D raster representation of the elevation grid variation estimated by subtracting the DEM of the first epoch (DEM1) from the DEM of the next period (DEM2) (Equation 6.12) and is a useful tool for assessing geomorphological changes between multi-epoch surveys (Wheaton et al., 2010).

$$DoD = (DEM_1 - DEM_2) \quad (6.1)$$

In particular, if calculated between DEMs belonging to the same epoch, as in the case of this study, it makes it possible to quantify the uncertainties on the vertical component of the DEMs which corresponds to the vertical component of the error δz . It can therefore be expressed as in Equation 6.13:

$$\delta_z = (Z_2 - Z_1) \quad (6.2)$$

where Z_1 and Z_2 represent the vertical component of the two successive DEMs. A high value of δz affects the reliability and consistency between the products of the results examined as it implies the presence of noise. On the contrary, a low value reveals that the two DEMs can be considered interchangeable in terms of elevation. Furthermore, in the case of co-registration, it indicates how often the software consistently co-registers pairs of multi-epoch datasets, giving an idea of possible problems detectable in subsequent automatic comparisons (Coulter et al., 2019).

Looking at Figure 6.12, uniformity of colour corresponds to the zones with absence or extremely low value of uncertainty (δz is close to zero); conversely, the inhomogeneity in colour is related to uncertainty δz on vertical component. The scalar fields in Figure 6.12 showed how the differences between the DEMs, returned by running the two alignment methods, attested to uncertainty values mostly close to zero. In line with the results reported by (Coulter et al., 2019), the most extreme values were traced in the outermost areas where noise and distortions are commonly non-attenuating, and, consequently, change detection studies should be focused on innermost areas. In the DG cases, the values increased and were not regular (see DEC case) due to the low inherited precision by co-registration. As noted in Table 6.3, the high variance associated with the low accuracy of the image geo-tags transferred a high degree of lability to the DG clouds. This caused an equally high δz value and therefore, although ME and RMSE values were improved (Table 6.3), these high uncertainties could affect the reliability of any change detection. Slight improvements were recorded in georeferenced cases with 20 GCPs compared to cases with 10 GCPs, demonstrating that ex-

cept for highly accurate purposes it is possible to opt for this latter choice by reducing manual operations and processing time.

The co-alignment methodology did not generate significant uncertainties along with the vertical component, leaving co-registration between clouds essentially tied to the georeferencing strategy adopted.

A suitable test to assess any record is related to the analysis of spatial trends in the data applying a cloud-to-cloud comparison (Coulter et al., 2019). In this step, the Multiscale Model-to-Model Cloud Comparison (M3C2), discussed in Section 6.2, was used to calculate the distribution of cloud-to-cloud distances existing between the equal month and GCPs-implemented datasets. This provides an index of point cloud-to-cloud variations. The results of M3C2 are influenced by the value of the radius (r) selected to calculate it. Therefore, identifying its optimal value for the scenario under consideration is essential to calculate these distances. In section 6.1 the criteria was defined, based on the calculation of the geometric characteristics of the point clouds, to detect the appropriate scale parameter. Therefore, these characteristics were first calculated by varying r from 0.05 to 0.50 m and identifying the optimal value of r able to describe the most significant geometric entity of the area, i.e., the rock masses (DiFrancesco et al., 2020). The value of r was set at 0.35 m.

The results of the M3C2 plug-in were presented in Figure 6.13, providing the maximum distance, between +0.752 and -0.752, between the clouds: points without deviation are in green. Once again, the highest deviation values were found on the DG scenarios due to the tolerances of the receiver onboard the UAV. However, as the distance was uniformly distributed over the study area, it was recognised as a systematic error mainly due to the relative positioning between the clouds that did not affect the morphology of the area. In all cases, the largest deviations must be attributed to noise caused by water reflectance and lack of coherence in the outer areas.

The case of the MAR dataset, geo-referenced with 20 GCPs, was emblematic: larger deviations were recorded throughout the area under investigation, except for the coastal strip, which is green. As expected, the deviations tend to cancel out in the vi-

cinity of the GCPs, demonstrating once again (section 3.4.2) the importance of the distribution of GCPs in the area under investigation.

This last test has therefore validated the results already obtained in the previous sections, confirming that the co-alignment methodology does not produce artefacts or distortions even on planar components. The investigated morphology is therefore not distorted, thus proving useful in the detection of changes.

Given the accuracy and reliability of the results, the detection of changes achieved by co-alignment approaches may become commonplace in SfM-based workflow. The outcomes achieved in these tests show that a particularly large gain of co-alignment is that it forces low quality surveys to achieve a more robust collective geometry, feasibly established by the other surveys, which strongly increases the comparability of surveys and the accuracy of change detection.

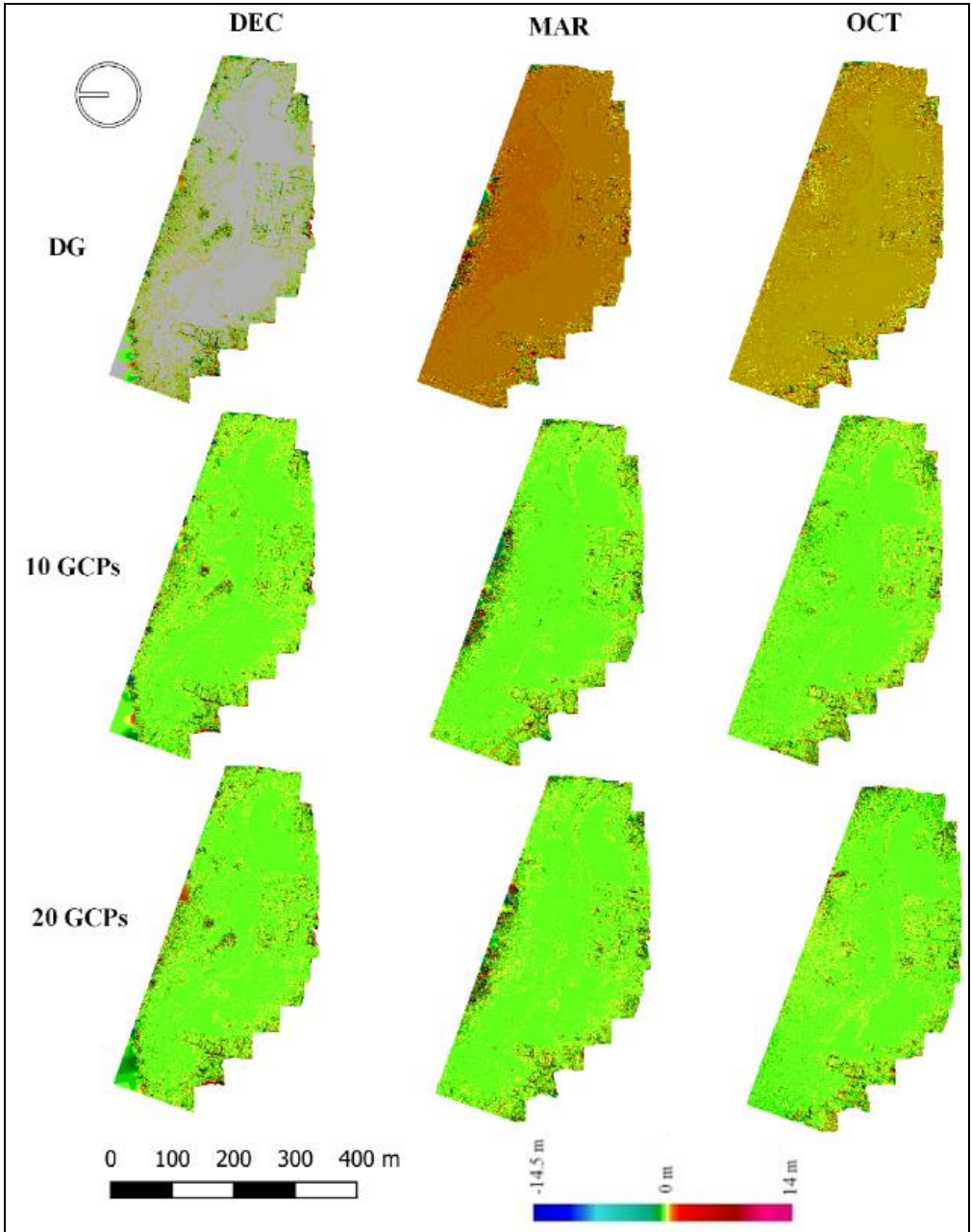


Figure 6.12. Representation of the scalar fields 2.5D DoD obtained by superposition of DEM processed by traditional approach or using co-alignment.

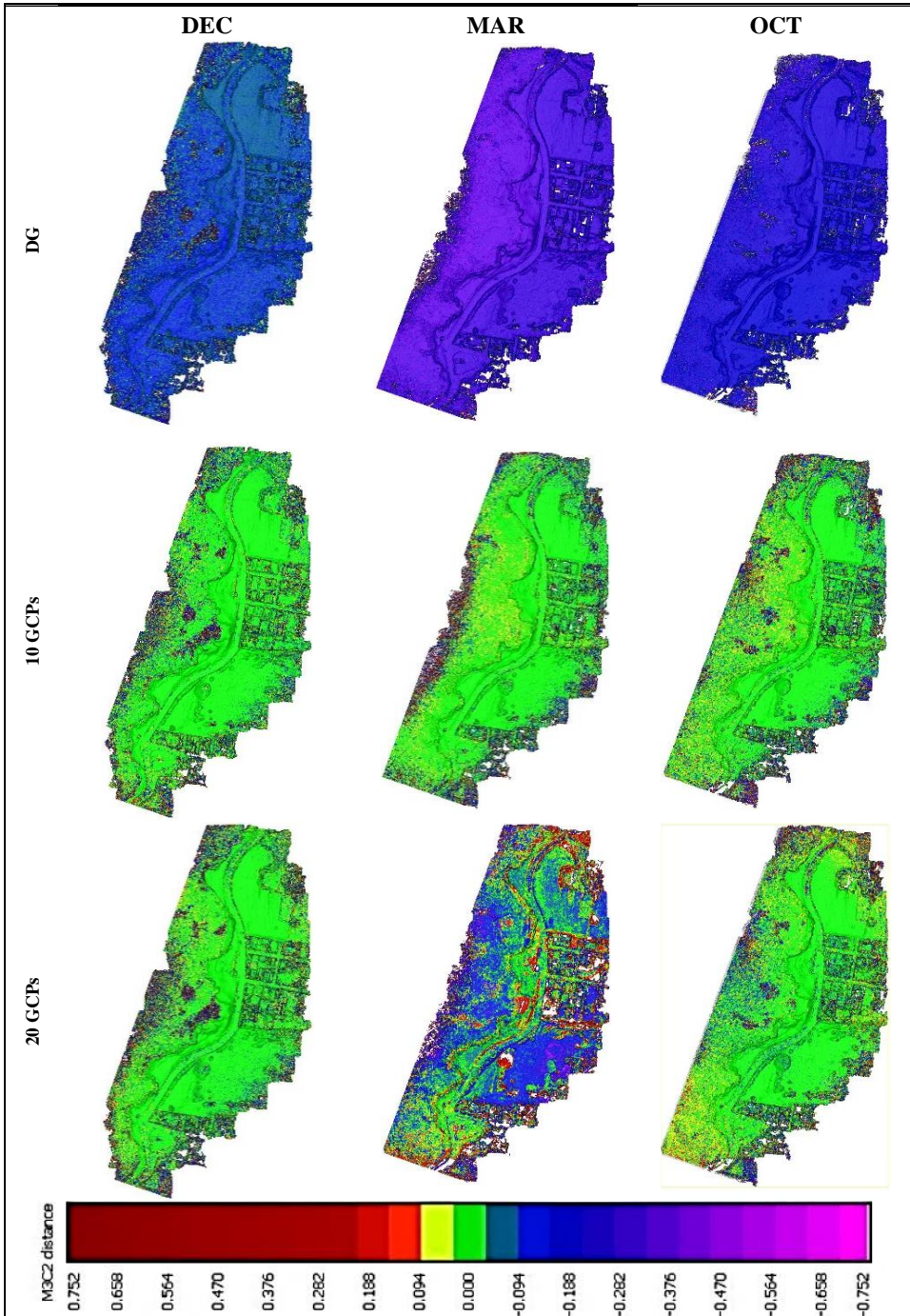


Figure 6.13. M3C2 maximum distance obtained by comparing dense point clouds derived from the two processing approaches for all georeferencing strategies.

6.4. MULTI-SENSOR DATA FUSION

Given the co-registration between point clouds, in planning survey activities the operator must comply with the combined use of several acquisition platforms, such as TLS and UAVs. In many scenarios, however, it is the need to overlap and cooperate the two techniques that make it necessary to define how to manage and process multi-source data. Therefore, taking advantage of the lessons learned about cloud-to-cloud comparisons in the previous paragraphs, the differences and points of contact between the two aforementioned technologies are explored and the potential of data fusion is assessed.

TLS has been intensively employed in various industrial, archaeological and environmental fields as it readily provides highly dense 3D point clouds of the feature under investigation (Jo and Hong, 2019), ensuring its accurate reconstruction. However, depending on the distance of the instrument support point from the site and its angle of detection, the resulting point clouds suffer from an inhomogeneous point density that affects the final results (Son et al., 2020): optimal effectiveness can be achieved if the instrument support position is located relatively close to the site to be investigated and in a perpendicular direction (Jo and Hong, 2019). In addition, its use is also limited by other disadvantages due to the difficulty of reaching inaccessible areas and the high costs in terms of both instrumental equipment and data acquisition time (Son et al., 2020).

Meanwhile, UAV point cloud is homogeneously distributed, it is less dense than that extracted by TLS. Having already discussed the limitations of this technology, it follows that none of the above techniques is free from limitations and, consequently, the integration of data collected from different platforms, commonly referred to as the “data fusion” method, can be fruitful to exploit their advantages and overcome their weakness. Indeed, the data fusion approach is widely used to produce a coherent and accurate digital representation (Tarantino and Figorito, 2014). According to the processing stage at which fusion takes place, this procedure is classified as low (raw data are fused to generate new raw data), medium (features from different raw data inputs are fused) or high (statistical and fuzzy logic methods are used to fuse data)

(Ramos and Remondino, 2015). Many manuscripts point to integrated geomatic surveying techniques as efficient solutions that allow the various experts involved, for example, in the cultural heritage recovery process to collect accurate documentation, to be used as a privileged knowledge tool for diagnostic analyses (Caroti et al., 2019). In particular, the acquisition of geospatial information based on numerical data is very useful for methodical management to detect possible deformations. The management of 3D coordinates of millions of points for polyhedral analysis has increased the ability of any user to compare 3D models point by point automatically (Jo and Hong, 2019). More specifically, 3D measurement studies performed at certain intervals can be used to more accurately determine the deformations occurring in monitored structures and, if necessary, to plan a targeted project more quickly and effectively (Ilci et al., 2019).

A crucial assignment is consequently to test the potential accuracies of latest measurement technologies and techniques to produce high-quality results.

From a theoretical point of view, as described by (Jo and Hong, 2019), laser scanning started as a much more accurate technique than photogrammetry. With the evolution of CV algorithms and new computational techniques, factors known as weaknesses of the classical technique, including photogrammetric image processing, have been made less time-consuming and mostly automated in a digital environment. In the literature, several research works have explored a methodology to compare these technologies: for example, (Roşca et al., 2018) compare the results that can be obtained from these technologies, acknowledge pros and cons in terms of operability for both technologies and at the same time obtain a high positive Pearson's coefficient and a relatively small RMSE value that demonstrates a strong similarity between the results that can be obtained, as also demonstrated by (Medjkane et al., 2018). Their analytical comparison has been carried out in (Moon et al., 2019) who also develop a fusion approach to generate a hybrid model in order to maximise usage for any task; (Seier et al., 2017) show how indeed the two technologies can be considered complementary rather than adversaries, finding that data registration by the two technologies will be strongly influenced by the acquisition perspective and scenario slope.

Lastly, (Joshua et al., 2016) address the comparison in change detection in a multi-temporal monitoring by stating that, after resampling and pre-processing the results to make them homogeneous, the two technologies can be considered interchangeable.

Under these assumptions and considering the accessibility in terms of cost and usage, obtaining photogrammetric products from UAV acquisitions comparable to TLS-based 3D data represents an exciting challenge for the efficiency of operations required for multi-temporal analysis.

By performing a cloud-to-cloud comparison, interesting considerations were made regarding the achievable accuracy and technical limitations of the two methodologies. Considering the cost-effectiveness and ease of use, if used correctly, an UAV supported by proper geo-referencing and optimised data processing can produce 3D reconstructions as accurate and consistent as those derived from TLS.

6.4.1. Comparison between UAV- and TLS-clouds

In this phase of the research work, the potential of two competing survey methods such as TLS and UAV in producing a digital representation of the Monastery of All Saints of Cuti located in the province of Bari (Italy) was explored. In particular, the convergences and divergences between them were evaluated, taking into account the data acquisition and processing time, the accuracy and the number of points composing the generated dense point clouds. After assessing their compatibility, a data fusion procedure was applied to generate a final 3D high detail reconstruction of the building. The reader is referred to (Capolupo et al., 2020a) for a detailed description of the technologies used, the datasets recorded and the processing carried out. The two generated point clouds were then imported into the CloudCompare environment (Girardeau-Montaut, 2015). The point clouds were realigned and co-registered by detecting GCPs in the two models (Son et al., 2020). After this phase, the less accurate edge areas were cleaned up using the Segment tool. The characteristics of the clouds, i.e., volume density, anisotropy, and roughness, were studied. The value of the radius of the sphere within which the software constructs, point by point, the sca-

lar field was set to 0.05 m (James et al., 2017b) to study the heterogeneity of the area, as suggested by (Lague et al., 2013b).

The selection of appropriate metrics is essential to examine different aspects of the generated point clouds (Fugazza et al., 2018).

From an analysis of the geometric characteristics of the point clouds, as discussed in Section 6.1 and 6.2, the comparison M3C2 was calculated by setting the normal scale equal to 0.10 m and the maximum depth of the cylindrical projection to 0.5 m. Conversely, the projection scale was set at 0.10 m.

The time required to acquire and process the collected data, as well as the characteristics of the final results, are shown in Table 6.4. While the UAV make accessible to collect data in a short time (14 min), this technique is not suitable in terms of processing time, as the process take over 974 min. In contrast, TLS requires a higher acquisition time (~ 150 min) but a mild processing time (~ 300 min). The UAV and TLS techniques needed a total of 978 and 450 min, respectively, without contemplating the time spent to evaluate GCPs and CPs (~ 40 min). Thus, only seeing time, TLS looks to be the most reasonable approach as it lets to drastically minimise the total time needed to generate the digital twins.

As a first step, the resulting final dense point clouds were compared, considering the number of points and the volume density (Table 6.4, Figure 6.14). As highlighted in Table 6.4, by returning a larger number of points (195,939,535 vs. 28,202,789), TLS should generate a more detailed digital representation of the building geometry. However, it was difficult to handle and, as suggested by (Son et al., 2020), all unnecessary elements were filtered out, reducing the number of points (from 195,939,535 to 191,519,447) and homogenising the final result. The evaluation of the number of points composing the clouds was not sufficient to detect significant divergences between the two proposed reconstruction techniques and to easily recognise the overlapping surfaces in both corresponding point clouds (Cucchiario et al., 2020a). The “volume density” was calculated because, as demonstrated by previous works in the literature (Jo and Hong, 2019), the distribution of points is an essential parameter for assessing the effectiveness and reliability of 3D reconstruction in accurately repro-

ducing a physical asset. Although TLS presented the highest value of Volume density, Figure 6.14 showed a loss of data belonging to the roof, to the central part and to the ground. This caused the impossibility to reconstruct these areas using only TLS scans. Furthermore, the points were unevenly distributed as their assignment depends on the distance of the object from the instrumental point of view. This strongly influences the homogeneity of the final model, as demonstrated by (Cucchiario et al., 2020a). It should also be noted that the uncertainty of the data, although more numerous than in UAV acquisitions, increases proportionally, due to the low ambiguity range of the adopted TLS instrument, as the acquisition distance from the station point rises. In contrast, the cloud obtained by applying UAV photogrammetry had the lowest volume density value even though the points were distributed evenly throughout the study area, covering both horizontal and vertical faces merits to the acquisition of nadiral and oblique images. This ensures a coherent reconstruction of the whole area under investigation even if the irregular distribution of points on a different dataset strongly influences the user's ability to recognise overlapping areas (Cucchiario et al., 2020a). However, none of the studied approaches suffered from severe occlusions and, consequently, the vertical facades were totally reconstructed.

Table 6.4. Comparison between UAV and TLS performance in terms of obtained final dense clouds, acquisition and processing time.

	UAV	TLS
Acquisition Time (min)	~14	~150
Processing Time (min)	~974	~300
Dense Point Cloud Numerosity (n° points)	28,202,789	195,939,535

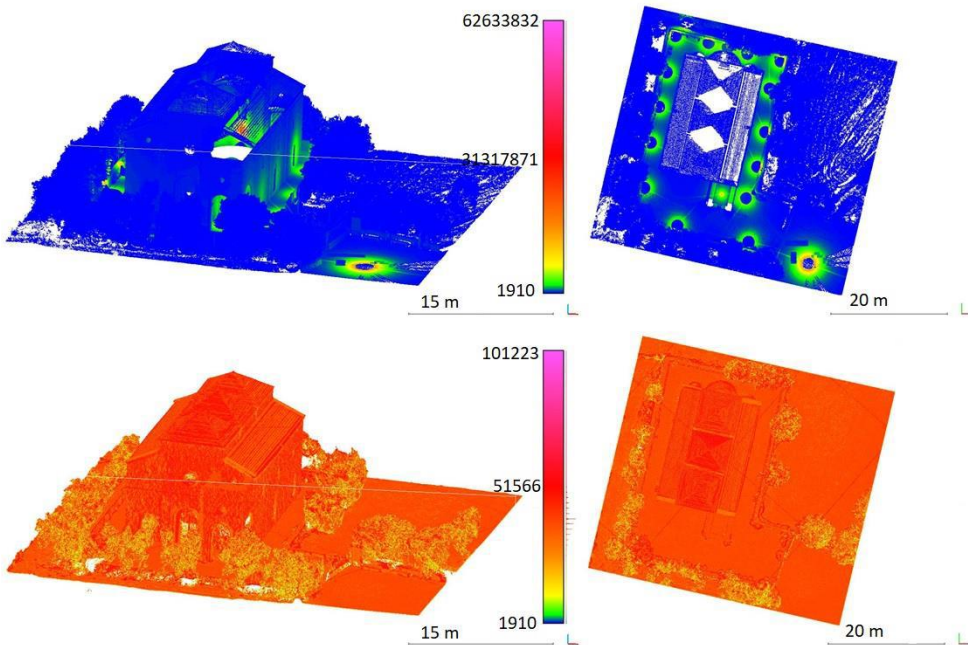


Figure 6.14. Volume density of point clouds generated from data acquired by applying TLS (on the top) and by UAV (on the bottom). XZ and XY perspectives are reported on the left and the right, respectively.

The anisotropy map, shown in Figure 6.15, provides information about the ability of a material to exhibit different properties in different directions. Its range is between 0 and 1: where 0 implies an isotropic behaviour of the object, while 1 describes the opposite tendency. As this characteristic is closely related to the roughness of the material, this result implies that the performance of the proposed methods is not influenced by the material surface. The roughness map shown in Figure 6.16, examined for its relevance in the subsequent matching phase (Blomley et al., 2014), confirms this result. A slightly higher roughness value was found in the UAV-based model, probably due to the higher contribution of noise that affects the final result, making it less reliable.

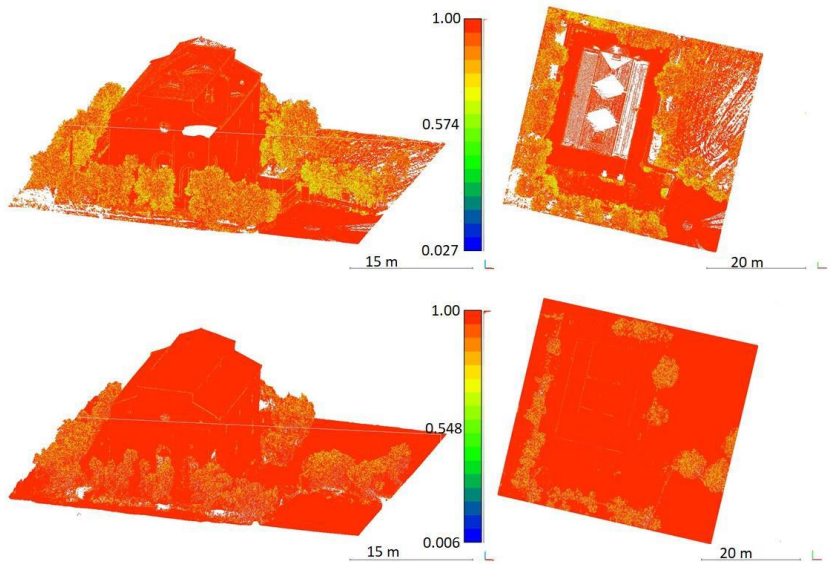


Figure 6.15. Anisotropy of point clouds generated from data acquired employing TLS (on the top) and UAV (on the bottom). XZ and XY perspectives are reported on the left and the right, respectively.

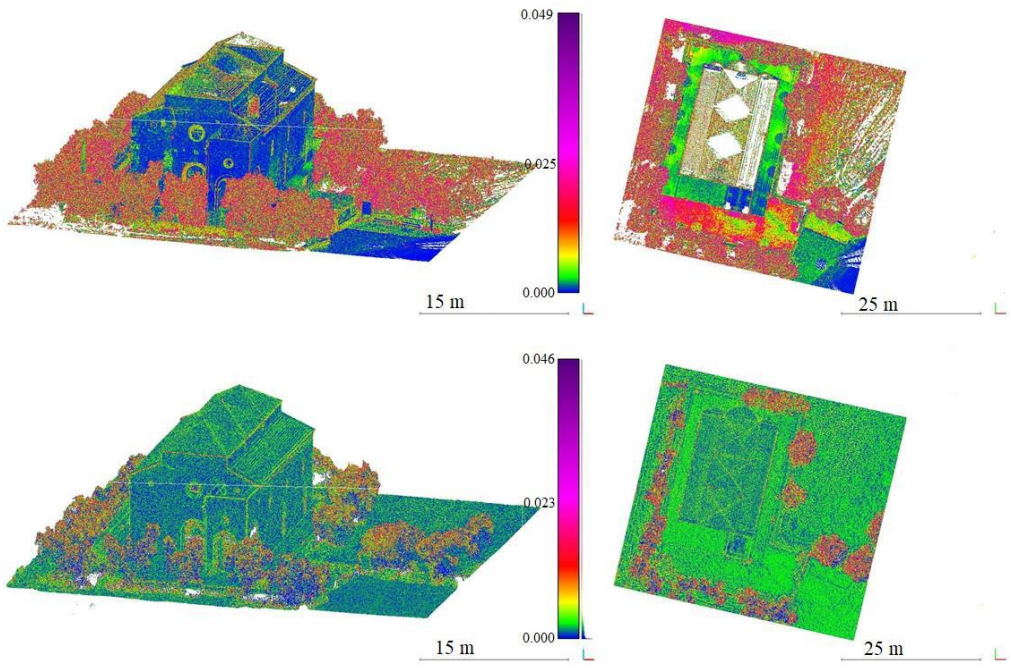


Figure 6.16. The roughness of point clouds is generated from data acquired by applying TLS (on the top) and UAV (on the bottom). XZ and XY perspectives are reported on the left and the right, respectively.

The application of CloudCompare's M3C2 tool was shown in Figure 6.17. It returns a value between -0.500 and 0.500 m. The largest discrepancies were found on the "green areas" and the "roof", mainly due to the lack of information. In contrast, there is a small distance on the horizontal and vertical facades of the Monastery (-0.063; 0.005 m) and a small difference on the portal and the rose window (-0.2; -0.1 m). The uncertainty of the M3C2 result was also evaluated and used as an indicator of the accuracy of the measurement (Figure 6.18). Its value varied between 0.065 and 0.085 m and between 0.09 and 0.146 m for the monastery surface and the vegetated environment, respectively. This ensured the comparability of the models even though both approaches showed some weaknesses.

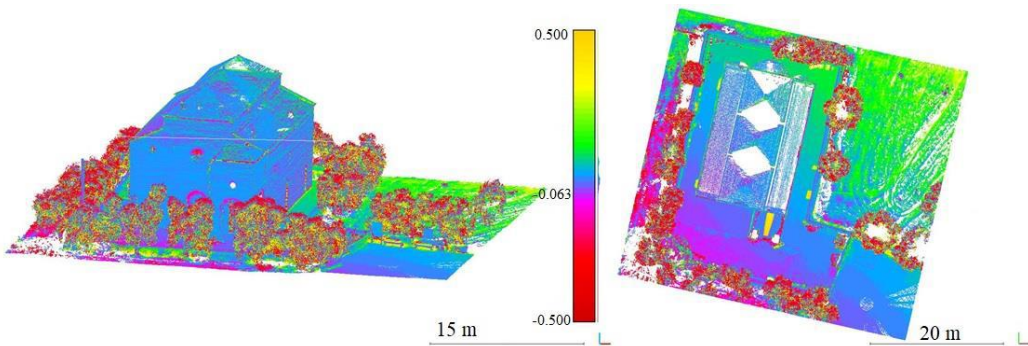


Figure 6.17. M3C2 distance. The meter is assumed as the unit of measurement.

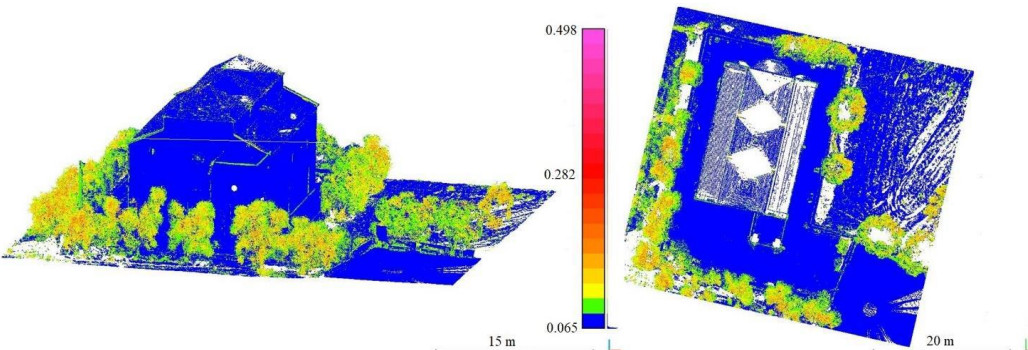


Figure 6.18. Distance uncertainty XZ and XY perspectives are reported on the left and the right, respectively. The meter is assumed as the unit of measurement.

From a theoretical point of view, laser scanning is more accurate than photogrammetry, which generates point clouds with less regular spacing between points and results in more artefacts. Though on the one hand nadiral acquisition prevents to register points below the TLS station plane, on the other hand, TLS scans from the ground permit to acquire more perspective information due to the performance related to the laser incidence angle. The smoothing of certain sections occurs in the case of UAV, unlike TLS where detail is maintained. However, in view of greater technological and technical accessibility even for the less experienced, UAV acquisitions are more convenient in terms of time and cost as they require shorter field operations. Looking at the results obtained from their comparison, the overall discrepancies between the two technologies can be considered sufficient to generate convergent, integrable and comparable models unless the commissioned accuracy is below the centimetre order.

6.4.2. Merging Techniques Peculiarities

After assessing the suitability of two Dense Points (DPCs) to be merged, they were merged by applying equation 6.14:

$$DPC_F = DPC_T + DPC_U \quad (6.14)$$

where DPC_F represents the fused model, DPC_T and DPC_U are the TLS-based and UAV-based point clouds respectively.

The result of the data fusion approach is shown in Figure 6.19. Finally, the contribution of the input clouds to the resulting result was evaluated through the Original Cloud Index parameter aimed at identifying the points from which the clouds are derived. This parameter is expected to be 0 if the points are originated from TLS-cloud and 1 if they fit the UAV model (Hämmerle et al., 2016) (Figure 6.20). All missing data in the TLS-based model, as well as the areas belonging to the main façade, were extracted from the UAV model. The remaining areas (side facades and vegetation environment) were derived from the TLS model.



Figure 6.19. Fused model results. XZ and XY perspectives are reported on the left and the right, respectively.

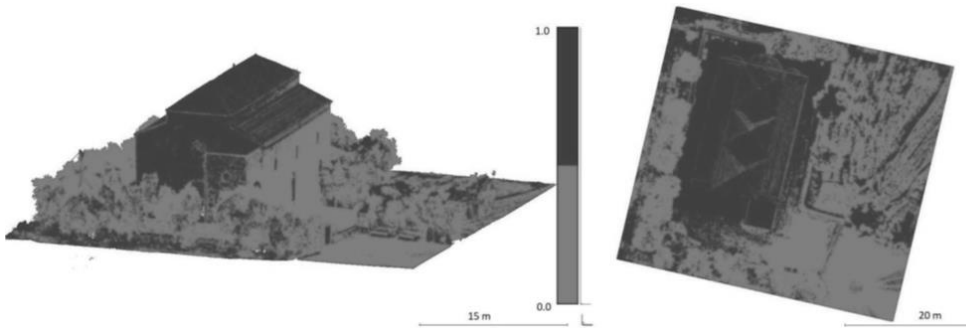


Figure 6.20. Original Cloud Index: 0 light grey (points from TLS) and 1 dark grey (points from UAV). XZ and XY perspectives are reported on the left and the right, respectively.

Both generated point clouds showed several limitations. Once the accuracy and comparability of the models have been assessed, the data fusion methodology appears to be an effective solution for accurately reconstructing a physical building stock. To ensure an accurate hybrid result, an appropriate operational workflow was applied. As demonstrated in the literature (Farella et al., 2019a), the combination of data from complementary acquisition techniques generates comprehensive models in which the limitations of one technique are compensated by the other but considering a reduction in computational capacity. However, in order to control the reduction in computational capacity due to the mass of the fused cloud, it will be necessary to analyse possible filters able to eliminate redundant data and lighten the final cloud.

6.5. ONE STEP TOWARDS BIM

Obtaining a 3D point cloud model leads to various applications in the context of civil structures management. Conventional inspections are carried out by trained operators who visually assess the condition of structures, manually draft inspection documents and evaluate the condition of artefacts with a certain degree of subjectivity. Conventional in-situ investigations generally require the use of temporary structures that increase inspection time and require restrictions and disruptions to services surrounding the structure. The revolutionary change in the conventional approach is brought about by these innovative methodologies using sensors to monitor structural health and innovative non-contact RS techniques. In addition to the technical visual inspections carried out in the field or by analysing the UAV images of the dense point cloud obtained (possibly processed in the textured mesh), it is possible to recognise and collect degradation phenomena affecting the different structural components even in a virtual environment. (Otero, 2015) discussed the influence of several UAV characteristics such as manoeuvrability, payload, size, adaptability etc. which are decisive for an accurate field inspection. Furthermore, through point segmentation or classification of structural components recognised in UAV images, it is possible, as already seen, to extract geometric features and metric and material information of the detected structure. Several studies focus on the quantitative assessment of damage conditions through damage detection and crack measurement algorithms based on 3D point cloud models (Lee and Park, 2019). Crack detection and damage recognition are performed using machine learning techniques. Several authors have stated that automatic structural assessment algorithms that consider both the degradation condition and mechanical quantification of structural deformations should follow UAV-based inspections.

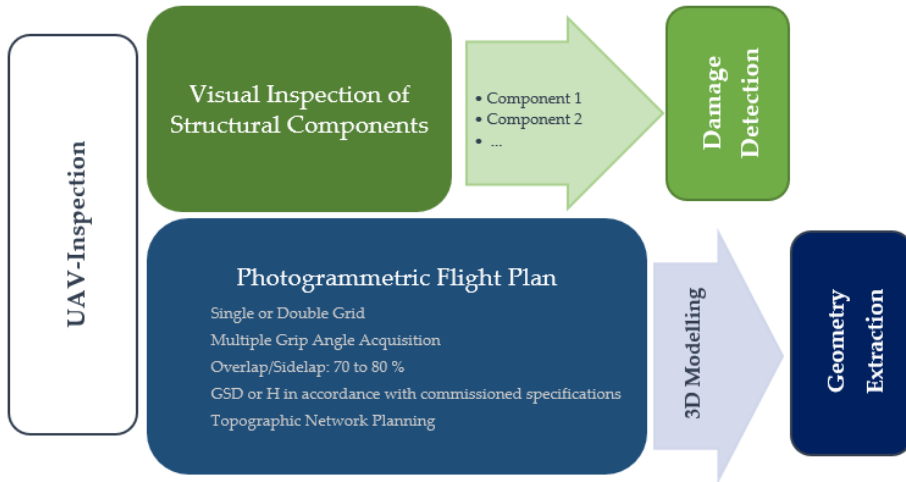


Figure 6.21. UAV-based Inspection in a simplified schematization (Nettis et al., 2020).

These applications induce strong innovations in the management, maintenance, and decommissioning processes of civil works. In this regard, the interest of various industries in obtaining intelligent mock-ups of complex civil structures suitable for digital navigation and inspection is constantly growing (Isailović et al., 2019). On the other hand, the storage of huge amounts of data, which could be easily interrogated and interpreted, brings census operations to an advanced state of control aimed at effective management of the entire portfolio of structures. The digital model not only acts as a virtual representation but turns out to be a container of different types of information (e.g. geometry, construction methodology, mechanical aspects) on all the components of the construction (structural and non-structural components, systems, etc.) and on the overall structure itself (e.g. maintenance scheduling, remaining useful life or even structural vulnerability) thus ensuring interoperability between the various actors of the structure's life (Wu and Zhang, 2019). In this regard, the BIM paradigm combines and connects acquired and processed data for rational management of the entire life cycle of any civil works. These components drive towards complete automated workflows that start with data collection and processing and go directly to quantitative structural evaluation.

The geometric interpretation of point clouds is essential within a BIM approach. Once the dense point cloud is obtained, the extraction phase of the mere geometries of each component can follow automatic or semi-automatic modelling through Scan to BIM algorithms or through manual tracing operations from the cloud itself (López Iglesias et al., 2020). Once the geometries have been extracted and converted to the BIM environment, the entire structure can be dismembered into its polygonised components, defined as BIM objects or multilayer containers. Automated or semi-automated procedures decrease operational time and speed up the entire workflow (Wang et al., 2015, Yang et al., 2020). Recognition of significant geometric features is essential for both continuation modes and analysis, using the techniques seen in Section 6.1, yields enormous benefits in the interpretation of photogrammetric products. This type of point cloud management is in its infancy and the segmentation and automated classification of point clouds are very active research topics (López Iglesias et al., 2020, Barrile et al., 2019a). Most segmentation algorithms are tailored to work with 2.5D surface models or in 3D space. Consequently, the point cloud is classified and portioned with reference to the different structural components. As a result, the segmented structural parts are converted from point clouds into 3D polygons.

On the other hand, the manual tracing of geometries from the dense point cloud is a primitive methodology but capable of establishing a feedback relationship between the operator and the software used (López Iglesias et al., 2020). The operator then manually models the structural (or non-structural) components from the photogrammetric model, due to a large amount of work time involved, especially in cases of complicated geometries or when a large number of structures have to be modelled. Although the manual approach is costly in terms of time and modelling effort, the operator's expert contribution allows the recognition and categorisation of structural members that may be essential for further mechanically based structural analysis.

Conclusively, once the complex architecture of the structure has been reproduced in the BIM environment and a geo-referenced system has been defined to which it can

be anchored, it is possible to integrate, and update disaggregated and heterogeneous information for each extracted geometric block (Figure 6.22).

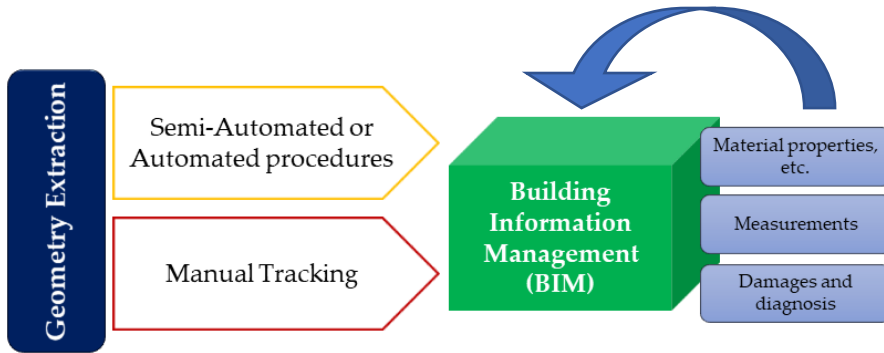


Figure 6.22. Modelling of a structure in BIM environment and collection of disaggregated and heterogeneous information (Nettis et al., 2020).

6.5.1. From Dense Point Clouds to BIM

A six-span RC bridge of the Basilicata road network, representing a typical Italian bridge typology, is selected to practically describe the operational phases of UAV inspection, photogrammetric modelling, and extraction of geometric information useful in a BIM approach. The reader is referred to (Nettis et al., 2020) for more details about the technologies used, the datasets created and the processing carried out.

Once the dense point cloud was obtained, the process of extraction of the geometries of the structural components in the BIM environment was started. The entire flow of operations was conducted in the Autodesk Revit 2020 working environment, a software platform with a commercial license widely used in the construction industry.

The geometric modelling of the viaduct was carried out using a manual approach, in order to adequately capture the characteristics of even the smallest structural components.

Using Families libraries defined as Industry Foundation Classes (IFC) (Barrile et al., 2019b), each structural component was converted from a portion of a point cloud into a solid block. Briefly, for the modelling of each block, the main dimensions were

measured and fixed from the dense point clouds and then the most suitable family was selected in the library or created by extrusion using the appropriate editor. An object was then generated by plotting the observable shapes and assigning all the properties associated with it (e.g., materials, mechanical properties). Finally, the positioning of the generated object was performed by anchoring it to an appropriate spatial reference system. Each extracted geometric block became a container for a variety of information. In addition to the inherited data on the physical properties of the materials constituting the specific element, several layers of information on visual inspection and damage analysis were added. Each component was surveyed and structured into the composition of the structure, and diagnostic reports prepared by the operator in the field were attached to it.

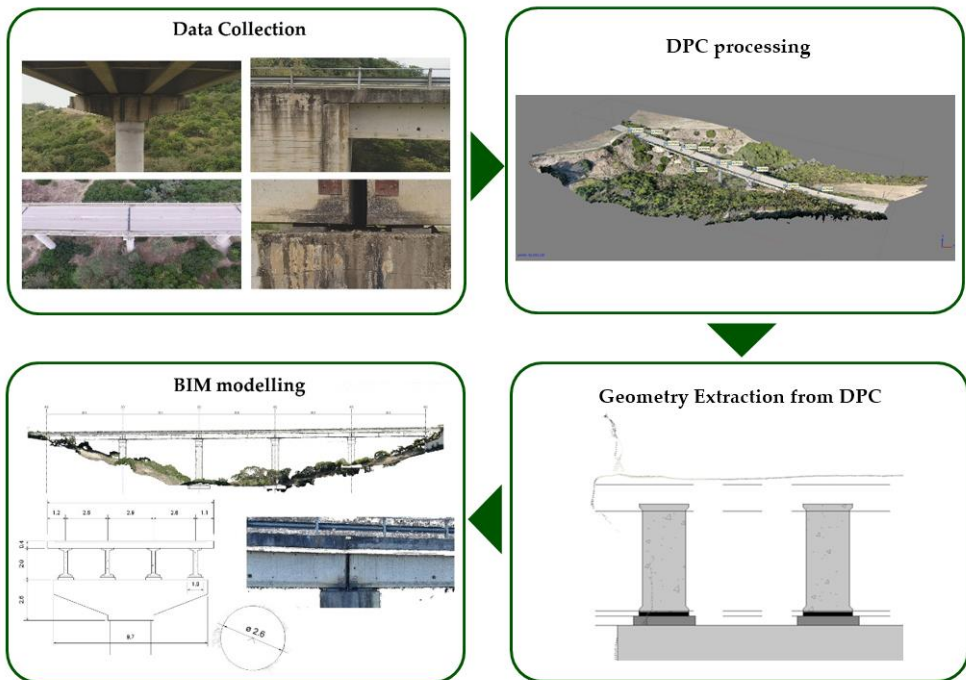


Figure 6.23. The sequence of steps for the geometry extraction and allocation of data in BIM and Excel spreadsheet to perform the seismic risk assessment. A list of the data necessary for the risk calculation is indicated.

As pointed out by (Bassier et al., 2019), further developments will be directed towards improving the potential of UAV data collection employing automated algorithms to extract and manage data for BIM archiving or to address analytical processes for structural assessment.

CONCLUSIONS

Environmental and industrial applications are deeply encouraged by the revolution fostered by EO technologies and techniques. New satellite, airborne and ground-based systems characterised by high spatial, temporal and radiometric resolution are continuously evolving, and large masses of data are thus flowing into Big Geospatial Data, oriented to help multiple industries and academia with a new approach in a cross-sectoral way. Likewise, a profound need has emerged for a system to make sense of this vast spatial data. Despite the abundance of this data, most of it is still not well exploited mainly due to system inadequacies. While these data contain important information, on the other hand they are heterogeneous, multi-source, multi-temporal, multi-scale, highly dimensional, highly complex and unstructured. Due to the aforementioned heterogeneity and high dimensionality of Big Data in RS, important computational and statistical challenges related to processing scalability, noise accumulation, spurious correlation, accidental endogeneity and measurement errors have been addressed in the scientific literature. New patterns can be identified, new knowledge discovered, and new rules established, hidden behind the data, to help understand and interpret the real world and guide people towards correct decisions and efficient performance. But there are still some disadvantages, such as the lack of guarantees for data continuity, data uncertainty, the fact that the multi-source RS data network has not been optimised, that the data assimilation process lacks data validation, and that EO information has not yet met the requirements of model parameters. These factors mean that the sensors cannot be fully utilised and limit the use of the data for many applications.

If, in systemic terms, a paradigm shift is therefore underway, this includes validation of analysis methods and models in order to achieve shared standardisation and, above all, validation of each data source in order to make it conform to the whole system. This is the typical example of data from UAVs, now a disruptive technology in any sector that requires formalisation of the techniques, processes, and methodologies to be implemented. The developing market for UAV-based data requires industry to define and establish supply chain management and processing of this data.

At the same time, the adoption of increasingly high-performance and widely accessible FOSS4G software platforms is revolutionising the way of working, driving a shift towards open science, knowledge sharing and reproducibility. Evidently, these renovations require the tailor-made implementation of high-level value chain frameworks, but many issues still need to be resolved.

Among the many already discussed by the scientific community, it has been pointed out that manual interpretation and analysis of integrated data is no longer adequate, which is why sophisticated automatic analysis methods are needed to make the process efficient and effective.

In this thesis work it was therefore proposed to develop a FOSS4G framework from pre-processing to post-processing of photogrammetric products, useful for the extraction of near real-time information applied to high-resolution, multiscale, multi-temporal and multi-sensor data for environmental monitoring and innovative inspection of buildings and territories using MMT techniques.

As already pointed out in the introductory chapters of this dissertation, the main contributions of this thesis were to:

- investigate multi-sensor and multi-resolution EO platforms and in-depth study UAV technologies used for photogrammetric operations;
- structure a comprehensive open-source framework ranging from acquisition strategy and georeferencing step, geometric and radiometric pre-processing, output processing, and analysis;

- apply open methodologies for pixel-based and point-based analysis of producible photogrammetric results for multi-scale, multi-temporal, and multi-sensor surveys;
- achieve these with high quality but using low-cost technologies and techniques to increase their accessibility.

During the dissertation, a step-by-step structure was investigated, focusing on the use of purely low-cost UAV platforms equipped with inexpensive sensors. An extensive discussion on the configuration and optimisation of field acquisition and pre-processing activities was addressed in order to reduce both ancillary costs and operations effort. Several innovative, but at the same time FOSS4G and user-friendly, methodologies were tested to extract information from data characterised by different spectral and spatial resolutions. Validation procedures of the products obtainable from the FOSS4G photogrammetric process chain have been proposed in order to identify their place among different commercial alternatives but also with respect to more established Earth Observation data acquisition technologies. As a general result, this thesis has therefore reconstructed a repeatable and reproducible procedure, tested and validated the products that can be rendered, and proposed innovative image- and point-based analysis methods.

The work then sought to address some of the limitations regarding the collection and pre-processing of information in a timely and cost-effective manner, and the lack of an accredited framework for processing photogrammetric data that can be considered reproducible, repeatable, and widely accessible in the context of the democratisation of Data Science. Therefore, a workflow was proposed in an open-source photogrammetric software, such as MicMac, whose results were compared with those found from the adoption of commercial software platforms, widely used in the professional field. The results were verified by varying the operating conditions in the field, in order to integrate into the analysis an optimisation of the topographic operations in terms of costs and execution times. The same results were validated by comparison with the planar, vertical and three-dimensional accuracy standards promulgated by the ASPRS in 2015 for geospatial products. The proposed

photogrammetric processing chain was found to be compliant and competent with those already shared by the scientific community, convenient and suitable for practical purposes.

Subsequently, the influence of the pre-processing phases on the datasets acquired by UAVs was discussed, in particular the geometric and radiometric calibration of the images, in order to identify a synthetic procedure, accessible to any user and at the same time effective. In the case of geometric calibration, a self-calibration procedure was adopted, proposing an innovative methodology to solve the problems of overparametrisation. Briefly, a three-parameter synthetic index and a predictive function of the final accuracy were proposed by applying a PCA analysis on the calibration parameters of a low-cost sensor described by the Brown Lens Model. For the radiometric calibration, a process chain was set up in the FOSS4G environment to apply the ELM methodology. From the comparison with the spectral signatures commonly accepted by the scientific community, the technique has obtained radiometric calibrations of images in the visible bands (RGB) suitable for possible post-processing of the radiometric information. This leads to an obvious optimisation of the time and cost of field operations, but also to a rediscovery of the hidden potential of low-cost sensors.

After all, the work proposes an answer to the complexity of dealing with high spectral and spatial resolution data, such as large amounts of data in real-time applications, to extract targeted information to solve specific problems. Open methodologies were applied for pixel-based and point-based analysis of producible photogrammetric results for multiscale, multitemporal and multisensor surveys. In the pixel-based analysis, the behaviour of ten vegetation indices applied on images in the visible bands was analysed and differences in separability in the identification of vegetated and non-vegetated areas were appreciated. Using the best performing indices, in particular the TGI and ExG indices, Random Forest supervised classification algorithms and K-Means unsupervised classification algorithms were run to analyse their performance, also varying the spatial resolution of the orthomosaics. From the confusion matrices, performance indices were extracted, such as the F-scores index,

which show values quite comparable with those obtainable in the multispectral domain and, more precisely, a better efficiency for the Random Forest algorithms when applied to RGB images from low-cost sensors. It is not possible to identify a linear relationship between the efficiency of the VIs and the spatial resolution and, above all, a close dependence of the efficiency of the VIs on the scenario investigated.

In the point-based analysis, a study was carried out on the extraction of significant geometries from a neighbourhood analysis as the scale parameter changes. This led to highlighting linear, planar or three-dimensional behaviours as the parameter varies and thus to obtaining a greater focus on possible geometric elements to be monitored. An innovative method was then proposed for setting up the cloud-to-cloud comparison using M3C2 algorithm in the open-source software CloudCompare. At last, an innovative and alternative method of co-registration between multi-temporal and/or multi-sensor point clouds, defined as “co-alignment”, was proposed, capable of reducing the time dedicated to the georeferencing phase and improving the co-registration between models.

In view of the results obtained in the various phases of the project, a procedure was proposed for the implementation of the results in a BIM environment, in order to collect further data sources and deliver a highly functional and innovative product to the final user.

In the light of these studies, it is possible to draw the following conclusions:

- Data acquisition techniques based on UAV platforms and low-cost sensors are proving to be a complementary choice and/or interchangeable to more traditional technologies.
- Optimisation of acquisition, pre-processing, processing, and post-processing procedures in order to reduce costs and execution times can also be addressed in an open-source environment in order to democratise the sector and make it more accessible.
- The process engineering analysed in this thesis shows how the use of low-cost techniques and hardware can guarantee the extraction of high-quality

geospatial data which, if assisted by the automation of operations, validates the potential of Big Geospatial Data.

Interesting perspectives emerge from the results of this research work. First of all, as often defined in the thesis, the objectives centred by this work will allow the definition of paths for the automation of processes and the obtaining of a detailed application capable of autonomously executing the operations carried out in the various steps. The evolving machine learning and deep learning algorithms will make the whole process exciting for many industrial and academic sectors and many more professionals will be included in the innovation process due to the high accessibility and democratisation of the techniques and technologies. This Big Geospatial Data represents a great opportunity, and it is up to us to take full advantage of its potential.

LIST OF ABBREVIATIONS

- 1D** – One Dimensional
- 2D** – Two Dimensional
- 3D** – Three Dimensional
- AGL** – Above Ground Level
- AI** – Artificial Intelligence
- ALS** – Airborne Laser Scanning
- ANN** – Approximate Nearest Neighbour
- AoI** – Area of Interest
- APC** – Antenna's Phase Center
- ASPRS** – American Society for Photogrammetry and Remote Sensing
- AT** – Aero-Triangulation
- BA** – Bundle Adjustment
- BBA** – Bundle Block Adjustment
- BIM** – Building Information Modeling
- BRDF** – Bidirectional Reflectance Distribution Function
- C2C** – Cloud to Cloud
- C2M** – Cloud to Mesh
- CCD** – Charge-Coupled Device
- CEOS** – Committee on Earth Observation Satellites
- CIVE** – Color Index of Vegetation
- CMOS** – Complementary Metal-Oxide-Semiconductor
- CORS** – Continuously Operating Reference Stations
- COTS** – Consumer off-the-shelf
- CP** – Check Point
- CPU** – Central Processing Unit
- CUT** – Cyprus University of Technology

Cv – Coefficient Variation
CV – Computer Vision
DEM – Digital Elevation Model
DG – Direct Georeferencing
DGNSS – Differential GNSS
DICATECh – Department of Civil, Environmental, Land, Construction and Chemistry
DNN – Deep Neural Networks
DoD – DEM of Difference
DSLR – Digital Single Lens Reflex
DSM – Digital Surface Model
DTM – Digital Terrain Model
EDM – Electronic Distance Measurement
EGNOS – European Geostationary Navigation Overlay System
ELM – Empirical Line Method
EM – Environmental Monitoring
EO – Earth Observation
EUREF-EPN - EUREF GNSS Permanent Network
ExG – Excess Green Index
EXIF – Exchangeable Image File Format
ExO – Exterior Orientation
FOSS4G – Free and Open-Source Software for Geospatial
GCP – Ground Control Point
GIS – Geographical Information System
GLI – Green Leaf Index
GM – Global Monitoring
GNSS – Global Navigation Satellite System
GPS – Global Positioning System
GPU – Graphics Processing Unit
GSD – Ground Sample Distance
HIS – Hyperspectral Imaging Sensor
IFC – Industry Foundation Classes
IG – Indirect Georeferencing
IGM – Istituto Geografico Militare Italiano

IMU – Inertial Measurement Unit
IO – Interior Orientation
IoT – Internet of Things
IRG – Red-Green Ratio Index
JPEG – Joint Photographic Experts Group
LC – Land Cover
LiDAR – Light Detection And Ranging
LoD – Level of Detection
LU – Land Use
LULC – Land Use/ Land Cover
M3C2 – Multiscale Model-to-Model Cloud Comparison
ME – Mean Error
MGRVI – Modified Green-Red Vegetation Index
MMT – Multi-Sensor Multi-Resolution Techniques
MSI – Multispectral Imaging Sensor
NA – Not Acceptable
NDVI – Normalized Difference Vegetation Index
NGRDI – Normalized Green-Red Difference Index
NIR – Near-Infrared
nRTK – network Real-Time Kinematic
OBIA – Object-based Image Analysis
ODM – OpenDroneMap
PAN – Panchromatic
PBIA – Pixel-based Image Analysis
PC – Principal Component
PCA – Principal Component Analysis
PhD – Doctor of Philosophy
POLIBA – Polytechnic University of Bari
PPK – Post-Processing Kinematic
PRS – Permanent Reference Settings
R – Pearson's Coefficient
R&D – Research and Development
RADAR – Radio Detection And Ranging

RAM – Random Access Memory
RANSAC – RANdom Sample Consensus
RDN2008 – Rete Dinamica Nazionale Italiana
RE – Reprojection Error
RF – Random Forest
RGB – Red Green Blue
RGBVI – Red-Green-Blue Vegetation Index
RGRI – Red-Green Ratio Index
RMSE – Root Mean Square Error
ROA – Remotely Operated Aircraft
RPA – Remotely Piloted Aircraft
RPAS – Remotely Piloted Aircraft System
RPV – Remotely Piloted Vehicle
RS – Remote Sensing
RTK – Real-Time Kinematic
SaaS – Software as a Service
SI – Synthetic Index
SIFT – Scale Invariant Feature Transform
SONAR – Sound Navigation and Ranging
SSD – Solid-State Memory
SVD – Singular Value Decomposition
SWIR – Short-Wave Infrared
TGI – Triangular Greenness Index
TIFF – Tagged Image File Format
TLS – Terrestrial Laser Scanner
TS – Total Station
UAS – Unmanned Aerial System
UAV – Unmanned Aerial Vehicle
UAV(*) – Uninhabited Aerial Vehicle
VARI – Visible Atmospherically Resistant Index
VI – Vegetation Index

LIST OF TABLES

Table 3.1. Average errors and RMSE values resulting from the comparison of positional measurement techniques from TS and nRTK-GNSS, in the same 10 targets homogeneously distributed in the investigated scene.	121
Table 3.2. Full description of the RMSE _{xyz} [m] values and the Error [pix] (i.e. RE) recorded in the 42 generated Chunks. The red box highlights the results considered as optimal for the model georeferencing. In the green box, the results obtained for the complete IG cases.	126
Table 4.1. Photogrammetric datasets acquired during the five UAV campaigns and related GSD values.	153
Table 4.2. Statistics of I.O. parameter evaluations calculated with respect to the 31 replications for the 5 processed datasets (December 2018, January 2019, February 2019, March 2019, October 2019); Stat—statistic; Max—maximum; Min—minimum; SD—standard deviation; f—focal length; xp and yp coordinates of principal point; B1; B2—skew coefficients; K1, K2, K3, K4 —radial distortion coefficients; P1, P2, P3, P4—decentering distortion coefficients.	154
Table 4.3. Correlation matrix of camera IO parameters as estimated from the December 2018 dataset (f= focal length (pix); xp and yp coordinates of the principal point offset; B1, B2 = Skew parameters; K1, K2, K3, K4= radial distortions; P1, P2, P3, P4= components of the decentering distortions).	161
Table 4.4. Correlation matrix of camera IO parameters as estimated from the January 2019 dataset (f= focal length (pix); xp and yp coordinates of the principal point offset (pix); B1, B2 = Skew parameters; K1, K2, K3, K4= radial distortions; P1, P2, P3, P4= components of the decentering distortions).	162
Table 4.5. Correlation matrix of camera IO parameters as estimated from the February 2019 dataset (f= focal length (pix); xp and yp coordinates of the principal point offset (pix); B1, B2 = Skew parameters; K1, K2, K3, K4= radial distortions; P1, P2, P3, P4= components of the decentering distortions).	162
Table 4.6. Correlation matrix of camera IO parameters as estimated from the March 2019 dataset (f= focal length (pix); xp and yp coordinates of the principal point offset (pix); B1, B2 = Skew parameters; K1, K2, K3, K4= radial distortions; P1, P2, P3, P4= components of the decentering distortions).	163
Table 4.7. Correlation matrix of camera IO parameters as estimated from the October 2019 dataset (f= focal length (pix); xp and yp coordinates of the principal point offset	

(pix); B1, B2 = Skew parameters; K1, K2, K3, K4= radial distortions; P1, P2, P3, P4= components of the decentering distortions).	163
Table 4.8. Synthetic index (SI) as computed by eq. 4.4 for the December, January, February and October datasets.	167
Table 4.9. Correlation coefficient between RMSE _j and SI computed for each dataset (GCPs=Ground control Points; CPs=Check points; E= East coordinate; N=North coordinate; H= height coordinate; T=3D error; I=positioning error in the image space).....	167
Table 4.10. Coefficients of the calibrated predictive functions (E = East coordinate; N= North coordinate; H= height coordinate; T= total (3D) error; I= positioning error in the image space).....	169
Table 4.11. Differences between RMSE _j values as estimated by the calibrated predictive models and the correspondent ones from BBA for the March dataset.	170
Table 5.1. Summary of surveyed scenarios adopted technologies and acquired datasets.....	181
Table 5.2. List of spatial resolution solutions generated per scenario. The GSD values below represent an approximation to the nearest millimetre of the effective values.	182
Table 5.3. The normalised difference (%) between the mean value \bar{VI} for each index over vegetated areas and non-vegetated areas. Blue colour indicates negative normalised difference value, while red colour, positive value per vegetation index for each spatial resolution. Lighter colours thus indicate a low degree of separability, while the acronym NA identifies Not Acceptable values due to failure of the T-test.....	197
Table 5.4. Confusion matrices and related metrics for the analysed cases of RF supervised classification.	227
Table 5.5. Confusion matrices and related metrics for analysed cases of unsupervised classification with K-Means algorithms.....	231
Table 6.1. Summary of the used scale parameters r.	248
Table 6.2. Summary of points included in the Sparse Point Clouds (SPC) and Dense Point clouds (DPC) for the three different setups (0, 10 and 20 GCPs) per each analysed sub-chunk. Percentage rate (ΔN) between the amount of points contained in the co-aligned clouds and the original ones. The labels DEC, MAR, OCT indicate respectively the datasets of December, March, October; the labels preceded by the prefix CO are the ones obtained by Co-Split.	270
Table 6.3. Summary of statistics measured on the 10 CPs distributed in the investigated scene. For each variable, the comparison between the models obtained from conventional and co-aligned procedures is presented in terms of percentage (Δ).	271
Table 6.4. Comparison between UAV and TLS performance in terms of obtained final dense clouds, acquisition and processing time.	281

LIST OF FIGURES

Figure 1.1. Resolution demands (temporal, spatial, spectral and swath) in the main fields of application of RS and supply of data sources. Figure based on (Emilien et al., 2021). EO: Earth Observation; EM: Environmental Monitoring; GM: Global Monitoring; sat.: satellite; LC: Land Cover; LU: Land Use.	35
Figure 1.2. Diagram of UAV/Satellite synergies. Figure based on (Emilien et al., 2021)	36
Figure 1.3. Data inter-calibration strategy. Figure based on (Emilien et al., 2021).	37
Figure 1.4. Components of an IMU. Image posted by Stephanie Stocker in Optimize your IMU (CEVA's Experts Blog).	42
Figure 1.5. Electromagnetic reference spectrum for equipable sensors.	45
Figure 2.1. Accuracy potentialities employing UAV photogrammetry in surveying. Image based on (Deliry and Avdan, 2021).....	54
Figure 2.2. Comparison of geomatic techniques and technologies for the acquisition of objects and territories. Image based on (Smith et al., 2016)	59
Figure 2.3. The three key phases in a SfM-MVS workflow: (1) key point identification and matching (e.g., SIFT), (2) SfM with camera parameters and a sparse point cloud as output, and (3) the densified point cloud following MVS. Image based on (Iglhaut et al., 2019)	61
Figure 2.4. Schematic workflow of the SfM-MVS process resulting in a dense point cloud from image sets. The point cloud is georeferenced by providing positional information for images and/or GCPs.	63
Figure 2.5. General framework for the SfM-MVS pre-treatment, processing, and post-processing manipulation of UAV-based datasets.	72
Figure 2.6. Sparse point cloud in Agisoft Metashape	84
Figure 2.7. Dense Points Cloud in Agisoft Metashape	87
Figure 2.8. DEM of the examined area integrated of contour lines with altitude above sea level.	87
Figure 2.9. Distortions related to the blending mode in Agisoft Metashape.....	88
Figure 2.10. Sparse Points Cloud in Pix4D Mapper	91
Figure 2.11. Dense Points Cloud in Pix4D Mapper	93
Figure 2.12. DSM of the surveyed area.	95
Figure 2.13. Orthomosaic of the surveyed area.	95
Figure 2.14. Distortions related to the blending mode in PIX4D Mapper software.	95

Figure 2.15. Example of application of the OriConvert and Tapioca commands. Refer to the MicMac manual for more precise details of the arguments defined for each command. 97

Figure 2.16. Example of application of the Tapas, Bascule, AperiCloud and Campari commands. Refer to the MicMac manual for more precise details of the arguments defined for each command. 100

Figure 2.17. Sparse point cloud displayed in CloudCompare. 102

Figure 2.18. Example of application of the CorrLA, Tapas, Bascule, AperiCloud and Campari commands. Refer to the MicMac manual for more precise details of the arguments defined for each command. 103

Figure 2.19. Example of application of the GCPConvert, SaisieAppuisPredicQT and GCPBascule commands. Refer to the MicMac manual for more precise details of the arguments defined for each command. 105

Figure 2.20. Example of application of the Campari, AperiCloud and GPCtrl commands. Refer to the MicMac manual for more precise details of the arguments defined for each command. 105

Figure 2.21. Example of GPCtrl command results. Refer to the MicMac manual for more precise details of the arguments defined for each command. 106

Figure 2.22. Example of application of the C3DC and PIMS2MNT commands. Refer to the MicMac manual for more precise details of the arguments defined for each command. 107

Figure 3.1. The study area and visualization of the disposition of the targets. In red the station O, origin of the network of vertices TS and useful for the conversion of points from the local reference system to the absolute. 119

Figure 3.2. Frequency histogram of the deviations GCP(ΔXYZ) between TLS and GNSS measurements. 121

Figure 3.3. Spatial Distribution of GCP planar deviations between TLS and GNSS measurements. Each circumference around each point represents the estimated average planar error. Circumferences have a scale factor 50 times the actual value. 123

Figure 3.4. a) CPs errors registered in “1- 70 m” dataset varying the GCPs number implemented b) CPs errors registered in “2- 70 m TI” dataset varying the GCPs number implemented. TI: Treated Image. 125

Figure 3.5. The test site and, in red, GCPs distributed in the area 128

Figure 3.6. Impact of GCPs spatial distribution. NAD dataset developments and trend line by varying the spatial distribution: 1st SP_DIS: first distribution, 2nd SP_DIS: second distribution, 3rd SP_DIS: third distribution. The red line identifies a polynomial trend line that smooths out the effects of spatial distributions. 129

Figure 3.7. On the left, in red, the road axis of the Pedemontana Veneta Highway in its extension. On the right, a detail of the road section under excavation, object of study, near km 60, and the distribution of the GCP/CP targets in the overflowed area. Image based on (Saponaro et al., 2020c). 132

Figure 3.8. Comparison of RMSEXYZ and Mean Error (ME) values obtained on CPs and GCPs from MicMac (MM) and Agisoft Photoscan (PS) processes. 134

Figure 3.9. Comparison of RMSE _{XYZ} and Mean Error (ME) values obtained on CPs and GCPs from MicMac (MM) and Pix4D Mapper (P4) processes.....	136
Figure 3.10. Assessment of the RMSE _{XY} and RMSE _Z values obtained in the three software, as the GCPs implemented vary, with the threshold values published by ASPRS for Digital Planimetric Data and Vertical Data, respectively.	138
Figure 4.1. Coefficients of variation (C_v , %) computed for all IO parameters for all the processed datasets.	155
Figure 4.2. Boxplot of IO parameters from the December dataset. f —focal length; x_p and y_p coordinates of the principal point offset; B_1 , B_2 —skew parameters; K_1 , K_2 , K_3 , K_4 —radial distortions; P_1 , P_2 , P_3 , P_4 —components of the decentering distortions.	156
Figure 4.3. Boxplot of IO parameters from the January dataset. f —focal length; x_p and y_p coordinates of the principal point offset; B_1 , B_2 —skew parameters; K_1 , K_2 , K_3 , K_4 —radial distortions; P_1 , P_2 , P_3 , P_4 —components of the decentering distortions.	157
Figure 4.4. Boxplot of IO parameters from the February dataset. f —focal length; x_p and y_p coordinates of the principal point offset; B_1 , B_2 —skew parameters; K_1 , K_2 , K_3 , K_4 —radial distortions; P_1 , P_2 , P_3 , P_4 —components of the decentering distortions.	158
Figure 4.5. Boxplot of IO parameters from the March dataset. f —focal length; x_p and y_p coordinates of the principal point offset; B_1 , B_2 —skew parameters; K_1 , K_2 , K_3 , K_4 —radial distortions; P_1 , P_2 , P_3 , P_4 —components of the decentering distortions.	159
Figure 4.6. Boxplot of IO parameters from the October dataset. f —focal length; x_p and y_p coordinates of the principal point offset; B_1 , B_2 —skew parameters; K_1 , K_2 , K_3 , K_4 —radial distortions; P_1 , P_2 , P_3 , P_4 —components of the decentering distortions.	160
Figure 4.7. Correlation plot between IO parameters and PC (Dim_i). a) December; b) January; c) February; d) October. (f = focal length; x_p and y_p coordinates of the principal point offset; B_1 , B_2 = Skew parameters; K_1 , K_2 , K_3 , K_4 = radial distortions; P_1 , P_2 , P_3 , P_4 = components of the decentering distortions).	166
Figure 4.8. Significant predictive functions of RMSEE, RMSEN calculated on GCPs. R^2 is the coefficient of determination.	169
Figure 4.9. Significant predictive functions of RMSE _N , RMSE _H , RMSE _T calculated on CPs. R^2 is the coefficient of determination.	170
Figure 5.1. Pilot sites: (a) a construction site located in Fasoula (EL), Cyprus, (b) an out-of-town viaduct in Grottole (MT), Italy, (c) an abandoned archaeological area in Bari (BA), Italy. The icon to the left of the reader identifies the north orientation of the areas.	181
Figure 5.2. Example of high (top) and low (bottom) reflectance targets selected for each case study.....	184
Figure 5.3. Regression lines obtained by applying ELM: DNs values in abscissa related to percentage reflectance values in ordinate. Scenarios (a), (b) and (c) are represented in spatial resolutions {1}, {2}, {3} and {4} in the three bands (B_1 , B_2 , B_3), red, green and blue respectively. In each graph, the regression equation and the coefficient of determination R^2 can be observed.	187
Figure 5.4. Spectral signatures of 15 control points were manually caught from radiometrically calibrated rasters. The points are scattered among 5 points in vegetated areas, 5 in	

asphalt areas, and 5 in bare soil areas. The results are shown in scenarios (a), (b) and (c) in spatial resolutions {1}, {2}, {3} and {4}. In abscissa the band number, in ordinate the percentage reflectance value recorded.....	189
Figure 5.5. Distribution of random points analysed for examining the yields of vegetation indices in scenarios (a), (b) and (c). The distribution for scenario (c) subjected to the masking operation of the water zones, called (cmask), was also represented.	194
Figure 5.6. Counting of points in vegetated and non-vegetated areas. Points removed due to incorrect reflectance values were shaded in grey.	194
Figure 5.7. Normalised difference (%) for all case studies among all vegetation indices concerning the NGRDI index is considered the reference.	200
Figure 5.8. Example of AOI vectors identified in scenario (a). In fuchsia AOIs concerning asphalt, in blue those concerning bare soil and in green those concerning vegetation.	211
Figure 5.9. Statistical distribution of signatures in the containers of AOI vectors regarding Band 1 for asphalt, bare soil and vegetation.	212
Figure 5.10. Statistical distribution of signatures in the containers of AOI vectors regarding Band 2 for asphalt, bare soil and vegetation.	213
Figure 5.11. Statistical distribution of signatures in the containers of AOI vectors regarding Band 3 for asphalt, bare soil and vegetation.	214
Figure 5.12. Statistical distribution of signatures in the containers of AOI vectors regarding Band IRG index for asphalt, bare soil and vegetation.	215
Figure 5.13. Statistical distribution of signatures in the containers of AOI vectors regarding Band TGI index for asphalt, bare soil and vegetation.	216
Figure 5.14. RF maps for all cases analysed.	220
Figure 5.15. K-Means algorithm results for all cases analysed.	225
Figure 6.1. Triangular domain of possible proportions of eigenvalues (Brodu and Lague, 2012).....	244
Figure 6.2. Trends in the spatial orientation of point clouds (Qin et al., 2018).	244
Figure 6.3. Local neighbourhood approach based on a radial distance r (Brodu and Lague, 2012).	246
Figure 6.4. Example of Scalar Fields obtained for [100 m] Eigenvalues and scale parameter r equal to 0.215.	248
Figure 6.5. Histograms of the three eigenvalues as the scale parameter r changes. The abscissae show the values of the eigenvalues, the ordinates the number of points in each class. Below is the legend with the colour scale for each scale parameter r	251
Figure 6.6. Histograms of the three eigenvalues as the scale parameter r changes. The abscissae show the values of the eigenvalues, the ordinates the number of points in each class.	252
Figure 6.7. Histograms of the Anisotropy and Omnivariance as the scale parameter r changes. The abscissae show the values of the eigen-features, the ordinates the number of points in each class.	254

Figure 6.8. Histograms of Linearity and Planarity as the scale parameter r changes. The abscissae show the values of the eigen-features, the ordinates the number of points in each class.	255
Figure 6.9. Histograms of Eigenentropy as the scale parameter r changes. The abscissae show the values of the eigen-feature, the ordinates the number of points in each class.	257
Figure 6.10. Representation of the functioning of the M3C2 algorithm (Lague et al., 2013b).	260
Figure 6.11. Schematisation of the operations carried out for the planned tests.	269
Figure 6.12. Representation of the scalar fields 2.5D DoD obtained by superposition of DEM processed by traditional approach or using co-alignment.	275
Figure 6.13. M3C2 maximum distance obtained by comparing dense point clouds derived from the two processing approaches for all georeferencing strategies.	276
Figure 6.14. Volume density of point clouds generated from data acquired by applying TLS (on the top) and by UAV (on the bottom). XZ and XY perspectives are reported on the left and the right, respectively.	282
Figure 6.15. Anisotropy of point clouds generated from data acquired employing TLS (on the top) and UAV (on the bottom). XZ and XY perspectives are reported on the left and the right, respectively.	283
Figure 6.16. The roughness of point clouds is generated from data acquired by applying TLS (on the top) and UAV (on the bottom). XZ and XY perspectives are reported on the left and the right, respectively.	284
Figure 6.17. M3C2 distance. The meter is assumed as the unit of measurement.	284
Figure 6.18. Distance uncertainty XZ and XY perspectives are reported on the left and the right, respectively. The meter is assumed as the unit of measurement.	285
Figure 6.19. Fused model results. XZ and XY perspectives are reported on the left and the right, respectively.	286
Figure 6.20. Original Cloud Index: 0 light grey (points from TLS) and 1 dark grey (points from UAV). XZ and XY perspectives are reported on the left and the right, respectively.	286
Figure 6.21. UAV-based Inspection in a simplified schematization (Nettis et al., 2020).	288
Figure 6.22. Modelling of a structure in BIM environment and collection of disaggregated and heterogeneous information (Nettis et al., 2020).	290
Figure 6.23. The sequence of steps for the geometry extraction and allocation of data in BIM and Excel spreadsheet to perform the seismic risk assessment. A list of the data necessary for the risk calculation is indicated.	291

ACKNOWLEDGEMENTS

I will be brief and concise, like all engineers. This achievement would not have been possible if someone like Prof. Eufemia Tarantino had not believed in me. My most sincere gratitude goes to her for having accompanied me all the way from my Master's degree to the end of my PhD, keeping her advice and guidance for me. My thanks to Prof. Umberto Fratino for being available at all times and supporting my PhD journey. My due gratitude to Dr. Alessandra Capolupo, PhD and Dr. Alberico Sonnessa, PhD with whom I shared experiences, work and simple frivolous moments. Thanks also to Eng. Giacomo Caporusso and Eng. Cristina Monterisi, colleagues in the same laboratory.

Thanks to the PhD students' coordinator Prof. Michele Mossa for having supported me in the bureaucratic quarrels and directed me towards the resolution of problems.

My deepest appreciation to the leading figures who enhanced my skills and changed my professional approach: in particular, to Eng. Adriano Turso and all the guys in the R&D team at Sipal S.p.A. in Grottaglie (TA), and to my dear co-mentors Prof. Diofantos Had and Prof. Athos Agapiou of the Cyprus University of Technology (CUT).

If on the professional side this goal was possible thanks to these people, on the emotional side it would have been unreachable if I had not had the support, at the limit of strength, of my wife Angela and the whole family. There have been very difficult moments, psychologically complicated, and if I am here to take this result it is only thanks to them.

Now there are more goals ahead of me and I'm sure you will never stop standing by my side.

A muso duro,
Mirko

REFERENCES

- AASEN, H., BURKART, A., BOLTEN, A. & BARETH, G. 2015. Generating 3D hyperspectral information with lightweight UAV snapshot cameras for vegetation monitoring: From camera calibration to quality assurance. *ISPRS Journal of Photogrammetry and Remote Sensing*, 108, 245-259.
- AASEN, H., HONKAVAARA, E., LUCIEER, A. & ZARCO-TEJADA, P. J. 2018. Quantitative remote sensing at ultra-high resolution with UAV spectroscopy: A review of sensor technology, measurement procedures, and data correction workflows. *Remote Sensing*, 10, 1091.
- ABATE, D. & STURDY-COLLS, C. 2018. A multi-level and multi-sensor documentation approach of the Treblinka extermination and labor camps. *Journal of Cultural Heritage*, 34, 129-135.
- ABDI, H. 2007. Singular value decomposition (SVD) and generalized singular value decomposition. *Encyclopedia of measurement and statistics*, 907-912.
- ABDI, H. & WILLIAMS, L. J. 2010. Principal component analysis. *WIREs Computational Statistics*, 2, 433-459.
- ACCURACY, H. 1990. ASPRS Accuracy standards for large-scale maps.
- ADAMI, A., FREGONESE, L., GALLO, M., HELDER, J., PEPE, M. & TRECCANI, D. Ultra light UAV systems for the metrical documentation of cultural heritage: Applications for architecture and archaeology. 6th International Workshop LowCost 3D-Sensors, Algorithms, Applications, 2019. 15-21.
- ADAMOPOULOS, E. & RINAUDO, F. 2020. UAS-Based Archaeological Remote Sensing: Review, Meta-Analysis and State-of-the-Art. *Drones*, 4, 46.
- AGAPIOU, A. 2020a. Optimal Spatial Resolution for the Detection and Discrimination of Archaeological Proxies in Areas with Spectral Heterogeneity. *Remote Sensing*, 12, 136.
- AGAPIOU, A. 2020b. Vegetation Extraction Using Visible-Bands from Openly Licensed Unmanned Aerial Vehicle Imagery. *Drones*, 4, 27.

- AGÜERA-VEGA, F., CARVAJAL-RAMÍREZ, F., MARTÍNEZ-CARRICONDO, P., SÁNCHEZ-HERMOSILLA LÓPEZ, J., MESAS-CARRASCOSA, F. J., GARCÍA-FERRER, A. & PÉREZ-PORRAS, F. J. 2018. Reconstruction of extreme topography from UAV structure from motion photogrammetry. *Measurement*, 121, 127-138.
- AL-ALI, Z. M., ABDULLAH, M. M., ASADALLA, N. B. & GHOLOUM, M. 2020. A comparative study of remote sensing classification methods for monitoring and assessing desert vegetation using a UAV-based multispectral sensor. *Environmental Monitoring and Assessment*, 192, 389.
- ALIF, A. A., SHUKANYA, I. F. & AFEE, T. N. 2018. *Crop prediction based on geographical and climatic data using machine learning and deep learning*. BRAC University.
- ANDERSON, K., WESTOBY, M. J. & JAMES, M. R. 2019. Low-budget topographic surveying comes of age: Structure from motion photogrammetry in geography and the geosciences. *Progress in Physical Geography: Earth and Environment*, 43, 163-173.
- ANSI. *American National Standards Institute - Web Page* [Online]. Available: <https://ansi.org/> [Accessed 06/08/2021].
- ATHANASIS, N., THEMISTOCLEOUS, M., KALABOKIDIS, K. & CHATZITHEODOROU, C. Big Data Analysis in UAV Surveillance for Wildfire Prevention and Management. 2019 Cham. Springer International Publishing, 47-58.
- AWASTHI, B., KARKI, S., REGMI, P., DHAMI, D. S., THAPA, S. & PANDAY, U. S. Analyzing the Effect of Distribution Pattern and Number of GCPs on Overall Accuracy of UAV Photogrammetric Results. 2020 Cham. Springer International Publishing, 339-354.
- BANGEN, S., WHEATON, J., BOUWES, N., JORDAN, C., VOLK, C. & WARD, M. B. 2014a. Crew variability in topographic surveys for monitoring wadeable streams: a case study from the Columbia River Basin. *Earth Surface Processes and Landforms*, 39, 2070-2086.
- BANGEN, S. G., WHEATON, J. M., BOUWES, N., BOUWES, B. & JORDAN, C. 2014b. A methodological intercomparison of topographic survey techniques for characterizing wadeable streams and rivers. *Geomorphology*, 206, 343-361.
- BAPPY, A., ASFAK-UR-RAFI, M., ISLAM, M., SAJJAD, A. & IMRAN, K. N. 2015. *Design and development of unmanned aerial vehicle (Drone) for civil applications*. BRAC University.
- BARLOW, P. 2018. A comparative study of raster and vector based approaches in vegetation mapping on Five Islands off the coast of Port Kembla.

- BARRILE, V., CANDELA, G. & FOTIA, A. 2019a. Point Cloud Segmentation Using Image Processing Techniques for Structural Analysis. *ISPRS - International Archives of the Photogrammetry, Remote Sensing and Spatial Information Sciences*, XLII-2/W11, 187-193.
- BARRILE, V., FOTIA, A., CANDELA, G. & BERNARDO, E. 2019b. Integration of 3D Model From UAV Survey in BIM Environment. *ISPRS - International Archives of the Photogrammetry, Remote Sensing and Spatial Information Sciences*, XLII-2/W11, 195-199.
- BASSI, E. 2020. From Here to 2023: Civil Drones Operations and the Setting of New Legal Rules for the European Single Sky. *Journal of Intelligent & Robotic Systems*, 100, 493-503.
- BASSIER, M., MATTHEUWSEN, L. & VERGAUWEN, M. 2019. Bim Reconstruction: Automated Procedural Modeling from Point Cloud Data. *The International Archives of Photogrammetry, Remote Sensing and Spatial Information Sciences*, 42, 53-60.
- BELGIU, M. & STEIN, A. 2019. Spatiotemporal image fusion in remote sensing. *Remote sensing*, 11, 818.
- BENASSI, F., DALL'ASTA, E., DIOTRI, F., FORLANI, G., MORRA DI CELLA, U., RONCELLA, R. & SANTISE, M. 2017. Testing accuracy and repeatability of UAV blocks oriented with GNSS-supported aerial triangulation. *Remote Sensing*, 9, 172.
- BERRA, E. F. & PEPPA, M. V. 2020. Advances and Challenges of UAV SfM MVS Photogrammetry and Remote Sensing: Short Review. *Int. Arch. Photogramm. Remote Sens. Spatial Inf. Sci.*, XLII-3/W12-2020, 267-272.
- BIANCO, S., CIOCCA, G. & MARELLI, D. 2018. Evaluating the performance of structure from motion pipelines. *Journal of Imaging*, 4, 98.
- BISNATH, S., WELLS, D., SANTOS, M. & COVE, K. Initial results from a long baseline, kinematic, differential GPS carrier phase experiment in a marine environment. PLANS 2004. Position Location and Navigation Symposium (IEEE Cat. No. 04CH37556), 2004. IEEE, 625-631.
- BLOMLEY, R., WEINMANN, M., LEITLOFF, J. & JUTZI, B. 2014. Shape Distribution Features for Point Cloud Analysis - A Geometric Histogram Approach on Multiple Scales. *ISPRS Ann. Photogramm. Remote Sens. Spatial Inf. Sci.*, II-3, 9-16.
- BOULTON, G. 2018. The challenges of a Big Data Earth. *Big Earth Data*, 2, 1-7.
- BREIMAN, L. 2001. Random forests. *Machine learning*, 45, 5-32.
- BRODU, N. & LAGUE, D. 2012. 3D terrestrial lidar data classification of complex natural scenes using a multi-scale dimensionality criterion:

- Applications in geomorphology. *ISPRS Journal of Photogrammetry and Remote Sensing*, 68, 121-134.
- BROVELLI, M. A., MINGHINI, M., MORENO-SANCHEZ, R. & OLIVEIRA, R. 2017. Free and open source software for geospatial applications (FOSS4G) to support Future Earth. *International Journal of Digital Earth*, 10, 386-404.
- CANDIAGO, S., REMONDINO, F., DE GIGLIO, M., DUBBINI, M. & GATTELLI, M. 2015. Evaluating Multispectral Images and Vegetation Indices for Precision Farming Applications from UAV Images. *Remote Sensing*, 7, 4026-4047.
- CAPOLUPO, A., MALTESE, A., SAPONARO, M. & COSTANTINO, D. 2020a. *Integration of terrestrial laser scanning and UAV-SFM technique to generate a detailed 3D textured model of a heritage building*, SPIE.
- CAPOLUPO, A., MONTERISI, C., SAPONARO, M. & TARANTINO, E. 2020b. *Multi-temporal analysis of land cover changes using Landsat data through Google Earth Engine platform*.
- CAPOLUPO, A., SAPONARO, M., BORGOGNO MONDINO, E. & TARANTINO, E. 2020c. Combining Interior Orientation Variables to Predict the Accuracy of Rpas-Sfm 3D Models. *Remote Sensing*, 12, 2674.
- CAPOLUPO, A., SAPONARO, M., FRATINO, U. & TARANTINO, E. 2020d. Detection of spatio-temporal changes of vegetation in coastal areas subjected to soil erosion issue. *Aquatic Ecosystem Health and Management*.
- CAPRIOLI, M., FIGORITO, B., SCOGNAMIGLIO, A. & TARANTINO, E. Historical Documentation of Rock Churches in the “Sassi” of Matera with Terrestrial Laser Data in A 3D GIS. Proceedings of the ISPRS Workshop'3D-ARCH, 2007.
- CARBONNEAU, P. E. & DIETRICH, J. T. 2017. Cost-effective non-metric photogrammetry from consumer-grade sUAS: implications for direct georeferencing of structure from motion photogrammetry. *Earth Surface Processes and Landforms*, 42, 473-486.
- CARBONNEAU, P. E., LANE, S. N. & BERGERON, N. E. 2003. Cost-effective non-metric close-range digital photogrammetry and its application to a study of coarse gravel river beds. *International Journal of Remote Sensing*, 24, 2837-2854.
- CAROTI, G., PIEMONTE, A., BEVILACQUA, M. G. & CROCE, V. 2019. *Geomatics for Cultural Heritage conservation: integrated survey and 3D modeling*.

- CARRIVICK, J. L., SMITH, M. W. & QUINCEY, D. J. 2016. *Structure from Motion in the Geosciences*, John Wiley & Sons.
- CARVAJAL, F., AGÜERA, F. & PÉREZ, M. 2011. Surveying a landslide in a road embankment using unmanned aerial vehicle photogrammetry. *International Archives of the Photogrammetry, Remote Sensing and Spatial Information Sciences*, 38, 201.
- CARVALHO, R. C., KENNEDY, D. M., NIYAZI, Y., LEACH, C., KONLECHNER, T. M. & IERODIACONOU, D. 2020. Structure-from-Motion photogrammetry analysis of historical aerial photography: determining beach volumetric change over decadal scales. *Earth Surface Processes and Landforms*, 45, 2540-2555.
- CASELLA, V., CHIABRANDO, F., FRANZINI, M. & MANZINO, A. M. Accuracy Assessment of a Photogrammetric UAV Block by using Different Software and Adopting Diverse Processing Strategies. *GISTAM*, 2019. 77-87.
- CHAMBERS, J. 2008. *Software for data analysis: programming with R*, Springer Science & Business Media.
- CHEHATA, N., GUO, L. & MALLETT, C. Airborne lidar feature selection for urban classification using random forests. *Laserscanning*, 2009.
- CHEN, L. & WANG, L. 2018. Recent advance in earth observation big data for hydrology. *Big Earth Data*, 2, 86-107.
- CHI, M., PLAZA, A., BENEDIKTSSON, J. A., SUN, Z., SHEN, J. & ZHU, Y. 2016. Big Data for Remote Sensing: Challenges and Opportunities. *Proceedings of the IEEE*, 104, 2207-2219.
- CHOW, J. C. & LICHTI, D. D. A study of systematic errors in the PMD CamBoard nano. *Videometrics, Range Imaging, and Applications XII; and Automated Visual Inspection*, 2013. International Society for Optics and Photonics, 87910X.
- COLOMINA, I. & MOLINA, P. 2014. Unmanned aerial systems for photogrammetry and remote sensing: A review. *ISPRS Journal of photogrammetry and remote sensing*, 92, 79-97.
- COMERT, R., AVDAN, U. & GORUM, T. 2018. Rapid mapping of forested landslide from ultra-high resolution unmanned aerial vehicle data. *International Archives of the Photogrammetry, Remote Sensing and Spatial Information Sciences*, 42.
- COMERT, R. & KAPLAN, O. 2018. Object Based Building Extraction and Building Period Estimation from Unmanned Aerial Vehicle Data. *ISPRS Annals of Photogrammetry, Remote Sensing & Spatial Information Sciences*, 4.

- CONG, M., XI, J., HAN, L., GU, J., YANG, L., TAO, Y. & XU, M. 2020. Multi-resolution classification network for high-resolution UAV remote sensing images. *Geocarto International*, 1-25.
- COOK, K. & DIETZE, M. 2019. A simple workflow for robust low-cost UAV-derived change detection without ground control points. *Earth Surface Dynamics*, 7, 1009-1017.
- COOK, K. L. 2017. An evaluation of the effectiveness of low-cost UAVs and structure from motion for geomorphic change detection. *Geomorphology*, 278, 195-208.
- COOPER, H. M., WASKLEWICZ, T., ZHU, Z., LEWIS, W., LECOMPTE, K., HEFFENTRAGER, M., SMABY, R., BRADY, J. & HOWARD, R. 2021. Evaluating the Ability of Multi-Sensor Techniques to Capture Topographic Complexity. *Sensors*, 21, 2105.
- COSTA, L., NUNES, L. & AMPATZIDIS, Y. 2020. A new visible band index (vNDVI) for estimating NDVI values on RGB images utilizing genetic algorithms. *Computers and Electronics in Agriculture*, 172, 105334.
- COULTER, L. L., PLUMMER, M. J., ZAMORA, N. H., STOW, D. A. & MCCREIGHT, R. W. 2019. Assessment of automated multitemporal image co-registration using repeat station imaging techniques. *GIScience & Remote Sensing*, 56, 1192-1209.
- CRAMER, M., PRZYBILLA, H. J. & ZURHORST, A. 2017. UAV Cameras: Overview and Geometric Calibration Benchmark. *Int. Arch. Photogramm. Remote Sens. Spatial Inf. Sci.*, XLII-2/W6, 85-92.
- CUCCHIARO, S., FALLU, D. J., ZHANG, H., WALSH, K., VAN OOST, K., BROWN, A. G. & TAROLLI, P. 2020a. Multiplatform-SfM and TLS Data Fusion for Monitoring Agricultural Terraces in Complex Topographic and Landcover Conditions. *Remote Sensing*, 12, 1946.
- CUCCHIARO, S., MASET, E., CAVALLI, M., CREMA, S., MARCHI, L., BEINAT, A. & CAZORZI, F. 2020b. How does co-registration affect geomorphic change estimates in multi-temporal surveys? *GIScience & Remote Sensing*, 57, 611-632.
- CUMMINGS, A. R., MCKEE, A., KULKARNI, K. & MARKANDEY, N. 2017. The rise of UAVs. *Photogrammetric Engineering & Remote Sensing*, 83, 317-325.
- D'OLEIRE-OLTMANN, S., MARZOLFF, I., PETER, K. D. & RIES, J. B. 2012. Unmanned aerial vehicle (UAV) for monitoring soil erosion in Morocco. *Remote Sensing*, 4, 3390-3416.
- DAAKIR, M., PIERROT-DESEILLIGNY, M., BOSSER, P., PICHARD, F., THOM, C., RABOT, Y. & MARTIN, O. 2017. Lightweight UAV with on-board photogrammetry and single-frequency GPS positioning for

- metrology applications. *ISPRS Journal of Photogrammetry and Remote Sensing*, 127, 115-126.
- DAINELLI, R., TOSCANO, P., DI GENNARO, S. F. & MATESE, A. 2021. Recent Advances in Unmanned Aerial Vehicle Forest Remote Sensing—A Systematic Review. Part I: A General Framework. *Forests*, 12, 327.
- DASH, J. P., PEARSE, G. D. & WATT, M. S. 2018. UAV Multispectral Imagery Can Complement Satellite Data for Monitoring Forest Health. *Remote Sensing*, 10, 1216.
- DE CASTRO, A. I., TORRES-SÁNCHEZ, J., PEÑA, J. M., JIMÉNEZ-BRENES, F. M., CSILLIK, O. & LÓPEZ-GRANADOS, F. 2018. An Automatic Random Forest-OBIA Algorithm for Early Weed Mapping between and within Crop Rows Using UAV Imagery. *Remote Sensing*, 10, 285.
- DE HAAS, T., NIJLAND, W., MCARDELL, B. W. & KALTHOF, M. W. M. L. 2020. Short Communication: Optimizing UAV-SfM based topographic change detection with survey co-alignment. *Earth Surf. Dynam. Discuss.*, 2020, 1-17.
- DE LUCA, G., N. SILVA, J. M., CERASOLI, S., ARAÚJO, J., CAMPOS, J., DI FAZIO, S. & MODICA, G. 2019. Object-Based Land Cover Classification of Cork Oak Woodlands using UAV Imagery and Orfeo ToolBox. *Remote Sensing*, 11, 1238.
- DELIRY, S. I. & AVDAN, U. 2021. Accuracy of Unmanned Aerial Systems Photogrammetry and Structure from Motion in Surveying and Mapping: A Review. *Journal of the Indian Society of Remote Sensing*.
- DEMANTKÉ, J., MALLET, C., DAVID, N. & VALLET, B. Dimensionality based scale selection in 3D lidar point clouds. *Laserscanning*, 2011.
- DESEILLIGNY, M. P. & CLÉRY, I. Apero, an open source bundle adjustment software for automatic calibration and orientation of set of images. *Proceedings of the ISPRS Symposium, 3DARCH11*, 2011.
- DEVOTO, S., MACOVAZ, V., MANTOVANI, M., SOLDATI, M. & FURLANI, S. 2020. Advantages of Using UAV Digital Photogrammetry in the Study of Slow-Moving Coastal Landslides. *Remote Sensing*, 12, 3566.
- DGIWC. *Defense Geospatial Information Working Group - Web Page* [Online]. Available: <https://www.dgiwg.org/> [Accessed 06/08/2021].
- DIFRANCESCO, P.-M., BONNEAU, D. & HUTCHINSON, D. J. 2020. The Implications of M3C2 Projection Diameter on 3D Semi-Automated Rockfall Extraction from Sequential Terrestrial Laser Scanning Point Clouds. *Remote Sensing*, 12, 1885.

- DIN. *German Institute for Standardization - Web Page* [Online]. Available: <https://www.din.de/en> [Accessed 06/08/2021].
- DOUMIT, J. A. & POGORELOV, A. V. 2017. Multi-scale Analysis of Digital Surface Models Based on UAV Datasets. *Modern Environmental Science and Engineering (ISSN 2333-2581)*, 3, 460-468.
- DUANE, C. B. 1971. Close-range camera calibration. *Photogramm. Eng.*, 37, 855-866.
- EFFIOM, A. E., VAN LEEUWEN, L., NYKTAS, P., OKOJIE, J. A. & ERDBRÜGGER, J. 2019. Combining unmanned aerial vehicle and multispectral Pleiades data for tree species identification, a prerequisite for accurate carbon estimation. *Journal of Applied Remote Sensing*, 13, 034530.
- ELBERINK, S. O. & MAAS, H.-G. 2000. The use of anisotropic height texture measures for the segmentation of airborne laser scanner data. *International archives of photogrammetry and remote sensing*, 33, 678-684.
- ELKHRACHY, I. 2021. Accuracy Assessment of Low-Cost Unmanned Aerial Vehicle (UAV) Photogrammetry. *Alexandria Engineering Journal*, 60, 5579-5590.
- ELTNER, A., KAISER, A., CASTILLO, C., ROCK, G., NEUGIRG, F. & ABELLÁN, A. 2016. Image-based surface reconstruction in geomorphometry – merits, limits and developments. *Earth Surf. Dynam.*, 4, 359-389.
- ELTNER, A. & SOFIA, G. 2020. Chapter 1 - Structure from motion photogrammetric technique. In: TAROLLI, P. & MUDD, S. M. (eds.) *Developments in Earth Surface Processes*. Elsevier.
- EMILIEN, A.-V., THOMAS, C. & THOMAS, H. 2021. UAV & satellite synergies for optical remote sensing applications: A literature review. *Science of Remote Sensing*, 3, 100019.
- ERENOGLU, R. C., AKCAY, O. & ERENOGLU, O. 2017. An UAS-assisted multi-sensor approach for 3D modeling and reconstruction of cultural heritage site. *Journal of Cultural Heritage*, 26, 79-90.
- ESCHMANN, C., KUO, C.-M., KUO, C.-H. & BOLLER, C. 2012. Unmanned aircraft systems for remote building inspection and monitoring.
- FARELLA, E. M., TORRESANI, A. & REMONDINO, F. 2019a. Quality Features for the Integration of Terrestrial and UAV Images. *Int. Arch. Photogramm. Remote Sens. Spatial Inf. Sci.*, XLII-2/W9, 339-346.
- FARELLA, E. M., TORRESANI, A. & REMONDINO, F. 2019b. Sparse Point Cloud Filtering Based on Covariance Features. *Int. Arch. Photogramm. Remote Sens. Spatial Inf. Sci.*, XLII-2/W15, 465-472.

- FAWCETT, D., PANIGADA, C., TAGLIABUE, G., BOSCHETTI, M., CELESTI, M., EVDOKIMOV, A., BIRIUKOVA, K., COLOMBO, R., MIGLIETTA, F., RASCHER, U. & ANDERSON, K. 2020. Multi-Scale Evaluation of Drone-Based Multispectral Surface Reflectance and Vegetation Indices in Operational Conditions. *Remote Sensing*, 12, 514.
- FERNÁNDEZ-HERNANDEZ, J., GONZÁLEZ-AGUILERA, D., RODRÍGUEZ-GONZÁLVEZ, P. & MANCERA-TABOADA, J. 2015. Image-Based Modelling from Unmanned Aerial Vehicle (UAV) Photogrammetry: An Effective, Low-Cost Tool for Archaeological Applications. *Archaeometry*, 57, 128-145.
- FEURER, D. & VINATIER, F. 2018. Joining multi-epoch archival aerial images in a single SfM block allows 3-D change detection with almost exclusively image information. *ISPRS Journal of Photogrammetry and Remote Sensing*, 146, 495-506.
- FGDC. *Federal Geographic Data Committee - Web Page* [Online]. Available: <https://www.fgdc.gov/> [Accessed 06/08/2021].
- FISCHLER, M. A. & BOLLES, R. C. 1981. Random sample consensus: a paradigm for model fitting with applications to image analysis and automated cartography. *Communications of the ACM*, 24, 381-395.
- FLORES-DE-SANTIAGO, F., VALDERRAMA-LANDEROS, L., RODRÍGUEZ-SOBREYRA, R. & FLORES-VERDUGO, F. 2020. Assessing the effect of flight altitude and overlap on orthoimage generation for UAV estimates of coastal wetlands. *Journal of Coastal Conservation*, 24, 35.
- FRANKLIN, S. 2018. Pixel- and object-based multispectral classification of forest tree species from small unmanned aerial vehicles. *Journal of Unmanned Vehicle Systems*, 6.
- FRASER, C. S. 2013. Automatic Camera Calibration in Close Range Photogrammetry. *Photogrammetric Engineering & Remote Sensing*, 79, 381-388.
- FRYER, J. G. 1996. Camera calibration. *Close range photogrammetry and machine vision*, 156-179.
- FUENTES-PEAILILLO, F., ORTEGA-FARIAS, S., RIVERA, M., BARDEEN, M. & MORENO, M. Comparison of vegetation indices acquired from RGB and Multispectral sensors placed on UAV. 2018 IEEE International Conference on Automation/XXIII Congress of the Chilean Association of Automatic Control (ICA-ACCA), 2018. IEEE, 1-6.
- FUGAZZA, D., SCAIONI, M., CORTI, M., D'AGATA, C., AZZONI, R. S., CERNUSCHI, M., SMIRAGLIA, C. & DIOLAIUTI, G. A. 2018. Combination of UAV and terrestrial photogrammetry to assess rapid

- glacier evolution and map glacier hazards. *Nat. Hazards Earth Syst. Sci.*, 18, 1055-1071.
- FURUKAWA, Y. & PONCE, J. 2009. Accurate, dense, and robust multiview stereopsis. *IEEE transactions on pattern analysis and machine intelligence*, 32, 1362-1376.
- GABRLIK, P., COUR-HARBO, A. L., KALVODOVA, P., ZALUD, L. & JANATA, P. 2018. Calibration and accuracy assessment in a direct georeferencing system for UAS photogrammetry. *International Journal of Remote Sensing*, 39, 4931-4959.
- GAŠPAROVIĆ, M., ZRINJSKI, M., BARKOVIĆ, Đ. & RADOČAJ, D. 2020. An automatic method for weed mapping in oat fields based on UAV imagery. *Computers and Electronics in Agriculture*, 173, 105385.
- GERKE, M. & PRZYBILLA, H.-J. 2016. Accuracy analysis of photogrammetric UAV image blocks: Influence of onboard RTK-GNSS and cross flight patterns. *Photogrammetrie, Fernerkundung, Geoinformation (PFG)*, 17-30.
- GEVAERT, C. M., TANG, J., GARCÍA-HARO, F. J., SUOMALAINEN, J. & KOOISTRA, L. Combining hyperspectral UAV and multispectral Formosat-2 imagery for precision agriculture applications. 2014 6th Workshop on Hyperspectral Image and Signal Processing: Evolution in Remote Sensing (WHISPERS), 24-27 June 2014 2014. 1-4.
- GIRARDEAU-MONTAUT, D. 2015. Cloud compare—3d point cloud and mesh processing software. *Open Source Project*, 197.
- GRAYSON, B., PENNA, N. T., MILLS, J. P. & GRANT, D. S. 2018. GPS precise point positioning for UAV photogrammetry. *The Photogrammetric Record*, 33, 427-447.
- GREEN, D. R., HAGON, J. J., GÓMEZ, C. & GREGORY, B. J. 2019. Using low-cost UAVs for environmental monitoring, mapping, and modelling: Examples from the coastal zone. *Coastal Management*. Elsevier.
- GRIFFITHS, D. & BURNINGHAM, H. 2019. Comparison of pre- and self-calibrated camera calibration models for UAS-derived nadir imagery for a SfM application. *Progress in Physical Geography: Earth and Environment*, 43, 215-235.
- GRUEN, A. 2012. Development and status of image matching in photogrammetry. *The Photogrammetric Record*, 27, 36-57.
- GRUEN, A. & BEYER, H. A. 2001. System calibration through self-calibration. *Calibration and orientation of cameras in computer vision*. Springer.
- GUO, H.-D., ZHANG, L. & ZHU, L.-W. 2015. Earth observation big data for climate change research. *Advances in Climate Change Research*, 6, 108-117.

- GUO, H. 2017. Big Earth data: A new frontier in Earth and information sciences. *Big Earth Data*, 1, 4-20.
- GUO, H., LIU, Z., JIANG, H., WANG, C., LIU, J. & LIANG, D. 2017. Big Earth Data: a new challenge and opportunity for Digital Earth's development. *International Journal of Digital Earth*, 10, 1-12.
- GUO, H., NATIVI, S., LIANG, D., CRAGLIA, M., WANG, L., SCHADE, S., CORBAN, C., HE, G., PESARESI, M., LI, J., SHIRAZI, Z., LIU, J. & ANNONI, A. 2020. Big Earth Data science: an information framework for a sustainable planet. *International Journal of Digital Earth*, 13, 743-767.
- HAGHIGHATTALAB, A., GONZÁLEZ PÉREZ, L., MONDAL, S., SINGH, D., SCHINSTOCK, D., RUTKOSKI, J., ORTIZ-MONASTERIO, I., SINGH, R. P., GOODIN, D. & POLAND, J. 2016. Application of unmanned aerial systems for high throughput phenotyping of large wheat breeding nurseries. *Plant Methods*, 12, 35.
- HÄMMERLE, M., SCHÜTT, F. & HÖFLE, B. 2016. Terrestrial and unmanned aerial system imagery for deriving photogrammetric three-dimensional point clouds and volume models of mass wasting sites. *Journal of Applied Remote Sensing*, 10, 026029.
- HAMYLTON, S. M., MORRIS, R. H., CARVALHO, R. C., RODER, N., BARLOW, P., MILLS, K. & WANG, L. 2020. Evaluating techniques for mapping island vegetation from unmanned aerial vehicle (UAV) images: Pixel classification, visual interpretation and machine learning approaches. *International Journal of Applied Earth Observation and Geoinformation*, 89, 102085.
- HAN, S., PARK, J. & LEE, W. 2016. On-site vs. laboratorial implementation of camera self-calibration for UAV photogrammetry. *Journal of the Korean Society of Surveying, Geodesy, Photogrammetry and Cartography*, 34, 349-356.
- HASTEDT, H., EKKEL, T. & LUHMANN, T. 2016. Evaluation of the Quality of Action Cameras with Wide-Angle Lenses in UAV Photogrammetry. *International Archives of the Photogrammetry, Remote Sensing & Spatial Information Sciences*, 41.
- HASTEDT, H. & LUHMANN, T. 2015. Investigations on the quality of the interior orientation and its impact in object space for UAV photogrammetry. *International Archives of the Photogrammetry, Remote Sensing & Spatial Information Sciences*, 40.
- HE, Y. & WENG, Q. 2018. *High spatial resolution remote sensing: data, analysis, and applications*, CRC press.

- HENDRICKX, H., VIVERO, S., DE COCK, L., DE WIT, B., DE MAEYER, P., LAMBIEL, C., DELALOYE, R., NYSSSEN, J. & FRANKL, A. 2019. The reproducibility of SfM algorithms to produce detailed Digital Surface Models: the example of PhotoScan applied to a high-alpine rock glacier. *Remote Sensing Letters*, 10, 11-20.
- HOSSIN, M. & SULAIMAN, M. N. 2015. A review on evaluation metrics for data classification evaluations. *International journal of data mining & knowledge management process*, 5, 1.
- HU, J., ZHANG, Z., ZHAO, C., WANG, D., FAN, B., LI, S. & PAN, Q. A brief review on the positioning technologies for unmanned aerial vehicles. 2017 IEEE International Conference on Unmanned Systems (ICUS), 2017. IEEE, 527-532.
- HUANG, B. & WANG, J. 2020. Big spatial data for urban and environmental sustainability. *Geo-spatial Information Science*, 23, 125-140.
- HUANG, Y., CHEN, Z.-X., YU, T., HUANG, X.-Z. & GU, X.-F. 2018. Agricultural remote sensing big data: Management and applications. *Journal of Integrative Agriculture*, 17, 1915-1931.
- HUGENHOLTZ, C., BROWN, O., WALKER, J., BARCHYN, T., NESBIT, P., KUCHARCZYK, M. & MYSHAK, S. 2016. Spatial accuracy of UAV-derived orthoimagery and topography: Comparing photogrammetric models processed with direct geo-referencing and ground control points. *Geomatica*, 70, 21-30.
- HUNT, E. R., DORAISWAMY, P. C., MCMURTREY, J. E., DAUGHTRY, C. S. T., PERRY, E. M. & AKHMEDOV, B. 2013. A visible band index for remote sensing leaf chlorophyll content at the canopy scale. *International Journal of Applied Earth Observation and Geoinformation*, 21, 103-112.
- IGLHAUT, J., CABO, C., PULITI, S., PIERMATTEI, L., O'CONNOR, J. & ROSETTE, J. 2019. Structure from motion photogrammetry in forestry: A review. *Current Forestry Reports*, 5, 155-168.
- IHDE, J., HABRICH, H., SACHER, M., SÖHNE, W., ALTAMIMI, Z., BROCKMANN, E., BRUYNINX, C., CAPORALI, A., DOUSA, J. & FERNANDES, R. 2014. EUREF's contribution to national, European and global geodetic infrastructures. *Earth on the Edge: Science for a Sustainable Planet*. Springer.
- ILCI, V., OZULU, I. M., BILGI, S. & ALKAN, R. M. 2019. The usage of unmanned aerial vehicles (UAVs) for 3D mapping of archaeological sites. *FEB-Fresenius Environmental Bulletin*, 28, 968-974.
- ISAILOVIĆ, D., PETRONIJEVIĆ, M. & HAJDIN, R. The future of BIM and Bridge Management Systems. IABSE Symposium 2019: Towards a Resilient Built Environment-Risk and Asset Management, 2019.

- International Association for Bridge and Structural Engineering (IABSE), 1673-1680.
- JAFARI, B., KHALOO, A. & LATTANZI, D. 2017. Deformation Tracking in 3D Point Clouds Via Statistical Sampling of Direct Cloud-to-Cloud Distances. *Journal of Nondestructive Evaluation*, 36, 65.
- JAMES, M. & ROBSON, S. 2014. Sequential digital elevation models of active lava flows from ground-based stereo time-lapse imagery. *ISPRS Journal of Photogrammetry and Remote Sensing*, 97, 160-170.
- JAMES, M. R., CHANDLER, J. H., ELTNER, A., FRASER, C., MILLER, P. E., MILLS, J. P., NOBLE, T., ROBSON, S. & LANE, S. N. 2019. Guidelines on the use of structure-from-motion photogrammetry in geomorphic research. *Earth Surface Processes and Landforms*, 44, 2081-2084.
- JAMES, M. R., ROBSON, S., D'OLEIRE-OLTMANN, S. & NIETHAMMER, U. 2017a. Optimising UAV topographic surveys processed with structure-from-motion: Ground control quality, quantity and bundle adjustment. *Geomorphology*, 280, 51-66.
- JAMES, M. R., ROBSON, S. & SMITH, M. W. 2017b. 3-D uncertainty-based topographic change detection with structure-from-motion photogrammetry: precision maps for ground control and directly georeferenced surveys. *Earth Surface Processes and Landforms*, 42, 1769-1788.
- JAYANTHI, S. & VENNILA, C. 2020. Performance improvement in satellite image classification using adaptive supervised multi-resolution approach. *Computer Communications*, 150, 200-208.
- JIANG, J., CAI, W., ZHENG, H., CHENG, T., TIAN, Y., ZHU, Y., EHSANI, R., HU, Y., NIU, Q., GUI, L. & YAO, X. 2019. Using Digital Cameras on an Unmanned Aerial Vehicle to Derive Optimum Color Vegetation Indices for Leaf Nitrogen Concentration Monitoring in Winter Wheat. *Remote Sensing*, 11, 2667.
- JIANG, S., JIANG, C. & JIANG, W. 2020. Efficient structure from motion for large-scale UAV images: A review and a comparison of SfM tools. *ISPRS Journal of Photogrammetry and Remote Sensing*, 167, 230-251.
- JO, Y. H. & HONG, S. 2019. Three-Dimensional Digital Documentation of Cultural Heritage Site Based on the Convergence of Terrestrial Laser Scanning and Unmanned Aerial Vehicle Photogrammetry. *ISPRS International Journal of Geo-Information*, 8, 53.
- JOSHUA, B., IGWE, C. F. & ADEKUNLE, I. 2016. Modelling and Assessment of Coastal Changes at Golspie Beach, Scotland, UK; An Integration of Terrestrial Laser Scanning and Digital Photogrammetric Techniques, for

- an Effective Coastal Land use Management. *International Journal of Scientific Research in Science and Technology*, 2, 361-371.
- JUNG, Y. G., KANG, M. S. & HEO, J. 2014. Clustering performance comparison using K-means and expectation maximization algorithms. *Biotechnology & Biotechnological Equipment*, 28, S44-S48.
- KAISER, H. F. 1960. The Application of Electronic Computers to Factor Analysis. *Educational and Psychological Measurement*, 20, 141-151.
- KAMILARIS, A., KARTAKOULLIS, A. & PRENAFETA-BOLDÚ, F. X. 2017. A review on the practice of big data analysis in agriculture. *Computers and Electronics in Agriculture*, 143, 23-37.
- KANDERA, B., ŠKULTÉTY, F. & BADÁNIK, B. 2020. New regulations for UAS flights.
- KARANTANELIS, E., ARAV, R., DILLE, A., LIPPL, S., MARSY, G., TORRESANI, L. & OUDE ELBERINK, S. 2020. Evaluating the Quality of Photogrammetric Point-Clouds in Challenging Geo-Environments – A Case Study in an Alpine Valley. *Int. Arch. Photogramm. Remote Sens. Spatial Inf. Sci.*, XLIII-B2-2020, 1099-1105.
- KASPRAK, A., BRANSKY, N., SANKEY, J., CASTER, J. & SANKEY, T. 2019. The effects of topographic surveying technique and data resolution on the detection and interpretation of geomorphic change. *Geomorphology*, 333.
- KERLE, N., NEX, F., GERKE, M., DUARTE, D. & VETRIVEL, A. 2020. UAV-Based Structural Damage Mapping: A Review. *ISPRS International Journal of Geo-Information*, 9, 14.
- KEYPORT, R. N., OOMMEN, T., MARTHA, T. R., SAJINKUMAR, K. & GIERKE, J. S. 2018. A comparative analysis of pixel-and object-based detection of landslides from very high-resolution images. *International journal of applied earth observation and geoinformation*, 64, 1-11.
- KIM, A., OLSEN, R. & KRUSE, F. 2013. *Methods for LiDAR point cloud classification using local neighborhood statistics*, SPIE.
- KINGSLAND, K. 2020. Comparative analysis of digital photogrammetry software for cultural heritage. *Digital Applications in Archaeology and Cultural Heritage*, 18, e00157.
- KLÁPŠTĚ, P., FOGL, M., BARTÁK, V., GDULOVÁ, K., URBAN, R. & MOUDRÝ, V. 2020. Sensitivity analysis of parameters and contrasting performance of ground filtering algorithms with UAV photogrammetry-based and LiDAR point clouds. *International Journal of Digital Earth*, 1-23.

- KOLEY, S. & JEGANATHAN, C. 2020. Estimation and evaluation of high spatial resolution surface soil moisture using multi-sensor multi-resolution approach. *Geoderma*, 378, 114618.
- KRAFT, T., GEBNER, M., MEIBNER, H., PRZYBILLA, H.-J. & GERKE, M. Introduction of a photogrammetric camera system for rpas with highly accurate gnss/imu information for standardized workflows. XXII ISPRS Congress, Technical Commission III, 2016. The International Archives of the Photogrammetry, Remote Sensing and Spatial ..., 71-75.
- KRESSE, W. 2004. Standardization of geographic information. *International Archives of ISPRS, Nummer XXXV. Istanbul*.
- KRESSE, W. 2008. Development of an international standard for calibration and validation of remote sensing imagery sensors and data. *Int. Arch. Photogram. Rem. Sens. Spatial Inf. Sci*, 38.
- KRESSE, W. 2010. Status of ISO standards for photogrammetry and remote sensing. *International Archives of ISPRS*.
- KUBOTA, S., HO, C. & NISHI, K. Construction and Usage of Three-dimensional Data for Road Structures Using Terrestrial Laser Scanning and UAV with Photogrammetry. 2019.
- KWAN, C., GRIBBEN, D., AYHAN, B., LI, J., BERNABE, S. & PLAZA, A. 2020. An Accurate Vegetation and Non-Vegetation Differentiation Approach Based on Land Cover Classification. *Remote Sensing*, 12, 3880.
- LABBÉ, S., GÓMEZ-CANDÓN, D., EL-NATOUR, G., DORADO, J., FERNÁNDEZ-QUINTANILLA, C., LÓPEZ-GRANADOS, F., PEÑABARRAGÁN, J., DE CASTRO, A., TORRES-SÁNCHEZ, J. & RABATEL, G. Automatic mosaicking of very high spatial resolution UAV multispectral images for precision agriculture: test of MICMAC freeware. Proceedings of the First International Conference on Robotics and Associated High-technologies and Equipment for Agriculture. Applications of automated systems and robotics for crop protection in sustainable precision agriculture,(RHEA-2012) Pisa, Italy-September 19-21, 2012, 2012. University of Pisa, 269-274.
- LAGUE, D. 2020. Chapter 8 - Terrestrial laser scanner applied to fluvial geomorphology. In: TAROLLI, P. & MUDD, S. M. (eds.) *Developments in Earth Surface Processes*. Elsevier.
- LAGUE, D., BRODU, N. & LEROUX, J. 2013a. Accurate 3D comparison of complex topography with terrestrial laser scanner: Application to the Rangitikei canyon (N-Z). *ISPRS Journal of Photogrammetry and Remote Sensing*, 82, 10-26.

- LAGUE, D., BRODU, N. & LEROUX, J. 2013b. Accurate 3D comparison of complex topography with terrestrial laser scanner: Application to the Rangitikei canyon (NZ). *ISPRS journal of photogrammetry and remote sensing*, 82, 10-26.
- LECUN, Y., BENGIO, Y. & HINTON, G. 2015. Deep learning. *nature*, 521, 436-444.
- LEE, K. W. & PARK, J. K. 2019. Modeling and Management of Bridge Structures Using Unmanned Aerial Vehicle in Korea. *Sensors and Materials*, 31, 3765-3772.
- LENG, C., ZHANG, H., LI, B., CAI, G., PEI, Z. & HE, L. 2018. Local feature descriptor for image matching: A survey. *IEEE Access*, 7, 6424-6434.
- LI, D., SHEN, X. & WANG, L. 2018. Connected Geomatics in the big data era. *International Journal of Digital Earth*, 11, 139-153.
- LICHTI, D., GORDON, S., STEWART, M., FRANKE, J. & TSAKIRI, M. Comparison of digital photogrammetry and laser scanning. Proc. International Society for Photogrammetry and Remote Sensing, 2002. 39-44.
- LIM, P., SEO, J., SON, J.-H. & KIM, T. 2019. Analysis of Orientation Accuracy of an UAV Image According to Camera Calibration. *ISPRS - International Archives of the Photogrammetry, Remote Sensing and Spatial Information Sciences*, XLII-2/W13, 437-442.
- LIMA-CUETO, F. J., BLANCO-SEPÚLVEDA, R., GÓMEZ-MORENO, M. L. & GALACHO-JIMÉNEZ, F. B. 2019. Using Vegetation Indices and a UAV Imaging Platform to Quantify the Density of Vegetation Ground Cover in Olive Groves (*Olea Europaea* L.) in Southern Spain. *Remote Sensing*, 11, 2564.
- LÓPEZ IGLESIAS, J., DÍAZ SEVERIANO, J. A., LIZCANO AMOROCHO, P. E., MANCHADO DEL VAL, C., GÓMEZ-JÁUREGUI, V., FERNÁNDEZ GARCÍA, O., PRECIADOS ROYANO, A. & OTERO GONZÁLEZ, C. Revision of Automation Methods for Scan to BIM. 2020 Cham. Springer International Publishing, 482-490.
- LOWE, D. G. 2004a. Distinctive Image Features from Scale-Invariant Keypoints. *International Journal of Computer Vision*, 60, 91-110.
- LOWE, G. 2004b. SIFT-The Scale Invariant Feature Transform. *Int. J.*, 2, 91-110.
- LUCIEER, A., JONG, S. M. D. & TURNER, D. 2014. Mapping landslide displacements using Structure from Motion (SfM) and image correlation of multi-temporal UAV photography. *Progress in physical geography*, 38, 97-116.

- LUDWIG, M., M. RUNGE, C., FRIESS, N., KOCH, T. L., RICHTER, S., SEYFRIED, S., WRAASE, L., LOBO, A., SEBASTIÀ, M.-T., REUDENBACH, C. & NAUSS, T. 2020. Quality Assessment of Photogrammetric Methods—A Workflow for Reproducible UAS Orthomosaics. *Remote Sensing*, 12, 3831.
- LUHMANN, T., FRASER, C. & MAAS, H.-G. 2016. Sensor modelling and camera calibration for close-range photogrammetry. *ISPRS Journal of Photogrammetry and Remote Sensing*, 115, 37-46.
- LV, Z., YANG, L., HE, Y., LIU, Z. & HAN, Z. 3D environment modeling with height dimension reduction and path planning for UAV. 2017 9th International Conference on Modelling, Identification and Control (ICMIC), 2017. IEEE, 734-739.
- MA, Y., WU, H., WANG, L., HUANG, B., RANJAN, R., ZOMAYA, A. & JIE, W. 2015. Remote sensing big data computing: Challenges and opportunities. *Future Generation Computer Systems*, 51, 47-60.
- MAFANYA, M., TSELE, P., BOTAI, J., MANYAMA, P., SWART, B. & MONATE, T. 2017. Evaluating pixel and object based image classification techniques for mapping plant invasions from UAV derived aerial imagery: *Harrisia pomanensis* as a case study. *ISPRS Journal of Photogrammetry and Remote Sensing*, 129, 1-11.
- MAFANYA, M., TSELE, P., BOTAI, J. O., MANYAMA, P., CHIRIMA, G. J. & MONATE, T. 2018. Radiometric calibration framework for ultra-high-resolution UAV-derived orthomosaics for large-scale mapping of invasive alien plants in semi-arid woodlands: *Harrisia pomanensis* as a case study. *International Journal of Remote Sensing*, 39, 5119-5140.
- MALLET, C., BRETAR, F., ROUX, M., SOERGEL, U. & HEIPKE, C. 2011. Relevance assessment of full-waveform lidar data for urban area classification. *ISPRS Journal of Photogrammetry and Remote Sensing*, 66, S71-S84.
- MANCINI, F., CASTAGNETTI, C., ROSSI, P., DUBBINI, M., FAZIO, N. L., PERROTTI, M. & LOLLINO, P. 2017. An Integrated Procedure to Assess the Stability of Coastal Rocky Cliffs: From UAV Close-Range Photogrammetry to Geomechanical Finite Element Modeling. *Remote Sensing*, 9, 1235.
- MANCINI, F., DUBBINI, M., GATTELLI, M., STECCHI, F., FABBRI, S. & GABBIANELLI, G. 2013. Using unmanned aerial vehicles (UAV) for high-resolution reconstruction of topography: The structure from motion approach on coastal environments. *Remote sensing*, 5, 6880-6898.
- MANFREDA, S., DVORAK, P., MULLEROVA, J., HERBAN, S., VUONO, P., ARRANZ JUSTEL, J. J. & PERKS, M. 2019. Assessing the Accuracy of

- Digital Surface Models Derived from Optical Imagery Acquired with Unmanned Aerial Systems. *Drones*, 3, 15.
- MANFREDA, S., DVORAK, P., MULLEROVA, J., HERBAN, S., VUONO, P., JUSTEL, J. J. A. & PERKS, M. 2018a. Accuracy assessment on unmanned aerial system derived digital surface models.
- MANFREDA, S., MCCABE, M. F., MILLER, P. E., LUCAS, R., PAJUELO MADRIGAL, V., MALLINIS, G., BEN DOR, E., HELMAN, D., ESTES, L., CIRAOLO, G., MÜLLEROVÁ, J., TAURO, F., DE LIMA, M. I., DE LIMA, J. L. M. P., MALTESE, A., FRANCES, F., CAYLOR, K., KOHV, M., PERKS, M., RUIZ-PÉREZ, G., SU, Z., VICO, G. & TOTH, B. 2018b. On the Use of Unmanned Aerial Systems for Environmental Monitoring. *Remote Sensing*, 10, 641.
- MARR, D. & POGGIO, T. 1976. Cooperative computation of stereo disparity. *Science*, 194, 283-287.
- MAYBANK, S. 2012. *Theory of reconstruction from image motion*, Springer Science & Business Media.
- MAYR, A., BREMER, M. & RUTZINGER, M. 2020. 3D Point Errors and Change Detection Accuracy of Unmanned Aerial Vehicle Laser Scanning Data. *ISPRS Ann. Photogramm. Remote Sens. Spatial Inf. Sci.*, V-2-2020, 765-772.
- MEDJKANE, M., MAQUAIRE, O., COSTA, S., ROULLAND, T., LETORTU, P., FAUCHARD, C., ANTOINE, R. & DAVIDSON, R. 2018. High-resolution monitoring of complex coastal morphology changes: Cross-efficiency of SfM and TLS-based survey (Vaches-Noires cliffs, Normandy, France). *Landslides*, 15, 1097-1108.
- MEINEN, B. U. & ROBINSON, D. T. 2020. Mapping erosion and deposition in an agricultural landscape: Optimization of UAV image acquisition schemes for SfM-MVS. *Remote Sensing of Environment*, 239, 111666.
- MESAS-CARRASCOSA, F.-J., DE CASTRO, A. I., TORRES-SÁNCHEZ, J., TRIVIÑO-TARRADAS, P., JIMÉNEZ-BRENES, F. M., GARCÍA-FERRER, A. & LÓPEZ-GRANADOS, F. 2020. Classification of 3D Point Clouds Using Color Vegetation Indices for Precision Viticulture and Digitizing Applications. *Remote Sensing*, 12, 317.
- MICHELETTI, N., CHANDLER, J. H. & LANE, S. N. 2015. Investigating the geomorphological potential of freely available and accessible structure-from-motion photogrammetry using a smartphone. *Earth Surface Processes and Landforms*, 40, 473-486.
- MILLER, H. J. & GOODCHILD, M. F. 2015. Data-driven geography. *GeoJournal*, 80, 449-461.

- MOHD NOOR, N., ABDULLAH, A. & HASHIM, M. 2018. Remote sensing UAV/drones and its applications for urban areas: a review. *IOP Conference Series: Earth and Environmental Science*, 169, 012003.
- MOON, D., CHUNG, S., KWON, S., SEO, J. & SHIN, J. 2019. Comparison and utilization of point cloud generated from photogrammetry and laser scanning: 3D world model for smart heavy equipment planning. *Automation in Construction*, 98, 322-331.
- MOSBRUCKER, A. R., MAJOR, J. J., SPICER, K. R. & PITLICK, J. 2017. Camera system considerations for geomorphic applications of SfM photogrammetry. *Earth Surface Processes and Landforms*, 42, 969-986.
- MUHAISEN, A. A. 2016. two dimensional geometric rectification techniques for remote sensing satellite images: gaza city as a case study.
- MUTANGA, O., SKIDMORE, A. K., KUMAR, L. & FERWERDA, J. 2005. Estimating tropical pasture quality at canopy level using band depth analysis with continuum removal in the visible domain. *International Journal of Remote Sensing*, 26, 1093-1108.
- NATIVI, S., MAZZETTI, P., SANTORO, M., PAPESCHI, F., CRAGLIA, M. & OCHIAI, O. 2015. Big Data challenges in building the Global Earth Observation System of Systems. *Environmental Modelling & Software*, 68, 1-26.
- NETTIS, A., SAPONARO, M. & NANNA, M. 2020. RPAS-Based Framework for Simplified Seismic Risk Assessment of Italian RC-Bridges. *Buildings*, 10, 150.
- NHAMO, L., MAGIDI, J., NYAMUGAMA, A., CLULOW, A. D., SIBANDA, M., CHIMONYO, V. G. P. & MABHAUDHI, T. 2020. Prospects of Improving Agricultural and Water Productivity through Unmanned Aerial Vehicles. *Agriculture*, 10, 256.
- NIEDERHEISER, R., WINKLER, M., DI CECCO, V., ERSCHBAMER, B., FERNÁNDEZ, R., GEITNER, C., HOFBAUER, H., KALAITZIDIS, C., KLINGRABER, B., LAMPRECHT, A., LORITE, J., NICKLAS, L., NYKTAS, P., PAULI, H., STANISCI, A., STEINBAUER, K., THEURILLAT, J. P., VITTOZ, P. & RUTZINGER, M. 2021. Using automated vegetation cover estimation from close-range photogrammetric point clouds to compare vegetation location properties in mountain terrain. *GIScience & Remote Sensing*, 1-18.
- O'CONNOR, J., SMITH, M. J. & JAMES, M. R. 2017. Cameras and settings for aerial surveys in the geosciences: Optimising image data. *Progress in Physical Geography: Earth and Environment*, 41, 325-344.
- OCAMPO, A. L. P. D., BANDALA, A. A. & DADIOS, E. P. Estimation of Triangular Greenness Index for Unknown Peak Wavelength Sensitivity of

- CMOS-acquired Crop Images. 2019 IEEE 11th International Conference on Humanoid, Nanotechnology, Information Technology, Communication and Control, Environment, and Management (HNICEM), 29 Nov.-1 Dec. 2019. 1-5.
- OLSSON, P.-O., VIVEKAR, A., ADLER, K., GARCIA MILLAN, V. E., KOC, A., ALAMRANI, M. & EKLUNDH, L. 2021. Radiometric Correction of Multispectral UAS Images: Evaluating the Accuracy of the Parrot Sequoia Camera and Sunshine Sensor. *Remote Sensing*, 13, 577.
- OTERO, L. D. 2015. Proof of concept for using unmanned aerial vehicles for high mast pole and bridge inspections. Florida. Dept. of Transportation. Research Center.
- PADRÓ, J.-C., MUÑOZ, F.-J., PLANAS, J. & PONS, X. 2019. Comparison of four UAV georeferencing methods for environmental monitoring purposes focusing on the combined use with airborne and satellite remote sensing platforms. *International Journal of Applied Earth Observation and Geoinformation*, 75, 130-140.
- PEPPA, M. V., MILLS, J. P., MOORE, P., MILLER, P. E. & CHAMBERS, J. E. 2019. Automated co-registration and calibration in SfM photogrammetry for landslide change detection. *Earth Surface Processes and Landforms*, 44, 287-303.
- PÉREZ, M., AGÜERA, F. & CARVAJAL, F. 2012. Digital Camera Calibration Using Images Taken From An Unmanned Aerial Vehicle. *ISPRS - International Archives of the Photogrammetry, Remote Sensing and Spatial Information Sciences*, XXXVIII-1/C22, 167-171.
- PFEIFER, N., LICHTI, D., BÖHM, J. & KAREL, W. 2013. 3D cameras: Errors, calibration and orientation. *TOF Range-Imaging Cameras*. Springer.
- PHOTOGRAMMETRY, A. S. F. & SENSING, R. 2015. ASPRS positional accuracy standards for digital geospatial data. *Photogrammetric Engineering and Remote Sensing*, 81, 1-26.
- POHL, C. & VAN GENDEREN, J. L. 1998. Review article multisensor image fusion in remote sensing: concepts, methods and applications. *International journal of remote sensing*, 19, 823-854.
- POMPILIO, L., MARINANGELI, L., AMITRANO, L., PACCI, G., D'ANDREA, S., IACULLO, S. & MONACO, E. 2018. Application of the empirical line method (ELM) to calibrate the airborne Daedalus-CZCS scanner. *European Journal of Remote Sensing*, 51, 33-46.
- POURALI, S., ARROWSMITH, C., CHRISMAN, N. & MATKAN, A. 2014. Vertical accuracy assessment of LiDAR ground points using minimum distance approach. *Proceedings Research@ Locate*, 14.

- PRZYBILLA, H.-J., LINDSTAEDT, M. & KERSTEN, T. 2019. Investigations into the Quality of Image-Based Point Clouds from UAV Imagery. *International Archives of the Photogrammetry, Remote Sensing & Spatial Information Sciences*.
- PRZYBILLA, H.-J., REUBER, C., BÄUMKER, M. & GERKE, M. 2015. Untersuchungen zur Genauigkeitssteigerung von UAV-Bildflügen. *Publikationen der Deutschen Gesellschaft für Photogrammetrie, Fernerkundung und Geoinformation e. V*, 24, 45-54.
- PRZYBILLA, H., BÄUMKER, M., LUHMANN, T., HASTEDT, H. & EILERS, M. 2020. Interaction between direct georeferencing, control point configuration and camera self-calibration for rtk-based uav photogrammetry. *The International Archives of Photogrammetry, Remote Sensing and Spatial Information Sciences*, 43, 485-492.
- PS, R. & JEYAN, M. L. 2020. Mini Unmanned Aerial Systems (UAV)-A Review of the Parameters for Classification of a Mini UAV. *International Journal of Aviation, Aeronautics, and Aerospace*, 7, 5.
- QI, J., GASTELLU-ETCHEGORRY, J.-P. & YIN, T. Reconstruction of 3D Forest Mock-Ups from Airborne LiDAR Data for Multispectral Image Simulation Using DART Model. *IGARSS 2018-2018 IEEE International Geoscience and Remote Sensing Symposium*, 2018. IEEE, 3975-3978.
- QIN, X., WU, G., LEI, J., FAN, F., YE, X. & MEI, Q. 2018. A Novel Method of Autonomous Inspection for Transmission Line based on Cable Inspection Robot LiDAR Data. *Sensors*, 18, 596.
- RACZYNSKI, R. J. 2017. *Accuracy analysis of products obtained from UAV-borne photogrammetry influenced by various flight parameters*. NTNU.
- RAMOS, M. M. & REMONDINO, F. 2015. Data fusion in cultural heritage-A review. *The International Archives of Photogrammetry, Remote Sensing and Spatial Information Sciences*, 40, 359.
- RANGEL, J. M. G., GONÇALVES, G. R. & PÉREZ, J. A. 2018. The impact of number and spatial distribution of GCPs on the positional accuracy of geospatial products derived from low-cost UASs. *International journal of remote sensing*, 39, 7154-7171.
- RÄSÄNEN, A. & VIRTANEN, T. 2019. Data and resolution requirements in mapping vegetation in spatially heterogeneous landscapes. *Remote Sensing of Environment*, 230, 111207.
- REHAK, M. & SKALOUD, J. 2017. Performance assessment of integrated sensor orientation with a low-cost GNSS receiver. *ISPRS Annals of the Photogrammetry, Remote Sensing and Spatial Information Sciences*, 4, 75-80.

- REMONDINO, F., DEL PIZZO, S., KERSTEN, T. P. & TROISI, S. Low-cost and open-source solutions for automated image orientation—A critical overview. *Euro-Mediterranean Conference*, 2012. Springer, 40-54.
- REMONDINO, F. & FRASER, C. 2006. Digital camera calibration methods: considerations and comparisons. *International Archives of the Photogrammetry, Remote Sensing and Spatial Information Sciences*, 36, 266-272.
- REMONDINO, F., NOCERINO, E., TOSCHI, I. & MENNA, F. 2017. A Critical Review of Automated Photogrammetric Processing of Large Datasets. *International Archives of the Photogrammetry, Remote Sensing & Spatial Information Sciences*, 42.
- REMONDINO, F., SPERA, M. G., NOCERINO, E., MENNA, F. & NEX, F. 2014. State of the art in high density image matching. *The photogrammetric record*, 29, 144-166.
- REN, H., ZHAO, Y., XIAO, W. & HU, Z. 2019. A review of UAV monitoring in mining areas: current status and future perspectives. *International Journal of Coal Science & Technology*, 6, 320-333.
- RIDOLFI, E., BUFFI, G., VENTURI, S. & MANCIOLA, P. 2017. Accuracy analysis of a dam model from drone surveys. *Sensors*, 17, 1777.
- RIEKE-ZAPP, D., WEGMANN, H., SANTEL, F. & NEARING, M. Digital photogrammetry for measuring soil surface roughness. *Proceedings of the American Society of Photogrammetry & Remote Sensing 2001 Conference—Gateway to the New Millennium?*. St Louis, MO.(American Society of Photogrammetry & Remote Sensing: Bethesda, MD), 2001.
- ROŞCA, S., SUOMALAINEN, J., BARTHOLOMEUS, H. & HEROLD, M. 2018. Comparing terrestrial laser scanning and unmanned aerial vehicle structure from motion to assess top of canopy structure in tropical forests. *Interface focus*, 8, 20170038.
- ROSNELL, T. & HONKAVAARA, E. 2012. Point cloud generation from aerial image data acquired by a quadcopter type micro unmanned aerial vehicle and a digital still camera. *Sensors*, 12, 453-480.
- RUIZ, J., DIAZ-MAS, L., PEREZ, F. & VIGURIA, A. 2013. Evaluating the accuracy of DEM generation algorithms from UAV imagery. *Int. Arch. Photogramm. Remote Sens. Spat. Inf. Sci*, 40, 333-337.
- RUPNIK, E., DAAKIR, M. & PIERROT DESEILLIGNY, M. 2017. MicMac – a free, open-source solution for photogrammetry. *Open Geospatial Data, Software and Standards*, 2, 14.
- SAFONOVA, A., GUIRADO, E., MAGLINETS, Y., ALCARAZ-SEGURA, D. & TABIK, S. 2021. Olive Tree Biovolume from UAV Multi-Resolution Image Segmentation with Mask R-CNN. *Sensors*, 21, 1617.

- SAID, K. O., ONIFADE, M., GITHIRIA, J. M., ABDULSALAM, J., BODUNRIN, M. O., GENC, B., JOHNSON, O. & AKANDE, J. M. 2021. On the application of drones: a progress report in mining operations. *International Journal of Mining, Reclamation and Environment*, 35, 235-267.
- SALVI, J., ARMANGUÉ, X. & BATLLE, J. 2002. A comparative review of camera calibrating methods with accuracy evaluation. *Pattern Recognition*, 35, 1617-1635.
- SANZ-ABLANEDO, E., CHANDLER, J. H., BALLESTEROS-PÉREZ, P. & RODRÍGUEZ-PÉREZ, J. R. 2020. Reducing systematic dome errors in digital elevation models through better UAV flight design. *Earth Surface Processes and Landforms*, 45, 2134-2147.
- SANZ-ABLANEDO, E., CHANDLER, J. H., RODRÍGUEZ-PÉREZ, J. R. & ORDÓÑEZ, C. 2018. Accuracy of Unmanned Aerial Vehicle (UAV) and SfM Photogrammetry Survey as a Function of the Number and Location of Ground Control Points Used. *Remote Sensing*, 10, 1606.
- SAPONARO, M., AGAPIOU, A., HADJIMITSIS, D. G. & TARANTINO, E. 2021. Influence of Spatial Resolution for Vegetation Indices' Extraction Using Visible Bands from Unmanned Aerial Vehicles' Orthomosaics Datasets. *Remote Sensing*, 13, 3238.
- SAPONARO, M., CAPOLUPO, A., CAPORUSSO, G., REINA, A., FRATINO, U. & TARANTINO, E. Exploring UAV and Cloud Platform Potentialities for Detecting Geomorphological Changes in Coastal Environment. In: PANAYOTIS C. YANNOPOULOS, P. E., IEROTHEOS ZACHARIAS, IOANNIS D. MANARIOTIS, GEORGE KORATIS, CHRISTOS CHRISTODOULATOS AND AGAMEMNON KOUTSOSPYROS, ed. Protection and Restoration of the Environment XV, 2020 2020a Patras, Greece.
- SAPONARO, M., CAPOLUPO, A., TARANTINO, E. & FRATINO, U. Comparative Analysis of Different UAV-Based Photogrammetric Processes to Improve Product Accuracies. *International Conference on Computational Science and Its Applications*, 2019a. Springer, 225-238.
- SAPONARO, M., CAPOLUPO, A., TURSO, A. & TARANTINO, E. Cloud-to-cloud assessment of UAV and TLS 3D reconstructions of cultural heritage monuments: the case of Torre Zozzoli. *Eighth International Conference on Remote Sensing and Geoinformation of the Environment (RSCy2020)*, 2020b. International Society for Optics and Photonics, 1152408.
- SAPONARO, M., TARANTINO, E. & FRATINO, U. Geometric accuracy evaluation of geospatial data using low-cost sensors on small UAVs.

- International Conference on Computational Science and Its Applications, 2018. Springer, 364-374.
- SAPONARO, M., TARANTINO, E. & FRATINO, U. Generation of 3D surface models from UAV imagery varying flight patterns and processing parameters. AIP Conference Proceedings, 2019b. AIP Publishing LLC, 280009.
- SAPONARO, M., TARANTINO, E., REINA, A., FURFARO, G. & FRATINO, U. 2019c. Assessing the Impact of the Number of GCPS on the Accuracy of Photogrammetric Mapping from UAV Imagery. *Baltic Surveying*, 43.
- SAPONARO, M., TURSO, A. & TARANTINO, E. Parallel Development of Comparable Photogrammetric Workflows Based on UAV Data Inside SW Platforms. In: GERVASI, O., MURGANTE, B., MISRA, S., GARAU, C., BLEČIĆ, I., TANIAR, D., APDUHAN, B. O., ROCHA, A. M. A. C., TARANTINO, E., TORRE, C. M. & KARACA, Y., eds. Computational Science and Its Applications – ICCSA 2020, 2020// 2020c Cham. Springer International Publishing, 693-708.
- SCHONBERGER, J. L. & FRAHM, J.-M. Structure-from-motion revisited. Proceedings of the IEEE conference on computer vision and pattern recognition, 2016. 4104-4113.
- SEIER, G., STANGL, J., SCHÖTTL, S., SULZER, W. & SASS, O. 2017. UAV and TLS for monitoring a creek in an alpine environment, Styria, Austria. *International Journal of Remote Sensing*, 38, 2903-2920.
- SERIFOGLU YILMAZ, C., YILMAZ, V. & GÜNGÖR, O. 2018. Investigating the performances of commercial and non-commercial software for ground filtering of UAV-based point clouds. *International Journal of Remote Sensing*, 39, 5016-5042.
- SHAHMORADI, J., TALEBI, E., ROGHANCHI, P. & HASSANALIAN, M. 2020. A Comprehensive Review of Applications of Drone Technology in the Mining Industry. *Drones*, 4, 34.
- SHI, B. & LIU, C. UAV for landslide mapping and deformation analysis. International Conference on Intelligent Earth Observing and Applications 2015, 2015. International Society for Optics and Photonics, 98080P.
- SHIROWZHAN, S., SEPASGOZAR, S. M. E., LI, H., TRINDER, J. & TANG, P. 2019. Comparative analysis of machine learning and point-based algorithms for detecting 3D changes in buildings over time using bi-temporal lidar data. *Automation in Construction*, 105, 102841.
- SHUKLA, A. & JAIN, K. 2020. Automatic extraction of urban land information from unmanned aerial vehicle (UAV) data. *Earth Science Informatics*, 13, 1225-1236.

- SIQUEIRA, H. L., MARCATO, J., MATSUBARA, E. T., ELTNER, A., COLARES, R. A. & SANTOS, F. M. The Impact of Ground Control Point Quantity on Area and Volume Measurements with UAV SFM Photogrammetry Applied in Open Pit Mines. IGARSS 2019 - 2019 IEEE International Geoscience and Remote Sensing Symposium, 28 July-2 Aug. 2019 2019. 9093-9096.
- SKOROBOGATOV, G., BARRADO, C. & SALAMÍ, E. 2020. Multiple UAV Systems: A Survey. *Unmanned Systems*, 08, 149-169.
- SMITH, D. & HEIDEMANN, H. K. 2015. New standard for new era: Overview of the 2015 ASPRS positional accuracy standards for digital geospatial data. *Photogrammetric Engineering & Remote Sensing*, 81, 173-176.
- SMITH, G. M. & MILTON, E. J. 1999. The use of the empirical line method to calibrate remotely sensed data to reflectance. *International Journal of Remote Sensing*, 20, 2653-2662.
- SMITH, M. W., CARRIVICK, J. & QUINCEY, D. 2016. Structure from motion photogrammetry in physical geography. *Progress in Physical Geography*, 40, 247 - 275.
- SMITH, M. W. & VERICAT, D. 2015. From experimental plots to experimental landscapes: topography, erosion and deposition in sub-humid badlands from structure-from-motion photogrammetry. *Earth Surface Processes and Landforms*, 40, 1656-1671.
- SNAVELY, N., SEITZ, S. M. & SZELISKI, R. 2006. Photo tourism: exploring photo collections in 3D. *ACM siggraph 2006 papers*.
- SNAY, R. & SOLER, T. 2008. Continuously Operating Reference Station (CORS): History, Applications, and Future Enhancements. *Journal of Surveying Engineering*, 134, 95-104.
- SOFIA, G., HILLIER, J. K. & CONWAY, S. J. 2016. Frontiers in Geomorphometry and Earth Surface Dynamics: possibilities, limitations and perspectives. *Earth Surface Dynamics*, 4, 721-725.
- SON, S. W., KIM, D. W., SUNG, W. G. & YU, J. J. 2020. Integrating UAV and TLS Approaches for Environmental Management: A Case Study of a Waste Stockpile Area. *Remote Sensing*, 12, 1615.
- SONNESSA, A., SAPONARO, M., ALFIO, V., CAPOLUPO, A., TURSO, A. & TARANTINO, E. 2020. Indoor Positioning Methods – A Short Review and First Tests Using a Robotic Platform for Tunnel Monitoring.
- SZELISKI, R. 2011. Structure from motion. *Computer Vision*. Springer.
- TANG, J., WANG, D., ZHANG, Z., HE, L., XIN, J. & XU, Y. 2017. Weed identification based on K-means feature learning combined with convolutional neural network. *Computers and electronics in agriculture*, 135, 63-70.

- TARANTINO, E. & FIGORITO, B. 2014. Steerable filtering in interactive tracing of archaeological linear features using digital true colour aerial images. *International Journal of Digital Earth*, 7, 870-880.
- TEAM, Q. D. 2021. *QGIS Geographic Information System* [Online]. Available: <https://www.qgis.org/> [Accessed].
- THEMISTOCLEOUS, K., METTAS, C., EVAGOROU, E. & HADJIMITSIS, D. The use of UAVs and photogrammetry for the documentation of cultural heritage monuments: the case study of the churches in Cyprus. *Earth Resources and Environmental Remote Sensing/GIS Applications X*, 2019. International Society for Optics and Photonics, 111560I.
- THEULE, J., BERTOLDI, G., COMITI, F., MACCONI, P. & MAZZORANA, B. 2015. Exploring topographic methods for monitoring morphological changes in mountain channels of different size and slope. *EGUGA*, 8893.
- THOMAS, H., GOULETTE, F., DESCHAUD, J.-E., MARCOTEGUI, B. & LEGALL, Y. Semantic classification of 3D point clouds with multiscale spherical neighborhoods. 2018 International conference on 3D vision (3DV), 2018. IEEE, 390-398.
- TMUŠIĆ, G., MANFREDA, S., AASEN, H., JAMES, M. R., GONÇALVES, G., BEN-DOR, E., BROOK, A., POLINOVA, M., ARRANZ, J. J. & MÉSZÁROS, J. 2020. Current practices in UAS-based environmental monitoring. *Remote Sensing*, 12, 1001.
- ULLMAN, S. 1979. The interpretation of structure from motion. *Proceedings of the Royal Society of London. Series B. Biological Sciences*, 203, 405-426.
- URBAN, R., ŠTRONER, M., BLISTAN, P., KOVANIČ, Ľ., PATERA, M., JACKO, S., ĎURIŠKA, I., KELEMEN, M. & SZABO, S. 2019. The Suitability of UAS for Mass Movement Monitoring Caused by Torrential Rainfall—A Study on the Talus Cones in the Alpine Terrain in High Tatras, Slovakia. *ISPRS International Journal of Geo-Information*, 8, 317.
- USGS. *What does "georeferenced" mean?* [Online]. Available: https://www.usgs.gov/faqs/what-does-georeferenced-mean?qt-news_science_products=0#qt-news_science_products [Accessed 06/08/2021].
- VESSET, D. & GEORGE, J. Worldwide Big Data and Analytics Spending Guide. *IDC. ULR*: <https://www.idc.com/getdoc.jsp>.
- VILLANUEVA, J. K. S. & BLANCO, A. C. 2019. Optimization of Ground Control Point (GCP) Configuration for Unmanned Aerial Vehicle (UAV) Survey Using Structure from Motion (SfM). *Int. Arch. Photogramm. Remote Sens. Spatial Inf. Sci.*, XLII-4/W12, 167-174.

- VILLAREAL, M. K. & TONGCO, A. F. 2019. Multi-sensor Fusion Workflow for Accurate Classification and Mapping of Sugarcane Crops. *Engineering, Technology & Applied Science Research*, 9, 4085-4091.
- VRINDTS, E., MOUAZEN, A. M., REYNIERS, M., MAERTENS, K., MALEKI, M., RAMON, H. & DE BAERDEMAEKER, J. 2005. Management zones based on correlation between soil compaction, yield and crop data. *Biosystems Engineering*, 92, 419-428.
- WALDHAUSER, C., HOCHREITER, R., OTEPKA, J., PFEIFER, N., GHUFFAR, S., KORZENIOWSKA, K. & WAGNER, G. 2014. Automated classification of airborne laser scanning point clouds. *Solving Computationally Expensive Engineering Problems*. Springer.
- WAN, L., LI, Y., CEN, H., ZHU, J., YIN, W., WU, W., ZHU, H., SUN, D., ZHOU, W. & HE, Y. 2018. Combining UAV-Based Vegetation Indices and Image Classification to Estimate Flower Number in Oilseed Rape. *Remote Sensing*, 10, 1484.
- WANG, C., CHO, Y. K. & KIM, C. 2015. Automatic BIM component extraction from point clouds of existing buildings for sustainability applications. *Automation in Construction*, 56, 1-13.
- WANG, C. & MYINT, S. W. 2015. A Simplified Empirical Line Method of Radiometric Calibration for Small Unmanned Aircraft Systems-Based Remote Sensing. *IEEE Journal of Selected Topics in Applied Earth Observations and Remote Sensing*, 8, 1876-1885.
- WARFIELD, A. D. & LEON, J. X. 2019. Estimating mangrove forest volume using terrestrial laser scanning and UAV-derived structure-from-motion. *Drones*, 3, 32.
- WEIDNER, L., WALTON, G. & KRAJNOVICH, A. 2021. *Classifying rock slope materials in photogrammetric point clouds using robust color and geometric features*.
- WEIDNER, L., WALTON, G. & KROMER, R. 2019. Classification methods for point clouds in rock slope monitoring: A novel machine learning approach and comparative analysis. *Engineering Geology*, 263, 105326.
- WEINMANN, M., JUTZI, B. & MALLETT, C. 2014. Semantic 3D scene interpretation: A framework combining optimal neighborhood size selection with relevant features. *ISPRS Ann. Photogramm. Remote Sens. Spatial Inf. Sci.*, II-3, 181-188.
- WEINMANN, M., SCHMIDT, A., MALLETT, C., HINZ, S., ROTTENSTEINER, F. & JUTZI, B. 2015. Contextual Classification of Point Cloud Data by Exploiting Individual 3D Neighbourhoods. *ISPRS Ann. Photogramm. Remote Sens. Spatial Inf. Sci.*, II-3/W4, 271-278.

- WESTAWAY, R., LANE, S. & HICKS, D. 2000. The development of an automated correction procedure for digital photogrammetry for the study of wide, shallow, gravel-bed rivers. *Earth Surface Processes and Landforms: The Journal of the British Geomorphological Research Group*, 25, 209-226.
- WHEATON, J. M., BRASINGTON, J., DARBY, S. E. & SEAR, D. A. 2010. Accounting for uncertainty in DEMs from repeat topographic surveys: improved sediment budgets. *Earth surface processes and landforms: the journal of the British Geomorphological Research Group*, 35, 136-156.
- WHITEHEAD, K. & HUGENHOLTZ, C. H. 2015. Applying ASPRS accuracy standards to surveys from small unmanned aircraft systems (UAS). *Photogrammetric engineering & remote sensing*, 81, 787-793.
- WILLIAMS, J. G., ROSSER, N. J., HARDY, R. J., BRAIN, M. J. & AFANA, A. A. 2018. Optimising 4-D surface change detection: an approach for capturing rockfall magnitude–frequency. *Earth Surf. Dynam.*, 6, 101-119.
- WINIWARTER, L., ANDERS, K. & HÖFLE, B. 2021. M3C2-EP: Pushing the limits of 3D topographic point cloud change detection by error propagation. *ISPRS Journal of Photogrammetry and Remote Sensing*, 178, 240-258.
- WOLD, S., ESBENSEN, K. & GELADI, P. 1987. Principal component analysis. *Chemometrics and Intelligent Laboratory Systems*, 2, 37-52.
- WOLF, P. R., DEWITT, B. A. & WILKINSON, B. E. 2014. *Elements of Photogrammetry with Applications in GIS*, McGraw-Hill Education.
- WU, J. & ZHANG, J. 2019. New Automated BIM Object Classification Method to Support BIM Interoperability. *Journal of Computing in Civil Engineering*, 33, 04019033.
- XIE, Y., SHA, Z. & YU, M. 2008. Remote sensing imagery in vegetation mapping: a review. *Journal of plant ecology*, 1, 9-23.
- XU, Z., WU, T., SHEN, Y. & WU, L. 2016. Three dimensional reconstruction of large cultural heritage objects based on uav video and tls data. *The International Archives of Photogrammetry, Remote Sensing and Spatial Information Sciences*, 41, 985.
- YANG, L., CHENG, J. C. P. & WANG, Q. 2020. Semi-automated generation of parametric BIM for steel structures based on terrestrial laser scanning data. *Automation in Construction*, 112, 103037.
- YANO, I. H., ALVES, J. R., SANTIAGO, W. E. & MEDEROS, B. J. T. 2016. Identification of weeds in sugarcane fields through images taken by UAV and Random Forest classifier. *IFAC-PapersOnLine*, 49, 415-420.
- YAO, H., QIN, R. & CHEN, X. 2019. Unmanned Aerial Vehicle for Remote Sensing Applications—A Review. *Remote Sensing*, 11, 1443.

- YU, H., WANG, J., BAI, Y., YANG, W. & XIA, G.-S. 2018a. Analysis of large-scale UAV images using a multi-scale hierarchical representation. *Geospatial Information Science*, 21, 33-44.
- YU, M., YANG, C. & LI, Y. 2018b. Big Data in Natural Disaster Management: A Review. *Geosciences*, 8, 165.
- YUSOFF, A. R., ARIFF, M. M., IDRIS, K. M., MAJID, Z. & CHONG, A. K. 2017. Camera calibration accuracy at different UAV flying heights. *The international archives of photogrammetry, remote sensing and spatial information sciences*, 42, 595.
- ZHANG, L., RUPNIK, E. & PIERROT-DESEILLIGNY, M. 2020. Guided Feature Matching for Multi-Epoch Historical Image Blocks Pose Estimation. *ISPRS Ann. Photogramm. Remote Sens. Spatial Inf. Sci.*, V-2-2020, 127-134.
- ZHANG, X., ZHANG, F., QI, Y., DENG, L., WANG, X. & YANG, S. 2019a. New research methods for vegetation information extraction based on visible light remote sensing images from an unmanned aerial vehicle (UAV). *International Journal of Applied Earth Observation and Geoinformation*, 78, 215-226.
- ZHANG, Y., WU, H. & YANG, W. 2019b. Forests growth monitoring based on tree canopy 3D reconstruction using UAV aerial photogrammetry. *Forests*, 10, 1052.
- ZHANG, Z. 2000. A flexible new technique for camera calibration. *IEEE Transactions on pattern analysis and machine intelligence*, 22, 1330-1334.
- ZHOU, Y., RUPNIK, E., MEYNARD, C., THOM, C. & PIERROT-DESEILLIGNY, M. 2020. Simulation and Analysis of Photogrammetric UAV Image Blocks—Influence of Camera Calibration Error. *Remote Sensing*, 12, 22.
- ZOU, Y., LI, G. & WANG, S. The Fusion of Satellite and Unmanned Aerial Vehicle (UAV) Imagery for Improving Classification Performance. 2018 IEEE International Conference on Information and Automation (ICIA), 11-13 Aug. 2018. 836-841.

CURRICULUM VITAE

Personal Information



Saponaro Mirko

Birthday 04/14/1989 | **Nationality** Italian

Strada Statale 16 Complanare Ovest 96/A 96/B – 70126 Bari (BA)

(+39) 349 00 62 790

saponaromirko@gmail.com

mirko.saponaro@pec.it

ORCID: <https://orcid.org/0000-0002-7211-0837>

Scopus Author ID: 57202950597

ResearchGate: https://www.researchgate.net/profile/Mirko_Saponaro

LinkedIn: <https://www.linkedin.com/in/mirko-saponaro-58aa98a1>

Scientific Publications

CONFERENCE PROCEEDINGS:

- Mirko Saponaro, Eufemia Tarantino, Umberto Fratino: Geometric Accuracy Evaluation of Geospatial Data Using Low-Cost Sensors on Small UAVs. Computational Science and Its Applications – ICCSA 2018, 07/2018: pages 364-374; ISBN: 978-3-319-95173-7, DOI:10.1007/978-3-319-95174-4_29
- Mirko Saponaro, Eufemia Tarantino, Umberto Fratino: Generation of 3D surface models from UAV imagery varying flight patterns and processing parameters. CENTRAL EUROPEAN SYMPOSIUM ON THERMOPHYSICS 2019 (CEST); 07/2019, DOI:10.1063/1.5114292
- Mirko Saponaro, Alessandra Capolupo, Eufemia Tarantino, Umberto Fratino: Comparative Analysis of Different UAV-Based Photogrammetric Processes to Improve Product Accuracies. International Conference on Computational Science and Its Applications; 06/2019, DOI:10.1007/978-3-030-24305-0_18
- M. Saponaro, L. Pratola, A. Saponieri, E. Tarantino, L. Damiani and U. Fratino, “Cloud-to-Cloud Comparison and Integration of TLS and UAV Surveys for the Maintenance of Coastal Protection Systems”, in Short Course/Conference on Applied Coastal Research 2019 – SCACR 2019

- Capolupo, C. Monterisi, M. Saponaro, U. Fratino and E. Tarantino, “Detecting Long-Term Changes of Vegetation in Vulnerable Coastal Areas Using Landsat Satellite Images”, in Short Course/Conference on Applied Coastal Research 2019 – SCACR 2019
- F. Argese, G. Erriquez, A. Galeandro, S.G. Manrique, M.G. Imperiale, M. Saponaro, A.R. Specchiarello, E. Tarantino, A. Turso, “Piattaforma HW/SW per la gestione dei Cantieri Tecnologici per Infrastrutture Civili” -XXIII Conferenza Nazionale ASITA, 12-14 Novembre 2019, Trieste
- Saponaro, M., Capolupo, A., Caporusso, G., Borgogno Mondino, E., and Tarantino, E.: Predicting the Accuracy of Photogrammetric 3D Reconstruction from Camera Calibration Parameters Through a Multivariate Statistical Approach, *Int. Arch. Photogramm. Remote Sens. Spatial Inf. Sci.*, XLIII-B2-2020, 479–486, <https://doi.org/10.5194/isprs-archives-XLIII-B2-2020-479-2020>, 2020
- Mirko Saponaro, Alessandra Capolupo, Adriano Turso, and Eufemia Tarantino “Cloud-to-cloud assessment of UAV and TLS 3D reconstructions of cultural heritage monuments: the case of Torre Zozzoli”, *Proc. SPIE 11524, Eighth International Conference on Remote Sensing and Geoinformation of the Environment (RSCy2020)*, 1152408 (26 August 2020); <https://doi.org/10.1117/12.2570771>
- Alessandra Capolupo, Cristina Monterisi, Mirko Saponaro, and Eufemia Tarantino “Multi-temporal analysis of land cover changes using Landsat data through Google Earth Engine platform”, *Proc. SPIE 11524, Eighth International Conference on Remote Sensing and Geoinformation of the Environment (RSCy2020)*, 1152419 (26 August 2020); <https://doi.org/10.1117/12.2571228>
- Saponaro, M., Turso, A., & Tarantino, E. (2020, July). Parallel development of comparable photogrammetric workflows based on SAPR data inside SW platforms. In *International Conference on Computational Science and Its Applications* (pp. 693-708). Springer, Cham
- Sonnessa, A., Saponaro, M., Alfio, V. S., Capolupo, A., Turso, A., & Tarantino, E. (2020, July). Indoor Positioning Methods—A Short Review and First Tests Using a Robotic Platform for Tunnel Monitoring. In *International Conference on Computational Science and Its Applications* (pp. 664-679). Springer, Cham
- Capolupo, A., Maltese, A., Saponaro, M., & Costantino, D. (2020, September). Integration of terrestrial laser scanning and SAPR-SfM technique to generate a detailed 3D textured model of a heritage building. In *Earth Resources and Environmental Remote Sensing/GIS Applications XI* (Vol. 11534, p. 115340Z). International Society for Optics and Photonics
- Saponaro, M.; Capolupo, A.; Caporusso, G.; Reina, A.; Fratino, U.; Tarantino, E. Exploring Sapr and Cloud Platform Potentialities for Detecting Geomorphological Changes in Coastal Environment. In *Proceedings of Protection and Restoration of the Environment XV*, Patras, Greece, 2020
- Saponaro, M., Capolupo, A., Caporusso, G., and Tarantino, E.: Influence of Co-Alignment Procedures on the Co-Registration Accuracy of Multi-Epoch SfM Points Clouds, *Int. Arch. Photogramm. Remote Sens. Spatial Inf. Sci.*, XLIII-B2-2021, 231–238, <https://doi.org/10.5194/isprs-archives-XLIII-B2-2021-231-2021>, 2021.
- Saponaro M. (2021) Dimensionality Features Extraction Based-on Multi-

scale Neighborhood of Multi-samples UAV Point Clouds. In: Gervasi O. et al. (eds) Computational Science and Its Applications – ICCSA 2021. IC-
CSA 2021. Lecture Notes in Computer Science, vol 12955. Springer,
Cham. https://doi.org/10.1007/978-3-030-87007-2_4

JOURNAL PUBLICATIONS:

- Saponaro Mirko, Tarantino Eufemia, Reina Alessandro, Furfaro Giuseppe, Fratino Umberto: Assessing the Impact of the Number of GCPs on the Accuracy of Photogrammetric Mapping from UAV Imagery. 06/2019; 10:43-51., DOI:10.22616/j.balticsurveying.2019.006
- Saponaro, M.; Pratola, L.; Capolupo, A.; Saponieri, A.; Damiani, L.; Fratino, U.; Tarantino, E. Data fusion of terrestrial laser scanner and remotely piloted aircraft systems points clouds for monitoring the coastal protection systems. Aquatic Ecosystem Health and Management 2020, 10.1080/14634988.2020.1807299, doi:10.1080/14634988.2020.1807299
- Capolupo, A.; Saponaro, M.; Fratino, U.; Tarantino, E. Detection of spatio-temporal changes of vegetation in coastal areas subjected to soil erosion issue. Aquatic Ecosystem Health and Management 2020, 10.1080/14634988.2020.1802983, doi:10.1080/14634988.2020.1802983
- Nettis, A.; Saponaro, M.; Nanna, M. RPAS-Based Framework for Simplified Seismic Risk Assessment of Italian RC-Bridges. Buildings 2020, 10, 150
- Capolupo, A.; Saponaro, M.; Borgogno Mondino, E.; Tarantino, E. Combining Interior Orientation Variables to Predict the Accuracy of Rpas-Sfm 3D Models. Remote Sens. 2020, 12, 2674
- Saponaro, Mirko, Athos Agapiou, Diofantos G. Hadjimitsis, and Eufemia Tarantino. 2021. "Influence of Spatial Resolution for Vegetation Indices' Extraction Using Visible Bands from Unmanned Aerial Vehicles' Orthomosaics Datasets" Remote Sensing 13, no. 16: 3238. <https://doi.org/10.3390/rs13163238>

Awards and Prizes

Best Paper Award of the *21st International Conference on Computational Science and Its Applications (ICCSA 2021)*

Professional Experiences

From 2nd November 2021

Geoservices Technical Specialist

Planetek Italia S.r.l. - Via Massaua, 12 - 70132 - Bari, Italy

From 2nd October 2020
to 2nd April 2021

Visiting PhD Student

Prof. Diofantos G. Hadjimitsis and Prof. Athos Agapiou
Cyprus University of Technology - Archiepiskopou Kyprianou 30, Limassol 3036, Cyprus

From 1st May 2019
To 1st November 2019

Visiting Research Fellow – R&S

Eng. Adriano Turso
Sipal S.p.A. – Aeroporto “Marcello Arlotta” - Grottaglie (TA)

Education

From 1st November 2018
to 31st October 2021

PhD PON-RI in Risk and Environmental, Territorial and Building Development - XXXIV Cycle

Project: *Development of a framework to extract geospatial information from multi-resolution data for spatial analyses*

Tutor: Prof. Eufemia Tarantino

Polytechnic University of Bari, Via Orabona 4, 70125 Bari, Italy

From October 2015
to February 2018

Master's Degree in Environmental Engineering (110 cum laude)

Thesis Title: *"Valutazione delle precisioni geometriche di un sensore low-cost su SAPR"*

Relators: Prof. Eufemia Tarantino, Co-Relators: Prof. Umberto Fratino, Ing. Antonio Novelli

Polytechnic University of Bari, Via Orabona 4, 70125 Bari, Italy

From October 2008
to October 2015

Bachelor's Degree in Environmental Engineering (100/110)

Thesis Title: *"Indagine in sito dello stato dei terreni di un versante instabile"*

Relators: Prof. Federica Cotecchia, Co-Relators: Prof. Osvaldo Bottiglieri, Prof. Francesca Santaloia

Polytechnic University of Bari, Via Orabona 4, 70125 Bari, Italy



Polytechnic University of Bari
Via Orabona 4, 70125 Bari (BA), Italy
www.poliba.it



Department of Civil, Environmental, Land, Construction and Chemistry
Polytechnic University of Bari
Via Orabona 4, 70125 Bari (BA), Italy
<https://dicatechpoliba.it/en/dicatech-dipartimento>



SIPAL S.p.a.
Corso Vittorio Emanuele II, 178, 10138 Torino (TO), Italy
R&D - Strada Provinciale 83, Aeroporto Marcello Arlotta, 74023,
Grottaglie (TA), Italy - www.sipal.it



Cyprus University of Technology (CUT)
Archiepiskopou Kyprianou 30, Limassol 3036, Cyprus
www.cut.ac.cy



ERATOSTHENES Centre of Excellence
Sariopolou 2-6, 3036 Achilleos 2 Building, Limassol, Cyprus
www.eratosthenes.org.cy



The EXCELSIOR H2020 Teaming Phase 2 Project
www.excelsior2020.eu

The PhD scholarship was co-funded with resources from the National Operational Program Research and Innovation 2014-2020 (CCI 2014IT16M20P005), European Social Fund, Action I.1 "Innovative Doctorates with Industrial Characterization".



UNIONE EUROPEA
Fondo Sociale Europeo



POLITECNICO DI BARI
DICATEch

24 Gennaio 2022